# Uncaging strategies based on the VIPER approach

Dissertation zur Erlangung
des Doktorgrades der Naturwissenschaften

vorgelegt beim Fachbereich Physik
der Johann Wolfgang Goethe-Universität
in Frankfurt am Main

von
Daniela Kern-Michler

Frankfurt 2019

(D 30)

# Abstract

To gain a better understanding of complex mechanisms in biological systems, simultaneous control over multiple processes is key. To this purpose selective photo-uncaging has been developed. Photo-uncaging is an experimental scheme in which a molecule of interest has been inactivated synthetically and is activated by light. Usually a bond is cleaved and a leaving group is set free. The molecule which inactivates the molecule of interest and sets the leaving group free is called (photo-)cage. In a selective photo-uncaging scheme a number of leaving groups can be released independently, usually by irradiation with light of different wavelengths. This approach is, however, seriously limited in its applicability due to the properties of the involved cages and irradiation schemes. A major drawback is the usually quite broad UV-Vis absorption of the cages. This makes a selective activation by light difficult and limits the maximal number of independent cages severely.

Therefore, the aim of this thesis is to introduce the **Vi**brationally **P**romoted **E**lectronic **R**esonance (VIPER) 2D-IR pulse sequence in a alternative selective uncaging scheme.

The VIPER 2D-IR pulse sequence is a spectroscopic tool which allows to generate 2D-IR signals whose lifetime are independent of the vibrational relaxation lifetime. It has been first used to monitor chemical exchange. It consists of a narrowband infared pump pulse, a subsequent UV-Vis pump pulse and a broadband infrared probe pulse. The UV-Vis pump pulse is off-resonant with regard to the UV-Vis absorption band. Electronic excitation becomes only possible, if the infrared pump pulse modulates the UV-Vis transition of the IR-excited molecule. This modulation brings the UV-Vis transition in resonance with the UV-Vis pump pulse. Thereby, only the molecules which were pre-excited with the infrared pulse can be excited into the electronically excited state. A computational prediction of the modulation was carried out by Jan von Cosel in the Burghardt group.

The narrowband infrared pump pulse can be used to selectively excite a sub-ensemble of molecules in a mixture into an electronically excited state even if the UV-Vis spectra of all molecules are virtually identical. For this the sub-ensemble needs to exhibit an identifiable infrared spectrum. Combined with the introduction of isotope labels, which lead to changes in the infrared absorption spectra, the larger selectivity in the infrared region can be exploited for an alternative selective uncaging approach. In VIPER uncaging the infrared pump pulse selects the species and the subsequent UV-Vis pulse provides the energy needed for electronic

excitation upon which the photo cleavage can occur.

After an introduction of the principle idea of uncaging and VIPER spectroscopy, the concept of VIPER uncaging is introduced and its limits and requirements are discussed. Some examples for possible VIPER cages are reviewed.

A coumarin molecule (7-diethylamino coumarin) which can release an azide group was chosen as a first test molecule for VIPER uncaging. Its isotopomers were characterized to determine suitable spectroscopic markers for successful uncaging and to find fitting experimental conditions. The chosen coumarin cage has an UV-Vis absorption band at approximately 380 nm and a steep flank on the high wavelength side of the band. The quantum yield for the azide compound is between 10-20 % depending on the solvent's water content. The release was found to be on a picosecond timescale which is among the fastest known photo reactions, but the photo reaction mechanism has proven to be not straightforward. For the VIPER experiment on the mixture two isotopomers were chosen with a $^{13}C$ atom at different positions. In one species a ring mode of the coumarin is changed by the $^{13}C$ atom. In the other isotopomer the carbonyl stretching mode is influenced. The change in the ring mode region allows to select one species or the other with the infrared pre-excitation. Because of experimental difficulties only isotopomers with the same leaving group could be used. The successful selective electronic excitation of the individual isotopomers in a mixture was monitored by probing the carbonyl region.

As a second VIPER cage, *para*-hydroxyphenacyl (*p*HP) was chosen. A thiocyanate group was selected as leaving group. *p*HP cages have their electronic transition in the UV, with a maximum absorption at 290 nm. The shape of the spectrum is suitable and the quantum yield is very high, with values in the literature of up to 90 %. Also the photo reaction is well studied and the expected byproducts are well characterized. The chosen isotopologues were characterized spectroscopically. The resulting data on the photo reaction were in agreement with the mechanism proposed in the literature. The mixture for the VIPER experiment consisted of two isotopologues, where for one species all the C atoms in the ring were labelled and for the other the C-atom in the thiocyanate leaving group was labelled. Here the release of the different leaving groups, labelled and unlabelled thiocyanate, could be monitored selectively. This shows that it is possible to selectively release a molecule in a mixture of caged molecules by applying the VIPER pulse sequence.

The samples were synthesized by Matiss Reinfelds from the Heckel group and the VIPER experiments were done together with Carsten Neumann and with support of the Bredenbeck group.

The leaving groups were chosen because of their infrared absorption which allowed to directly monitor the successful cleavage by spectroscopy. This was needed

for the proof-of-concept experiment and to allow direct optimization of the experimental parameters but is not necessarily a requirement for VIPER uncaging.

Concerning the selectivity of the VIPER uncaging, the approach is at the moment mainly limited by the infrared pulse energy. The selective VIPER excitation is competing with unselective excitation directly by just the UV-Vis pulse. A more intense infrared pump pulse would increase only the selective VIPER excitation and thereby improve the contrast to the unspecific background.

To address this issue, the first steps towards an alternative infrared light generation are undertaken. In this alternative approach the infrared light for pre-excitation is directly generated by difference frequency generation of the laser output, i.e. the high energy 800 nm fundamental, and the output of a non-collinear optical parametric amplifier (NOPA). To achieve a narrowband pump pulse the pulses are chirped before mixing. In the scope of this thesis a NOPA has been installed and the mixing has been tested with available test crystal medium. While infrared wavelength region and power were not in the aspired range with this alternative crystal the feasibility of mixing between a NOPA output and the fundamental could be shown.

Other possibilities to increase the contrast to the unspecific background excitation by the UV-Vis pump pulse are discussed. For most applications of selective VIPER uncaging the detection by fs-laser spectroscopy will not be needed and could be replaced by other methods e.g. chromatography. This will allow the experimental parameters of the VIPER pulse sequence to be changed in a way which reduces unspecific excitation i.e. reducing the UV-Vis-pump energy and result in much better contrast.

In conclusion, the experimental data in this thesis shows the VIPER pulse sequence to be applicable to selective uncaging schemes and indicates measures to arrive at the specificity necessary for uncaging applications. This thesis was focused on uncaging photo reactions with isotopomers and isotopologues, but other types of photo reactions could in principle be controlled in the same way. It should be possible to address different isomers in mixtures or different ground states of proteins selectively. The discussed experiments are a significant step towards control over photo reactions in mixtures.

iv

# Contents

# 1 Motivation

Our understanding of the processes of life on a molecular level is rapidly growing. A wealth of experimental data has led to detailed concepts of complex biological processes like the workings of the respiratory chain or protein biosynthesis to name two prominent examples.

It is, however, currently not possible to directly observe cellular processes like transcription or cellular respiration. Therefore, our perception of them is limited by the observables that can be monitored in experiments. Additionally, our knowledge is significantly influenced by the constraints we need to put on the systems to make them experimentally accessible at all.

Molecules of interest can often be isolated by sophisticated preparation processes and various physical and chemical properties are exploited to gain insight into their structure and function. This might mean to take them out of their native environment for e.g. crystallization or experiments in gas phase.

However, to gain knowledge of their function and interaction they need to be studied in their native environment with as little perturbation as possible. Tools to control the environment or interaction partners are needed to further understanding of biological processes.

In terms of triggers with low perturbation to the native environment light has proven to be a good choice. A commonly applied tool to gain control by light is to use a photolabile protecting group (PPG), also called photocage. A molecule of interest is inactivated synthetically by a PPG and activated by irradiation. In a photo uncaging scheme usually a bond is cleaved and the caged molecule is set free. This method allows control over a chemical or biological process with high temporal and spatial precision [1–5].

To unravel the inner workings of complex and dynamic networks in chemical and biological systems, simultaneous control over multiple processes is often needed and therefore orthogonal photolabile protection groups or PPGs that can be uncaged by different wavelengths have been of major interest [6–10].

The term *orthogonal photouncaging* has first been mentioned in a seminal paper from the group of Bochet in the year 2000 [11] and means that the PPGs must be cleavable in any order. Otherwise the experimental scheme is called wavelength-selective uncaging. In most experimental cases true orthogonal uncaging is not necessary since the compounds can be synthesized in a way to achieve the desired uncaging sequence.

To this point there are close to thirty publications on orthogonal photo uncaging mainly in the areas of material science [7, 12–15], organic synthesis [10, 16] and biological applications as well as one tutorial review by Hansen et al. [6] available.

In the area of biological applications there are publications on caged oligonucleotids [17–19], on neurotransmitters [9, 20–23], gene-expression [24, 25] and control over protein function [26, 27]. Two additional papers are concerned with orthogonal photorelease in hydrogels [28] and photocaged antibiotics [29].

The number of simultaneously controllable processes is however limited in all of these approaches to maximal four different cleavage reactions. This limitation is due to the nature of the interaction between visible light and the PPG. The visible absorption bands are broad in comparison to the used wavelength range and their selectivity is therefore inherently limited.

The aim of this thesis is the development of an orthogonal uncaging scheme using the VIPER (VIbrationally Promoted Electronic Resonance) pulse sequence [30, 31].

The VIPER 2D-IR pulse sequence has its origin in exchange spectroscopy with infrared fs-laser systems. It has first been used to circumvent the limit of vibrational lifetime in 2D-IR exchange spectroscopy [30] and is a part of the recent development in mixed (infrared and visible) pulse sequences [31]. Transient 2D-IR, for example, has been applied to access new spectroscopic information on transient species [32–37] or electronically excited species [38–42]. Triggered exchange spectroscopy can be used to study non-equilibrium situations [43–45]. Mixed pulse sequence spectroscopy techniques can also be used to disentangle photoreactions [43, 46, 47] or for steering of reactions [48, 49]. In addition to the techniques in which infrared transitions are probed, Raman [50–56] or fluorescence transitions [57–60] can be used and give different insights.

The VIPER 2D-IR pulse sequence uses a narrow-band infrared pulse to pre-excite the sample. The frequency of a subsequent visible pulse is chosen in a way that the vibrationally pre-excited molecules are excited to the electroncially excited state. The lifetime of an electronically excited state is normally much longer than the lifetime of an vibrationally excited state. This allows to monitor the sample over a longer timescale [30].

The infrared pre-excitation can, however, also be used to select one species in a mixture. If this species can undergo a photoreaction, the VIPER pulse sequence can be used to induce and monitor photochemistry species-selectively [30, 31, 61].

To develop this into an orthogonal uncaging scheme a set of suitable VIPER cages needs to be found and characterized. Furthermore, the experimental parameters of the VIPER excitation need to be optimized for selectivity.

Instead of engineering PPGs for orthogonality by making their UV-Vis spectra as different as possible or exploiting their different photo reaction dynamics,

this approach exploits differences in the infrared spectrum to gain orthogonality between species. The spectral features in the infrared region are much narrower with regard to the wavelength of the used light than this is the case in the UV or visbile region. Therefore, much smaller changes in the molecules can be exploited to distinguish between the PPGs. As an extreme case, isotope labels will be introduced into the molecules to create cages with the same photochemistry but different infrared spectra.

In this work the concept of VIPER uncaging is introduced and influences on selectivity are discussed. The requirements for VIPER cages are shown and two cages with isotope labelling are characterized. Their selectivity in VIPER uncaging is shown and the achieved contrast is discussed. Additionally, the first steps towards an alternative generation of the narrowband IR pump pulse are undertaken.

# 2 Introduction

After introducing general considerations for the interaction of molecules with light and the special case of photo uncaging, an overview about pump-probe spectroscopy is given. Then the VIPER effect is introduced to serve as background for chapter 3 on page 31, where the new concept of VIPER uncaging is discussed. Lastly, an introduction to non-linear wavemixing processes is given as preparation for the discussion of a new IR pump light source in section 5.3 on page 111.

## 2.1 Interaction of Molecules with Light

In this section firstly a general introduction to the interaction between molecules and light is given. Molecules are two or more atoms which are covalently bound to each other, meaning they share an electron pair [62]. For this thesis their electronic and vibrational properties are of interest and introduced. The relevant attributes of light are shown. This is followed by an overview of absorption processes and absorption spectra in the UV-Vis and the infrared region. Lastly, the possible processes after absorption are introduced.

**Electronic properties of Molecules**   Since electrons have a wave-like character as well as a particle-like character only a probability to find them at a certain place around the nuclei of the molecule can be given. This probability is calculated from an electronic wave function and only distinct eigen states, depending on the molecular structure, are possible. These states describe possible three-dimensional standing waves of the electron waves in the presence of the nuclei and correspond to distinct energies. An electronic wave function describing a single electron in a certain electronic state is called an orbital [63].

The simplest orbital corresponds to a spherically symmetric probability density of an electron around a nucleus and is called $s$ orbital. The next class of orbitals is called $p$ orbital and has a nodal plane at the nucleus. Each orbital can only be occupied by two electrons with opposite spins [63]. The distribution of the electrons to the orbitals leads to the electron configuration. It is common to speak of electron shells, which are orbitals with the same energy. The electrons in the outer shell are called valence electrons and take part in chemical bonds [62].

For a molecule linear combinations of atomic orbitals (LCAO) allow to approximate molecular orbits. Depending on the phase of the overlapping atomic orbitals, the molecular orbital can be bonding, antibonding (denoted by $*$) or nonbonding [64]. A molecular orbital formed of two $s$ orbitals is called a $\sigma$ orbital, while a orbital formed from $p$ orbitals is called a $\pi$ orbital. Bonding orbitals have a lower energy, antibonding orbitals a higher energy than the atomic orbitals. The highest occupied molecular orbital is usually called HOMO and the lowest unoccupied one LUMO [63].

**Vibrational properties of Molecules** In contrast to atoms, molecules have inner degrees of freedom, the atoms of a molecule can move with respect to each other and oscillate around their equilibrium position [65].

The most simple molecule can be described as two spheres (the atoms) connected by a spring (the covalent bond). The atoms oscillate around their equilibrium position and the distance between the nuclei varies. Since atoms can also be described as waves, the system has vibrational Eigen states. These eigenstates correspond to vibrational niveaus (which can be imagined as standing waves of the atomic wave function) on the potential energy surface for an electronic state. For a simple two atomic molecule this can be assumed to be the parabolic potential of an harmonic oscillator [65].

$$\hat{H}\Psi_n = E_n \Psi_n \tag{2.1}$$

The Schrödinger equation equation (2.1) for this system leads to the energies given in equation (2.2). $\hat{H}$ is the Hamilton operator, $\Psi$ the wave function, $E$ the energy and $n$ the vibrational quantum number of the respective vibrational state.

$$E_n = h \cdot \nu_0 (n + \frac{1}{2}) \tag{2.2}$$

$h$ is the Planck constant and $\nu_0$ is the eigenfrequency (equation (2.3)).

$$\nu_0 = \sqrt{\frac{k}{\mu}} \tag{2.3}$$

$k$ is the spring force constant and $\mu$ (equation (2.4)) is the reduced mass of the spheres with masses $m_1$ and $m_2$.

$$\mu = \frac{m_1 \cdot m_2}{m_1 + m_2} \tag{2.4}$$

For a more realistic description of the vibrations of a real molecule the anharmonic Morse potential instead of the harmonic potential is used. In the Morse

potential the vibrational niveaus are no longer equidistant and it allows for dissociation of the molecule and overtones (transitions between niveaus which are further apart than $n = \pm 1$) [66].

Figure 2.1 shows a sketch of the energy levels in a molecule. Two 1D-Morse-potentials symbolize the energy surfaces of the electronic states $S_0$ and $S_1$. The vibrational states $\nu$ are given as horizontal lines in the potentials. The probabilities to find a nucleus at a certain position relative to the equilibrium position are visualized for the vibrational energy levels.
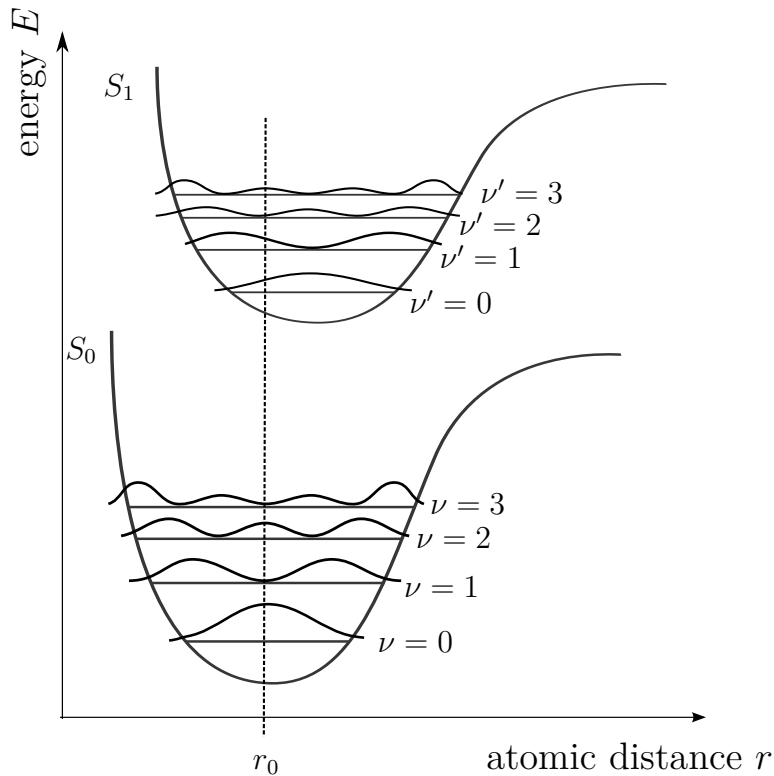


Figure 2.1: Schematic electronic and vibrational energy levels in a molecule. $S_0$ is the electronic ground state, $S_1$ is an electronically excited state, $\nu$ are the vibrational states, $r_0$ is the equilibrium position. The probabilities to find the nuclei at certain positions relative to the equilibrium position are visualized for the vibrational Eigen states.

The occupation of the different energy levels can be described by a Boltzmann distribution (equation (2.5) on the next page), where $N_{1/2}$ is the population of the states, $\Delta E$ the energy difference between them, $k_B$ the Boltzmann constant and

*T* the temperature [64].

$$\frac{N_2}{N_1} = e^{-\Delta E/k_B T} \tag{2.5}$$

At room temperature it is a good approximation to assume that all molecules are in the electronic and vibrational ground state [64].

**Light**   Similar to the electron, light has a wave-like and a particle-like character. In the wave model it can be imagined as an oscillation of electric and magnetic fields propagating through space. These oscillations are in phase and perpendicular to each other and to the propagation direction [63]. The distance between two maxima is the wavelength (given in nm) and can be converted into wavenumbers (cm$^{-1}$) the unit conventionally used in infrared spectroscopy [64].

The elementary particle of light is a photon and has a distinct energy $E$ depending on the wavelength $\lambda$ or wavenumber $\bar{\nu}$ of the light (given in equation (2.6), where $h$ is the Planck constant and $c$ the speed of light) [63].

$$E_\lambda = \frac{hc}{\lambda} = hc\bar{\nu} \tag{2.6}$$

If the energy of a photon matches a difference between energy levels (as depicted in figure 2.1 on the previous page) the photon can be absorbed. For transitions between electronic states light from the UV-Vis range (200-760 nm) is needed. For vibrational states infrared light (760 nm to 30 $\mu$m) is needed for excitation [64].

**Absorption**   If a molecule with a suitable electronic structure is irradiated by a wave of UV-Vis light, the electrons are affected by the oscillating electric field component of the light. A photon is absorbed and this results in an electronic structure rearrangement. For this it is important that the direction of the oscillation of the electric field (its polarization) matches the orientation of the wave functions describing the initial and final electronic state. The change in the charge distribution during the transition is described by the transition dipole moment, which can be calculated from the wave functions of the initial and the final electronic state. The probability for a transition depends on the projection of the polarization on the transition dipole moment ($cos^2(\alpha)$ where $\alpha$ is the angle between the polarization and the transition dipole moment). Therefore, the probability to excite an electron is the highest, if the light is polarized parallel to the transition dipole moment of the transition corresponding to the energy (i.e. wavelength) of the light. In an isotropic medium the orientation of the transition dipole moments with regard to the polarization of the incoming linearly polarized light is random.

Furthermore, the probability for a transition becomes larger with larger transition dipole moments and if a transition dipole moment is zero, the transition is called optically forbidden [63].

The positions of the nuclei factor also in the transition probability. The vibration of the heavy nuclei is much slower than the electronic excitation, which means that the molecular geometry stays the same during the excitation. Therefore, the probability for a transition is higher for similar geometries in the $S_0$ and $S_1$. This can be computed by squared nuclear overlap integrals:

$$P_{\nu \to \nu'} \propto \left[ \int \chi_\nu(\vec{r}) \chi_{\nu'}(\vec{r}) \mathrm{d}V \right]^2 \tag{2.7}$$

Where $\chi_\nu(\vec{r})$ is a vibrational wave function in the ground state $S_0$, while $\nu'$ indicates the $S_1$ and $\mathrm{d}V$ indicates that the integral is over all spatial coordinates. The squared wave functions give the probability to find a nucleus at a certain position and are sketched in figure 2.1 on page 7. The integral in equation (2.7) is called Franck-Condon integral.

In organic molecules the $S_0$, the electronic ground state, normally means that all orbitals up to the HOMO are occupied with two electrons. Therefore the $S_1$, the first electronically excited state, means usually that an electron has been promoted from HOMO to LUMO [63]. On the left side of figure 2.2 on the following page molecular orbitals according to their energy are shown. Antibinding orbitals (denoted with a ∗) have higher energy than nonbinding orbitals (n) and binding orbitals have the lowest energies. Transitions are labelled according to their initial and final state - $\pi \to \pi*$ for example [64].

For complex multi-atom molecules a schematic depiction in a Jablonski diagram (figure 2.2 on the next page right side) is helpful. The electronic ground state $S_0$ is depicted with horizontal lines representing the vibrational states.

**Spectroscopy**    The technique to monitor UV-Vis absorption is UV-Vis absorption spectroscopy. A transition is depicted in figure 2.3 on page 11 on the left side, while a corresponding UV-Vis spectrum in solution at room temperature is sketched next to it.

One observable in an UV-Vis spectrum is the position of the absorption band, which in theory corresponds directly to the transition, which has been excited. However, in solution and at room temperature the absorption band is not a narrow line. This is caused by the many different solvent micro environments the molecule is exposed to. Different momentary solvent charge distributions and other environmental effects result in slight shifts in the state energies and lead to a broadened absorption band [63].

In addition to the position and shape of the absorption band, the oscillator strength is of interest. The area under the absorption band is proportional to it. The absorption of photons by matter leads to changes in light intensity. These changes are observed in spectroscopy and can be described by the Lambert-Beer
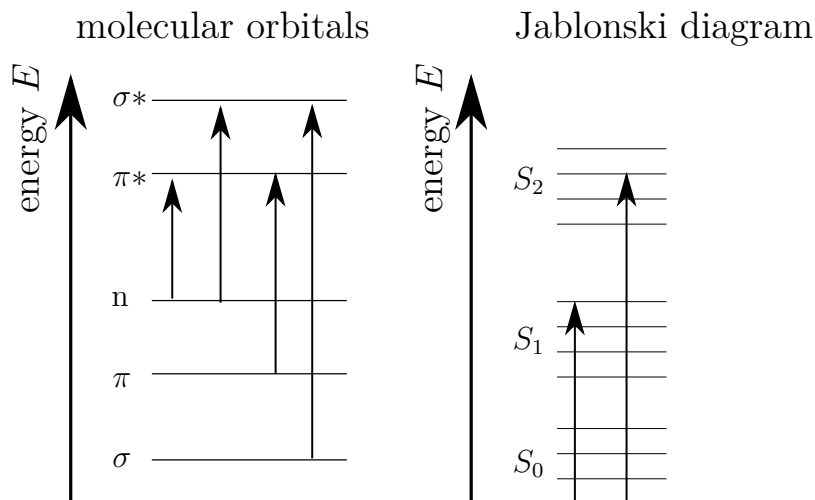
Figure 2.2: Left: Diagram of molecular orbitals with electronic transitions depicted as arrows. Right: Jablonski diagram, the horizontal lines are vibrational levels in the electronic states labelled $S$ for singlet, absorption is depicted as straight black up arrow.

law (equation (2.8)), where $A$ is called absorbance, $I_0$ and $I$ are the intensities before and after absorption, $\epsilon$ is the molecular extinction coefficient, $c$ the concentration of molecules and $d$ the optical pathlength [67].

$$A = lg\left(\frac{I_0}{I}\right) = \epsilon \cdot c \cdot d \tag{2.8}$$

UV-Vis spectra can be used to observe changes in the electronic structure, to determine UV-Vis absorption and to monitor photo reactions [67].

The energy of an infrared photon allows transitions between vibrational states of a molecule. The interaction between an electronic wave and a molecular vibration is possible if the molecular vibration coincides with a charge movement. This is the case, if the charges in a molecule are asymmetrically distributed or become unsymmetrical through the oscillation. A change in dipole moment is needed for a vibrational mode to be IR active. As for UV-Vis absorption the orientation of the transition dipole moment and the polarization of the absorbed light need to be parallel for the highest excitation probability.

We have already seen that the vibrational energy levels depend on the reduced mass and the force constant of the bond between the masses (equation (2.3) on page 6). This shows that the energy difference between states and thereby the energy of the absorbed photon are characteristic for the vibrations of the molecule.
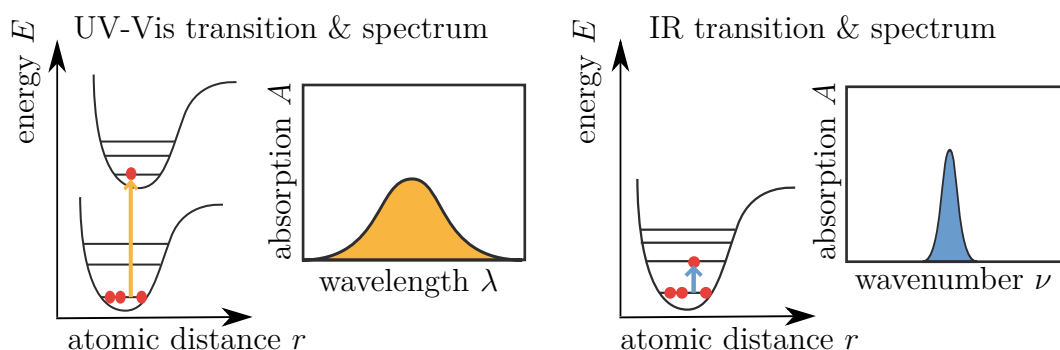
Figure 2.3: Illustration of an UV-Vis transition with corresponding spectrum and an IR transition with corresponding spectrum. The red dots indicate population and the arrows depict the transitions (yellow for UV-Vis and blue for IR).

One distinguishes between valence vibrations (stretch vibrations) and deformation vibrations (bending, torsional vibration ect.) [66].

A sketch of a steady-state IR absorption signal is given on the right side of figure 2.3, while the corresponding transition is depicted in the Morse potential on the left.

The position of a band is characteristic for the corresponding vibration. In solution at room temperature it is, however, no single line, but the absorption band has been broadened. Two different effects are causing the linewidth: one, the homogenous line broadening, is determined by the vibrational lifetime of the oscillator and the other, inhomogenous line broadening, is caused by an ensemble of oscillators sensing slightly different environments [68].

Typical IR observables are the central wavenumber, the intensity, the linewidth and the line shape. IR spectra can be used to identify oscillators, since for many common oscillators the wavenumber ranges, where they occur, are known, and to monitor changes in vibrational transitions.

Relaxation from a vibrationally excited state normally takes place via energy transfer to surrounding modes or the solvent (internal conversion) [69].

From an electronically excited state ($S_n$) different relaxation paths are possible. The depopulation of the excited state can take place directly by non-irradiating relaxation or internal conversion (as represented by straight dashed down arrows in figure 2.4 on the following page) or by fluorescence (black wavy arrow in figure 2.4 on the next page). Another possibility is intersystem crossing (ISC) to a triplet state $T_n$ (straight blue arrow in figure 2.4 on the following page) and relaxation via phosphorescence (wavy, blue arrow in figure 2.4 on the next page). Triplet states are electronic states with two unpaired electrons with the same spin [64].
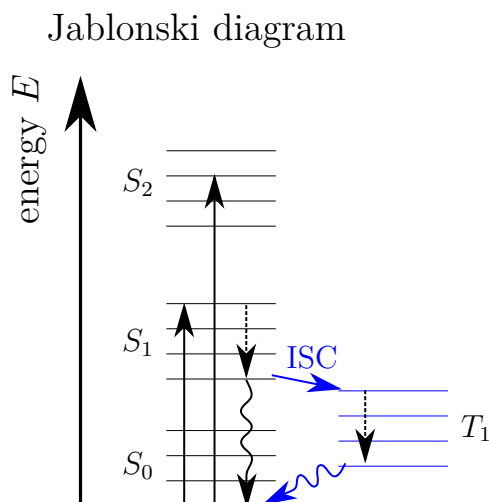
Jablonski diagram



Figure 2.4: Jablonski diagram with various relaxation pathways, the horizontal lines are vibrational levels in the electronic states labeled $S$ for singlet and $T$ for triplet, absorption is depicted as straight black arrow up, non-irradiating relaxation as dashed arrow pointing down, fluorescence as wavy black arrow pointing down, intersystem crossing as straight blue arrow and phosphorescence as wavy blue arrow.

The probability that a molecule which absorbed a photon undergoes one relaxation pathway is expressed in the quantum yield for that pathway (equation (2.9)).

$$\Phi_X = \frac{\eta_X}{\eta_{all}} \tag{2.9}$$

Where $X$ is the pathway of interest and $\eta$ the number of photons [63].

In the special case of a photolabile molecule a photo reaction is an additional pathway after absorption of a photon. The concept of (photo-)uncaging is discussed in section 2.2

## 2.2 Uncaging

This ssection introduces the concept of photo uncaging and the idea of orthogonal uncaging as a basis for the discussion of VIPER uncaging in chapter 3 on page 31.

If the energy of an absorped photon is used to cleave a bond in the molecule this reaction is called photo cleavage. Such a reaction can be used in a deprotection scheme also often refered to as (photo-)uncaging. A photolabile protection group (PPG) is attached to a molecule of interest, which is thereby deactivated. Upon

irradiation the bond between the PPG and the molecule of interest is cleaved and the molecule of interest becomes active again. The PPG is sometimes also called (photo)cage, while the molecule of interest is called caged molecule or leaving group (LG) [1, 2].

The possibility to photo cleave a bond depends on the energy of the light. To get an estimate which wavelength region is needed a normal $C - C$ bond is considered: it has an energy of 347 kJ/mol [62] with equation (2.6) on page 8 this leads to a wavelength of 345 nm. Longer wavelength light would not have enough energy to break a bond. 345 nm is in the UV-region, it is therefore plausible that uncaging by mid IR light (3 $\mu$m to 30 $\mu$m resulting in E<39 kJ/mol) is infeasible. There are some efforts towards longer wavelength (such as near IR) uncaging. One experimental scheme is two-photon uncaging [2].

Uncaging (depicted in figure 2.5) allows control over a chemical or biological process with high temporal and spatial precision [1–5]. It is non-invasive and the photo byproduct is the only sample contamination. However, the cleavage products need to be non-toxic for e.g. applications in living cells [2–5, 70–73].

The efficiency of the photo reaction depends on the extinction coefficient of the cage at the used wavelength as well as on the quantum efficiency of the cleavage. Another parameter of uncaging is the kinetic of the photoreaction [2, 74].
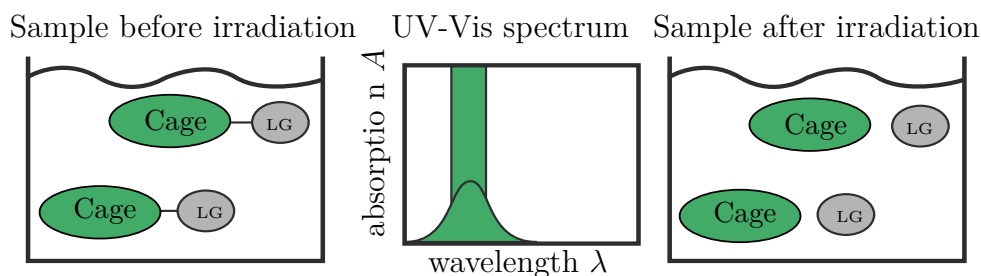


Figure 2.5: Photouncaging sketch. Left to right: Sketch to illustrate Photolabile Group (Cage) and Leaving Group (LG); Sketch of UV-Vis absorption spectrum of the cage with bar indicating the irradiation wavelength; Sketch of illuminated sample after photocleavage.

**Orthogonal Uncaging**   To unravel the inner workings of complex and dynamic networks in chemical and biological systems, simultaneous control over multiple processes is needed and therefore wavelength-selective or orthogonal photolabile protection groups have been of major interest [6–10].

In the orthogonal uncaging scheme described by Bochet a substrate is bound to two photolabile groups with different wavelengths. Depending on the wavelength

Sample before irradiation   UV-Vis spectrum   Sample after irradiation
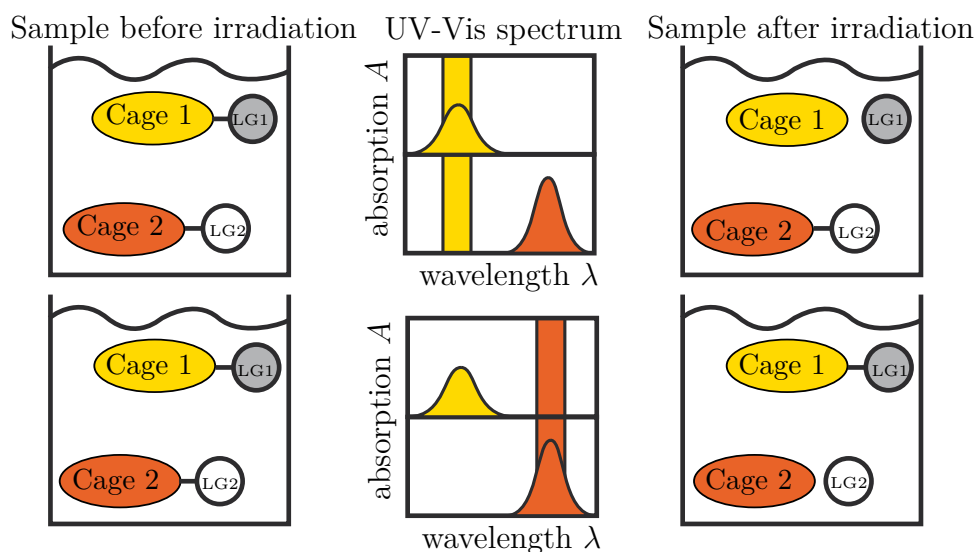


Figure 2.6: Orthogonal uncaging sketch. First row: the illumination is resonant with Cage 1 (yellow) and only cleavage of Cage 1 and LG 1 is observed. Second row: Cleavage of Cage 2 and LG 2 analogous to cleavage of Cage 1 and LG 1.

of the light used either one photolabile group or the other is cleaved leading to two different reaction products [11, 75, 76].

The same scheme can be applied to a mixture of two or more species protected by different photolabile groups (as illustrated in figure 2.6). The PPGs need to differ in their maximum absorption, their extinction coefficient or their quantum yield [6].

Orthogonal uncaging in the strictest sense means that the PPGs must be cleavable in any order otherwise the experimental scheme is called wavelength-selective uncaging. For wavelength-selective ungaging the irradiation must be in a certain sequence. For example both cages have an absorption band at 300 nm and one of them has an additional band at 400 nm. The second cage can be selectively cleaved by irradiation at 400 nm. This does not lead to cleavage of the other cage. Afterwards the cage with only an absorption band at 300 nm can be cleaved by irradiation at 300 nm. The sequence of irradiation cannot be changed, since both cages would be cleaved by 300 nm irradiation. In orthogonal uncaging as depicted in figure 2.6 there are wavelengths were only one cage and not the other absorbs for all cages involved. In most experimental application true orthogonal uncaging is not necessary. The desired wavelength selectivity can often be achieved by synthesising the compounds accordingly.

Wavelength selective uncaging has found applications in material science [7, 12–15], organic synthesis [10, 16] and biological studies [9, 17–29]

To illustrate the power of this approach one example in the area of gene control is highlighted. In the work from Chen and co-workers morphonlino oligonucleotides are caged with nitroso and coumarin cages to examine the mechanism of mesoderm pattering in zebrafish embryos [25]. Morpholino oligonucleotides can perturb targeted RNA in vivo and thereby influence gene control. They can be inactivated by cyclization with a photo cleavable linker and activated by irradiation with light. Since zebrafish embryos are translucent in the visible spectral range, the irradiation can be in vivo. With two differently caged morphonlino oligonucleotides that inhibit different gene expressions the importance of the timing of expression in the development of the embryos can be studied [25].

A major concern in the development of orthogonal uncaging schemes is the number of possible functional levels. The publication of San Miguel et al. shows that a combination of four different photocages allows selective uncaging with different uncaging wavelengths [14]. A recent paper of the Heckel group exploits different reaction rates of uncaging reactions to achieve four levels [8].

Additionally to the current limitation to four levels of selective uncaging, the illumination conditions in these schemes rely on UV-Vis light, which can be problematic in terms of photo-damage. The usage of different PPGs also leads to differences in release rates and reaction kinetics, which might in some applications be undesirable.

## 2.3 Pump-Probe Spectroscopy

In this section the principles of pump-probe spectroscopy are introduced. UV-Vis-pump and IR-pump IR-probe experiments are introduced as well as 2D-IR spectroscopy. Exchange spectroscopy is introduced to introduce VIPER spectroscopy (section 2.4 on page 19).

Ultrafast pump-probe spectroscopy methods can provide additional information compared to the one-dimensional steady-state methods. In the commonly used techniques the sample is irradiated with two ultra-short laser pulses in succession. The first laser pulse is called the pump pulse, the second the probe pulse. The difference between the probe spectrum with and without pump pulse is recorded. The timing between pump and probe pulse is controlled and thereby the time dependence can be studied [77]. The general concept has been demonstrated as early as 1899, when Abraham and Lemoine used a condenser to simultaneously produce a spark and activate a Kerr shutter [78]. The historical development has, for example, been discussed in Zewails Nobel lecture on femtochemistry [79], by Bloembergen [80] and by Shapiro [81]. An early review on subpicosecond spec-

troscopy has been written by Graham Fleming [82]; a more recent minireview is published here [83].

As in one dimension the laser light can belong to the IR or the UV-Vis range. The probe pulse is detected and determines thereby the observables whose dynamics can be observed. One distinguishes between IR-probe and Vis-probe. In this thesis only IR-probe experiments were carried out.

Whether the pump pulse is in the IR or UV-Vis region determines which type of excitation, vibrational or electronic, is studied.
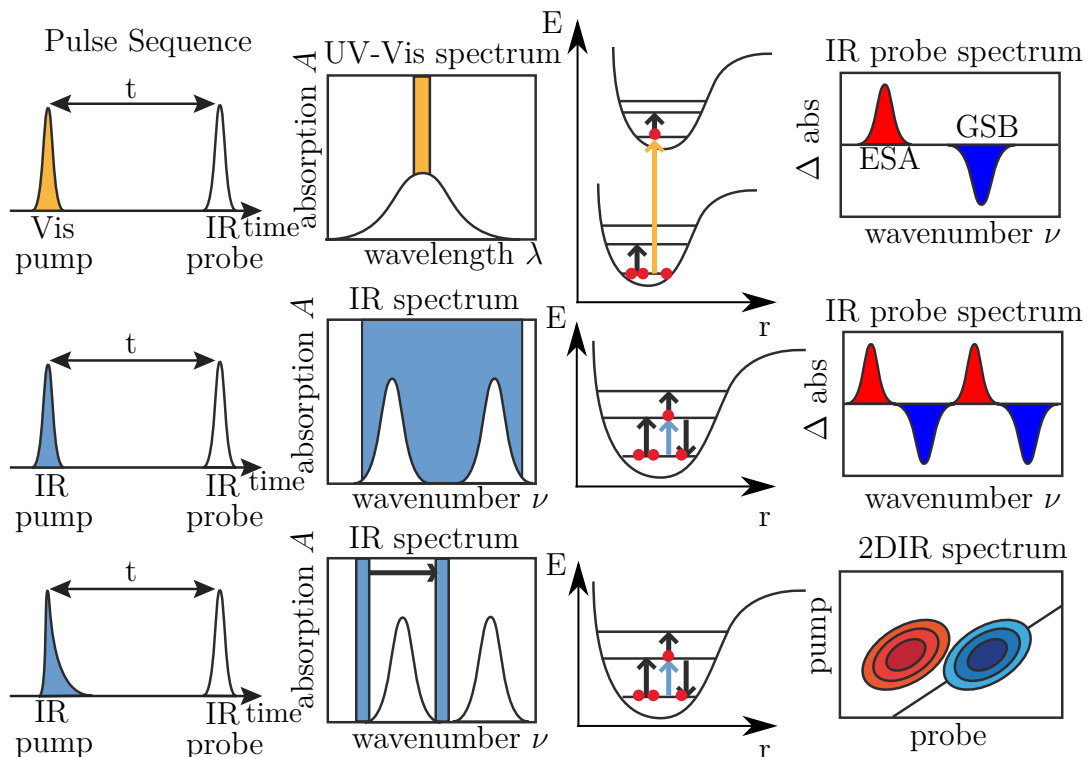


Figure 2.7: From left to right: Pulse sequence for each experiment, pulse shapes are in time dimension, color indicates excitation frequency. Sketch of IR or UV-Vis spectrum, the bars indicate the frequency of the pump pulse. Sketch of transitions in anharmonic oscillator, red dots indicate the population, coloured arrows the pump pulse and black arrows the probe pulse interaction. Sketch of the resulting spectra for each type of experiment. Negative signals in blue and positive in red. GSB is the ground state bleach and ESA the excited state absorption.

**Vis-pump IR-probe Spectroscopy**    A Vis-pump IR-probe experiment is also called TRansient InfraRed (TRIR) Spectroscopy. In this experimental scheme,

depicted in the first row of figure 2.7 on the facing page, the pump pulse frequency is in the UV-Visible region and resonant with an electronic transition of the studied molecules. The molecules are thereby excited into an electronically excited state. After a delay time t the sample is probed by a broadband infrared probe pulse. This IR light can excite less molecules from the ground state to a vibrationally excited state, since a part of the molecules has already been excited to the electronically excited state. This leads to a negative signal in the difference absorption spectrum at the wavenumber of the probed IR transition. This signal is called Ground State Bleach (GSB). Additionally, the IR light can excite the molecules in the electronically excited state into a vibrationally excited state. This transition causes a positive signal in the difference absorption spectrum at a lower wavenumber. This signal is called an Excited State Absorption (ESA).

TRIR measurements can give information on photo sensitive systems. The lifetimes of electronic excitations can be determined and kinetics, intermediates and photoproducts can be characterized [84–87]. A theoretical consideration can be found here [88].

In the case of molecules that are able to undergo photochemistry the bleaches remain for an infinite time. The excited molecules do not return to their former ground state because they undergo a photo reaction thereby becoming a different molecule with changed absorptions. Intermediates and products of the photo reaction appear as positive bands.

**IR-pump IR-probe Spectroscopy**   A broadband IR-pump IR-probe experiment (see second row of figure 2.7 on the preceding page) has the same experimental scheme as a TRIR experiment, but both probe and pump are broadband infrared pulses. In this case the IR-pump is resonant with IR transitions of the studied molecules and excites them to vibrationally excited states. This leads to a difference absorption spectrum with a negative signal at the wavenumber of the probed transition and a positive signal at the wavenumber of the transition from the first to the second vibrationally excited state. Also contributing to this negative signal is the stimulated emission (SE).

This type of experiment makes the lifetimes of vibrational excitations and the anharmonicity accessible. Additional information on a system can be gained by applying 2D-IR spectroscopy [68, 89–91].

There are different ways of recording a 2D-IR spectrum. In the first experimental scheme (third row of figure 2.7 on the facing page) the IR-pump pulse is spectrally narrow instead of broad. It is then scanned over the spectral region of interest and a probe spectrum for each pump pulse position is collected [89].

Plotting the difference signal intensity against the pump and the probe wavenumber yields a 2D-IR spectrum. For the time dependence a 2D-IR spectrum for

each chosen time delay (population time) can be collected.

The other possible experimental scheme involves two broadband IR pump pulses with varying delay between them. Here a Fourier transformation over the delay time (coherence time) between the IR pump pulses yields the pump axis, which is plotted against the probe axis (at a delay, providing the population time), resulting in the 2D-IR spectrum [68, 92, 93]. An alternative is using a pulse-shaper to provide the pump pulses.

Figure 2.8 shows a sketch of a 2D-IR spectrum for two oscillators at short (left) and at longer (right) delay times. The 1D-IR absorptions are schematically depicted on the pump and probe axis to illustrate the peak positions. As in the other methods described here there is a negative (blue) and a positive (red) signal for each oscillator. The processes leading to these signals are identical to the processes in broadband IR pump IR probe spectroscopy [93]. For each oscillator there is a signal pair at the diagonal of the 2D-IR spectrum. These signals are called diagonal peaks and they can give additional information by their line shape. In this sketch they are elongated along the diagonal, which is an indication for a heterogeneous environment or an ensemble of similar but slightly different oscillators [68].
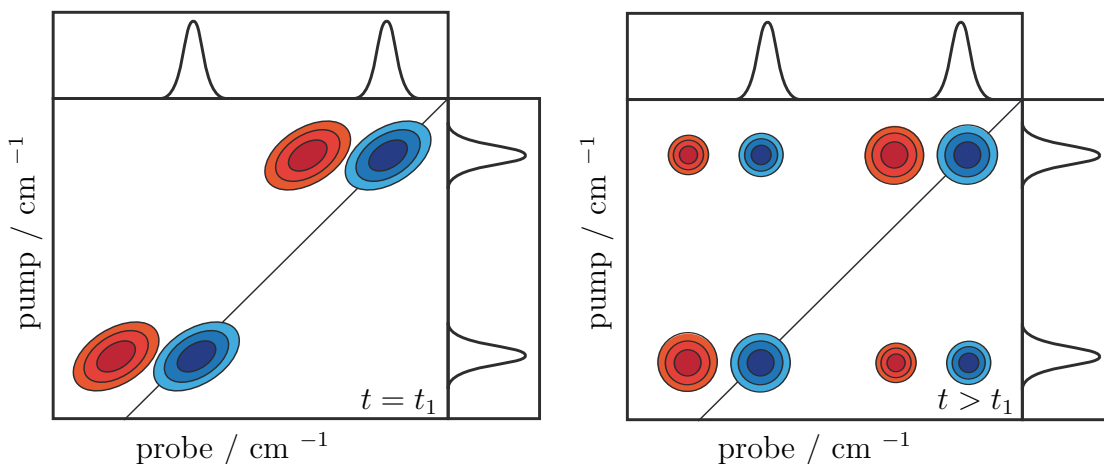


Figure 2.8: Sketch of a 2D-IR spectrum of two oscillators (1D absorption spectra depicted next to the axis) at early times (left) and at longer delay times (right). Negative signals are blue, positive signals are red.

At longer delay times the peaks become more round. This process is called spectral diffusion and gives information on the environment of the oscillators [94–97]. An additional spectral feature at longer delay times are the peaks appearing at the pump frequency of one oscillator and the probe frequency of the other.

These peaks are called cross peaks and they can be caused by direct anharmonic coupling, by energy transfer or by chemical exchange between the oscillators [68].

2D-IR spectroscopy can be used for structural analysis [68, 98–101], for solvation or energy transfer studies [102–106] or to monitor chemical exchange [107–111] between different species (e.g. H-bonded or free).

**Exchange Spectroscopy**  To study this process a 2D-IR exchange experiment (EXSY) can be carried out [107, 109, 112–115]. For a system consisting of various species, which can convert into each other, the kinetics of the exchange can be determined.

$$
\begin{array}{ccc}
A^* & \xrightleftharpoons[k_{BA}]{k_{AB}} & B^* \\
\downarrow{\scriptstyle k_A} & & \downarrow{\scriptstyle k_B} \\
A & & B
\end{array}
$$
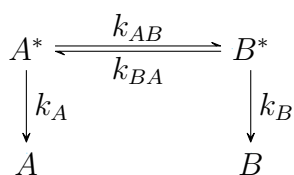
Figure 2.9: Decays involved in EXSY 2DIR spectroscopy.

In the most simple case (see scheme 2.9) two species $A$ and $B$ can each be vibrationally excited to their excited states ($A^*$ and $B^*$), decaying with their individual vibrational relaxation rates $k_A$ and $k_B$, and convert into each other with reaction rates $k_{AB}$ and $k_{BA}$. For such a system a set of coupled differential equations for the concentrations of the species can be derived and fitted with the experimental data.

From scheme 2.9 it becomes apparent that the time over which the chemical exchange can be monitored is limited by the vibrational relaxation rate of the oscillators. This is not only true for the excited state absorption, but also for the ground state bleach, since the excited molecules return to the ground state and the negative signal also decays. Normally these lifetimes are on a sub-picosecond to a hundred picosecond scale, while the timescales for chemical exchange can be significantly longer.

## 2.4 Vibrationally Promoted Electronic Resonance

In this section the VIPER effect is introduced. The general requirements for this effect are discussed. Then, VIPER spectroscopy is explained and compared to other mixed pulse sequences. This knowledge is needed for the discussion of the new concept of VIPER uncaging in chapter 3 on page 31.

In section 2.1 on page 5 we have seen that the energy of an UV-Vis photon needs to match the energetic difference between two electronic states to promote

a transition. The UV-Vis photon needs to be in resonance with the transition. If the energy is too low, the photon is off-resonant and no transition takes place. In a diagram of the electronic and vibrational states with transitions (figure 2.10) this would mean that the arrow depicting the transition is to short to reach an excited state (left in figure 2.10).

It is, however, possible to combine an off-resonant electronic excitation with a vibrational pre-excitation and thereby promote the elctronic resonance (right in figure 2.10).
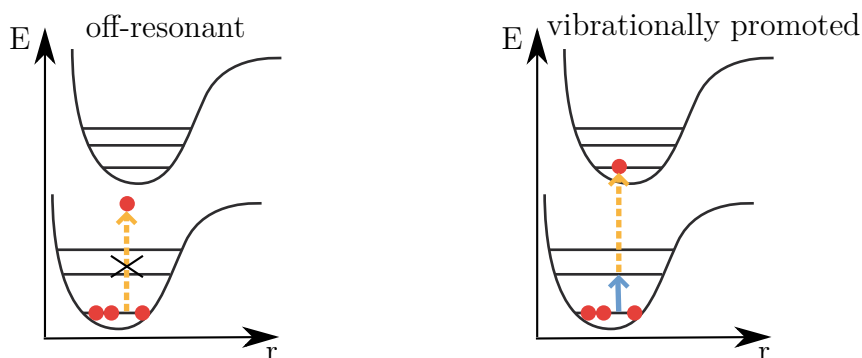


Figure 2.10:  Diagrams of electronic and vibrational states. $E$ is the Energy and $r$ the nucleic distance. The dashed yellow arrows are the UV-Vis photons, the blue arrow is an IR photon.

This **VI**brationally **P**romoted **E**lectronic **R**esonance is what we call VIPER [30]. Looking back at figure 2.1 on page 7, where the $S_0$ and $S_1$ with their vibrational levels and probabilities to find nuclei are depicted, it becomes clear that the Franck-Condon factors (equation (2.7) on page 9) are different for a VIPER transition if compared to direct electronic or direct vibrational excitation. Since in a VIPER experiment the electronic transition does not start in the vibrational ground state of the $S_0$, but in a vibrational excited state. The overlap will therefore be better for vibrational states in the $S_1$, that are similar to the excited state in the $S_0$. This might mean, that the favoured transitions are different for VIPER or direct UV-Vis excitation.

To promote an electronic transition by IR pre-excitation some requirements need to be fulfilled. Firstly, the UV-Vis transition needs to be modulated by the IR absorption and secondly the UV-Vis absorption needs to take place while the transition is modulated. Furthermore, the polarizations of the light pulses need to match. These requirements are discussed in more detail in the following paragraphs.

The vibrational mode, that is excited, needs to be coupled to the electronic transition. The UV-Vis absorption spectrum of the molecule needs to be modu-

lated by the infrared absorption. This can happen directly by vibronic coupling of the vibrational mode to the electronic transition or indirectly by internal vibrational redistribution (IVR). It has been shown that different infrared transitions couple with different strength to the UV-Vis transition [30, 57, 58]. A prediction of the influence can be made by computations of the UV-Vis absorption spectra of vibrationally excited molecules [116].
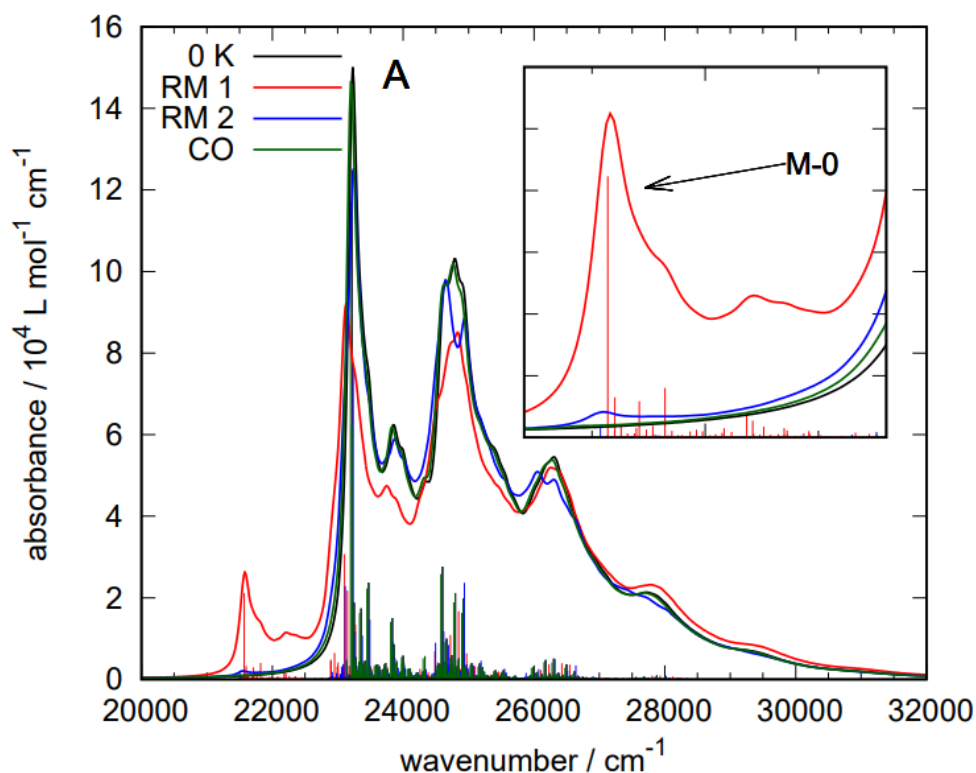


Figure 2.11:  Computed UV-Vis absorption spectra of DEACM-N$_3$ (introduced in section 3.4 on page 45) without vibrational pre-excitation (black labelled 0 K) and with pre-excitation of different vibrational modes (red labelled RM 1, blue labelled RM 2 and green labelled CO). The sticks represent the computed transitions, they are broadened and convoluted to yield the envelope spectra given by the coloured lines. The inset shows a zoom of the low wavenumber data. Adapted with permission from [116].

The energy (and consequently the wavenumber) and the intensity (which can be converted into absorbance)of the UV-Vis transitions of a molecule in the vibrational ground state and various vibrationally excited states are computed and plotted. The differences between the excited state spectra and the ground state

spectrum are a measure for the strength of the VIPER effect. Exemplary computational data on the PPG [7-(diethylamino)coumarin-4-yl]methyl (DEACM), which is introduced in detail in section 3.4 on page 45, is given in figure 2.11 on the preceding page.

The computed transitions are represented as "sticks". Each computed transition is infinitely narrow and represented by a a narrow line. An IR pre-excitation leads to new transitions with lower energies as the 0-0 transition (compare red to black sticks). The lowest transition is red-shifted by $\nu$ which depends on the IR mode that is excited. For a good VIPER contrast the red-shift should be big and the new transition should have a significant intensity.

To better match experimental spectra the "sticks" are broadened and convoluted to yield the envelope spectra given by the coloured lines. Black is the computed spectrum without pre-excitation. Red, blue and green show the computed spectra for the molecule with IR excitation in different IR modes. DEACM has two prominent ring modes and a carbonyl mode. These three modes were selected for pre-excitation. The red spectrum corresponds to one ring mode vibration and the blue spectrum to another. The green spectrum corresponds to the IR pre-excitation on the carbonyl mode.

For this example molecule the wavenumber difference to the ground state spectrum is the largest for the ring mode vibration depicted in red. This would indicate that excitation of this ring mode leads to the largest VIPER effect.

Spectroscopic VIPER data on DEACM-$N_3$ showed that the VIPER signal is indeed the largest for the IR pump positioned on the vibrational band corresponding to the ring mode, which is coloured red in figure 2.11 on the previous page. The direct comparison between the vibrationally resolved computed spectra and the broad measured steady-state spectra in solution and at room temperature was not straightforward and has been improved in the progress of this thesis. The prediction of the computations on the IR mode with the largest influence on the UV-VIS spectrum and therefore with the largest VIPER effect was in agreement with the experiments for all computed molecules. The comparison of the computed prediction and the experimental data has been published [116].

The computations for different molecules to predict their VIPER efficiency were part of Jan von Cosels PhD project [117] in the Burghardt group and were part of a collaborative effort in the CLiC graduate school. A summary of the collaborative efforts is given in chapter B on page 189.

The influence of the IR-pre-excitation on the UV-Vis absorption can directly be measured in an IR-pump Vis-probe experiment [118, 119].

The second requirement for a successful VIPER excitation is that the subsequent UV-Vis photon is absorbed, while the modulation of the infrared photon takes place. The probability that one molecule has absorbed both the IR and the UV-

Vis photon needs to be high enough. This can be achieved by using a pulsed laser system, where the delay between the pump pulses is short enough so that the infrared excitation, which normally decays within a picosecond timescale, has not completely decayed, when the UV-Vis photon is absorbed. In some instances coupling to other (low) frequency modes or IVR could be exploited. A continues wave instead of a pulsed laser might work if the intensities are high enough to achieve a sufficient probability of molecules being excited by both an IR and an UV-Vis photon.

The next requirement concerns the polarization of the pulses. As for simple infrared or UV-Vis absorption measurements, the direction of the polarization of the absorbed light and the transition dipole moments need to match for maximal signal.

For the probability of VIPER excitation the angles between the pump pulses and the transition dipole moments have to be considered. The dependency for a VIPER excitation is the same as for a third-order experiment, e.g. 2D-IR or pump-probe spectroscopy. For the pure VIPER excitation without probing in the IR the consideration of the pump pulses is sufficient. The polarization dependent factor $D(\alpha)$ is given in equation (2.10), where $\alpha$ is the angle between the polarization of the two pump pulses and $\theta$ is the angle between the pumped UV-Vis and IR transition dipole moments.

$$D(\alpha) = \frac{|\mu_i|^2 |\mu_j|^2}{45}(cos^2(\alpha)[5 + 4 < P_2 cos(\theta_{ij}) >] + sin^2(\alpha)[5 - 2 < P_2 cos(\theta_{ij}) >])$$
(2.10)

$P_2(x) = \frac{3cos^2(x)-1}{2}$ is the second Legendre polynomial [120]. If the combinations of the transition dipole angles and the polarization dipole angles is unfavourable, the probability for VIPER excitation can be up to a factor three smaller than for the optimal case [68, 121, 122]. For the influence of the match between the polarisations and the transition dipole moments on the signal size in VIPER spectroscopy also the probe pulse needs to be considered and this dependency will be discussed below [61].

**VIPER Spectroscopy** VIPER 2DIR spectroscopy has been introduced to circumvent the time limitation for 2D-IR EXSY spectroscopy [30, 31]. The VIPER excitation is used to store vibrational information in the electronic excitation and is followed by an IR probe pulse.

An illustration of the experimental scheme is given in figure 2.12 on the following page. The pulse sequence (first panel) consists of a narrowband IR pump and a subsequent UV-Vis pump pulse. The probe pulse is a broadband IR pulse.

The IR pump pulse is centered on a vibrational mode of the molecule (blue bar
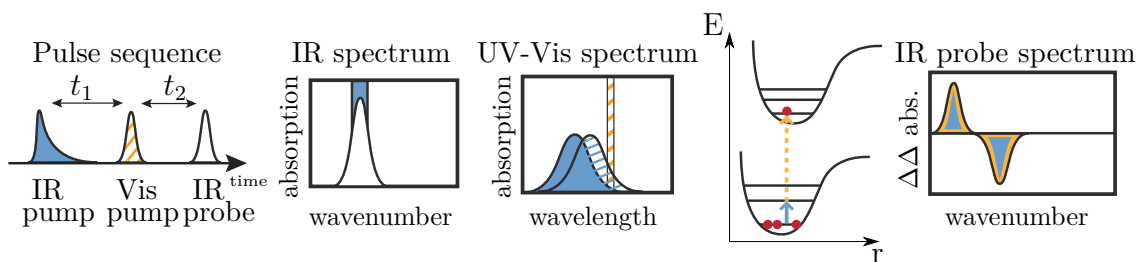
Figure 2.12: From left to right: VIPER pulse sequence with narrowband IR pump, off-resonant Vis pump and broadband IR probe pulse. Sketch of IR spectrum, colored bar indicates IR pump position. Sketch of UV-Vis spectrum, dashed bar shows wavelength of Vis pump pulse, dashed spectrum is UV-Vis spectrum after IR pre-excitation. Schematic of excitations in anharmonic oscillator, blue arrow indicates IR pump pulse, yellow dashed arrow indicates Vis pump pulse. Sketch of IR probe spectrum.

in the second panel) and the infrared excitation influences the UV-Vis spectrum (shifted dashed spectrum in the third panel). The UV-Vis pump pulse is positioned off-resonantly to the UV-Vis absorption band of the molecule (dashed orange bar in the third panel) and can only excite molecules to the electronically excited state, if the IR pump pulse shifts the UV-Vis spectrum into resonance. In the energy level scheme this means that the sum of the energy of the IR and UV-Vis photon is needed to arrive at the electronically excited state.

The VIPER signals arise only from the molecules which were excited by both infrared and UV-Vis pump pulse (fourth panel). Since VIPER is still an IR probe experiment the observables are IR transitions. One way of considering the signals is a difference spectrum of a TRIR spectrum with and without IR pre-excitation. This means that VIPER signals are double difference absorption signals. In contrast to conventional TRIR spectroscopy the IR pre-excitation in VIPER allows to study the spectra of a selected electronically excited species in a mixture since the higher selectivity of the IR spectrum can be exploited.

In terms of EXSY spectroscopy this means that the molecules which were excited to the vibrationally excited state, and would in conventional EXSY decay with the vibrational lifetime, are now further excited to the electronically excited state and the lifetime of their signals is therefore extended to the electronic lifetime, which is normally on a significantly longer timescale [30, 31].

As for the VIPER effect in general, VIPER spectroscopy needs the IR-pre-excitation to modulate the UV-Vis transition. Since only the double difference

spectrum is of interest for spectroscopy application this modulation does not need to full-fill any additional requirements. For instance, if there is also direct excitation of the UV-Vis transition causing a background signal, this can just be subtracted.

Concerning the influence of the polarization on the VIPER signal size, two cases have to be distinguished. If the delay between the pump pulses and the probe pulse is long and the sample can become isotrope by rotational diffusion again, equation (2.10) on page 23 applies and a change in probe polarization does not have an effect on the VIPER signal. As for pump-probe, the signal can vary by up to a factor three, when the relative polarization of pump pulses is changed. But if the delay between pump and probe pulses is too short for rotational diffusion, the dependency is that of a fifth order experiment and the signal size can for the worst combination of angles be up to a factor 15 smaller than for the optimal case. The polarization dependent factor $D(\alpha, \beta)$ is given in equation (2.11), where $\alpha$ and $\beta$ are the angles formed between the polarizations of the pump and probe pulses. $\Theta_{i0}$ and $\Theta_{j0}$ are the angles between the pumped IR and UV transition dipoles and $\Theta_{ij}$ between the pumped and probed IR transition dipoles in the laboratory frame [120].

$$D(\alpha, \beta) = \frac{|\mu_0|^2|\mu_i|^2|\mu_j|^2}{2 \times 3 \times 5 \times 7}$$

$$(cos^2\alpha cos^2\beta[2 + 4\langle cos^2\Theta_{i0}\rangle + 4\langle cos^2\Theta_{j0}\rangle + 4\langle cos^2\Theta_{ij}\rangle + 16\langle cos\Theta_{i0}cos\Theta_{j0}cos\Theta_{ij}\rangle]$$
$$+cos^2\alpha sin^2\beta[6 + 12\langle cos^2\Theta_{i0}\rangle - 2\langle cos^2\Theta_{j0}\rangle - 2\langle cos^2\Theta_{ij}\rangle - 8\langle cos\Theta_{i0}cos\Theta_{j0}cos\Theta_{ij}\rangle]$$
$$+sin^2\alpha cos^2\beta[6 - 2\langle cos^2\Theta_{i0}\rangle + 12\langle cos^2\Theta_{j0}\rangle - 2\langle cos^2\Theta_{ij}\rangle - 8\langle cos\Theta_{i0}cos\Theta_{j0}cos\Theta_{ij}\rangle]$$
$$+sin^2\alpha sin^2\beta[6 - 2\langle cos^2\Theta_{i0}\rangle - 2\langle cos^2\Theta_{j0}\rangle + 12\langle cos^2\Theta_{ij}\rangle - 8\langle cos\Theta_{i0}cos\Theta_{j0}cos\Theta_{ij}\rangle]$$
$$+sin\,\alpha\,cos\,\alpha\,sin\,\alpha\,cos\,\beta[-4 - 8\langle cos^2\Theta_{i0}\rangle - 8\langle cos^2\Theta_{j0}\rangle + 20\langle cos^2\Theta_{ij}\rangle + 24\langle cos\Theta_{i0}cos\Theta_{j0}cos\Theta_{ij}\rangle])$$

$$(2.11)$$

For VIPER signal size also the intensities of the pump pulses and the wavelength of the UV-Vis pump pulse, as well as the delay between the pulses are of importance. This will be described in detail in Carsten Neumann's PhD thesis [123], which is also part of the CLiC collaboration. When optimizing the signal in a VIPER uncaging experiment (discussed in chapter 3 on page 31), also minimization of the background signals has to be taken into account.

**Distinction from other mixed pulse sequences**  The field of mixed ultrafast pulse sequence spectroscopy is expanding and keeping track of various sequences and their differences and uses can be challenging. Here, in particular transient 2D-IR (T2D-IR) and triggered exchange spectroscopy (triggered EXSY) are highlighted, as they are similar to the VIPER pulse sequence. All three sequences (see

figure 2.13) consist of an IR-pump, an UV-Vis-pump and an IR-probe pulse and work on molecules that are sensitive to UV-Vis light [31].
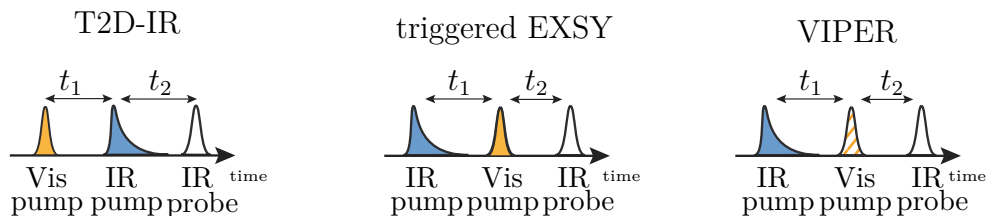


Figure 2.13: Pulse sequences for transient 2D-IR (T2D-IR), triggered exchange (triggered EXSY) and VIPER spectroscopy. Solid yellow pulse is resonant with UV-Vis transition, dashed yellow pulse is off-resonant, blue pulse is resonant with IR transition and white pulse is the broadband IR-probe pulse.

A T2D-IR spectrum is a 2D-IR difference spectrum. The difference is between a 2D-IR spectrum with UV-Vis excitation and one without excitation. In the pulse sequence the first pump pulse is resonant with a UV-Vis transition and followed by a conventional 2D-IR pulse sequence. The difference between electronic ground state and electronically excited state can be monitored using conventional 2D-IR observables. This allows to study transient species [32–37] or electronically excited species [38–42].

In triggered EXSY the resonant UV-Vis pump pulse is sent in between the IR-pump and the IR-probe pulse. Molecules are "tagged" by the IR pump pulse. Following this, all molecules (including the tagged ones) are excited into an electronically excited state by the UV-Vis pulse. Now the exchange between states can be monitored by the IR probe pulse. This technique can be used to correlate vibrations in the electronic ground state with vibrations in the excited state and allows to study intermediates and products of a photoreaction [43, 45, 124].

In VIPER the pulse sequence is the same as in triggered EXSY, but the UV-Vis-pump pulse is off-resonant in VIPER and therefore cannot directly promote molecules to the electronically excited state. Only molecules which were excited by the IR and the UV-Vis-pump pulse contribute to the VIPER signal, which allows to conserve the information gained by the IR excitation in the electronically excited state.[30]

A similar experiment with fluorescence detection has recently been carried out by the Tokmakoff-group [59, 60]. In their Fluorescence-Encoded Infrared (FEIR) spectroscopy an IR pre-excitation and a NIR two-photon absorption pulse excite the molecule to the electronic state and the fluorescence is detected. In contrast to coherent infrared detection this fluorescence detection is very sensitive and works

at lower concentrations. The spectroscopic observable is however the fluorescence, which means, that only fluorophors can be studied. In contrast to VIPER, it is not possible to follow exchange or to identify intermediates or products with FEIR unless they have a very specific fluorescence by which they can be identified.

## 2.5 Non-Linear Wavemixing Processes

This section introduces some non-linear wavemixing processes, which are used to generate the pump and probe pulses for the spectroscopic techniques. It serves as preparation for section 5.3 on page 111, where the first steps towards an alternative IR pump light generation will be shown.

Theses processes are non-linear light-matter interactions in special materials. The incoming electromagnetic field causes a non-linear polarization in the material, which in turn results in an non-linear electromagnetic field response. A material suited for this kind of light-matter interaction needs a non-vanishing higher order susceptibility $\chi$. This attribute depends on the symmetry of the medium. The second order susceptibility, for example, vanishes in media with inversion symmetry like liquids, gases, amorphous solids or centrosymetric crystals.

The most common processes are Harmonic Generation, Sum-Frequency Generation and Difference-Frequency Generation [125, 126]. They and their corresponding energy schemes are depicted in figure 2.14.
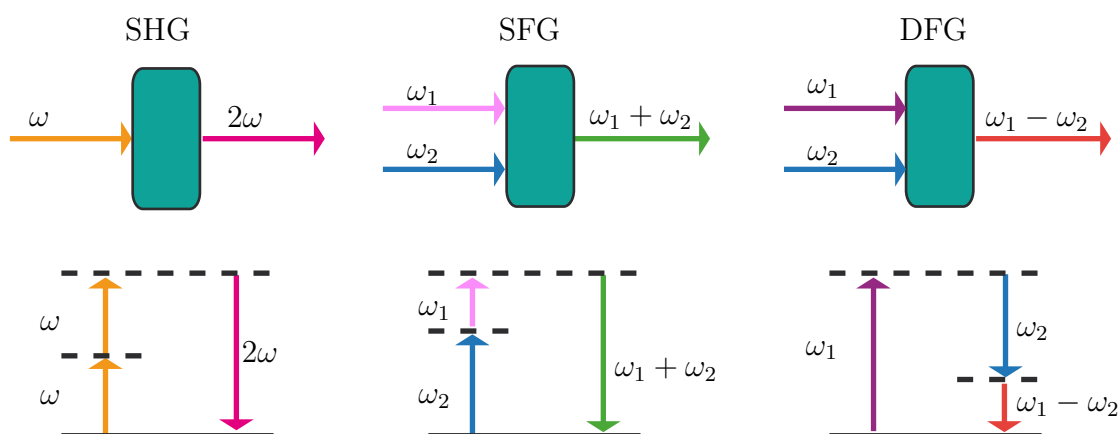


Figure 2.14: Mixing schemes and corresponding energy schemes for Second Harmonic Generation (SHG), Sum-Frequency Generation (SFG) and Difference Frequency Generation (DFG).

For Harmonic Generation a number of photons (e.g. two for second harmonic generation, three for third harmonic generation) with the same frequency $\omega$ interact with a non-linear crystal, resulting in the emission of a photon of a multiple of the original frequency corresponding to the number of photons involved (e.g. 2 $\omega$ for second harmonic generation, 3 $\omega$ for third harmonic generation) [126].

In Sum-Frequency generation (SFG) two photons with different frequencies $\omega_1$ and $\omega_2$ interact with the medium and a photon with a frequency that is the sum of the incoming photons' frequencies is emitted [126].

In Difference-Frequency generation (DFG) the emitted photon has the frequency of the difference between the incoming frequencies. A special case of DFG is optical parametric generation, where the interaction of one photon with the medium leads to emission of two photons. One of these photons is called signal, the other one is called idler and the frequency of the idler is the difference between the frequency of the incoming photon and the frequency of the signal [126].

Such a process, taking place in a setup called optical paramteric amplifier (OPA), can also be seeded. This means that an additional photon is send as seed into the medium. The frequency of the seed determines the frequency of the signal and therefore also of the idler [126].

To achieve amplification the phase-matching condition must be met. This means that the dipoles in the medium need to be in phase, since their contributions will cancel each other out otherwise. Dispersion, meaning different velocities for different frequencies, in the medium hinders meeting the phase matching condition further. A solution can be the exploitation of birefringence [126].

In birefringence the refractive index depends on the polarization direction. One distinguishes between an ordinary ($n_o$) and an extraordinary ($n_e$) refractive index.

In angle phase-matching the crystal and the light beams are oriented in a way, that the ordinary refractive index for one frequency matches the extraordinary refractive index for the other frequency. The angle under which this condition is met is called the phase-matching angle and the experimental scheme is called birefringent or critical phase matching. For most processes the resulting frequencies can be tuned in a certain range by turning the crystal with regard to the beam. This is referred to as angle-tuning [126].

The VIPER pulse sequence (left in figure 2.12 on page 24) consists of three pulses with different requirements for an optimal VIPER signal.

The IR-probe pulse intensity has no direct influence on the magnitude of the VIPER signal (as long as the detector behaves linearly for small variations in the used probe intensity), but it influences the noise and limits the sample's thickness. The pulse should have a broad spectrum, since the probe spectrum limits the region that can be monitored. One way to generate a MID-IR-probe pulse is a white light seeded optical parametric amplification with a consecutive DFG between signal

and idler.

The UV-Vis-pump pulse needs to be tunable in the right wavelength region, corresponding to the UV-Vis spectrum of the sample and the spectral range of the pulse should not be too broad to prevent unspecific background absorption. For the different samples different combinations of the processes mentioned above are applied with special regard on a single Gaussian, a narrow spectral shape and a suitable pulse intensity.

The same processes as for the IR-probe light can be used to generate the light for the IR-pump pulse. To achieve a narrowband pulse a Fabry-Perot Etalon can be used. Such an Etalon consists of two mirrors. The mirrors are close to each other and the incoming light is reflected in the cavity and a part is transmitted with each round trip. This leads to a pulse with an exponential decay in the time domain and therefore to a Lorentzian shaped pulse in the frequency domain. The distance between the mirrors determines the central wavenumber of the pump pulse [89].
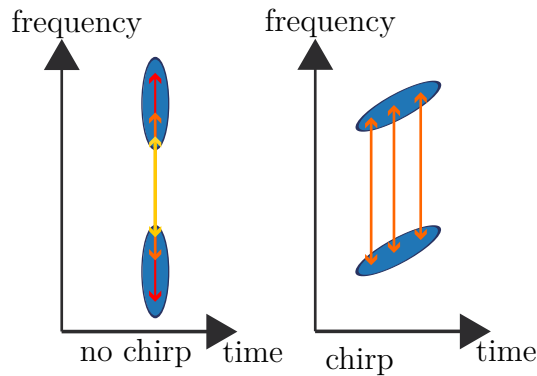


Figure 2.15: Scheme of frequencies vs time in the pulses involved in mixing if the pulses are not chirped (left) and if they are chirped (right). The coloured arrows represent mixing of matching frequencies, the blue ellipses represent the pulses.

An alternative approach to achieve a narrowband mid-IR pulse is to make a DFG directly with the fundamental. This needs a crystal that is efficient for this kind of mixing and an optical process which results in light with 900 - 1000 nm to be mixed with the fundamental.

Such light could be generated by a NOPA (non-collinear optic parametric amplifier) [127].

A NOPA is pumped with the doubled fundamental and therefore can produce pulses between 900 and 1000 nm. The beams in a NOPA are sent into the crystals under an angle which allows to generate shorter pulses in time. In an OPA the shortness of the pulse is limited by the group-velocity mismatch or temporal walk-off in the crystal. The pulse becomes elongated since different frequencies have

29

different velocities in the medium. In a NOPA the mismatch is compensated and allows a shorter pulselength [128].

For narrowband IR generation the DFG between the NOPA output and a fundamental is done with chirped pulses. This is illustrated by figure 2.15 on the preceding page. If the pulses are not chirped (left sketch), different frequencies (indicated by different colors) can mix at the same time. By stretching both pulses in the same way (right sketch) the DFG is only possible between one set of frequencies (only one colour). This should result in a narrowband pulse.

# 3 VIPER uncaging

This chapter of the thesis introduces and discusses VIPER uncaging. First, the concept is explained, then influences on the selectivity are discussed. Lastly, the properties of various PPGs in terms of suitability for VIPER uncaging are shown. These properties are especially important for the contrast and are no general limitations for VIPER spectroscopy, but only factors worth considering in the design of a VIPER uncaging scheme and selection of VIPER cages.

## 3.1 Concept

The species selectivity of the VIPER pulse sequence can also be used to develop an orthogonal uncaging scheme (see figure 3.1 on the next page).

To illustrate the selectivity of the VIPER pulse sequence the first row of figure 3.1 on the following page shows a TRIR experiment on a mixture of two cages with different leaving groups. The visible excitation is resonant with both species and both LGs get cleaved. The IR-probe spectrum shows a congestion of signals of each species.

In contrast, in the second and third row only the vibrationally pre-excited species undergoes photoreaction. The IR-pump pulse is chosen to be resonant with an IR mode of one of the species in a mixture. In the second row figure 3.1 on the next page this is indicated by the blue colour of the IR-pump pulse, corresponding to the blue Cage 1 and the blue IR absorption band in the sketch of the IR spectrum. The IR excitation causes a shift of the UV-Vis absorption which is indicated by the blue dashed spectrum in the UV-Vis spectrum sketch. This shift brings the molecules in resonance with the UV-Vis-pump pulse causing the cleavage of LG1. In a double difference spectrum only the signals of the selected species are seen.

The VIPER uncaging principle can be exploited for each species in a mixture as long as the IR bands can be excited selectively by the IR-pump pulse [30, 31].
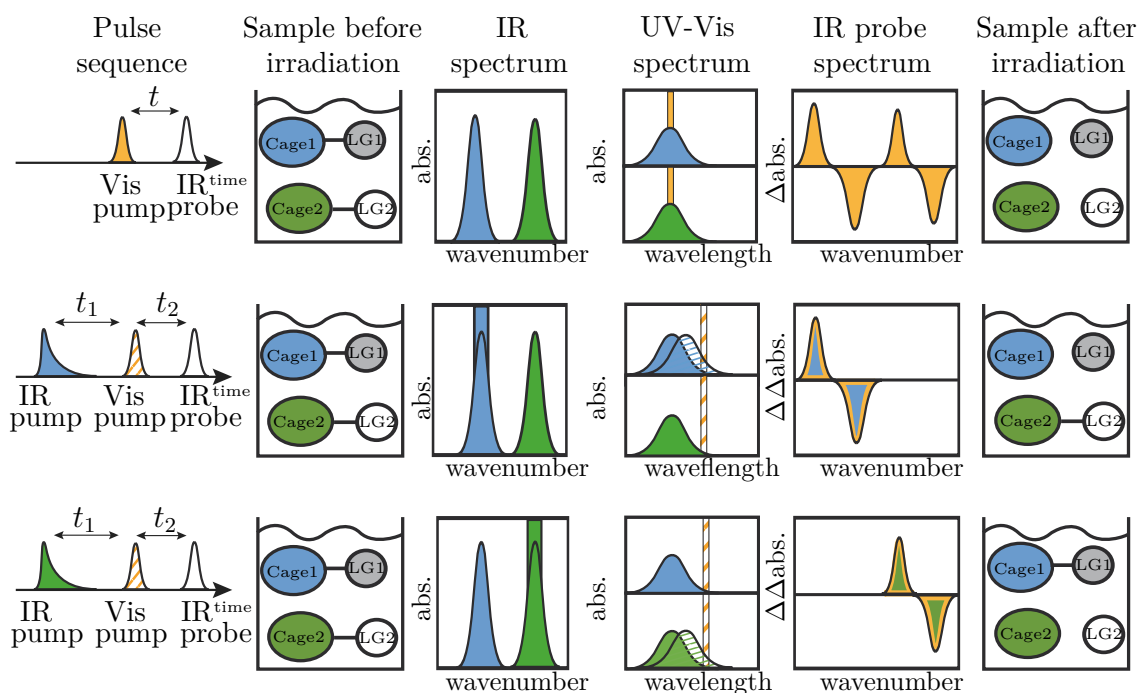
Figure 3.1: Schematic VIPER uncaging. First row: Unspecific uncaging with the TRIR pulse sequence, IR-probe signals from both species and uncaging of both species. Second row: VIPER pulse sequence, IR-pump pulse resonant with Cage 1, IR and UV-Vis spectrum with pump positions depicted, resulting IR-probe spectrum shows only signals of Cage 1, Sample after illumination, only LG 1 has been set free. Third row: Analogous VIPER uncaging for LG 2.

## 3.2 Contrast

The aim of this thesis is to develop an experimental scheme and choose suitable PPGs to provide a proof-of-concept orthogonal VIPER uncaging. However, the parameters for optimal VIPER spectroscopy and for optimal VIPER uncaging are not identical.

For orthogonal VIPER uncaging the most important goal is maximal contrast. If you plan to selectively excite one species in a mixture to undergo a photoreaction, you only want this species to undergo the photoreaction.

In terms of contrast in VIPER uncaging we have to distinguish between the contrast of the IR pre-excited species versus each other and between the contrast of the VIPER excited molecules versus an unspecific excitation of all species directly by the UV-Vis photon. As has been mentioned before, the unspecific background

by direct excitation through the UV-Vis-pump pulse is no problem for the spectroscopic application of VIPER, since it will be suppressed in the double difference spectra. It will, however, seriously impact the contrast in selective uncaging.

For distinguishing between the pre-excited species the main issue is the IR selectivity. The IR bands for the different species have to be clearly distinct. One convenient way to achieve this, is to customize a suitable PPG by isotope labeling: The introduction of a $^{13}$C atom, for instance, causes a shift to lower wavenumbers due to the changed reduced mass of the oscillator. By varying the number and position of the $^{13}$C atoms a set of very similar but selectively pre-excitable cages can be engineered.

In some cases different strengths in vibronic coupling, different absorption cross-sections or different orientations of transition dipole moments could be exploited to improve the contrast.

Concerning the unspecific background, a large shift or modulation of the UV-Vis absorption by the IR transition is helpful for a good contrast. The vibronic coupling should be as strong as possible. Also a steep slope on the high wavelength side of the UV-Vis spectrum helps. In the best case the high wavelength slope is just an exponential tail due to thermic occupation at room temperature. This could then even be reduced by cooling the sample. Solvents which broaden the absorption band are less favourable.

The ratio of (resonant) IR to (non-resonant) UV-Vis excitation is crucial for low unspecific excitation. This can be influenced by the IR-pump pulse energy, the UV-Vis-pump pulse energy and the wavelength of the UV-Vis pulse.

Another experimental influence is the delay between the IR- and UV-Vis-pump pulses. The vibrational relaxation determines the amount of IR pre-excited molecules which can be electronically excited at a given time. Effects like internal vibrational energy transfer can be exploited, if the receiving modes have a better coupling to the electronic transitions. Otherwise dissipation of the vibrational energy into the solvent would decrease the VIPER excitation.

A detailed study of the parameters influencing the VIPER signal size and the signal to background ratio is carried out in the PhD thesis of Carsten Neumann in the Bredenbeck group [123].

For VIPER uncaging the detection in the IR with a fs time resolution is in principle not necessary. The successful uncaging could be detected by another technique (e.g. HPLC). If one were to build a setup just for VIPER uncaging a synchronized narrow band ps laser could be used for the IR-pump pulse. This would mean losing the current fs time resolution, but if narrowband IR pulses were generated directly, no Fabry-Pérot would be needed. As cutting a narrowband IR-pump pulse out of a broad spectrum is currently the step in which most IR-pump energy is lost, making this step unnecessary would lead to much more IR-pump

energy being available.

Another idea, already possible with the current setup, would be to set the UV-Vis-pump pulse energy as low as possible and to set the wavelength for optimal contrast. With this conditions no VIPER signal could be observed spectroscopically, but after irradiation the contrast could be confirmed by other methods, e.g. NMR-spectroscopy or chromatography.

For this work the detection of the orthogonally uncaged leaving groups is to be done by fs-laser spectroscopy. This means the free LG infrared bands should be clearly distinctive and their oscillator strength should be large enough for convenient monitoring. The uncaging quantum yield should be big and because of experimental setup limitations the uncaging should occur within 3 ns as the delay line in the current setup limits the observable time range to this value.

Our experimental setup leads to IR-pump pulses with a Full-Width-Half-Maximum of 12 to 18 $cm^{-1}$ , therefore, the IR bands should be farther apart than this and their relative intensities should favour selective excitation if maximum contrast is aimed for. If the contrast is not the major concern alsoa distance of 10 $cm^{-1}$ between the bands should still work.

## 3.3 VIPER Cage Attributes and Examples

A vital part of this thesis was the screening of the photocage literature for suitable VIPER cages. Both in general and for the proof-of-concept experiments in this work. In this section the most commonly used PPGs are introduced and discussed in terms of their suitability for VIPER uncaging.

Since the first introduction of photocages [1], there have been lots of publications on this topic. Reviews concerning structures [129], applications [3, 130–133] and mechanisms [2, 64, 74] show different photocages sorted by their basic structures, ranging from nitroaryls (1) over benzoins (2) and coumarins (or quinolins) (3) to phenacyls (4). More exotic structures are cinnamic acids and the boron dipyrromethene core (5). The basic structures are shown in figure 3.2 on the facing page.

However, there are lots of publications without UV-Vis spectra. For a great number of cages only maximal absorption wavelengths are given as photophysical characterization. Sadly, all these potential VIPER cages have to be discarded in my screening, since the shape of the UV-Vis absorption is a vital information concerning the suitability for VIPER uncaging. In the appendix (chapter A on page 125) the cages that were analysed for suitability are shown. Here some selected examples are shown to explain the importance of cage attributes with regard to VIPER uncaging.

A word of caution should be given on the influence of substituents and leaving
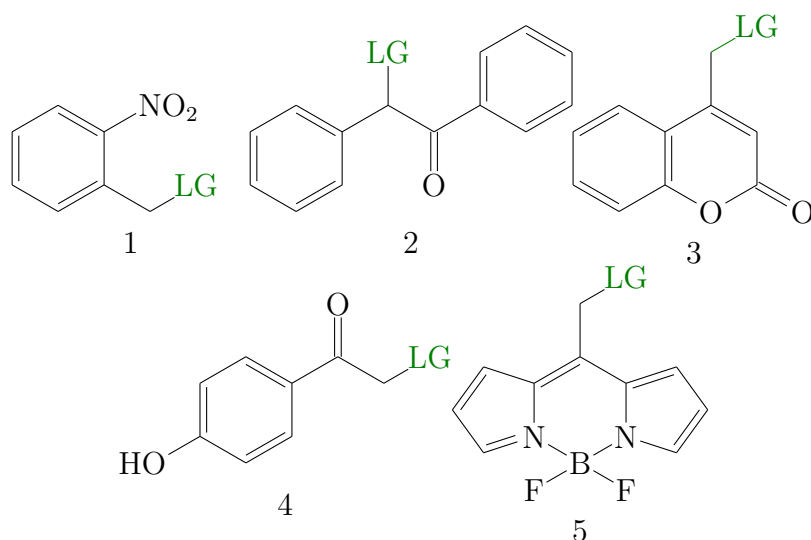
Figure 3.2: Basic structures of selected PPGS: 1 Nitroaryl, 2 Benzoin, 3 Coumarin,
4 *p*HP, 5 Boron Dipyrromethene. [2]

groups: Even molecules belonging to the same class of photocages can show very
different spectral properties. As the data in the appendix show, the nitroaryl group
is especially diverse. These differences can be, but are not limited to, the shape of
the spectrum, the extinction coefficient, the quantum yield and the kinetics of the
photo-reaction. Therefore a generalization from one cage with a specific LG and
specific substituents to all photocages from this class should be made with caution.
The solvent can also have a significant influence on all of the factors mentioned
above [2, 134].

As has been pointed out above (chapter 3 on page 31) a number of attributes
from the PPG influence the VIPER signal and the selectivity of VIPER uncaging.
Some of these are only relevant, if the detection of the photoproducts is carried
out by IR fs-laser spectroscopy as in this work.

For my screening of the literature the spectral shape in the UV-Vis and the
quantum yield were the most important points. At this point cages without a steep
slope or with quantum yields under 50 % were discarded. Both characteristics do
not exclude them from VIPER spectroscopy or cage application in general, they
only make them unsuitable for the aspired proof-of-concept experiment.

For cages with suitable spectra and quantum yields the mechanistic data on
the photoreaction was taken into account. For now the photoreaction should be
clean and simple with a release of the LG faster than 3 ns. Again these are no
fundamental requirements but concessions to our experimental setup.

Finally, a remark on the solubility should be given. For biological applications
the used PPGs should be soluble in water and therefore lots of work was done to

modify well-working caging groups to increase their solubility in water [2]. For optimization of VIPER uncaging the solvent should be no limiting factor at the moment. Therefore solvents like acetonitrile or tetrahydrofuran in which the chromophors dissolve in high quantity are used.

**Spectral Shape in the UV-Vis** To start the discussion of suitable spectral shapes to achieve a good VIPER contrast, first, the theoretical spectra are considered. As has been explained in section 2.4 on page 19 theoretical UV-Vis spectra for ground state and electronically excited states of PPGs can be computed. The computation of the influences of an IR-pre-excitation on the UV-Vis spectrum has been part of the PhD project of Jan von Cosel in the Burghardt group and has led to a publication [116, 117].

The theoretical spectrum (figure 2.11 on page 21) shows the computed transitions in the UV-Vis spectrum as "sticks". The IR excitation in the VIPER scheme introduces new transitions with lower energies due to the modulation of the UV-Vis transitions by the IR excitation. If the transitions were as separated as the stick spectra suggest, an IR-pre-excitation would lead to a distinct transition which could be excited by the consequent UV-Vis pulse without exciting the non IR excited species. This would lead to a very high contrast between VIPER signal and the direct unspecific background UV-Vis excitation.

In solution and at room temperature, however, the transitions are not sticks but broadened. There are multiple effects leading to broadening: Inhomogeneity due to the solvent (which is less for apolar solvents), a mixture of various Isomers (less for rigid molecules) and lifetime broadening. Additionally, if the other effects are minor, a red tail at the higher wavelength side of the spectrum can be seen due to thermal excitation of the vibration levels (which could be reduced by cooling in an experiment). Compare figure 2.11 on page 21 to figure 3.6 on page 40 for an experimental UV-Vis spectrum of a coumarin cage in contrast to the computed spectrum.

A steep slope on the high wavelength side of the cage is closer to the ideal stick spectrum situation than a slow incline or a spectrum with plateaus and therefore should allow for a better contrast.

Experimental UV-Vis spectra in the literature were screened for a step slope on the high wavelength side.

As has been pointed out above, no general assessment of a class of cages can be made but each combination of leaving groups and substituents has to be evaluated. In the following a few examples are presented to illustrate suitable and unsuitable spectra.

A negative example is given by Tetramethoxybenzoin carbamate [135] in figure 3.3 on the next page, which has a low intensity plateau on the low energy
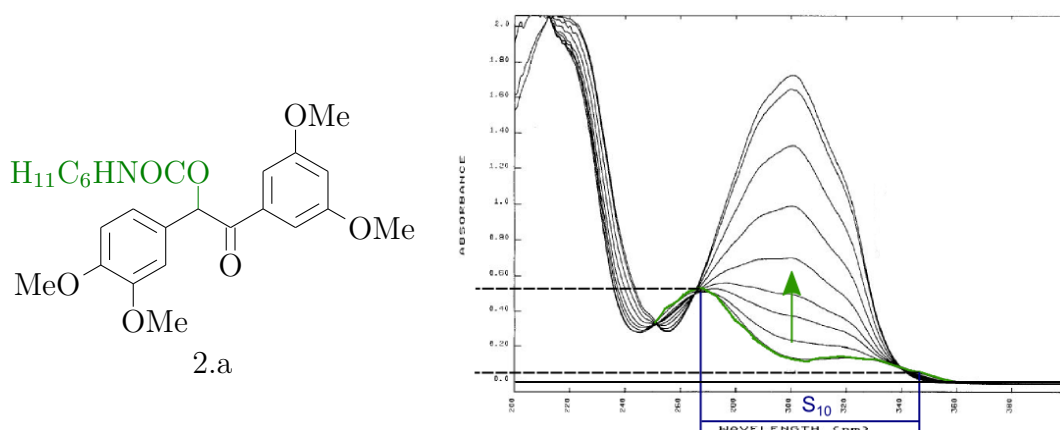
Figure 3.3: Left: Structure of Tetramethoxybenzoin carbamate, LG in green (2.7 in appendix). Right: UV-Vis spectra under irradiation with 350 nm light. Non-irradiated UV-Vis spectrum is higlighted in green. Left-most vertical blue line indicates the maximum of the absorption band at aproximately 265 nm, right-most vertical blue line indicates 10 % of intensity of this band. Wavelength difference between the blue lines is labelled $S_{10}$. Green arrow indicates changes uppon irradiation. Adapted with permission from [135]. Copyright 1996. American Chemical Society.

side. The non-irradiated spectrum is highlighted in green. An absorption band can be seen at approximately 265 nm. The absorbance decreases with longer wavelengths, but stays more or less constant between 290 nm and 325 nm. This plateau will prevent the VIPER cage from having a good contrast, because the spectrum can theoretically show a maximum shift of an IR photon. For this molecule, the off-resonant UV-Vis pulse would then be resonant with the plateau.

At first glance the spectrum of Dimethoxynitrobenzyl (DMNB) with a peptide model compound as LG [136] (black line in figure 3.4 on the following page, indicated by the green arrow) looks more promising. However, the perceived slope depends on the axis scaling.

To get a better estimate for the steepness of the slope for different cages I introduce the $S_{10}$ value. $S_{10}$ is the wavelength difference between the peak maximum of the relevant band and 10 % of its intensity. This quantity is used to compare the UV-Vis spectra of various cages. It has, compared to other concievable measures of steepness, the advantage that it can be easily extracted from figures in publications. For a suitable VIPER cage it should be as small as possible, as a small $S_{10}$ value indicates a steep slope. However, the difference in nm alone is not enough the judge the suitability. The red-shift needs to be compared to the energy
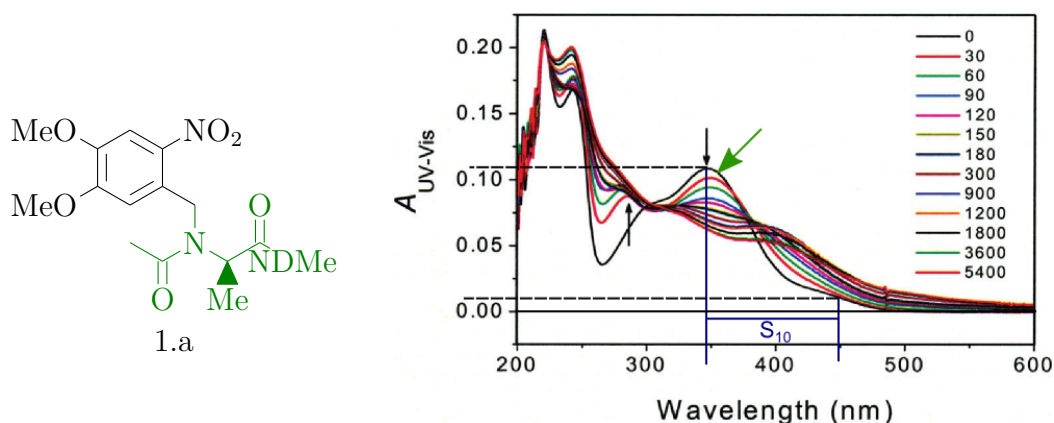
Figure 3.4: Left: Structure of Dimethoxynitrobenzyl peptide model, LG in green (1.12 in appendix). Right: UV-Vis spectra under irradiation with 355 nm light. Non-irradiated UV-Vis spectrum is indicated by green arrow. First vertical blue line indicates the maximum of the absorption band at approximately 350 nm, second blue line indicates 10 % of intensity of this band. Wavelength difference between the blue lines is labelled $S_{10}$. Colored lines are spectra under irradiation. Adapted with permission from [136]. Copyright 2008. American Chemical Society.

of an IR photon. Therefore, the $S_{10}$ is also converted to wavenumbers for easier comparison.

As an example for the calculation of $S_{10}$ the chosen intensities for Tetramethoxybenzoin carbamate are indicated in figure 3.3 on the previous page. The higher horizontal dashed line shows the maximum intensity of the non-irradiated band. The left blue vertical line indicates the wavelength. The second horizontal dashed line is at approximately 10 % of the band. An additional black horizontal line is drawn at 0 intensity. The right blue vertical line shows the wavelength for 10 % intensity. The difference between both blue lines is the $S_{10}$ value. For Tetramethoxybenzoin this value is 75 nm. To determine the difference in wavenumbers, the wavelengths for both blue lines are converted to wavenumbers and then the difference between these wavenumbers is calculated. This leads to 8500 $cm^{-1}$ for Tetramethoxybenzoin carbamate. For the DMNB peptide model (figure 3.4) it is 100 nm (6300 $cm^{-1}$), indicating that the slope of the DMNB peptide should be worse for VIPER applications even though it looks better at first glance. This illustrates one of the difficulties of deciding on a cage by screening the published UV-Vis spectra.

Another problem of the Tetramethoxybenzoin and DMNB cages are the photoproducts. These have a red-shifted absorption compared to the starting materials

5.a
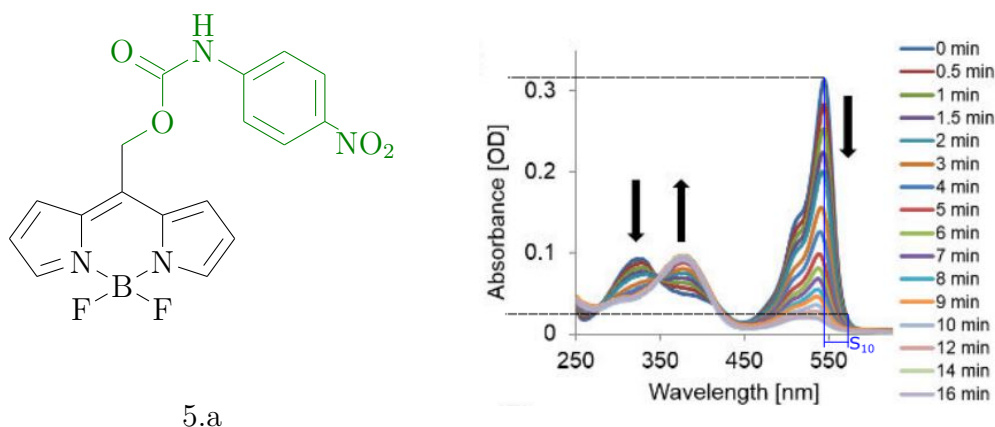
Figure 3.5: Left: Structure of *meso*-methylhydroxy BODIPY, LG in green (5.1 in appendix). Right: UV-Vis spectra under irradiation with 540 nm light. Colored lines are spectra under irradiation. Adapted from [137] with permission from The Royal Society of Chemistry.

which is not a fundamental problem for VIPER uncaging since it does not influence the pre-excitation and therefore the selection for uncaging. But it is inconvenient, since the product molecules absorb the off-resonant UV-Vis photons, which are intended to be absorbed by the IR pre-excited molecules. Therefore, the effective UV-Vis intensity is reduced. This can be compensated by using more UV-Vis energy. There might also be problems with overlapping signals from the products.

A PPG with a more suitable UV-Vis shape is for example given in cages based on the boron dipyrromethene core (BODIPY), shown in figure 3.5 [137]. The $S_{10}$ value is 70 nm (2700 $cm^{-1}$) and the spectral region of interest is conveniently above 500 nm. The spectral range on the higher wavelength side of the visible spectrum is favourable to reduce photo damage in biological applications.

The spectra for [7-(diethylamino)coumarin-4-yl]methyl (DEACM) (figure 3.6 on the following page [138]) and *para*-Hydroxyphenacyl (*p*HP ) (figure 3.7 on the next page [139] are also nicely suited for VIPER application. The $S_{10}$ values are for DEACM 40 nm (2500 $cm^{-1}$) and for pHP 35 nm (3700 $cm^{-1}$) . Structures and photophysical characterization of the DEACM and pHP cages used in this work are shown in section 5.1 on page 57 and section 5.2 on page 78.

Chapter A on page 125 includes UV-Vis spectra and $S_{10}$ values for the analysed cages.

To really make a more solid statement about the quality of a VIPER cage, the difference between the UV-Vis spectrum of the IR pre-excited molecules and the ground state spectrum is of interest.

This brings us back to the computations mentioned at the beginning of this
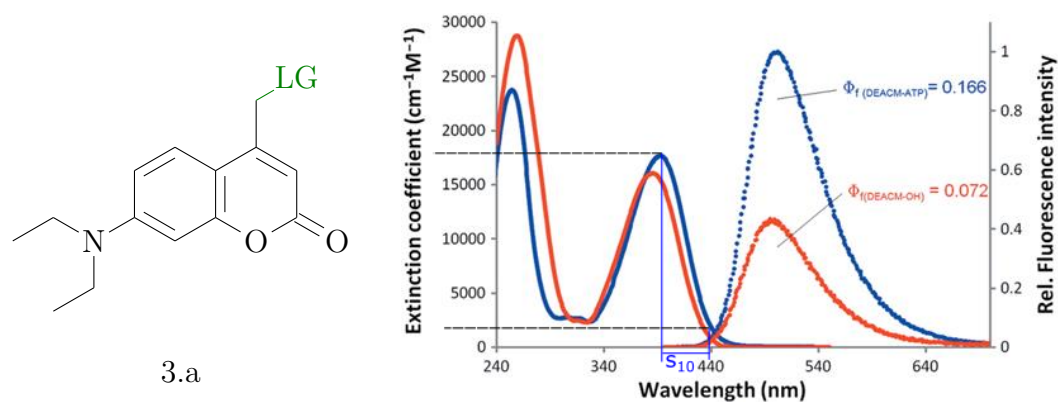
Figure 3.6: Left: Structure of [7-(diethylamino)coumarin-4-yl]methyl, LG is ATP or OH (3.6 in appendix). Right: UV-Vis absorption and emission spectra (with excitation at 385 nm). ATP in blue, OH in red. Adapted with permission from [138].
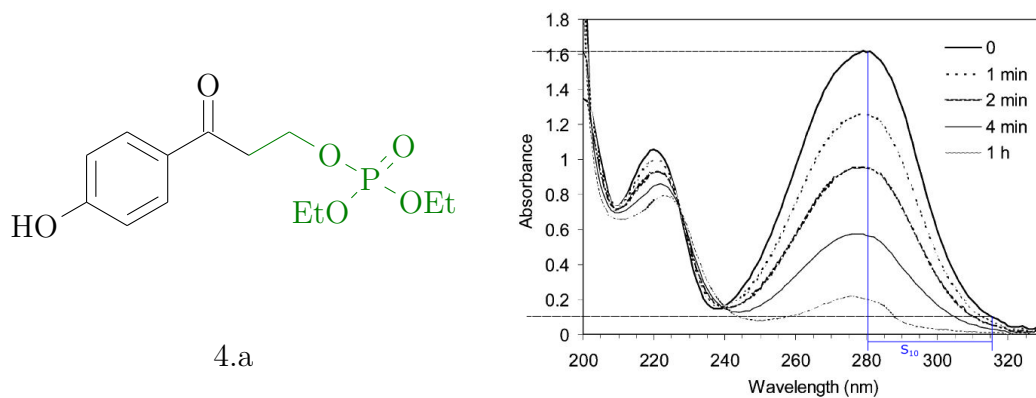


Figure 3.7: Left: Structure of *p*-Hydroxyphenacyl phosphate, LG in green (4.7 in appendix). Right: UV-Vis absorption spectra under irradiation with 267 nm. Reprinted with permission from [139]. Copyright 2006 American Chemical Society.

paragraph. They show in theory the ground state and the vibrationally excited state spectrum. But as has been discussed above the "stick" representation alone cannot be used to make assumptions about the shape of the UV-Vis spectrum at room temperature in solution. One way to improve this, is to broaden the computed spectrum till it fits an experimental spectrum and analyse the differences of the pre-excitation afterwards. Still, the computed UV-Vis spectra are mainly helpful in choosing the best IR mode of a VIPER cage for pre-excitation.

Experimentally, the measurement of the vibrationally excited state UV-Vis spectrum in addition to the ground state spectrum would be necessary to determine the VIPER suitability. UV-Vis spectra of the IR pre-excited molecules are, however, not in the literature at the moment. They could be measured by IR-pump-Vis-probe experiments as carried out by [118]. For this purpose the planing of a Vis-probe setup is part of Carsten Neumann's PhD thesis in the Bredenbeck group [123].

**Quantum Yield** To follow the photochemistry with IR fs-laser spectroscopy, adequate product signals are needed. This is not a principle requirement for the application of VIPER uncaging, since alternative techniques could be used to monitor successful uncaging (such as HPLC and NMR). Together with the IR extinction coefficient of the product signals, the quantum yield of the cage is of importance for this. The quantum yield depends among other things on the photocage class, the LG, the solvent, the irradiation wavelength and sometimes the pH-value.

For the DMB in figure 3.3 on page 37 the quantum yield is given as 65 % [135]. For other DMB cages and conditions the values range between 3 % and 45 % [2]. For DMNB (figure 3.4 on page 38) the literature gives quantum yields from less than 5 % up to 65 % [2].

BODIPY cages (figure 3.5 on page 39), which are derivatives of fluorophores have a quantum yield as low as $6 \cdot 10^{-4}$ for the photoreaction [137]. This very low quantum yield counterbalances the very good spectral shape for an optimal VIPER cage at the current point in VIPER uncaging development. A second generation of BODIPY cages has been published recently and has much higher quantum yields up to 90 % [140].

The quantum yields for coumarins also vary strongly with different LGs and they are seldom given in the literature. One exemplary value for a high quantum yield for a coumarin cage is 28 % for DMACM-cAMP [2]. This quantum yield is reasonable for conventional uncaging applications. To optimize a VIPER uncaging scheme a larger quantum yield would be helpful.

For pHP the quantum yields given in the literature are quite high. pHP formate in a 3 to 1 water to acetonitrile mixture has a quantum yield as high as 94 % [141].

In chapter A on page 125 quantum yields are given, if they were available.

**Photoreaction**   Not for all classes of cages mechanisms are available in the literature and even less cages have time resolved measurements to give reliable time scales.

Suitable data are published for example on DMB diethyl phosphate [142] and pHP phosphate [139].

The experimental scheme applied in both cases was Vis-pump Vis-probe spectroscopy, which gives access to lifetimes of excited states and intermediates, if they absorb visible light. In both cases no spectroscopic monitoring of the free leaving group was possible.

In figure 3.8 on the next page the photo reaction scheme for DMB diethyl phosphate as well as some transient absorption spectra are shown [142]. Since the LG does not absorb in the probed spectral range, no timescale of appearance can be given. The Vis-pump-probe data, however, suggest that major rearrangements of the chromophore are needed to cleave the bond to the LG. The complexity of the photoreaction and the long time scale (as well as its UV-Vis spectrum) make this cage unsuitable for VIPER optimization. The long time scale means that the product formation cannot be observed, since we can only cover delays up to 3 ns with the current setup. The complexity of the photoreaction makes assignment difficult and can perturb reproducibility.

The data for pHP phosphate (figure 3.9 on page 44) look more promising. The Vis-pump Vis-probe data show a vanishing absorption within 2000 ps and additional transient Raman data show that product bands arise on a timescale shorter than 6 ns. Even though also in this example the appearance of the free LG cannot be monitored, the data suggest a cleavage within the first 200 ps after irradiation [139].

For many cages the mechanism has not been elucidated on this short timescales. For DEACM for example the formerly proposed mechanism of the formation of a thight ion pair has been derived from fluorescence rates [143]. The characterization of DEACM photoreaction markers on short timescales to evaluate its usefulness for VIPER is shown in section 5.1 on page 57 and has lead to publication [134]. A detailed study of the photo product formation has been carried out in Carsten Neumann's PhD project in the Bredenbeck group and is part of Nicole Mielkes Masterthesis [123, 144].

Chapter A on page 125 does not include data on the photo reactions. The additional information was not deemed worth the effort, since for a new cage it would anyway be necessary to analyse the literature again for an up-to-date mechanism. The overview in the appendix is only meant to help in the first screening for potential VIPER cages.
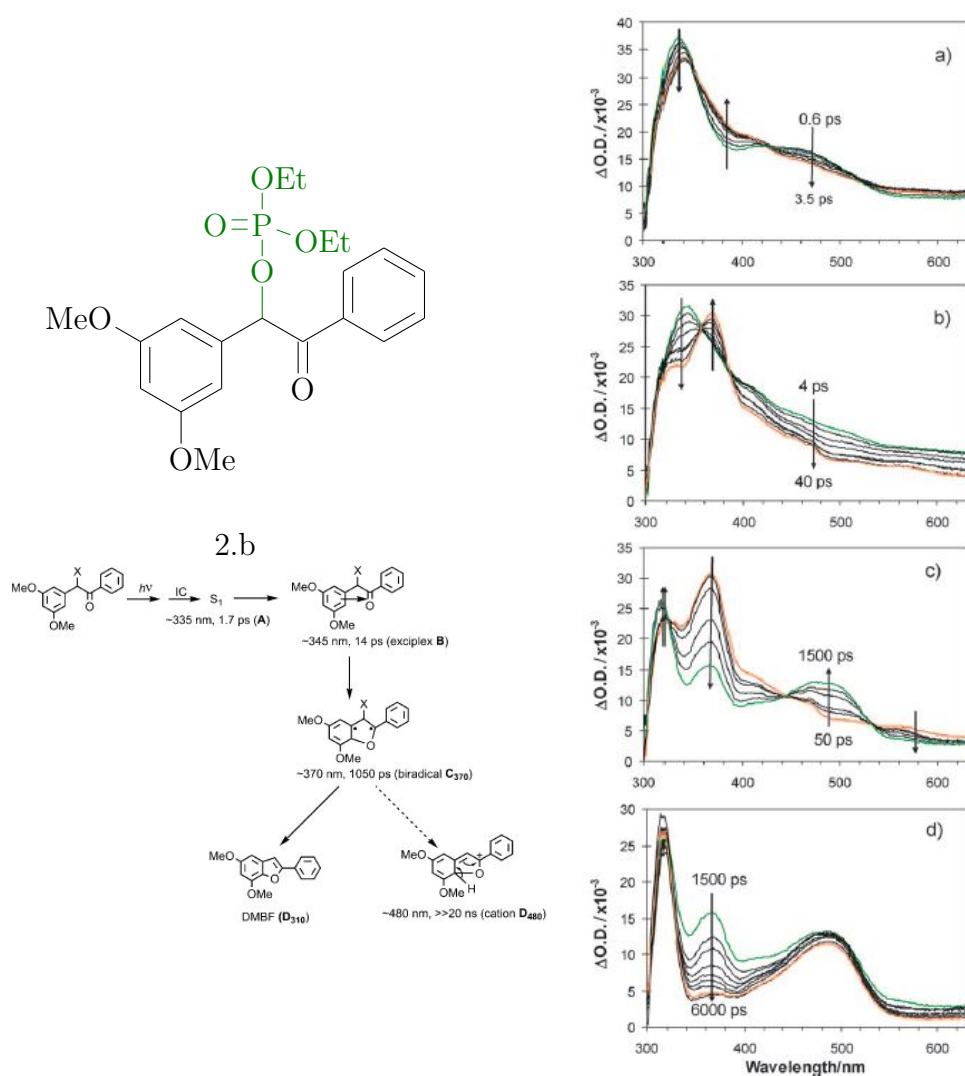
Figure 3.8: Structure, mechanism and Vis-pump Vis-probe data (a) 0.6 to 3.5 ps
b) 4 to 40 ps c) 50 to 1500 ps d) 1500 to 6000 ps) of DMB diethyl
phosphate in acetonitrile. [142] Copyright © 2010, John Wiley and
Sons
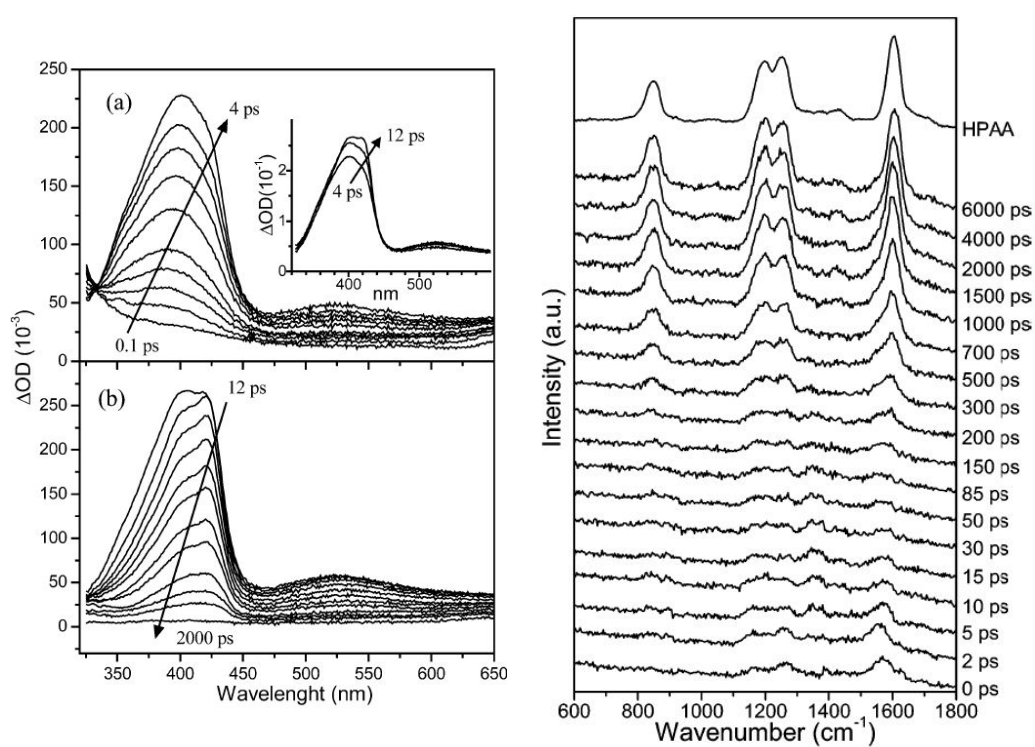
Figure 3.9: Transient absorption and Raman spectra of *p*HP phosphate (4.a) in H₂O:MeCN (1:1) (a) 0.1 to 12 ps b) 12 to 2000 ps) Reprinted with permission from [139]. Copyright 2006 American Chemical Society.

# 3.4 Used Photocages

**Coumarin Cage** The first PPG on which VIPER uncaging is carried out is DEACM, which has been mentioned in chapter 3.3 on page 34 as an example for a suitable UV-Vis spectrum (see figure 3.6 on page 40 for an exemplary structure and UV-Vis spectrum). DEACM is a coumarin derivative, where the coumarin ring is substituted on position 7 with a diethylamino group [2]. The first demonstration of coumarin uncaging was carried out by Givens and co-workers on a 7-Methoxycoumarin with a phosphate as LG [145]. Since then many derivatives have been developed (and some examples with UV-Vis spectra in the literature are shown in section A.3 on page 148) [2, 22, 23, 28, 131, 146, 147]. They are widly used because of their absorption maximum which is between 310 nm and 490 nm depending on substituents and solvent. This is a significantly longer wavelength than most photocages exhibit and therefore more suitable for biological application. Other favorable features are their fast release, improved stability and fluorescent properties (which can be used for monitoring). Water solubility can also be increased by the right substituents [2].

For DEACM cages the absorption maxima are at 390-400 nm and they have a reasonable quantum yield [131].

The uncaging mechanism was studied by fluorescence measurements on the nanosecond time scale [143, 148, 149]. After excitation of the $\pi, \pi*$ transition an heterolytic $C - X$ bond cleavage can take place. A tight ion pair between the coumarinylmethyl cation and the leaving group conjugate base has been postulated to be the key intermediate. DEACM-OH has been shown to be one of the photo products after cleavage [143].

However, the ultrafast UV-Vis pump IR-probe measurements carried out in Carsten Neumann's PhD project and published recently, could not verify the existence of a thight ion pair [123, 134]. Figure 3.10 on the following page shows the proposed transitions from the ultrafast laser data. After the initial excitation and cooling the excited state either recovers to the ground state or the bond between the cage and the azide is cleaved. The release of the LG azide was shown to be very fast between 35-115 ps depending on the water content in the solvent.

The quantum yield was determined to be between 10-20 % also depending on the water content [134].

The identifications of the coumarin photo products was not straight forward and is included in detail in Carsten Neumann's PhD thesis [123] and was part of the Masterthesis of Nicole Mielke [144].

DEACM was choosen as a first VIPER cage because of its structural similarity to the laserdye Coumarin 6 on which the first VIPER measurements were carried out and because of its convenient spectral range in the UV-Vis and the nice spectral shape. For azide as LG the absorption maximum in acetonitrile is at 390 nm and
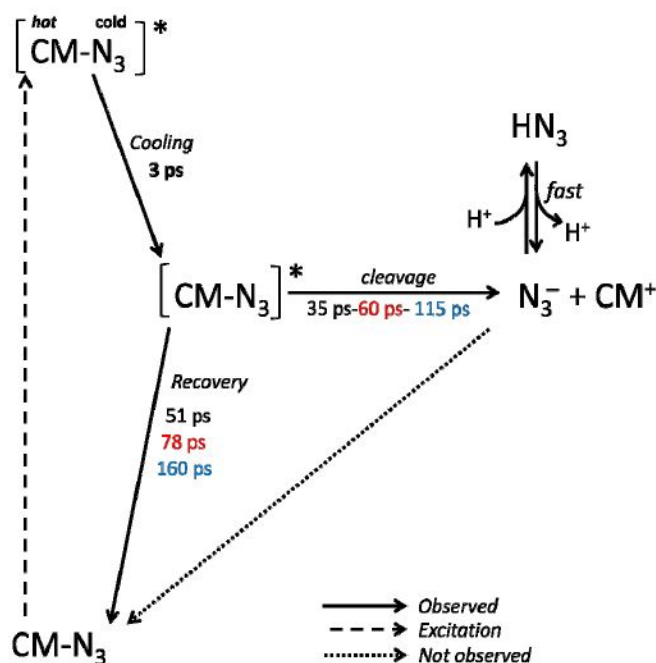
Figure 3.10: Reaction scheme proposed on the basis of the ultrafast laser data. Black is 0 % water, red is 5 % and blue is 50 %. The * denotes the electronically excited state. Permission!![134]

the $S_{10}$ value is about 40 nm (2385 $cm^{-1}$). Azide was choosen as LG due to its convenient absorption in the IR region.

The VIPER experiment was carried out on isotopomers, which are discussed in section 5.1.1 on page 57 and were synthesized by Matiss Reinfelds as part of his PhD project in the Heckel group [150].

**p-Hydroxyphenacyl Cage**  For a second try of orthogonal VIPER uncaging the pHP (figure 3.7 on page 40 for structure and spectrum) cage was chosen. The cage was first demonstrated by Givens and co-workers [151] and its high quantum yields (up to 90 %) and its clean photo reaction are given as its major advantages [2, 152, 153].

After photoexcitation pHP undergoes an intersystem-crossing from the $S_1$ to the $T_1$ state. In the presence of water the LG is then cleaved and a Photo-Favorskii rearrangement takes place [2, 141, 154]. A mechanism for the photo reaction of pHP is given in figure 3.11 on the next page.

The triplet allyloxy-phenoxy biradical (4.c in figure 3.11 on the facing page) was identified by transient absorption measurements [141]. The major product in the presence of water (4.g in figure 3.11 on the next page) was assigned by
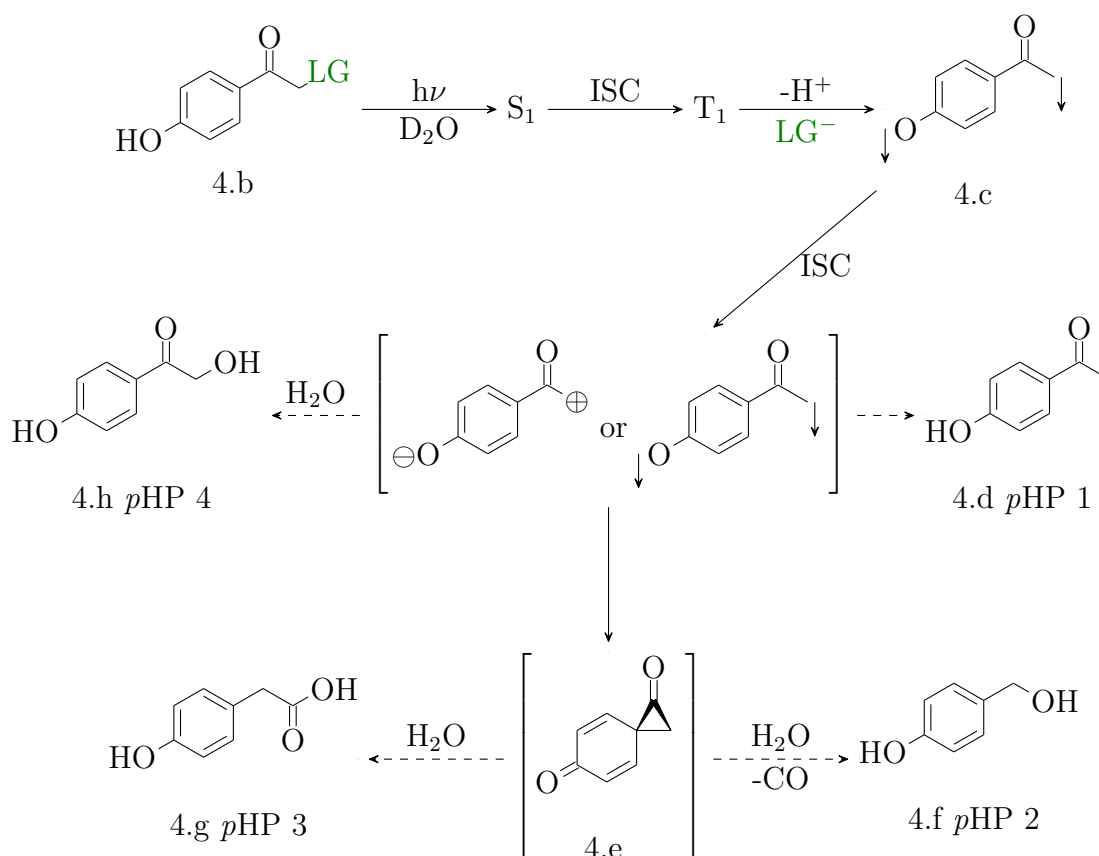
Figure 3.11: Mechanism of photo uncaging of pHP showing the possible photo products according to the literature [2, 141].

transient Raman experiments [155] and the minor product with cleavage of CO (4.f in figure 3.11) was identified by FTIR difference spectra [141]. The spirodienedione (4.e in figure 3.11) was studied by stereochemical probing of the mechanism [154]. It is important to note that the cleavage of the LG is said to be quite fast while the later rearrangements happen on longer time scales. There are, however, no spectral proofs of the free LG in the literature so far.

The shape of the UV-Vis spectrum of *p*HP was also deemed suitable for VIPER uncaging (figure 3.7 on page 40). However, the absorption maximum is at approximately 290 nm and therefore quite far in the UV-region. This is an inconvenient region for pump light generation and affects the $S_{10}$ value. Even though $S_{10}$ is 35 nm, because of the low wavelength this amounts to 3700 $cm^{-1}$ which is bigger than for DEACM.

The phenol group of pHP can be deprotonated depending on the pH of the solvent, which leads to a red-shifted UV-Vis spectrum. The photo reaction of the

deprotonated pHP is, however, much more unpredictable and unclean [156].

For a number of possible isotopomers the infrared band positions were computed and the most promising candidates were synthesized by Matiss Reinfelds in the Heckel group [150]. A detailed discussion is given in section 5.2 on page 78.

# 4 Materials and Methods

## Sample preparation

For this thesis DEACM samples were prepared by Matiss Reinfelds in the scope of his PhD thesis in the Heckel group (see chapter B on page 189 for details on the synthesis). The DEACM samples were dissolved in neat acetonitrile (dried with a molecular sieve).

The $p$HP samples (both cages and possible photo products) were provided by Matiss Reinfelds. The cages and their isotopomers were synthesised by Matiss (see chapter B on page 189). The other samples were purchased and used without further purification. $p$HP was dissolved in $D_2O$:ACN (acetonitrile) mixtures with various ratios.

## Steady-State measurements

**Infrared Absorption** All steady-state infrared spectra were measured with a Bruker Tensor 27 in a flow cell [157]. Irradiation of DEACM[1] was carried out with a LED box with two 365 nm LEDs. The sample was pumped as fresh sample was needed because of the irreversible photo reaction. Also this was meant to prevent problems caused by gas formation.

Irradiation of $p$HP was done with a BRITTA water sterilization lamp. The lamp spectrum is depicted in figure 4.1a on the following page. Various peaks can be seen. The peak at approximately 225 nm is of interest for the $p$HP irradiation. $p$HP has no absorption in the higher wavelength region. In the UV region needed for $p$HP uncaging the absorption of the sample container has to be taken into consideration. Absorption spectra of various containers are depicted in figure 4.1b on the next page. It becomes apparent that most sample containers are unsuitable. Only glass or quartz cuvettes are still transparent in the needed wavelength region. The illumination was carried out using two flow cells connected with a tube. Calcium fluoride windows were used. One cell was outside of the spectrometer and was irradiated. During irradiation the sample was continuously pumped. For

---

[1]The steady-state measurements on DEACM were carried out by Nicole Mielke and are described in detail in her Master's thesis [144].

spectrum collection the pump and the irradiation were paused. For *p*HP-azide the flow cell and the lamp outside of the spectrometer were covered by a plastic bag, which was flushed with nitrogen gas to prevent changes in the water vapor concentration during illumination. The optical path lengths and sample concentrations as well as solvents changed for the different measurements and are always given with the spectra.
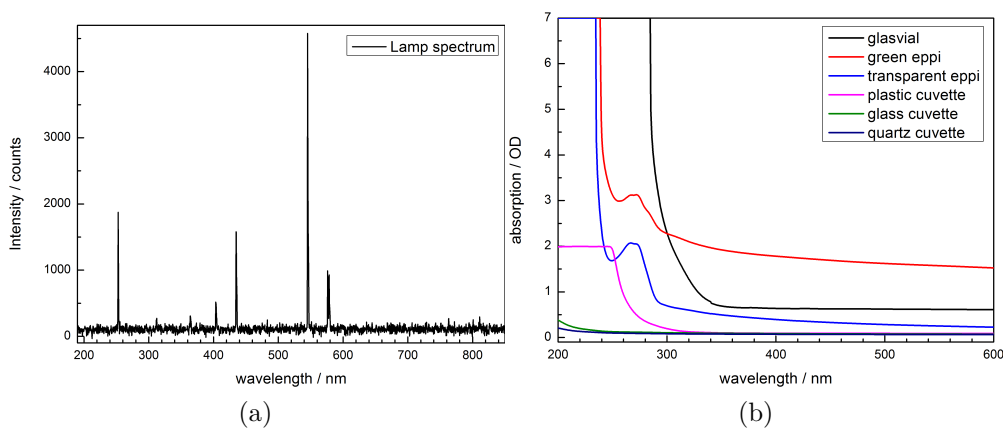


Figure 4.1: (a) Spectrum of the BRITTA water sterilization lamp collected with a fibre spectrometer. (b) Absorption spectra of various sample containers measured empty in the UV-Vis spectrometer.

**UV-Vis Absorption**   The UV-Vis spectra were measured with a JASCO V-670 spectrometer and a flow cell or a 1 mm quartz cuvette. The illumination conditions were the same for DEACM[2] and pHP as in the infrared measurements. The respective concentrations and solvents are given with the spectra.

# Ultrafast measurements

A Ti:Sapph regenerative amplifier (3.5 mJ, 800 nm, 90 fs, 1 kHz, Tsunami-Spitfire XP combination of Spectra Physics) was used to pump three home-build OPAs. Two OPAs were used to generate IR light. Signal and idler generated in a BBO subsequently underwent DFG in a $AgGaS_2$ crystal leading to light in the mid-IR region.

A low-power OPA (380 $\mu$J input) was used to generate the IR probe pulse. For DEACM measurements a wedge was used to split the light into a probe and a reference beam. For pHP measurements a beamsplitter was used for this purpose.

---

[2]These measurements were also carried out by Nicole Mielke [144]

Table 4.1: Foci sizes for the used beams.

|  | Mixing Process | Focus Size (in $\mu$m) |
|---|---|---|
| IR-probe | DFG of signal + idler | 70 x 80 |
| IR-reference | DFG of signal + idler | 80 x 80 |
| IR-pump | DFG of signal + idler | 110 x 120 |
| UV/Vis-pump | | |
| DEACM TRIR | Doubled fundamental | 150 x 150 |
| DEACM VIPER | Trippled signal | 190 x 160 |
| $p$HP TRIR | Trippled fundamental | 90 x 120 |
| $p$HP VIPER | SFG doubled fundamental + signal | 145 x 125 |

A high-power OPA (1.65 mJ input) was used to generate the IR pump pulse. The IR-light was sent through a Fabry-Pèrot Interferometer (FP) to generate a narrowband pulse. It traveled over a delay-stage, which was computer controlled to vary the waiting time between the pulses and passed a chopper running at 250 Hz.

A third OPA was used to generate visible or UV-light depending on the sample molecule absorption. The OPA-input was 550 $\mu$J. For DEACM TRIR the fundamental was doubled in a BBO. For DEACM VIPER the signal generated in a BBO was tripled in two additional BBOs with a retarder plate between them. For pHP TRIR the fundamental was tripled in two consequent BBOs with a retarder plate between them and for pHP VIPER the signal was mixed with the doubled fundamental in another BBO crystal. In all cases the light traveled over a delay line in front of the OPA and passed a chopper running at 500 Hz. The beam passed a polarizer and $\lambda$-half-waveplate suitable for the wavelength. The focus size varied between the processes and is given in table 4.1.

The chopping scheme described in [30] was used to obtain TRIR, 2D-IR and VIPER data.

Depending on the sample and the type of experiment different the sample concentration and volume were adjusted and are given for each measurement in the figure captions. For the final DEACM VIPER measurement 2 ml of 25 mM concentration were used. For $p$HP a 1.5 ml sample with 100 mM concentration in 12.5 % was used.

With exception of the 2D-IR measurement, the sample was always pumped with a micropump to refresh it on a shot-to-shot basis. The flow cell was translated up-and-down to prevent heating effects by the UV-Vis pump light. Additionally, a shutter blocked the visible or UV-light while the delay lines were moving.

The spectra were recorded with a TRIAX 180 spectrometer from HORIBA and a mercury cadmium telluride (MCT) detector (2 x 32 pixel, Infrared Associates).

# VIPER measurement routine

The output enegy and the noise from the laser was measured with an Ophir powermeter and documented in a labjournal on a day to day basis. The input energies into the IR-probe (380 $\mu$J), IR-pump (1.55 mJ to 1.7 mJ) and UV-Vis pump (550$\mu$J) OPA were adjusted with a wave plate and a polarizer on an Ophir powermeter. The input energy of the IR-pump OPA was varied to find an optiomal value for each measurement series.The input power was set as high as possible without generating white light in the BBO due to too high pump energies.

The IR-pump energy is especially important to the VIPER signal size. Therefore, an optimization routine was carried out befor each measurement. Signal and idler of the IR-pump OPA centered in the ring mode region were measured to be approximately 300 $\mu$J. This gave approximately 10 $\mu$J mid-IR light after the AgGaS$_2$ crystal and the dichroic mirror separating signal and idler from mid-IR. The beams were aligned through two irises in front of the mirror telescope (which was used to adjust the beam diameter and collimate the beam). The mirror telescope was necessary because flat mirrors instead of spherical mirrors were used in the intereferometer for DFG to prevent damage to the crystal due to high energies. The setup was flushed with dry air. After the telescope the IR beam was aligned on two irises in front of and after the delay line. Without FP the energy after the delay line was between 4.5 to 5.2 $\mu$J (at <0.1 % relative humidity). With FP the energy was to small to be measured, but is estimated to be around a factor 20 less. The energies were measured with the Coherent *LabMax_TOP* Powermeter set to 6250 *nm*.

The spatial overlap between the probe OPA and the IR pump OPA was aligned with a 50 $\mu$m pinhole. Then the temporal overlap was checked with the gallium arsenide labelled *IR*. For this the chopper in the IR pump beam path was run at 500 Hz and a *Zero Order Scan* was collected. It is important that the lids of the housing are closed and the setup is flushed with dry air for a sufficiently long time. Flushing after the sensors showed a relative humidity of <0.1 % often resulted in further improvement of the IR energy. The sensors probably show a local humidity and do not allow a complete control of the humidity in the setup.

The energy output of the visible pump OPA strongly varied with the wavelength. It was optimized on the Coherent Powermeter with a suitable wavelength setting and then the power was turned down with a filter wheel to below 1 $\mu$J to adjust the overlap. Higher energies might damage the pinhole or Gallium Arsenide. Spatial overlap between probe and visible pump OPA was adjusted with a 50 $\mu$m pinhole and the temporal overlap with a *Scan Delay UV* on the gallium arsenide labelled *UV*. The chopper in the UV-Vis beam path was running at 500 Hz and the setup was flushed. Afterwards the UV-Vis energy was adjusted with the filter wheel on the powermeter to the energy wanted for the measurement.

For the VIPER routine the chopper phases need to be controlled. For this the UV-Vis chopper is set as close as possible to 500 Hz without synchronizing it and the IR chopper to 250 Hz also without synchronizing. The knobs for the phases should be between 4 and 6. Otherwise they could sometimes be observed to „walk off"after some time. The UV chopper is synced first and the IR chopper second. Now the pattern for the choppers on the oscilloscope should look like the sketch in figure 4.2 (*Low→High→Middle-Low→Middle-High*).
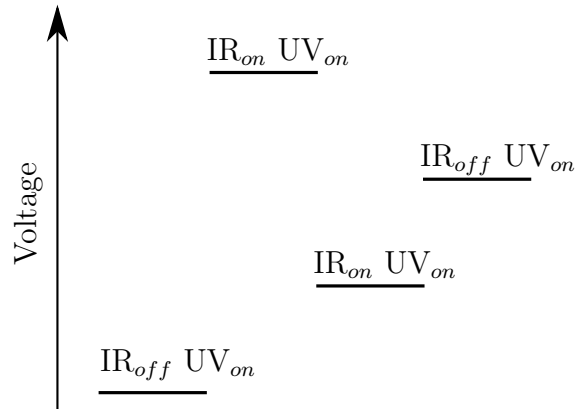


Figure 4.2: Schematic representation of the steps on the oscilloscope with labelling.

These steps should not flicker but be stable, otherwise the chopper phase knobs need to be adjusted. The UV-Vis beam after chopping needs to be controlled with a photodiode which was inserted in OPA 3 to pick up a reflection of the fundamental after chopping. The pattern should be *on-off-on-off*. Normally *off* still gives a small signal on the photodiode and this should be as small as possible and constant. If the phase of the chopper is not correctly set the photodiode's signal will flicker. The phase of the IR pump needs to be checked on the detector. The pattern is *on-on-off-off*. If the phase is correct both *on* signals have the same amplitude on the oscilloscope. This should also not flicker.

With the three pulses TRIR, 2D-IR and difference spectra can be recorded simultaneously. The two delay lines are controlled by the computer to adjust the timing between the three pulses. The delay line in front of the UV-Vis OPA controls the delay between UV-Vis pump and IR probe pulse. The delay line after the IR pump OPA controls the delay between the IR pump pulse and the IR-probe pulse.

The difference absorption signals in Gallium Arsenide or the sample can be checked with the measurement routine *Show Signal UV-Switch_new*. This routine

shows many coloured lines. Violet and yellow belong to the UV-Vis-pump IR-probe signal with and without IR pump, respectively. If the IR pump is blocked both should be identical. The blue and the red belong to the 2DIR signal with and without UV-Vis pump, respectively. Without the UV-Vis pump they have to be the same. The difference between each color pair is the VIPER signal. If the timings are suitable to give a VIPER signal (i.e. with the UV-Vis delay set to a time where a VIPER signal is expected, which is typically at the same time of the IR pulse, or about 1.5 ps after), blocking the UV-Vis pump should lead to a vanishing signal in yellow and violet and blue should resemble the red spectrum. Blocking the IR pump lets blue and red vanish and yellow resemble the violet spectrum.

The routine *Show Difference UV-Switch* shows directly the VIPER signal. Usually the spatial overlaps are adjusted on the individual pump-probe signals in the *Show Signal UV-Switch_new* routine. If it can be observed, the VIPER signal can also be optimized in this routine. For this it is helpful to go to a timing where no IR signal can be seen any more (i.e. after the vibrational excitation has decayed), then the overlap can be optimized on the additional spectral feature in the blue spectrum . The difference between the blue and red line should be increased. Normally, this works better, than optimizing in the *Show Difference UV-Switch* routine.

The Newport motor, which moves the sample cell up and down, needs to be initialized and its range needs to be set. This is necessary to prevent the sample from sticking to the glass window and being burnt by the visible light. The motor needs to be synchronized to the measurement routine in order to not interfere with the interleaves of the IR delay line for phase cycling. This is denoted by a *NP-motor* in the name of the routine.

For VIPER measurements a broadband (*UV-BBIR-IR_VIPER*) routine without FP is available. The VIPER routine with FP is called *UV-IR-IR_VIPER* and there is an additional routine which allows two-color VIPER measurements (this is denoted by a *Spec*). With this measurement routine one can use different pump and probe windows.

## 4.1 Data procession and analysis

The VIPER routine yields five files for the different signals. The UV-Vis-pump IR-probe spectra (the violet line in the *Show Signal UV-Switch_new* routine) are saved in the .LIN files. The 2D-IR spectra (red in *Show Signal UV-Switch_new*) are saved as .IR files. The VIPER spectra are saved as .DIFF files. The 2D-IR signal with UV-Vis pump on (blue in *Show Signal UV-Switch_new*) is saved as .UV file and the LIN signal with IR pump on (yellow in *Show Signal UV-Switch_new*)

is saved as .IRLIN file.

The data from the measurement routine needs to be processed. In this work a Matlab Script written by Luuk van Wilderen was used (*Lvw_IRUVIR2mat_VIPER _160611.m*). Afterwards the x-axis of the laser data needs to be calibrated for this another script by Luuk van Wilderen was used (*TRIAX_calibration_final.m*) and the correction factor was chosen in a way that the laser data matched the steady-state data.

The time points are calculated from the delay line positions. The timings are named as in the sketch of the VIPER pulse sequence in figure 2.12 on page 24: $t_1$ is the delay between IR and UV-Vis pump pulse, $t_2$ is the delay between the UV-Vis pump pulse and the IR-probe pulse. For the 2D-IR signal the delay is the sum of $t_1$+$t_2$ and for the TRIR signal the delay is $t_2$. For the VIPER spectrum both delays $t_1$ and $t_2$ need to be given. There is only a VIPER signal if $t_1$ and $t_2$ are positive and the IR-pump pulse comes before the UV-Vis pump pulse.

To analyse the dynamics in the measured data global analysis was used. For this the *Globe toolbox*[158] in Matlab (R2012a, The MathWorks Inc., Natick, MA) was used. Time zero was corrected for different spectral windows and the coherent artefact was fitted with 3 exponentials (not shown). Depending on the dataset a background at negative time delay was subtracted.

# 5 Results

## 5.1 Diethylaminocoumarin Cage

### 5.1.1 Characterization
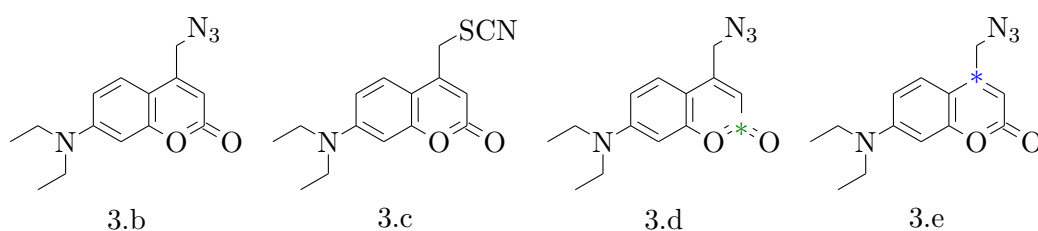


Figure 5.1: Structures of DEACM cages: 3.b DEACM-N$_3$, 3.c DEACM-SCN, 3.d
2$^{13}$C DEACM-N$_3$ (2$^{13}$C), 3.e 4$^{13}C$ DEACM-N$_3$ (4$^{13}C$)

The structures of DEACM cages and their LGs used in this work are shown
in figure 5.1. Two different LGs, azide ($N_3$) and thiocyanate ($SCN$), are used to
monitor the photo cleavage. Furthermore, two isotopomers of DEACM are used.
In 2$^{13}C$ DEACM the $^{13}C$ is at position two of the ring system (structure 3.d in
figure 5.1), while in 4$^{13}C$ DEACM the $^{13}C$ is at position four (3.e).

The UV-Vis spectra for the DEACM-N$_3$ isotopologues and isotopomers and for
DEACM-SCN are shown in figure 5.2 on the next page. For each cage a concen-
tration series was meassured and the extinction coefficient was determined. The
data quality for low concentrations was poor and since the spectra were averaged
without weighting, this can be seen in the shown spectra. Especially for DEACM-
SCN the baseline was noisy. This does, however, not perturb the analysis nor
interpretation of the data.

There are no significant band shifts or changes in the extinction coefficient for
the DEACM-N$_3$ isotopologues and isotopomers. The minor differences in the ex-
tinction coefficient, that can be seen, are most likely due to errors in concentration
determination and poor quality of spectra with low concentrations. DEACM-SCN
seems to absorb a little bit red-shifted compared to DEACM-N$_3$ and has a slightly
lower extinction coefficient.

In contrast, the steady-state infrared spectra for the same species (figure 5.3
on page 59) show distinct differences. For all DEACM cages three ring mode
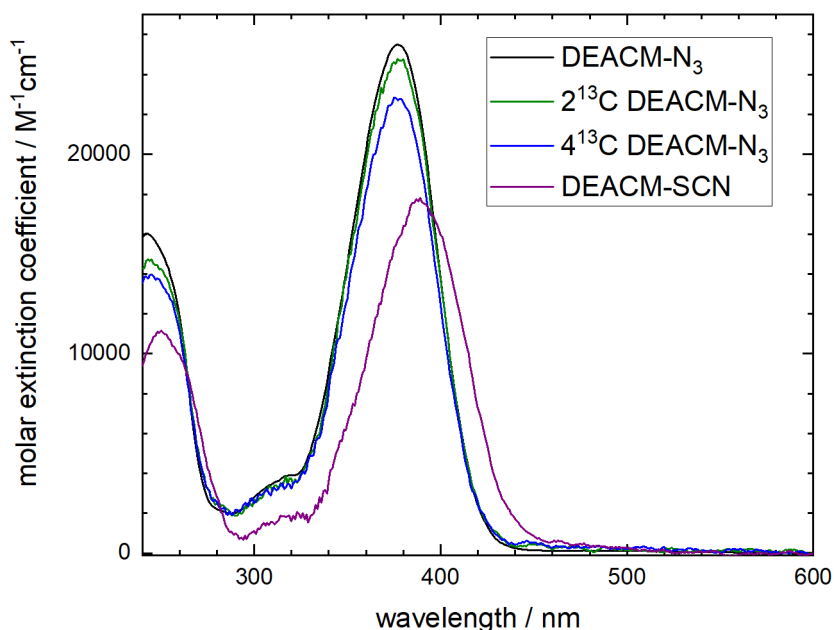
Figure 5.2: UV-Vis absorption spectra for different DEACM cages in acetonitrile. Concentration steps of 400 $\mu$M, 600 $\mu$M, 800 $\mu$M and 1000 $\mu$M were averaged. The optical path length was 100 $\mu$m.

vibrations are seen in the spectral range between 1500 and 1650 $cm^{-1}$. Their exact position and intensity depend on the existence and position of a $^{13}C$ label. For DEACM-N$_3$ and DEACM-SCN the ring mode positions are approximately 1530 $cm^{-1}$, 1605 $cm^{-1}$ and 1618 $cm^{-1}$. The intensities of the three bands are roughly the same for both LGs.

For $4^{13}$C a smaller band appears at 1586 $cm^{-1}$ while the 1605 $cm^{-1}$ band is gone. The 1618 $cm^{-1}$ band is very prominent. For $2^{13}$C the 1605 $cm^{-1}$ band is the most intense, while the 1618 $cm^{-1}$ band is overlapping with it. The band which is at 1530 $cm^{-1}$ for the other species is at slightly lower wavenumbers in $4^{13}$C.

For $2^{13}$C the carbonyl band is at 1683 $cm^{-1}$. For the other DEACM molecules it is more or less at 1720 $cm^{-1}$.

The LGs absorb between 2000 and 2200 $cm^{-1}$. The position for the azide band is the same for all DEACM-N$_3$ at 2113 $cm^{-1}$. The changes in intensity of the carbonyl and azide band between the isotopomers and the unlabeld DEACM are most likely due to changes in the background absorption of the acetonitrile and errors in the concentration determination. The SCN absorbs at 2159 $cm^{-1}$ and

has a significantly lower extinction coefficient.
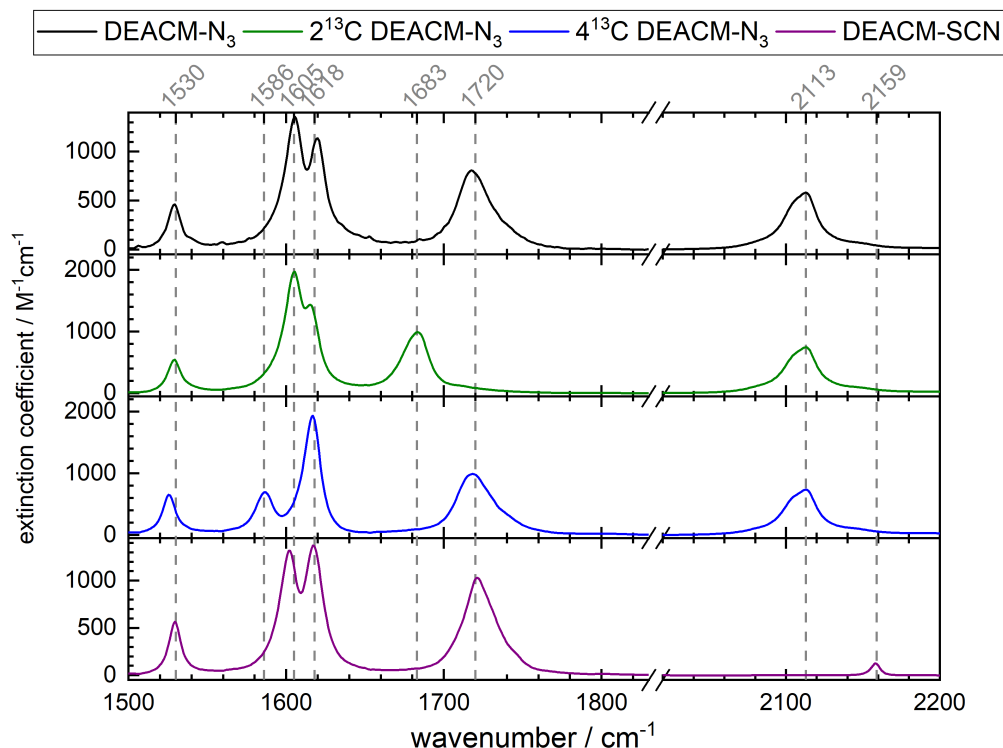


Figure 5.3:  Steady-state infrared absorption spectra for different DEACM cages
in acetonitrile. Concentration for all cages was 25 mM and the optical
path length was 50 $\mu$m. Data measured by Nicole Mielke [144].

For a selective uncaging experiment the IR modes for IR pre-excitation have to
be well separated. Taking this into consideration for choosing a set of species for
a mixture, the $4^{13}$C and one of the other three should be suitable. The separated
band at 1586 $cm^{-1}$ in $4^{13}$C and the 1605 $cm^{-1}$ band in the others might be pre-
excited with a sufficiently big contrast.

As has been shown in the first publication on VIPER, the different IR modes
couple differently to the UV-Vis transition [30]. If the coupling is similar for
DEACM and the laser dye Coumarin6, the published results lead to the assumption
that the 1605 $cm^{-1}$ band should give the biggest VIPER effect. This has been
validated in the experiments belonging to Carsten Neumann's PhD thesis [123] and
has recently been published together with computations of the UV-Vis spectrum
after IR excitation of various modes [116] (compare figure 2.11 on page 21). These
computations have been carried out in the PhD thesis of Jan von Cosel [117].

## 5.1.2 Markers of the Photoreaction

Figure 5.4 shows the changes in the IR due to irradiation with visible light. These are difference spectra where the spectrum without irradiation is subtracted from the spectrum with irradiation. Therefore, the negative bleaches indicate where the starting material vanishes and the positive bands are caused by photo products.
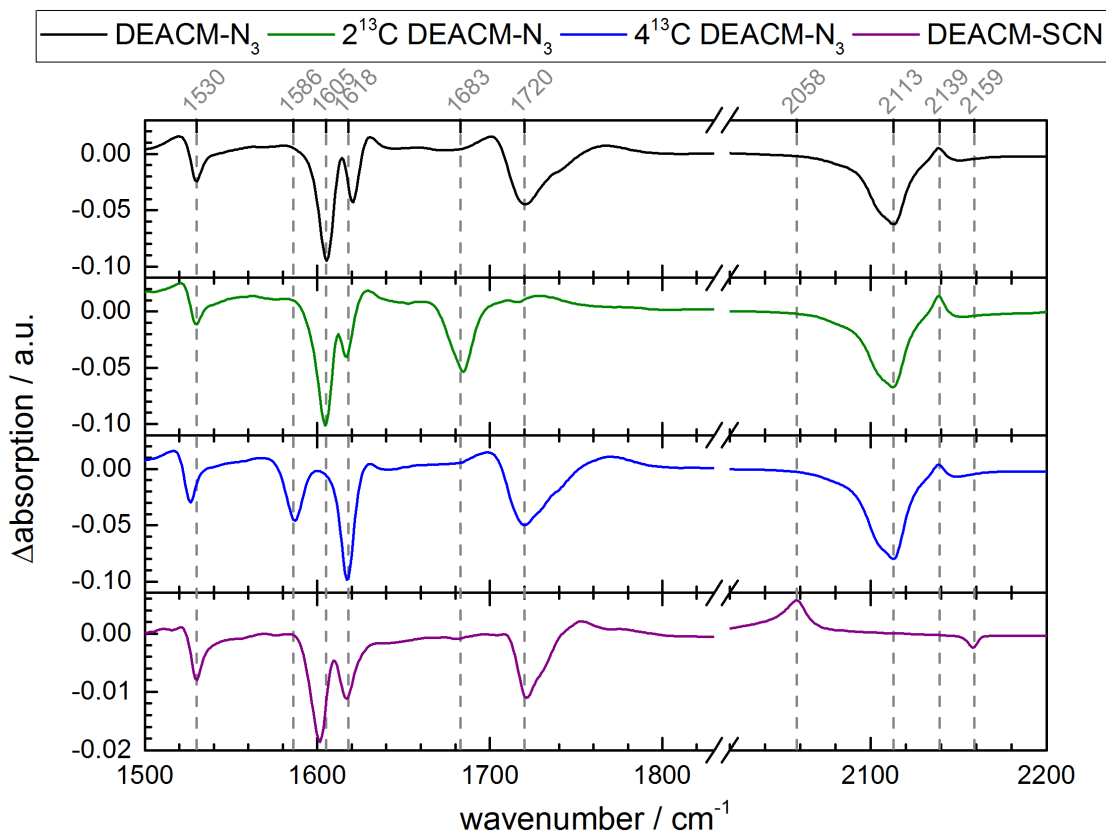


Figure 5.4:  Difference infrared absorption spectra for the various DEACM cages in acetonitrile under irradiation with 365 nm (irradiated minus non-irradiated). The concentration was 25 mM and the optical path length was 50 $\mu$m for all cages. Data measured by Nicole Mielke [144].

To keep the spectra as clear as possible only the bleaches and the new bands for the cleaved LG are indicated by the dashed grey lines and wavenumbers.

In the ringmode region for DEACM-$N_3$ three bleaches at the same positions as the bands in figure 5.3 on the previous page can be seen. Next to the 1530 $cm^{-1}$ bleach a red-shifted positive band appears. For the other two ringmodes no red-shifted positive feature can be observed. There seems to be a small positive feature on the high wavenumber side of the bleaches. The ring mode bleaches are partially

overlapping.

The carbonyl band at 1720 $cm^{-1}$ also leads to a significant bleach. There might be some small product bands both at higher and lower wavenumbers.

For the other species the bleaches in the ringmode and carbonyl region are also consistent with the band positions in figure 5.3 on page 59 due to isotope labelling.

The azide bleach is for all DEACM-N$_3$ at 2113 $cm^{-1}$ and a small product band appears at 2139 $cm^{-1}$. The detailed analysis of the DEACM-N$_3$ photoproducts is part of Carsten Neumann's PhD thesis and has also been part of Nicole Mielkes master thesis [123, 144]. It has recently been published [134] and will not be discussed here.

For DEACM-SCN a small bleach can be observed at the SCN position 2159 $cm^{-1}$ . As with the band in figure 5.3 on page 59 the SCN signal is significantly smaller than the azide signal. A SCN product band appears at 2058 $cm^{-1}$. This band is larger than the SCN bleach and assigned to free SCN$^-$. It is, however, still smaller than the N$_3$ bleach.

Concerning a selective uncaging experiment, where the selectivity should be proven by spectroscopy, the bands of the free LG should be easy to distinguish. Since the azide bleach is at the same position for all DEACM-N$_3$ species a mixture of DEACM-N$_3$ and DEACM-SCN seems most plausible.

Together with the consideration for the IR pre-excitation, this makes 4$^{13}$C DEACM-N$_3$ and DEACM-SCN the most promising pair.

Taking a look at the UV-Vis spectrum of DEACM-N$_3$ under irradiation (figure 5.5 on the following page) reveals a decrease of the main absorption band and the appearance of an additional band at lower wavelengths. The identification of this photo product is part of Carsten Neumann's PhD thesis and experiments on this were also carried out by Nicole Mielke for her master thesis [123, 144]. For the selective uncaging experiment the identification is not necessary, since the LG can be monitored in the IR. Nevertheless, the additional absorption on the lower wavelength side of the spectrum is inconvenient, since this photo product will absorb UV-Vis-pump light intended for the VIPER excitation.

The spectra shown so far show the differences under steady-state illumination conditions. Since VIPER is an ultrafast spectroscopy technique, the markers for photochemistry have to appear within the time scale of a VIPER experiment. To identify suitable markers TRIR spectra of the DEACM cages were measured (see figure 5.6 on page 63). Two spectral windows were measured: the carbonyl region and the azide/thiocyanate region. For each species an early and a late time point were plotted together in different colors and individual y-axis for better depiction of the signals.

In the carbonyl region the carbonyl bleach can be seen at 1720 $cm^{-1}$ for DEACM-N$_3$, 4$^{13}$C DEACM-N$_3$ and DEACM-SCN. For 2$^{13}$C DEACM-N$_3$ the carbonyl bleach
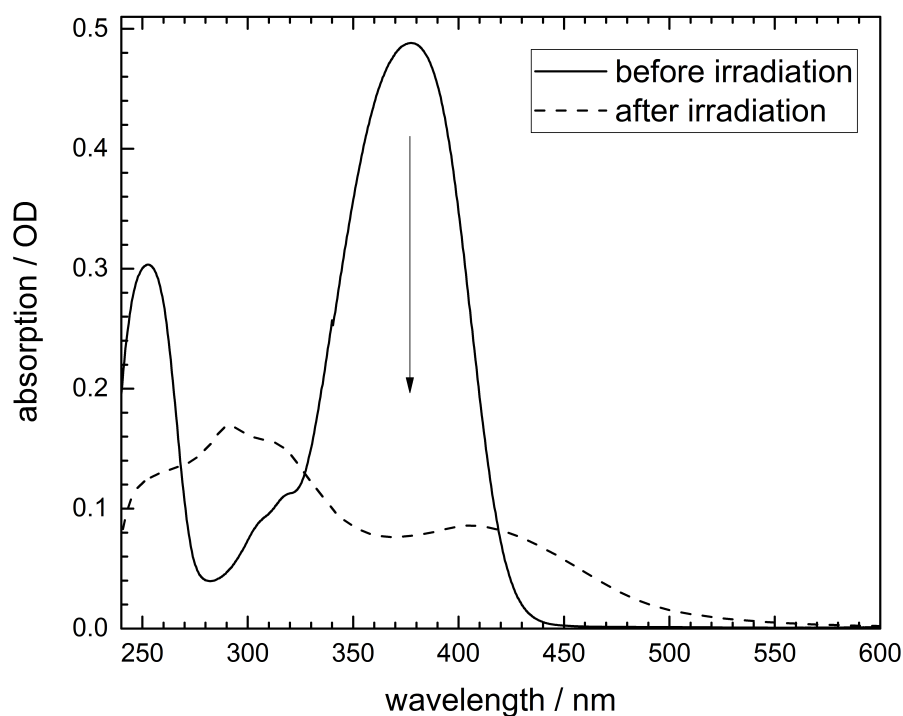
Figure 5.5: UV-Vis absorption spectra for DEACM-N$_3$ in acetonitrile before (solid line) and after (dashed line) irradiation with 365 nm. The concentration was 0.5 mM and the optical path length was 1 mm. Data measured by Nicole Mielke [144].

is shifted to 1683 $cm^{-1}$. This is in agreement with the steady-state IR spectra (figure 5.3 on page 59) and the irradiated difference IR spectra (figure 5.4 on page 60). The bleaches at the early time point are caused by the excitation into the electronic excited state. At the late time point the negative signal is due to the molecules which underwent photoreaction. For DEACM-N$_3$ and 4$^{13}$C DEACM-N$_3$ an excited state absorption can be seen in the early time points at 1670 $cm^{-1}$ and 1655 $cm^{-1}$. For 2$^{13}$C DEACM-N$_3$ this excited state overlaps with the ringmode bleach (which is not shown). For DEACM-SCN there is no pronounced ESA, but a broad positive feature at the low wavenumber side of the bleach. This can, however, be seen at early and late times.

In the other window the early timepoints for DEACM-N$_3$, 2$^{13}$C DEACM-N$_3$ and 4$^{13}$C DEACM-N$_3$ show a bleach for the azide at 2113 $cm^{-1}$ and an ESA at
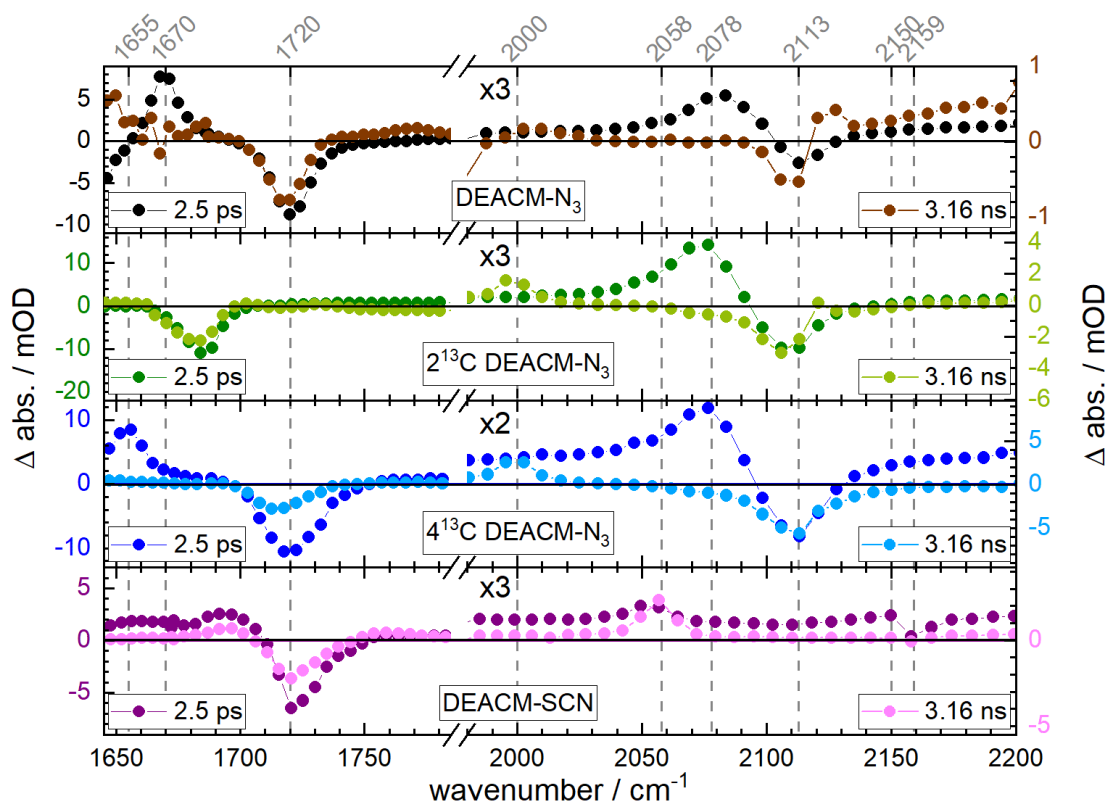
Figure 5.6: TRIR spectra of all species in acetonitrile. In each graph an early (2.5 ps) and a late (3.16 ns) timepoint are shown with individual y-axis. The colours on the axis labels correspond with the graphs. Note the x-axis break between 1785-1980 $cm^{-1}$. The data on the right side of the break is scaled. DEACM-$N_3$ was measured in Carsten Neumann's master thesis [159]. $2^{13}$C DEACM-$N_3$: VIS 1-3, VIS 8. $4^{13}$C DEACM-$N_3$: VIS 4-7. DEACM-SCN: VIS 9-11, VIS 14.

2078 $cm^{-1}$. The bleaches are in agreement with the steady-state data (figure 5.3 on page 59, figure 5.4 on page 60. The ESA is gone in the late timepoints, but the photoproducts can be seen at 2000 $cm^{-1}$ and 2122 $cm^{-1}$. As is in detail discussed in our publication on the DEACM-$N_3$ photochemistry [134] and in Carsten Neumann's PhD thesis [123], the photochemistry depends on the water content and the ratio between the azide photoproducts will be different. $N_3^-$ (2000 $cm^{-1}$) and $HN_3$ (2122 $cm^{-1}$) are formed. Depending on the pH value they form an equilibrium. In the measurement shown in the top panel the $HN_3$ is more prominent and overlaps with the bleach of the starting material azide. In the second panel the $N_3^-$ can be seen more clearly and in the third panel the $HN_3$ shows no significant contribution. These differences are probably due to small changes in the dryness

of the water-free acetonitrile. This sensitivity on hard to control conditions makes the product bands not ideal as markers for successful photo cleavage. Different water content also explains the differences between the azide products in figure 5.4 on page 60 and figure 5.6 on the previous page. For DEACM-SCN at the early time point a bleach can be seen at 2159 $cm^{-1}$ . This agrees with figure 5.3 on page 59 and figure 5.4 on page 60. The ESA is very close to the bleach at 2150 $cm^{-1}$ and therefore both cancel each other partially. The SCN$^-$ can be seen at 2058 $cm^{-1}$.

For the following VIPER experiment in a mixture of DEACM species unique spectral features should be selected as markers for the photoreaction. These do not necessarily need to be the product bands, even though they are the most obvious choice. Looking at the signals of the freed LGs, the signals at late time points are quite small for both azide and thiocyanate. Looking at the carbonyl region it becomes aparent, that $2^{13}$C DEACM-N$_3$ and $4^{13}$C DEACM-N$_3$ can be distinguished from each other, which is of course not possible in the azide region, since the azide vibrational mode is not affected by the isotope substitution on the ring system.

At this point the obvious choice for a mixture is still $4^{13}$C DEACM-N$_3$ and DEACM-SCN, but $2^{13}$C DEACM-N$_3$ and $4^{13}$C DEACM-N$_3$ could be an alternative, if the LG signals are inadequate. In addition, the Vis absorption spectra for SCN and N$_3$ cages are slightly shifted (see figure 5.2 on page 58), lowering the achievable contrast between the species as the off-resonant Vis pulse for N$_3$ is less off-resonant for SCN.

### 5.1.3 VIPER Spectroscopy on DEACM

To determine the right wavenumber positions for the IR pump pulse the ringmode region of DEACM-N$_3$ is probed first (figure 5.7 on the next page). As has been mentioned before 2D-IR, TRIR and VIPER data are measured for the same time points in one measurement. The delays are named as in the sketch of the VIPER pulse sequence in figure 2.12 on page 24: $t_1$ is the delay between IR and UV-Vis pump pulse, $t_2$ is the delay between the UV-Vis pump pulse and the IR-probe pulse. For the 2D-IR signal the delay is the sum of $t_1 + t_2$ and for the TRIR signal the delay is $t_2$. For the VIPER spectrum $t_1$ and $t_2$ are given to interpret the data.

The figure shows in the uppermost panel the steady-state infrared spectrum. The arrows on top indicate the pump positions. In the second panel the 2D-IR spectra for the three pump positions at $t_1 + t_2 = 2.5$ ps are shown. The colors of the spectra correspond to the arrow's colors. The grey arrow is selected to be off-resonant and the 2D-IR signal in the grey spectrum is accordingly small. The blue pump position hits the 1605 $cm^{-1}$ band. A bleach and an ESA overlap at this wavenumber. There is a smaller second bleach at higher wavenumbers (1623 $cm^{-1}$) which corresponds to the second ring mode band. The ESA of this transition prob-
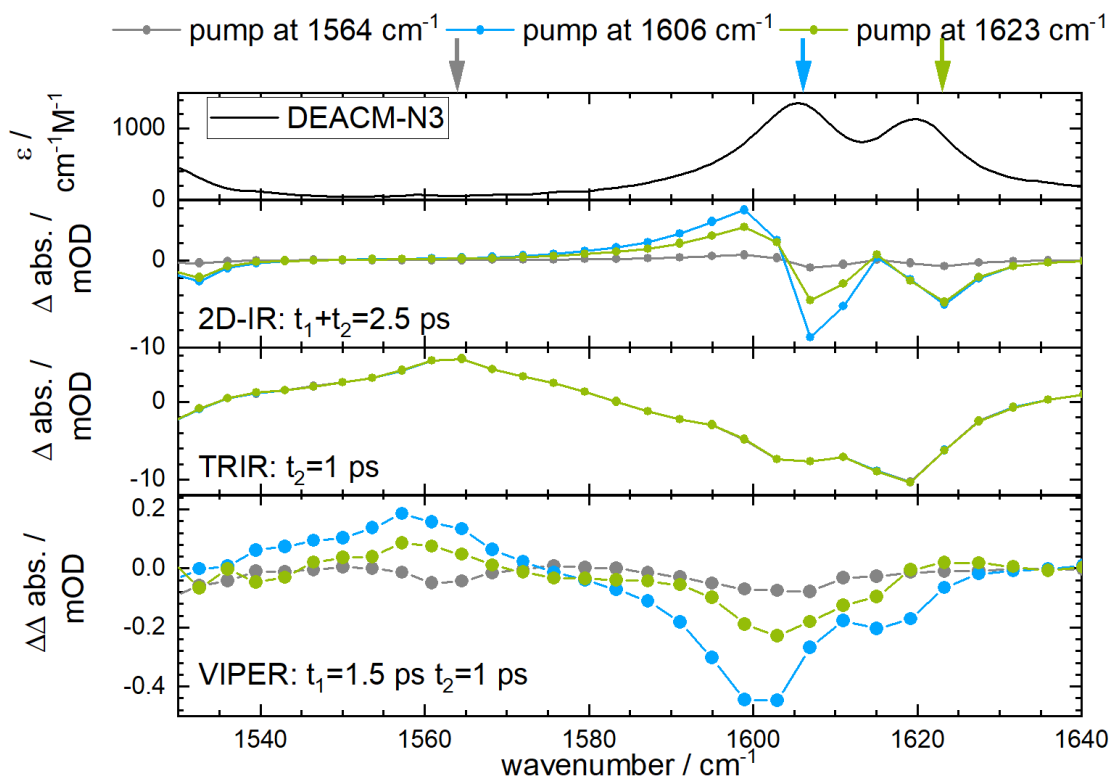
Figure 5.7: Ringmode region of DEACM-N$_3$. First panel shows steady-state infrared spectrum with colored arrows indicating IR pump positions. Second panel shows 2D-IR spectra at t$_1$+t$_2$=2.5 ps. Third panel shows UV-Vis-pump IR-probe spectra at t$_2$1 ps. Fourth panel shows VIPER spectra at t$_1$=1.5 ps t$_2$=1 ps. IR-pump positions and x-axis calibration is the same for the three laser data panels. 25 mM DEACM-N$_3$ in acetonitrile with 250 $\mu$m spacer. UV-Vis-pump at 436 nm. VIPER22.

ably cancels out with the much stronger 1605 $cm^{-1}$ bleach. At 1532 $cm^{-1}$ another small bleach can be seen, this is probably part of the 1530 $cm^{-1}$ ringmode transition. For the green pump positions the spectral features are at the same positions as in the blue spectrum. However, the relative amplitudes between the ringmode signals are different. The spectra indicate that the 1605 $cm^{-1}$ transition has the best cross-section with the IR pump pulse and/or a better matching transition dipole moment.

The third panel shows the Vis-pump IR-probe spectra (TRIR in the figure) collected in the same experiment at t$_2$=1 ps. Since there is no IR-pump there should be no difference between the pump positions, which is confirmed by all spectra laying completely on top of each other. Two bleaches (which are overlapping)

can be seen at approximately the ring mode positions. An ESA can be seen at 1560 $cm^{-1}$.

The lowest panel shows the VIPER spectra for the three pump positions at $t_1$=1.5+ps $t_2$=1 ps. As for the 2D-IR signal the grey spectrum is almost featureless (due to the slowly-decaying tail beyond the center wavenumber of the pump pulse a small fraction of near absorption bands can still be excited). The blue spectrum is bigger than the green spectrum. The spectra show the same spectral features as the TRIR spectra, but with different intensity ratios between the bands. In the TRIR spectra the higher wavenumber ringmode bleach is slightly larger than the lower wavenumber ringmode bleach. In the VIPER spectra it is the other way around. There also seems to be small shift to lower wavenumbers for the bleaches. In theory the VIPER spectrum should look like a TRIR spectrum if the delay between the pump pulses and the probe pulse is long enough. If the delay is short, the vibrationally excited population might not yet have relaxed into the vibrational ground state of the $S_1$ leading to an additional contribution to the spectra. Also, for short delays the polarization dependence of the signal is that of a fifth-order experiment (equation (2.11) on page 25). Another explanation for differences in this case might be accumulation of a photoproduct which is directly excited by the Vis-pump, but not by the IR pre-excitation and therefore appears in the TRIR data, but is chopped out in the VIPER spectra. All x-axes were calibrated as described in section 4.1 on page 54.

The time development of the VIPER signal is shown in figure 5.8 on the next page. The UV-Vis-pump pulse is $t_1$=1.5 ps after the IR-pump pulse. At early times the signal shows a prominent ESA which decreases over time. At at delay of $t_2$=75 ps the ESA can no longer be seen, but the bleach is still clearly observable. Between the delay of $t_2$=75 ps and the longest delay of $t_2$=250 ps no significant change can be observed indicating no observable reaction step on this time scale.

Since the aim was to observe spectroscopic markers for the photo-reaction, only the delay with the biggest signal ($t_1$=1.5 ps $t_2$=2.5 ps) is shown in the following graphs.

Figure 5.9 on page 68 shows the same type of experiment as figure 5.7 on the previous page but with the probe in the azide region of the DEACM-N$_3$. Only the off-resonant and the 1605 $cm^{-1}$ band pump positions were measured. The pump positions and the color coding is the same as in figure 5.7 on the preceding page. The first panel again shows the steady-state infrared spectrum. Only the absorption of the bound azide at 2113 $cm^{-1}$ can be seen. The second panel shows the 2D-IR signal at $t_1$+$t_2$=2.5 ps. The grey spectrum is with the IR-pump on an off-resonant position and accordingly small (as in figure 5.7 on the previous page, the tail of the non-resonant pump pulse still excites a small fraction). The blue spectrum belongs to the IR-pump on the lower ringmode band (1605 $cm^{-1}$)
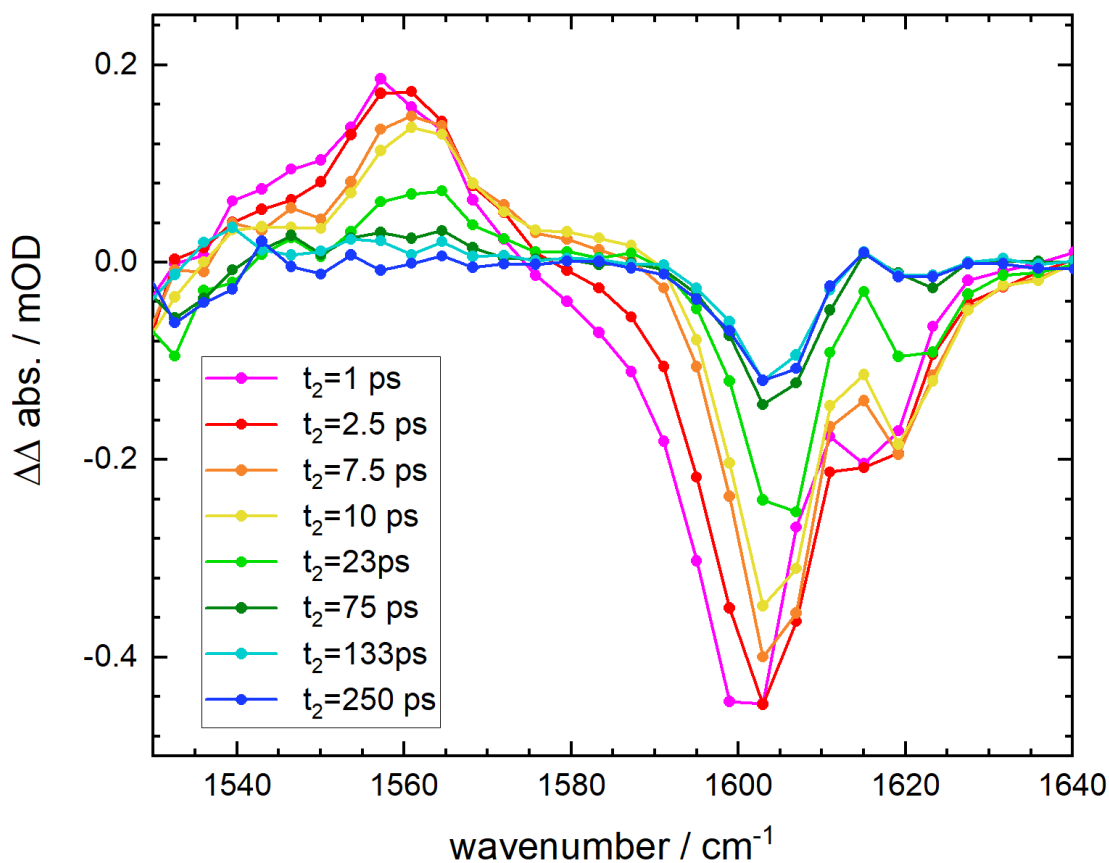
Figure 5.8: Ring mode region of DEACM-$N_3$. Same measurement as in figure 5.7 on page 65. Legend gives $t_2$, $t_1$=1.5 ps. VIPER22.

. A bleach and an ESA can be seen for the azide band. In the TRIR spectra at $t_1$=1 ps (third panel) again the collected spectra are identical, since there is no IR-pump. The bleach and ESA signal are in agreement with the Vis-pump IR-probe data shown in figure 5.6 on page 63. In the VIPER spectra (fourth panel) the off-resonant pump leads to a featureless spectrum, while the IR-pump on the lower ringmode leads to a spectrum, which is in agreement with the TRIR spectra.

While for the ring mode region the absolute signal size for the biggest VIPER signal (maximal positive - maximal negative signal) is about 600 $\mu$OD. The signal in the azide region is 40 $\mu$OD.

For the DEACM-SCN the same measurement was carried out and the data is shown in figure 5.10 on page 69.

The first panel shows the steady-state absorption of the bound SCN. In the 2D-IR data in the second panel a positive feature can be seen at slightly lower wavenumbers. This might be an ESA, there also might be a very shallow bleach
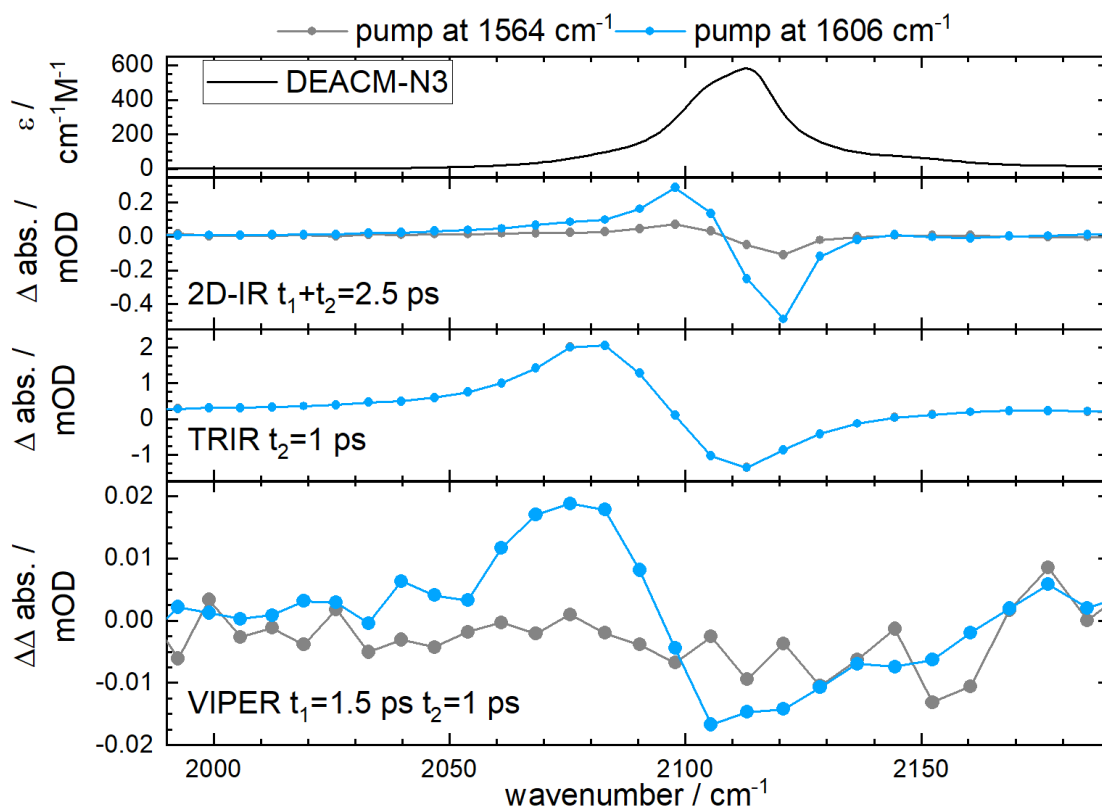
Figure 5.9: Azide region of DEACM-N$_3$. First panel shows steady-state infrared spectrum. Second panel shows 2D-IR spectra at $t_1$+$t_2$=2.5 ps. Third panel shows UV-Vis-pump IR-probe spectra at $t_2$=1 ps. Fourth panel shows VIPER spectra at $t_1$=1.5 ps $t_2$=2.5 ps. IR-pump positions and color code are the same as in figure 5.7 on page 65. X-axis calibration are the same for the three laser data panels. 25 mM DEACM-N$_3$ in acetonitrile with 250 $\mu$m spacer. Vis pump at 430 nm. VIPER35.

next to it. The 2D-IR signal is very small as the probed band is not directly excited by the IR pump, which is centered on the ring mode absorptions. The signal is due to internal energy transfer.

In the TRIR data a bleach and ESA can be seen at the bound SCN position. Also the product around 2058 $cm^{-1}$ can be observed. This is in agreement with the Vis-pump IR-probe data in figure 5.6 on page 63. In the VIPER spectra no spectral features can be seen for the off-resonant IR-pump position nor the IR-pump on the 1605 $cm^{-1}$ band. There can be multiple reasons for the absence of a VIPER signal both on the experimental conditions side and on the sample side.

Since the sample was already saturated and the spacer thickness quite high
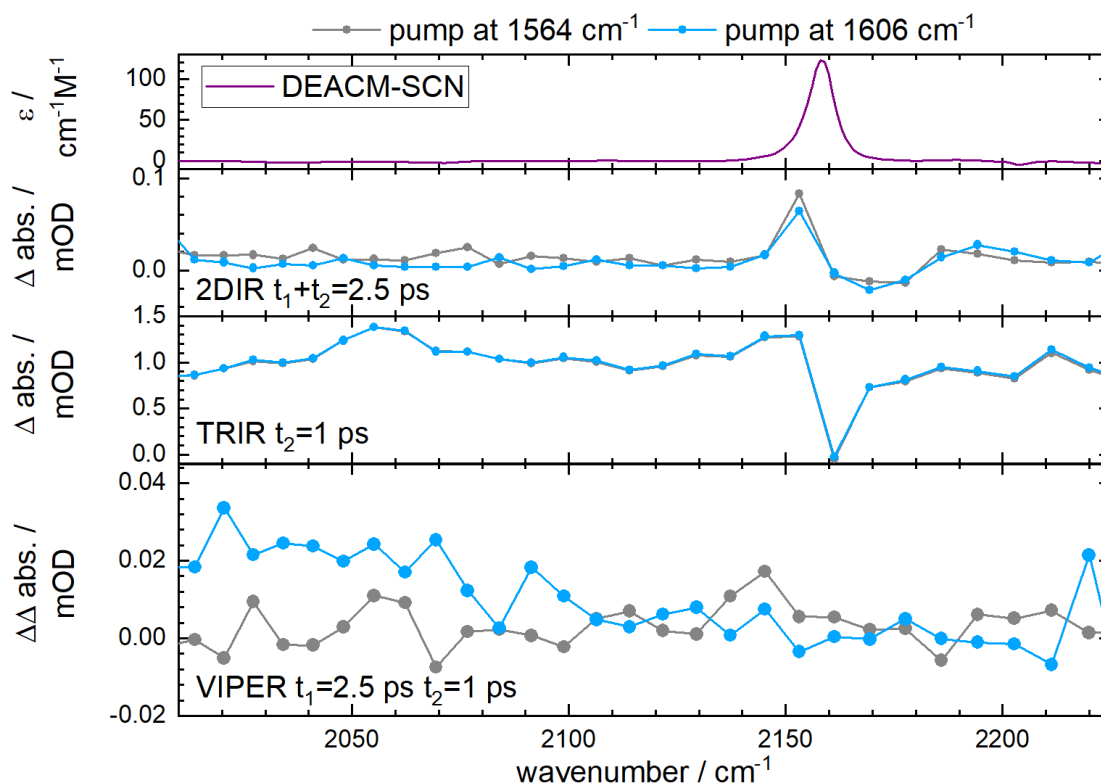
Figure 5.10: Thiocyanate region of DEACM-SCN. First panel shows steady-state infrared spectrum. Second panel shows 2D-IR spectra at $t_1+t_2=2.5$ ps. Third panel shows Vis-pump IR-probe spectra at $t_2=1$ ps. Fourth panel shows VIPER spectra $t_1=1.5$ ps $t_2=1$ ps. IR-pump positions and color code are the same as in figure 5.7 on page 65. X-axis calibrations are the same for the three laser data panels. Saturated DEACM-SCN in acetonitrile with 250 $\mu$m spacer. Vis pump at 437 nm. VIPER42.

(leading to too little transmitted probe light), the DEACM-SCN was deemed unsuitable for the proof-of-concept experiment. In a mixture with the DEACM-N$_3$ the signals for both LG signals would become even smaller, since not all molecules in the sample would contribute to it (i.e. it would be halved for a 1:1 mixture).

Instead a mixture of $2^{13}$C and $4^{13}$C was attempted. For these molecules no difference can be seen in the azide region, but the carbonyls can be monitored. The Vis-pump IR-probe data (figure 5.6 on page 63) has shown that the carbonyl bleach at early times can be used as signatures of the photo reaction. The time dependent TRIR data shows that a bleach in the carbonyl region is followed by the cleavage of the LG.

**DEACM isotopomers** Figure 5.11 shows the VIPER data for both individual iso-topomers. The steady-state spectra show the ringmode and carbonyl region with dots indicating the IR-pump positions, which are the same for both isotopomers. The IR-pump positions are 1564 $cm^{-1}$ (black), 1579 $cm^{-1}$ and 1583 $cm^{-1}$ (blue) and 1598 $cm^{-1}$ and 1606 $cm^{-1}$ (green). In the VIPER spectra below, the data belonging to the two blue and to the two green IR-pump positions have been binned to improve the signal-to-noise ratio (unbinned data in figure 5.12 on page 72). The axes are have the same scaling for both isotopomers to allow direct comparison.
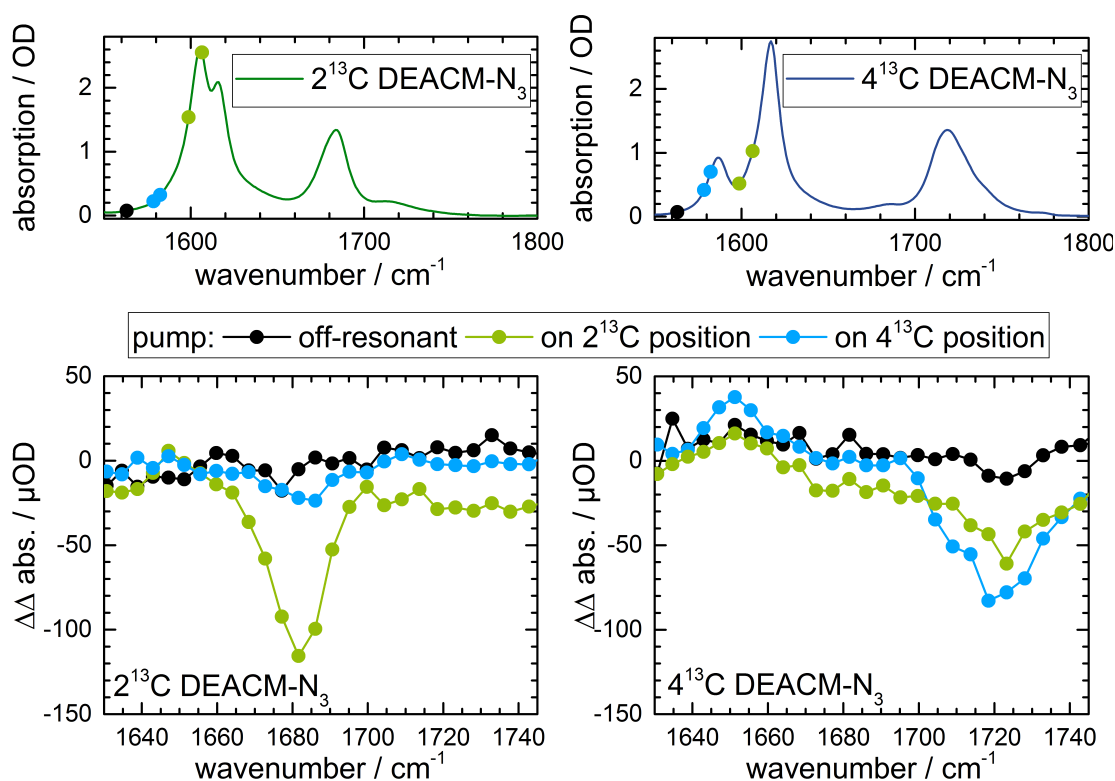


Figure 5.11: Top: Steady-state spectra of $2^{13}C$ (left in green) and $4^{13}C$ (right in blue). The dots indicate the IR-pump positions. Bottom: VIPER spectra of $2^{13}C$ (left) and $4^{13}C$ (right) for the IR-pump positions at $t_1=1.5$ ps $t_2=1$ ps. Spectra resulting from positions colored in the same color are binned (i.e. averaged). Saturation concentration for each isotopomer in acetonitrile with 250 $\mu$m spacer. Vis-pump at 437 nm. $2^{13}C$:VIPER353, $4^{13}C$:VIPER354.

The data on the left belong to the $2^{13}C$ isotopomer. The black pump position is off-resonant and the corresponding VIPER spectrum is essentially featureless. For this species the two blue positions are just at the beginning of the slope of the

1605 $cm^{-1}$ band. The corresponding VIPER spectrum has a small negative signal at the carbonyl position (1682 $cm^{-1}$). The signal is so small, that it might be just noise in the baseline. The green pump positions are on the 1605 $cm^{-1}$ band and a significant negative signal can be seen at the carbonyl position (1682 $cm^{-1}$). This is in agreement with the early time of the Vis-pump IR-probe data of this isotopomer (second panel in figure 5.6 on page 63). Since the position of the negative signals in the blue and the green spectra agree, the blue bleach is probably also a carbonyl signal. There is, however, a significant difference in the resulting signals between the two pump positions. The data on the right belongs to the $4^{13}$C isotopomer. The black pump position is again off-resonant and more or less featureless. There might be some minor negative signal at the carbonyl position (1718 $cm^{-1}$). Now the blue IR-pump positions match with the 1586 $cm^{-1}$ band of $4^{13}$C. In the VIPER spectrum the blue line shows a negative signal at the carbonyl position (1718 $cm^{-1}$) and a small positive signal at 1651 $cm^{-1}$. This agrees with the Vis-pump IR-probe data of this isotopomer (third panel in figure 5.6 on page 63). In the green spectrum the same spectral features can be seen, but are smaller. The difference between the pump positions is, however, not as big as for the $2^{13}$C isotopomer.

The comparison between the signal sizes for the IR-pump positions on one isotopomer is a direct estimate for the selectivity between them. The signal created by the IR-pump on the pump position for the other isotopomer (meaning the blue spectrum for $2^{13}$C and the green spectrum for $4^{13}$C, both in the VIPER spectra) show how much this isotopomer will contribute to the signal of the other isotopomer. Looking at the VIPER spectra of the pure isotopomers this means that in a mixture with the IR-pump on the position for $4^{13}$C should give a quite clean signal of the $4^{13}$C isotopomer. Since the blue spectrum in the $2^{13}$C VIPER spectrum is more or less featureless. If the IR-pump in a mixture is on the $2^{13}$C pump position, one might expect to see some spectral features of the $4^{13}$C isotopomer. Since there are still features in the green spectrum in the $4^{13}$C VIPER spectrum.

The absolute signal sizes of both isotopomers are also a point for discussion. The binned VIPER signal is 115 $\mu$OD for $2^{13}$C and 83 $\mu$OD for $4^{13}$C (just taking the difference from zero, without any further baseline corrections). Even though both measurements were carried out under the same measurement conditions, the $2^{13}$C signal is significantly larger. To analyse this, the unbinned TRIR, 2D-IR and VIPER signals for both isotopomers are shown in figure 5.12 on the following page (again with the same axes scaling for both isotopomers).

Comparing the TRIR spectra: the bleach of $2^{13}$C is approximately 2 mOD, while the bleach for $4^{13}$C is with 2.8 mOD a little bigger. This is in the opposite direction from the VIPER signal ratio. This probably means that the VIPER signal is not limited by the Vis pump energy. Measurements on Coumarin 6 showed
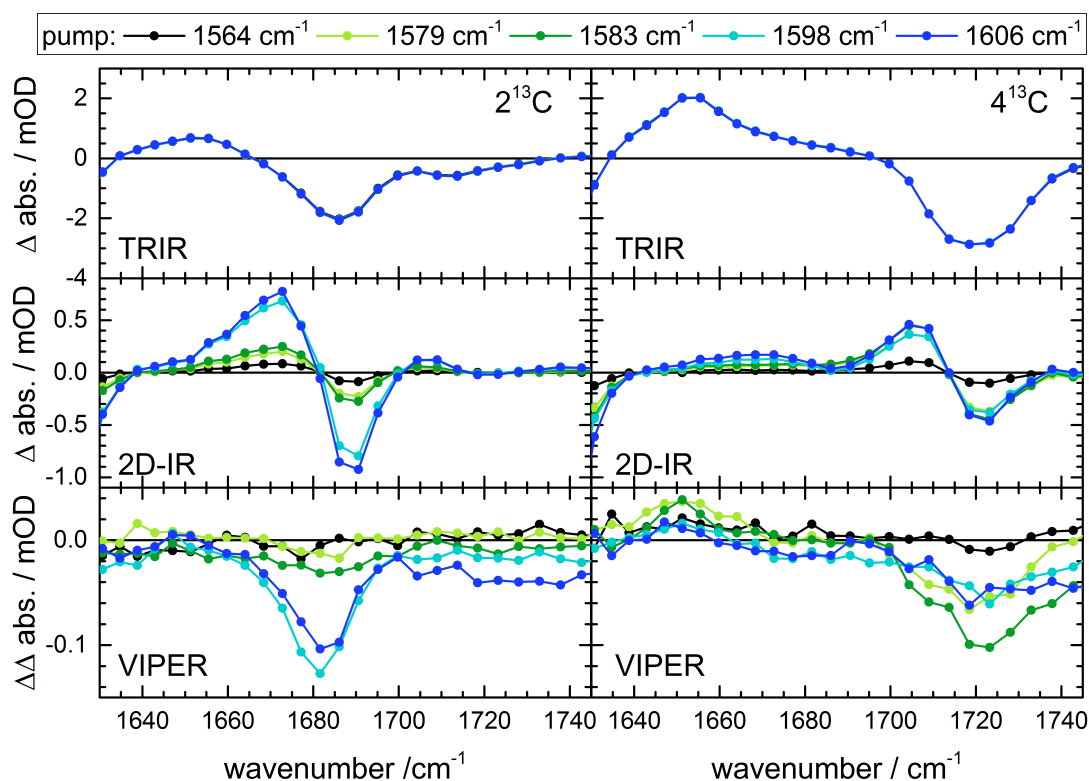
Figure 5.12: Top: TRIR data of $2^{13}C$ (left) and $4^{13}C$ (right) at $t_2$=1 ps delay. Middel: 2D-IR data of $2^{13}C$ (left) and $4^{13}C$ (right) at $t_1$+$t_2$=2.5 ps delay. Bottom: VIPER data of $2^{13}C$ (left) and $4^{13}C$ (right) at $t_1$=1.5 ps $t_2$=1 ps. IR-pump positions are the same for all panels. Saturation concentration for each isotopomer in acetonitrile with 250 $\mu$m spacer. Vis pump at 437 nm. $2^{13}C$: VIPER353, $4^{13}C$: VIPER354.

that increasing the Vis energy beyond a certain threshold only increases the TRIR signal and not the VIPER signal. To compare the 2D-IR signal size the difference between maximal positive and maximal negative signal is estimated. The $2^{13}C$ total signal amplitude is 1.7 mOD for the best pump position and the $4^{13}C$ signal is 0.92 mOD. This difference is in the same direction as the VIPER signal. For the $2^{13}C$ isotopomer there is an apparent difference between the resonant (blue) and off-resonant (green) IR-pump positions. For $4^{13}C$ this is much less prominent. This agrees with the observation, that the contrast in the VIPER spectra is better for $2^{13}C$. This can again be observed in the unbinned VIPER spectra for both species. For $2^{13}C$ the black and both green spectra are more or less featureless. Only the two blue spectra show the carbonyl bleach which agrees with the TRIR spectra. For $4^{13}C$ the blue spectra are very similar and show the same carbonyl

bleach as the green spectra just a little smaller.

There are different possible reasons for changes in the signal sizes between the isotopomers. The transition dipole moment might be different because of the different positions of the $^{13}C$. The orientation of the dipole moments might be different which means that polarization between the pump pulses is less ideal for one of the isotopomers.

Another explanation might be a difference in the coupling between the IR and UV-Vis transition. This has been computed by Jan von Cosel for both DEACM isotopomers and is part of our publication [61].
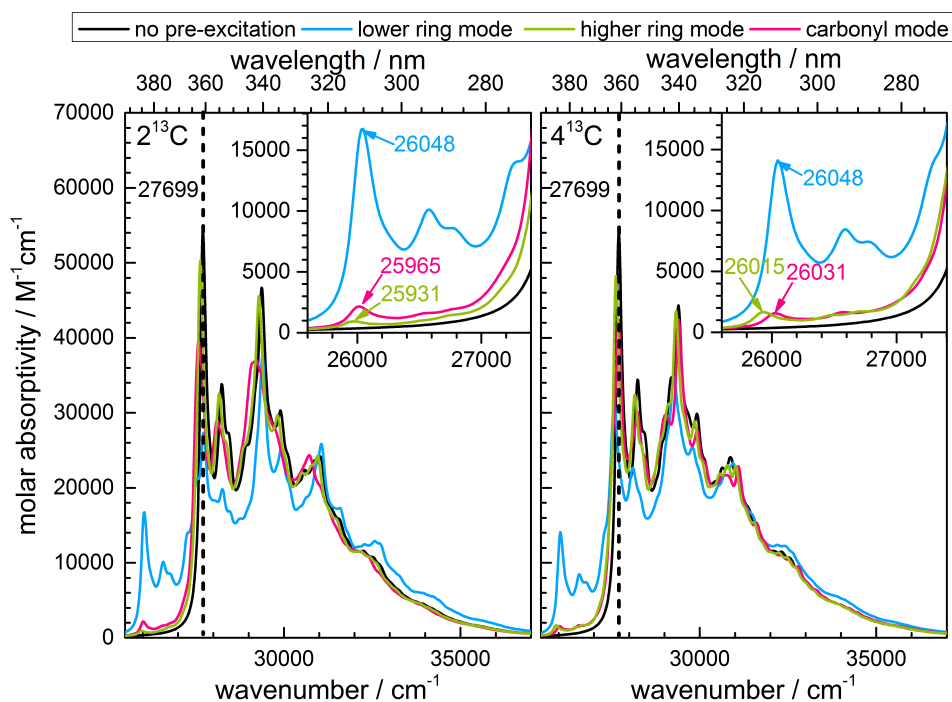


Figure 5.13: Computed UV-Vis absorption spectra without (black) and with IR-pre-excitation (blue on lower ring mode, green on higher ring mode and pink on carbonyl mode). The insert shows a zoom of the low wavenumber region.

Figure 5.13 shows the computed absorption spectra for both isotopomers with the same y-axis scaling. For both isotopomers the blue line (IR-pump on the lower ring mode) results in the largest difference. $4^{13}C$ seems to have a slightly smaller intensity. This together with the smaller 2D-IR signal could be an explanation for the varying VIPER signal sizes between the isotopomers.

However, each isotopomer was measured in an individual measurement and we observed significant VIPER signal size fluctuations from one measurement to an-

other. Parameters like the IR-pump energy can vary due to humidity changes or alignment. Therefore the difference between the isotopomers might not be completely caused by intrinsic differences in the species but could also at least in part be due to experimental circumstances.

## 5.1.4 Selective Photochemistry in a DEACM Isotopomer Mixture

Due to the differences in VIPER signal size of the isotopomers as outlined above the mixture used for the selective VIPER unacaging experiment does not consist of the isotopomers in equal parts, but 40 % $2^{13}$C and 60 % $4^{13}$C were chosen.

Figure 5.14 on the facing page shows the spectral data from the selective uncaging experiment. In panel A the steady-state FTIR spectrum of the mixture is shown in orange. The spectra of the isotopomers are shown with 50 % transparency in green ($2^{13}$C) and blue ($4^{13}$C). The orange spectrum shows a congestion of the spectral features of the individual species in the mixture. In the ring mode region of the spectra coloured arrows on top of the panel indicate the IR-pump positions for 2D-IR and VIPER experiment.

Panel B shows the UV-Vis spectrum of the mixture. No assignment of any bands can be made for the isotopomers, since their Vis spectra are identical. The dashed arrow indicates the position of the Vis-pump pulse at 437 nm.

Panel C shows the TRIR data of the mixture in orange. The data of the individual species is again shown transparently in the background. The delay between the UV-Vis-pump and the IR-probe pulse is 2.5 ps. Vertical lines show the positions of the carbonyl signals of each isotopomer. As in the steady-state IR spectrum, the TRIR spectrum of the mixture clearly shows the overlapping signals of the isotopomers. No selective excitation is possible.

Panel D shows the VIPER spectra at $t_1$=1.5 ps, $t_2$=2.5 ps of the mixture corresponding to the coloured arrows in Panel A. The black line is an off-resonant IR-pump position. No distinct spectral features can be seen. The green line corresponds to the IR-pump centered on the $2^{13}$C lower ring mode. This leads to a bleach at the position of the $2^{13}$C carbonyl. The expectation that this IR-pump position would result in signals from both isotopomers (as discussed on the basis of figure 5.11 on page 70) has not proven true. No negative spectral feature at the $4^{13}$C carbonyl position can be observed. If the IR-pump is on the position of the $4^{13}$C lower ring mode a bleach at the $4^{13}$C carbonyl position and a small ESA can be seen. As in figure 5.11 on page 70 two pump positions were binned in the VIPER data (unbinned data in figure 5.16 on page 77).

Figure 5.14 on the facing page is the spectroscopic proof, that the selective excitation of one species in a mixture, leading to selective photochemistry, worked.
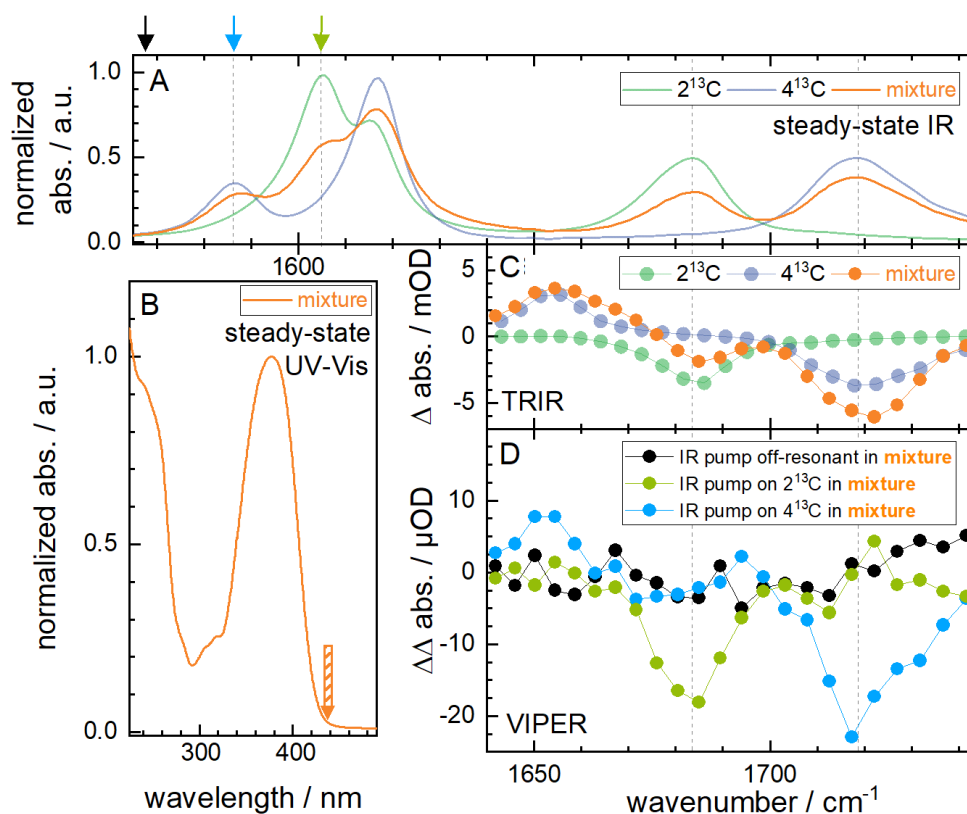
Figure 5.14:  A: IR spectra of ring and carbonyl regions of pure $2^{13}C$ (transparent green) and of pure $4^{13}C$ (transparent blue) and of 40 % $2^{13}C$ and 60 % $4^{13}C$ (orange). B: UV-Vis spectrum of the mixture. The arrow indicates the Vis-pump wavelength. C: TRIR spectra at $t_2=2.5$ ps in the carbonyl region of pure $2^{13}C$ (transparent green) and of pure $4^{13}C$ (transparent blue) and of 40 % $2^{13}C$ and 60 % $4^{13}C$ (orange). D: Binned VIPER spectra (two IR-pump positions each) of the carbonyl region of the isotopomer mixture at $t_1=1.5$ ps $t_2=2.5$ ps. Vis-pump pulse is at 437 nm. VIPER54.

The data has been published recently [61].

A flaw of the dataset is the short delay between the pump and probe pulses. The IR excitation has not yet decayed at 2.5 ps, as can be seen in figure 5.15 on the next page. This figure shows the carbonyl region of the VIPER mixture. Two bleaches and their corresponding ESAs can be seen. They partially overlap. The signal for the IR-pump position of 1606 $cm^{-1}$ (green) is the biggest. However, the ratio between the species changes if the pump is on 1579 $cm^{-1}$ (blue) and therefore predominantly on the $4^{13}C$ species. The black line is supposed to be off-resonant, but still results in a minor signal. The fact that at the delay where
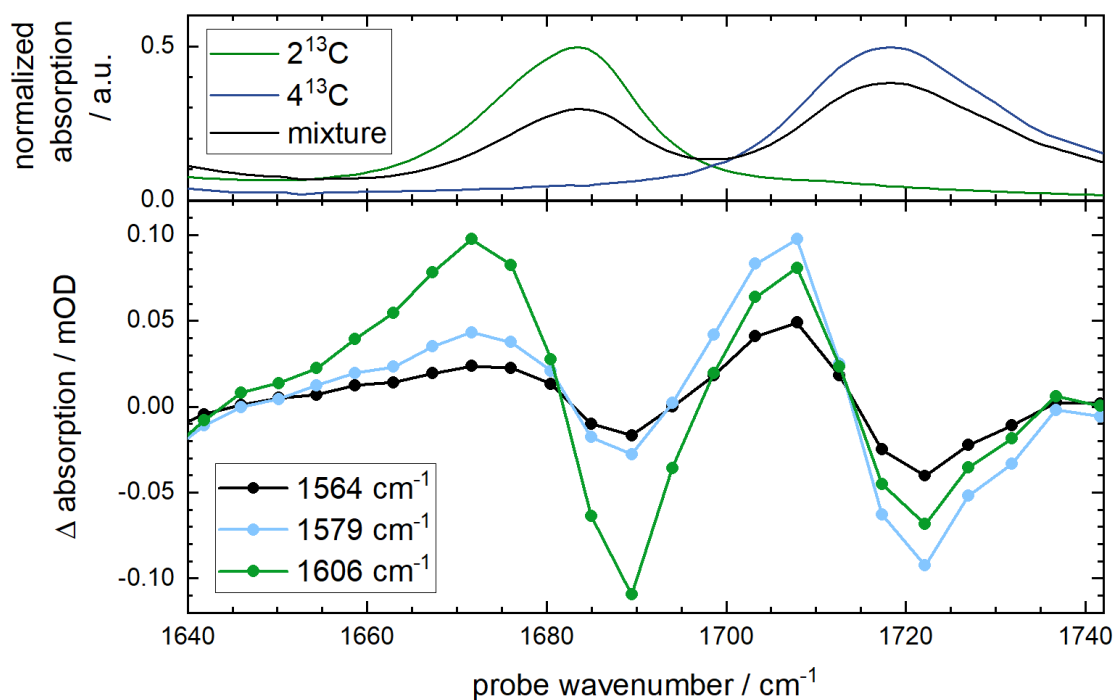
Figure 5.15: Top: steady-state FTIR spectrum of the carbonyl region of the mixture (black) and the isotopomers ($2^{13}$C in green, $4^{13}$C in blue) normalized on the azide band (not shown). Bottom: 2DIR spectra of the mixture at $t_1+t_2=2.5$ ps. IR-pump positions are given in the legend. VIPER54.

the VIPER signal is measured, there still is a significant 2DIR signal, might lead to doubts about the validity of the VIPER signals. The interpretation of the data can be additionally complicated by the fact that short time between the pump and the probe pulses means that the polarization dependence of the signals is that of a fifth order experiment (equation (2.11) on page 25). To counter such doubts figure 5.16 on the next page shows all measured VIPER times without binning and two different background subtractions.

On the left side the VIPER spectrum, where the Vis-pump was set at -20 ps was subtracted. On the right side the equivalent for the IR-pump was subtracted. As can be seen this leads to small changes in the baseline, but does not effect the signals. The longer delays do also not really impact the signals, but the intensity decreases slightly. For figure 5.14 on the preceding page the delay and background correction which lead to the clearest distinction between the species was chosen, i.e. the data in the middle right panel was selected. Figure 5.16 on the next page proves that the signals at the early delay are valid VIPER signals.
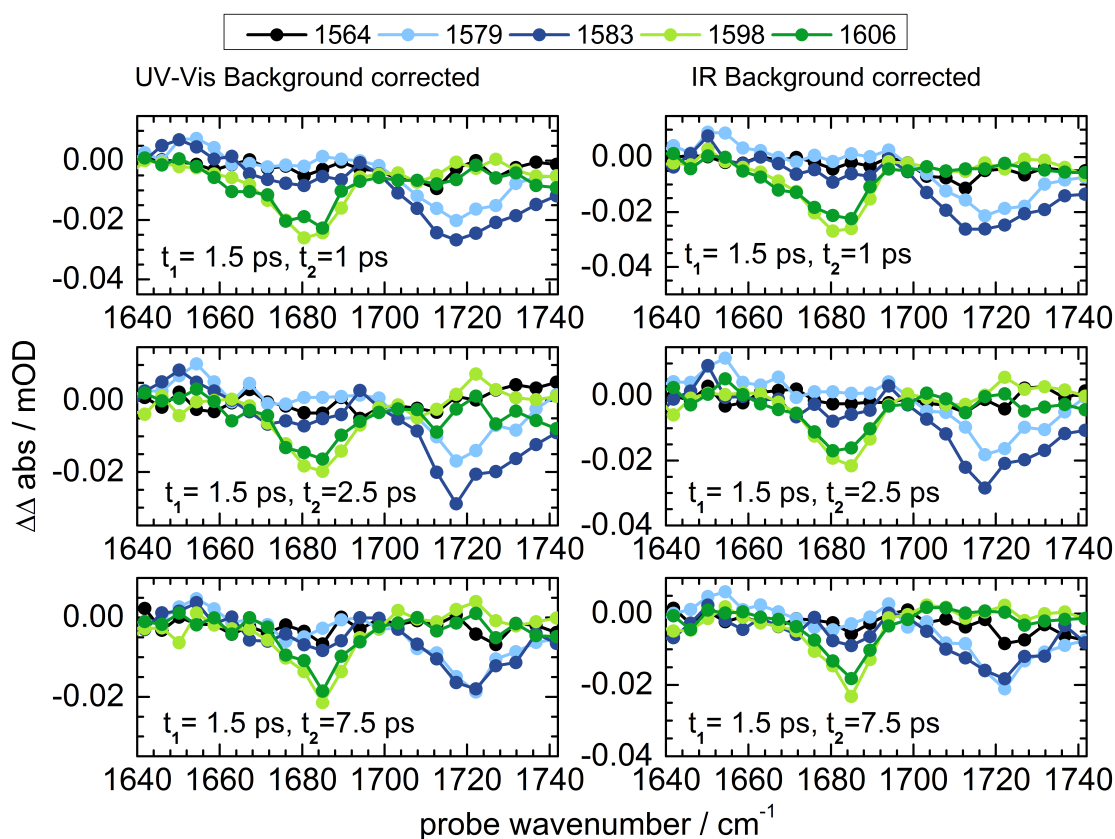
Figure 5.16: Unbinned VIPER spectra of the mixture with two different background corrections and various delays. VIPER54.

Still it would be desirable to measure VIPER spectra at longer delays, when the IR excitation has decayed, resulting in a spectrum that has the same shape as a TRIR spectrum. Also the picture would be clearer if the selective cleavage of the LG could be observed directly instead of the selective excitation via the carbonyl bands.

Another point to criticize is the ratio between the VIPER signal and the TRIR signal. The TRIR signal is the unspecific direct excitation by the UV-Vis-pump pulse. For selective uncaging applications this should be orders of magnitude smaller than the VIPER signal. In principle there is no reason why this should not be achievable with DEACM under suitable experimental conditions. However, experimentally we were limited in our options to vary parameters, since the VIPER signals were just on the edge of what can be measured. We did therefore not continue to optimize with this cage. But an in-depth variation of experimental parameters was carried out on Coumarin 6 and is part of Carsten Neumann's PhD thesis [123].

## 5.2 *para*-Hydroxyphenacyl Cage

### 5.2.1 Selection of Leaving Groups
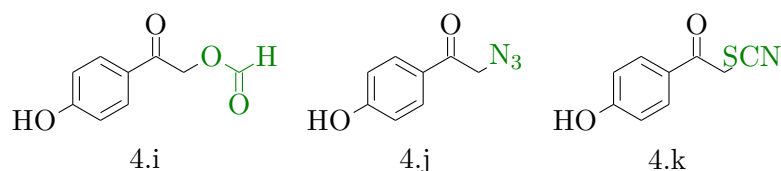


Figure 5.17: Structures of *p*HP cages with different LG: 4.i *p*HP formate, 4.j *p*HP azide and 4.k *p*HP thiocyanate. The LG is in green.

To begin the characterisation of *p*HP as a VIPER cage three different LGs were taken into consideration. *p*HP formate (4.i in figure 5.17) was chosen because of its well studied photo reaction in the literature. *p*HP azide (4.j in figure 5.17) and thiocyanate (4.k in figure 5.17) because of the suitable IR absorption of their LGs.
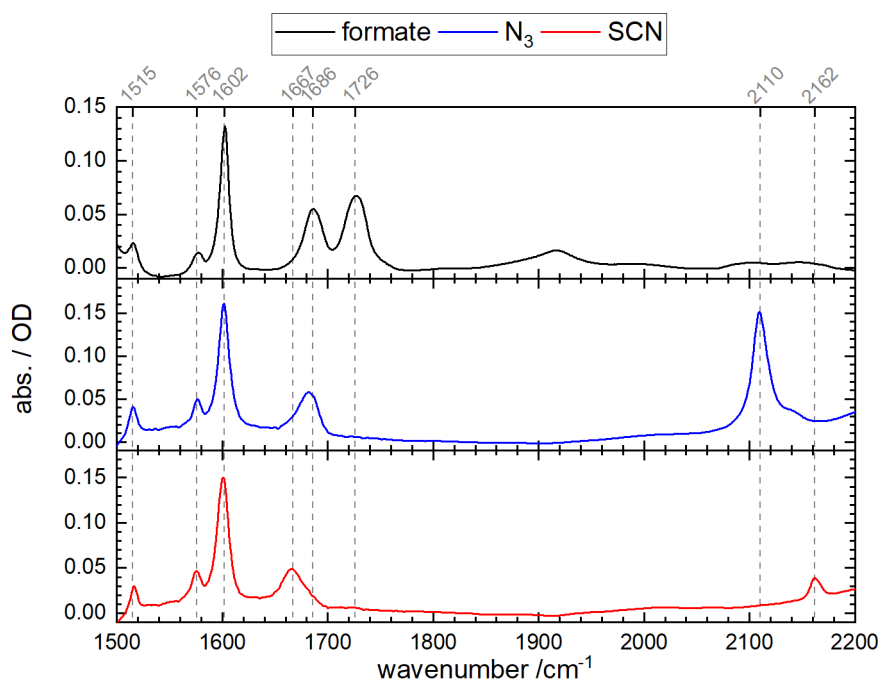


Figure 5.18: Steady-state FTIR spectra of *p*HP with different LGs in a 1:1 D$_2$O:ACN mixture (solvent background was subtracted). 50 $\mu$m spacer and 30 mM concentration.

Steady-state FTIR spectra in a 1:1 mixture of D$_2$O:acetonitrile are shown in figure 5.18). For all three LGs three ringmode bands at 1515 $cm^{-1}$, 1576 $cm^{-1}$,

and 1602 $cm^{-1}$ can be seen. Below the 1515 $cm^{-1}$ band the baseline comes up in the first panel and down in the other two panels, because of a high intensity absorption band in the background. The 1602 $cm^{-1}$ band has the highest intensity and the ratio between the ring mode absorption intensities seems to be the same for all LGs. The small changes between the spectra of the different species might be due to little differences in the subtracted background band because of temperature fluctuations or small differences in the water content of the used acetonitrile. For *p*HP SCN the lowest ring mode band seems to have its maximum at 1517 $cm^{-1}$ instead of 1515 $cm^{-1}$. This might be caused by the subtraction of the background absorption.

The *p*HP formate shows two carbonyl features at 1686 $cm^{-1}$ and 1726 $cm^{-1}$. It is possible to distinguish between the carbonyl next to the ring and the carbonyl in the LG, as the *p*HP azide only has a similar carbonyl feature at 1686 $cm^{-1}$. Therefore, it is assumed, that the lower carbonyl feature in the formate belongs to the carbonyl group next to the ring. In the *p*HP thiocyanate the carbonyl feature is slightly lower at 1667 $cm^{-1}$. For the formate no spectral features can be seen in the azide or thiocyanate regions. The small bump at approximately 1910 $cm^{-1}$ is attributed to imperfect background subtraction. The *p*HP azide shows an azide absorption band at 2110 $cm^{-1}$ and the thiocyanate shows a band at 2162 $cm^{-1}$. As for the DEACM the SCN signal is significantly smaller than the N$_3$ signal.

Figure 5.19 on the following page shows an irradiation series for *p*HP formate. Only the wavenumber region between 1500 $cm^{-1}$ and 1800 $cm^{-1}$ is shown. Between 1800 $cm^{-1}$ and 2200 $cm^{-1}$ only small baseline fluctuations can be seen. The upper panel shows again the steady-state spectrum for orientation. The lower spectrum shows difference signals of the irradiated sample minus the non-irradiated sample. The irradiation duration increases from light pink to green. Positive features in these difference spectra are product bands, negative signals are due to disappearing starting material. Here it seems as if the lowest ring mode band is at 1516 $cm^{-1}$. Under irradiation a positive band grows in at this position, while the ring mode bands at 1575 $cm^{-1}$ and 1602 $cm^{-1}$ disappear. A small positive feature appears at 1617 $cm^{-1}$. This is probably caused by a shift of the ring mode band to higher wavenumbers. In the carbonyl region two negative features around 1686 $cm^{-1}$ and 1726 $cm^{-1}$ (the carbonyl absorption bands) can be seen. A large positive band appears between the two negative signals and a smaller positive band appears at higher wavenumbers. The irradiation causes a shift in the carbonyl absorptions, which indicates the photo cleavage. However, the signals overlap and it is unclear which spectral feature belongs to the LG. Therefore, the *p*HP formate was deemed unsuitable for the continuation of the design of the VIPER uncaging experiment and no further measurements were carried out on it.

The next LG that was characterized was the azide (4.j). The irradiation dif-
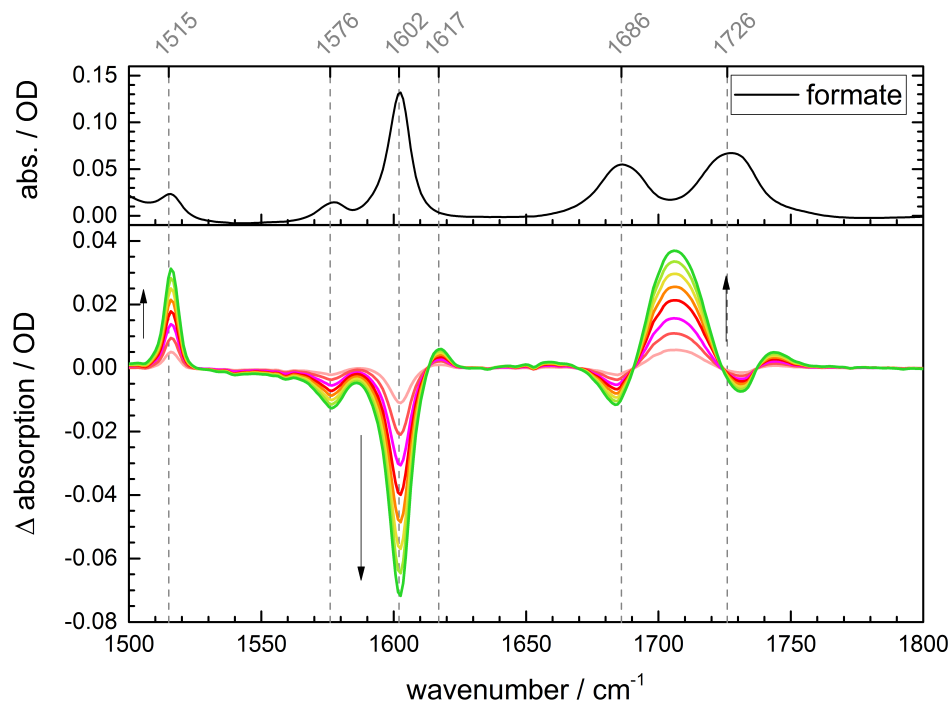
Figure 5.19: Top: Steady-state FTIR of *p*HP formate (4.i) in 1:1 D$_2$O:ACN. Bottom: Irradiation series with Britta water sterilization lamp without filter (see figure 4.1a on page 50). Difference spectra of irradiated minus non-irradiated. Irradiation duration increases from pink to green.

ference spectra are shown in figure 5.20 on the next page. The top panel shows the steady-state spectrum for orientation. The three panels below show three different tries at measuring the irradiation spectra. The irradiation time increases from pink over green to blue. The solvent and irradiation conditions were the same in all measurements. But especially in the azide region significant differences between the three tries can be seen. In the second panel from the top a positive feature at 2040 $cm^{-1}$ appears while the 2111 $cm^{-1}$ band becomes negative. The carbonyl at 1685 $cm^{-1}$ and the ringmode at 1602 $cm^{-1}$ can also be seen as small negative signals. In the panel below the ratio between the negative features at 2111 $cm^{-1}$ and at 1685 $cm^{-1}$ seems to be more or less the same, but the positive band at 2040 $cm^{-1}$ is much smaller. This is even worse in the bottom panel, where basically no positive feature at 2040 $cm^{-1}$ can be seen. There might be a small positive feature at 2160 $cm^{-1}$ instead. In the ring mode and carbonyl region in this panels the baseline under irradiation varies. It seems as if a water absorption band grows in. This assumption also agrees with the appearance of a 2160 $cm^{-1}$
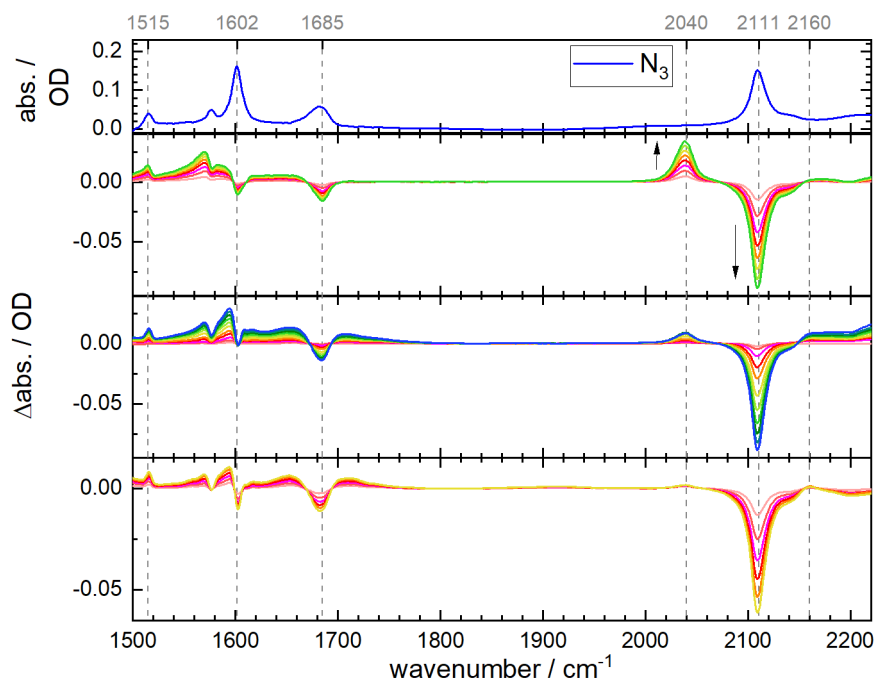
Figure 5.20:  Top:  Steady-state FTIR of *p*HP azide (4.j) in 1:1 D$_2$O:ACN. Bottom:  Three different irradiation series with Britta water sterilization lamp.  All measured under the same conditions.  Difference spectra of irradiated minus non-irradiated.  Irradiation duration increases from pink to blue.

band instead of a 2040 $cm^{-1}$ band, as 2160 $cm^{-1}$ is assigned to HN$_3$ and 2040 $cm^{-1}$ to N$_3^-$ and HN$_3$ should be favoured with higher water content.  In the two lower panels a positive feature on the higher wavenumber side of the carbonyl seems to grow in.  During irradiation bubble formation could be observed.

For the *p*HP azide as for the DEACM azide (see figure 5.4 on page 60 for infrared difference spectrum) two products would be expected N$_3^-$ and HN$_3$.  They should form a equilibrium depending on the pH value [134].  The changes between the intensity of the 2040 $cm^{-1}$ band and the 2160 $cm^{-1}$ band are probably caused by different ratios between the two products.  The problem in the case of *p*HP, is that the photo cleavage influences the pH value.  The sample becomes more acidic since for each successful cleavage a proton is given to the solvent (compare figure 3.11 on page 47).

One would expect that the formation of N$_3^-$ precedes the HN$_3$ formation.  Therefore, the markers might be more reliable in the laser experiment on a much shorter timescale.  TRIR spectra of *p*HP azide are shown in figure 5.21 on the following page.  Only the azide region is shown at early times (pink), where a bleach can be
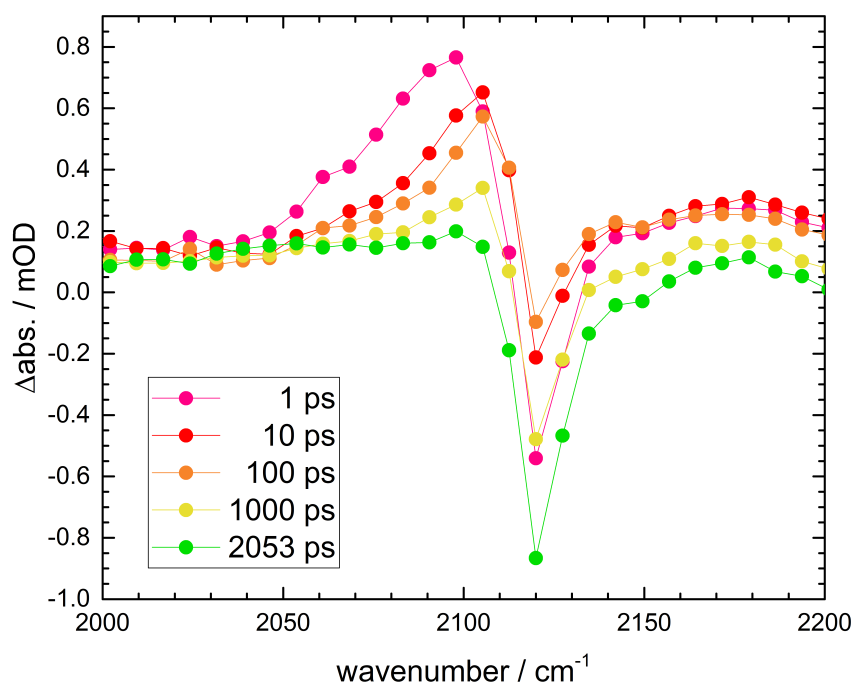
Figure 5.21: TRIR spectra of *p*HP azide (4.j) in 1:1 D$_2$O:ACN. UV-pump at 266 nm. VIS 73.

seen at 2120 $cm^{-1}$ and an ESA at approximately 2100 $cm^{-1}$. Between the spectral cut at 1 ps and at 10 ps (red) cooling occurs, evident by the shift of the ESA to higher wavenumbers. With longer delays the ESA decays. The bleach becomes first smaller and increases than again probably due to the photo reaction. However, no positive band at 2040 $cm^{-1}$ (where the $N_3^-$ is expected) appears. It cannot be excluded that $HN_3$ is formed which overlaps with the bleach, although $N_3^-$ should be formed first. Formation of $HN_3$ on an ultrafast time scale can in principle only occur if a proton is already nearby, as this process is generally diffusion limited. Another attempt of this measurement was done with a buffer:acetonitrile mixture, but also here no clear marker for the photo reaction could be identified.

Therefore, *p*HP azide was discarded as a possible cage for a selective VIPER uncaging experiment.

The next LG that was studied was thiocyanate. The infrared difference spectra under irradiation are shown in figure 5.22 on the next page.

The top panel shows the steady-state FTIR spectrum of *p*HP SCN (4.k) for
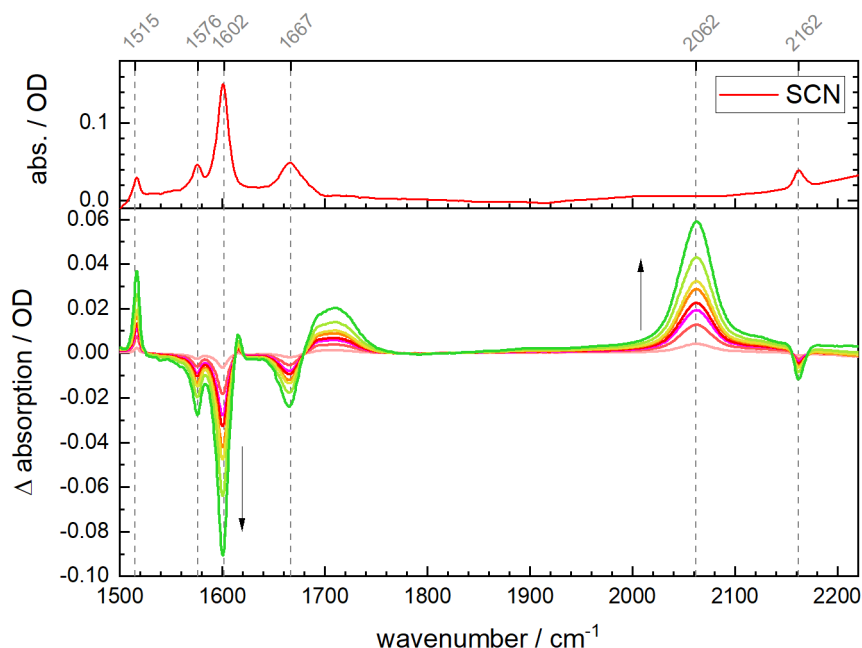
Figure 5.22: Top: Steady-state FTIR of *p*HP thiocyanate (4.k) in 1:1 D$_2$O:ACN. Bottom: Irradiation series with Britta water sterilization lamp. Difference spectra of irradiated minus non-irradiated. Irradiation duration increases from pink to green.

orientation. The bottom panel shows the difference spectra (irradiated minus non-irradiated) with increasing irradiation times from pink to green. As for the *p*HP formate a positive band appears at the position of the lowest ring mode band (at 1517 $cm^{-1}$) while the bands at 1576 $cm^{-1}$ and 1600 $cm^{-1}$ disappear. A small positive band appears at 1615 $cm^{-1}$. The carbonyl at 1667 $cm^{-1}$ also decreases while a broad band appears at higher wavenumbers. Comparing to the other LG, the lowest and highest ring mode bands are shifted a few wavenumbers, but the assignment is still straight forward.

In the thiocyanate region a small bleach at the position of the bound SCN (2162 $cm^{-1}$) can be seen. A larger positive product band appears at 2062 $cm^{-1}$ and is assigned as $SCN^-$. This band looks very promising as a marker for the successful cleavage of the *p*HP SCN.

## 5.2.2 Characterization of Photo products

A closer look at the photo reaction and products of *p*HP SCN is taken. The top panel in figure 5.23 on the following page shows the UV-Vis spectrum. The

absorption maximum is at 287 nm. At 340 nm a small step can be seen in the spectrum. This is caused by the lamp change in the used UV-Vis spectrometer. The tail on the longer wavelength side is assigned to a deprotonated species of the $p$HP.
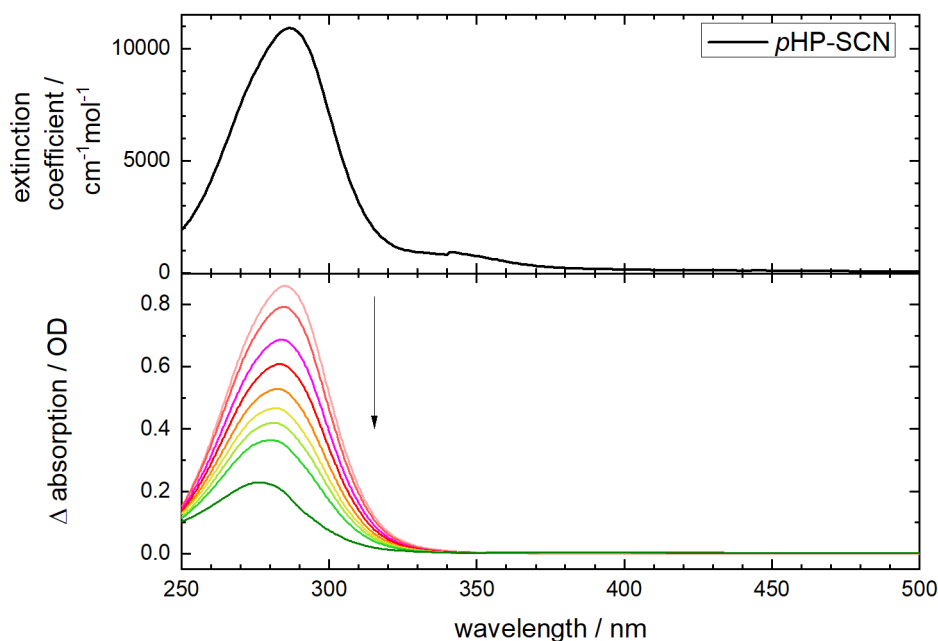


Figure 5.23: UV-Vis spectra of $p$HP thiocyanate (4.k) in 1:1 D$_2$O:ACN under irradiation with Britta water sterilization lamp. Light pink spectrum is before irradiation. Irradiation duration increases from pink to green.

The lower panel shows the difference spectra under irradiation. The irradiation duration increases from pink to green. Already in the light pink spectrum, the signal from the deprotonated phenol can no longer be seen. This is due to the pH-value being changed by the photo reaction (i.ee the protons produced in the uncaging reaction are scavenged by deprotonated $p$HP). Under irradiation with UV light the $p$HP absorption band decreases. The absorption maximum shifts slightly to shorter wavelengths. In the green spectrum the maximum is at 277 nm. In contrast to DEACM no red-shifted products can be seen. This makes $p$HP a promising VIPER cage candidate, since the UV-pump light will not be absorbed by a formed product, meaning all of it can be used for the uncaging.

The possible byproducts for the photo reaction from the literature for $p$HP are shown in figure 5.24 on the next page and the reaction scheme figure 3.11 on page 47. $p$HP acetate ($p$HP 3, 4.g ) is the most common byproduct. The others are mainly formed as side products if the photo reaction takes place without
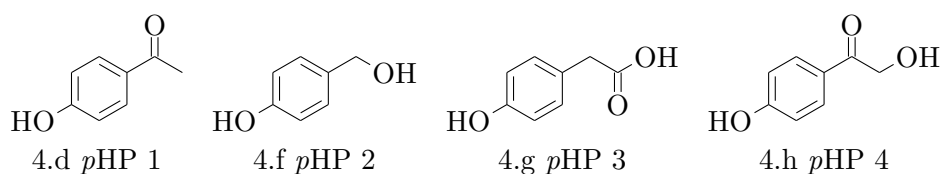
Figure 5.24: Structures of possible *p*HP byproducts: 4.d *p*-hydroxyacetophenone (*p*HP 1), 4.f *p*-hydroxybenzyl alcohol (*p*HP 2) and 4.g *p*-hydroxyphenyl-acetic acid (*p*HP 3) and 4.h *p*-hydroxyphenacyl alcohol (*p*HP 4).

water [2]. The irradiation difference spectrum of *p*HP SCN and the steady-state FTIR spectra of the possible byproducts are shown in figure 5.25.
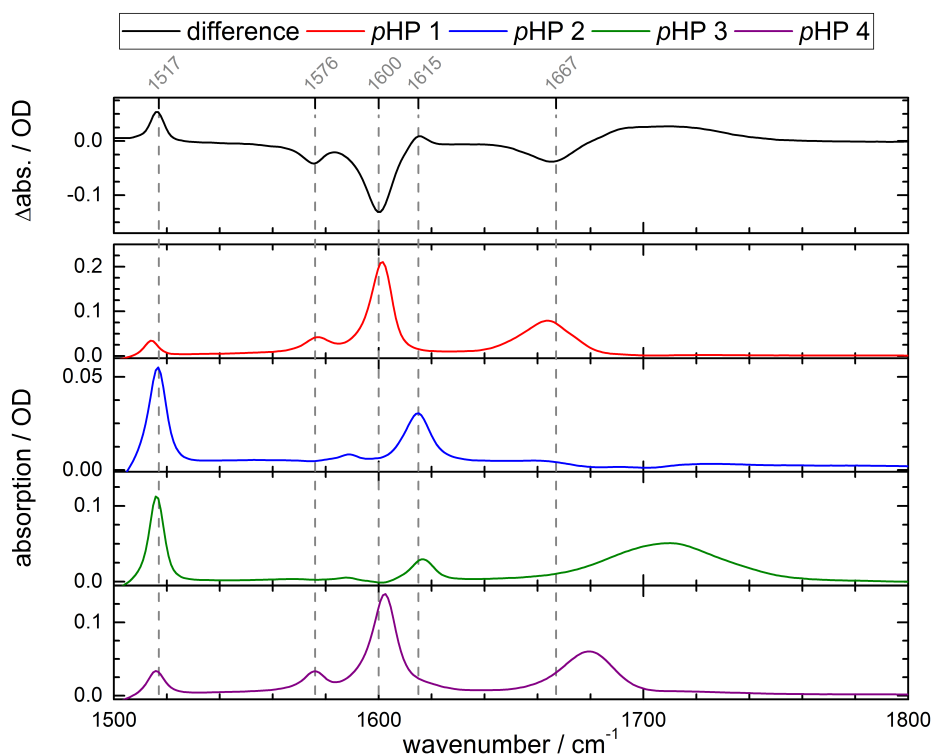


Figure 5.25: TOP panel: Difference spectrum of *p*HP thiocyanate (4.k) in 1:1 D$_2$O:ACN (irradiated minus non-irradiated). Lower panels: Steady-state FTIR spectra of possible *p*HP byproducts in 1:1 D$_2$O:ACN. Red *p*-hydroxyacetophenone (*p*HP 1), blue *p*-hydroxybenzyl alcohol (*p*HP 2), green *p*-hydroxyphenyl-acetic acid (*p*HP 3) and violet *p*-hydroxyphenacyl alcohol (*p*HP 4).

In the light-induced difference spectrum in the top panel 3 positive features

85

can be seen. The band appearing at 1517 $cm^{-1}$, the one at 1615 $cm^{-1}$, and the broad band between 1680 $cm^{-1}$ and 1740 $cm^{-1}$. The bands at 1576 $cm^{-1}$, 1600 $cm^{-1}$ and 1667 $cm^{-1}$ disappear. For a byproduct to be visible in the difference spectrum, it should have absorption bands at the position of the positive features in the difference spectrum and no absorption bands at the position of the negative features. The red spectrum, belonging to *p*HP 1 does not fit, as becomes apparent by the very prominent ring mode band at approximately 1600 $cm^{-1}$. For the same reason *p*HP 4 can be excluded. Both of them have also only small bands at 1515 $cm^{-1}$ and their carbonyl absorption do not match. This leaves *p*HP 2 and *p*HP 3. Both have big absorption bands at 1517 $cm^{-1}$ and smaller bands at 1615 $cm^{-1}$, but only *p*HP 3 has a broad spectral feature between 1680 $cm^{-1}$ and 1740 $cm^{-1}$.
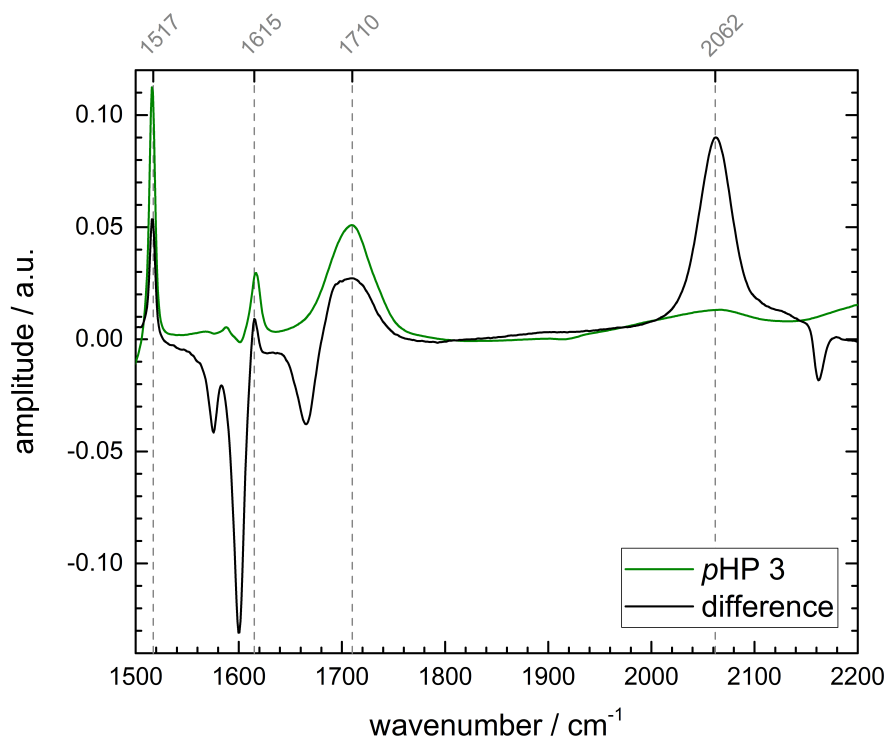


Figure 5.26: Comparison of difference (irradiated minus non-irradiated *p*HP SCN with *p*HP 3 (*p*HP acetate 4.g) in 1:1 $D_2O$:ACN. The y-axis is in arbitrary units as a absorption spectrum is compared to a difference absorption spectrum.

A more detailed comparison between the difference spectrum and the absorp-

tion spectrum of *p*HP 3 is given in figure 5.26 on the facing page. Here also the thiocyanate region is shown, where none of the possible byproducts show an absorption. In this plot it can be seen that the positive features in the difference are very nicely matched by the absorption bands in the *p*HP 3 spectrum. Only the free $SCN^-$ appears as an additional band at 2062 $cm^{-1}$.

In the next step ultrafast measurements were carried out on *p*HP SCN to determine the timescale on which the LG is set free. Figure 5.27 shows the results of a global analysis fit with a sequential model applied to the TRIR data (see also section 4.1 for details on the analysis).
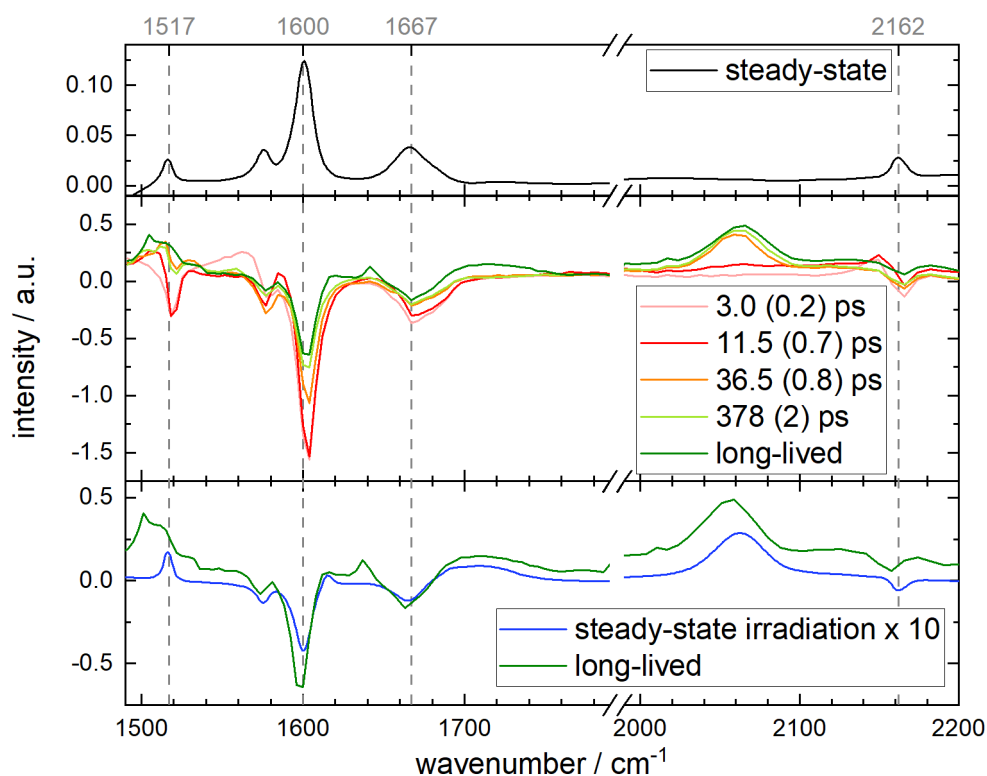


Figure 5.27: Top: Steady-state FTIR spectrum of *p*HP SCN for orientation in 1:1 D₂O:ACN. Middle: Species associated difference spectra (resulting from a global analysis with a sequential model applied to TRIR data). Bottom: Comparison of long-lived spectrum from global fit to steady-state irradiation difference spectrum. VIS 62, VIS 64-66.

The top panel shows again the non-irradiated steady-state spectrum of *p*HP SCN with some wavenumber markers. The middle panel shows the species associated difference spectra and their decays. The exponential decay time in the legend is the time it takes the spectrum of the corresponding color to decay into the next. The

errors are given in brackets (the residues for this fit are in figure C.1 on page 191). This fit was carried out with seven components, the fastest two are associated with the coherent artefact around time zero and are not shown. The light pink spectrum decays with 3 ps into the red spectrum. The major difference between those two spectra is a positive feature in the pink spectrum at approximately 1560 $cm^{-1}$. This is probably an ESA of one or more of the ring modes. In the SCN region the ESA of the bound SCN around 2140 $cm^{-1}$ down shifts from pink to red. This indicates cooling. The red spectrum decays with 11.5 ps into the orange spectrum. Here the main difference is the appearance of the SCN$^-$ signal at 2050 $cm^{-1}$. Also the bound SCN ESA at 2140 $cm^{-1}$ disappears. From orange to light green the free SCN signal shifts a bit. This might be caused by solvation of the SCN$^-$ ion. From light green to dark green a small positive feature at approximately 1500 $cm^{-1}$ begins to appear and there might already be some signal in the region above 1700 $cm^{-1}$ where the $p$HP acetate is expected.

In the bottom panel the long lived spectrum is compared to the scaled steady-state irradiation difference spectrum (aso shown in figure 5.22 on page 83). The spectra show in principle similar features. The 1515 $cm^{-1}$ band is probably already evolving in the long-lived spectrum. The free SCN is shifted with regards to the steady-state spectrum, which could be solvation effects or issues with the wavelength calibration of the global fit data. The small positive feature at 1637 $cm^{-1}$ cannot be seen in the steady-state difference. This indicates a transient band which might belong to an intermediate. The position would indicate that it is related to a carbonyl absorption, although it could also be a up-shifted ring mode.

This TRIR data and the fit results can be compared to the proposed mechanism in the literature (figure 3.11 on page 47), which was elucidated by measuring $p$HP formate in a 1:1 mixture of $H_2O$ and acetonitrile. The $S_1$ was assigned a lifetime of 4 ps and the $T_1$ of 60 ps. The LG was supposed to be cleaved from the tripplet state [2, 141]. In our data we cannot distinguish between the $S_1$ and the $T_1$, but we can directly see the cleavage of the LG by the appearance of the free SCN$^-$. The positive feature at 1560 $cm^{-1}$ is probably the ring mode ESA and decays with 3 ps. The SCN is set free within 11.5 ps. We observe two additional intermediates (orange and green spectrum). Since both still show the bleach at approximately 1517 $cm^{-1}$, they are probably intermediates formed before the rearrangements of the carbonyl.
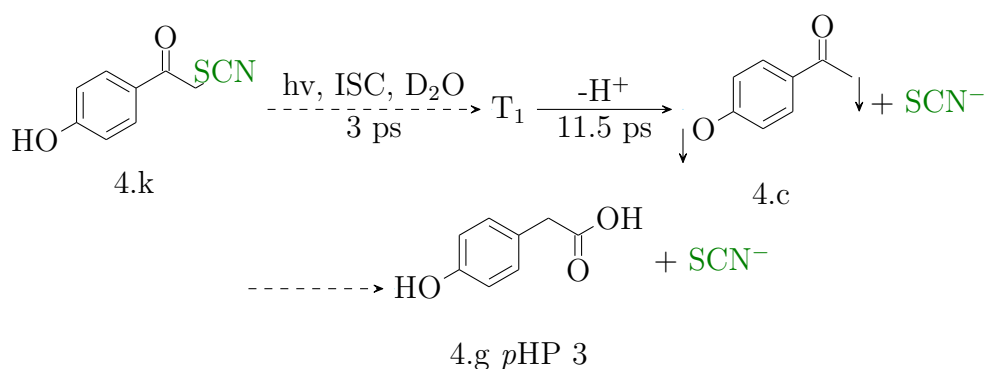
Figure 5.28: Proposed photo reaction for *p*HP SCN.

## 5.2.3 Selection of a mixture of Isotopologues for VIPER Uncaging

As with the DEACM a set of $^{13}C$ labelled cages is needed for the VIPER uncaging experiment, which was described in chapter 3 on page 31. Possible isotopologues and isotopomers are shown in figure 5.29.
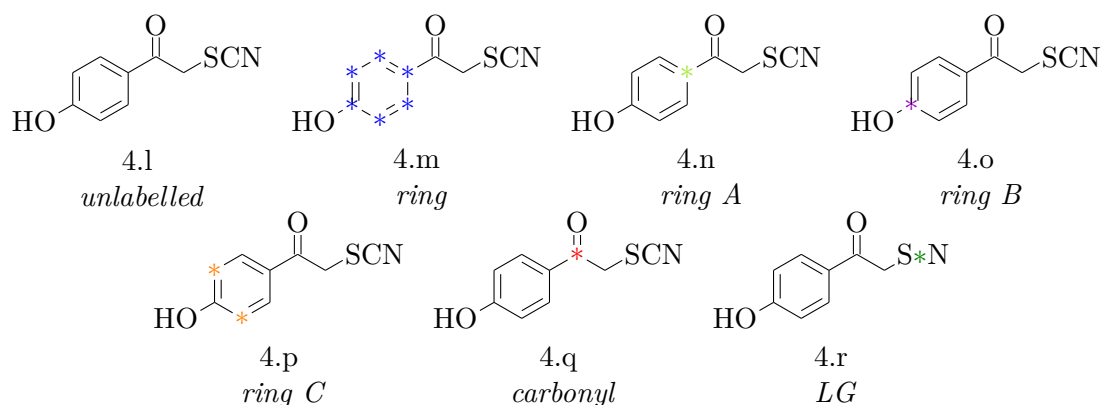


Figure 5.29: Structures of *p*HP SCN isotopologues. The stars indicate the position of the label: *unlabelled*(4.l) without $^{13}$C, *ring*(4.m) with six $^{13}$C atoms in the ring, *ring A* (4.n) with $^{13}$C at position 4 in the ring, *ring B* (4.o) with $^{13}$C at position 1 in the ring, *ring C* (4.p) with two $^{13}$C atoms at position 2 and 6 in the ring, *carbonyl* (4.q) with $^{13}$C in the carbonyl group and *LG* (4.r) with $^{13}$C in the LG.

DFT computations were carried out to get an estimate of the influence of the label positions on the FTIR spectra. The results are shown in figure 5.30 on the next page. For the unlabelled *p*HP SCN (black) the three ring mode vibrations can
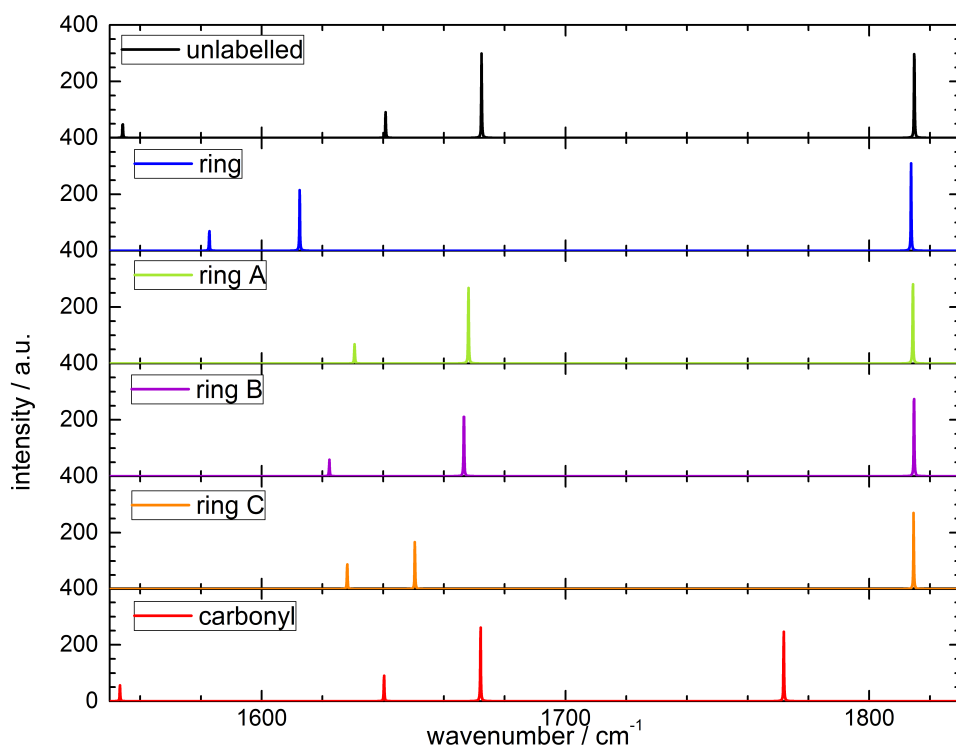
Figure 5.30: DFT computations of *p*HP SCN isotopologues: 4.l black, 4.m blue, 4.n lime green, 4.o violet, 4.p orange and 4.q green. Carried out with Gaussian [160], M06 functional, by Carsten Neumann.

be seen at 1554 $cm^{-1}$, 1641 $cm^{-1}$, and 1672 $cm^{-1}$ and the carbonyl at 1815 $cm^{-1}$. The intensity ratio between the bands is similar to the experimental data, but the wavenumbers are off. This is no major problem since the computations are only meant to help predicting which label will influence which vibrational mode. For the isotopomer where all ring atoms are labelled (*ring*, 4.m), the ring absorption bands are at lower wavenumbers. The lowest ring mode has shifted out of the shown wavenumber range (as this ring mode is not relevant for the experiment according to the VIPER efficiency predictions carried out by Jan von Cosel the spectral window has not been adapted). The carbonyl stayed at the same position. For *ring A* (4.n) the $^{13}C$ label was in position 4 of the ring *para* to the hydroxyl group. The ring modes are slightly down shifted. The shift for the ring mode with the highest intensity is, however, quite small. The lowest ring mode cannot be seen in the shown wavenumber region. *Ring B* (4.o) looks similar to *ring A*, the lowest ring mode is not in the shown window and the high intensity ring mode is shifted a bit to lower wavenumbers. The middle ringmode is further down shifted as in *ring A*. For *ring C* (4.p) the high intensity ring mode loses intensity and

is significantly down shifted with regards to the unlabelled species. The distance between the high intensity and the lower ring mode is smaller than for the others. In the *carbonyl* (4.q) the ring modes are very similar to the unlabelled species. The carbonyl mode is down shifted. This is the only species where a change in the carbonyl band is observed.

To get the highest possible VIPER spectroscopically observable uncaging contrast between the species the unlabelled, the ring and the carbonyl-labelled species were chosen. As a mixture the unlabelled *p*HP and the ring-labelled *p*HP with different LG were envisioned. The carbonyl-labelled *p*HP was also chosen for synthesis, to have a backup. If the VIPER signals of the LGs would be to small to be observed in a measurement of a mixture (as it was the case for DEACM), it could be tried to observe the signals of the carbonyls in a mixture instead.

As has been shown in the first part of this section not all of the considered LGs gave a signal which was deemed suitable as an observable for successful VIPER uncaging. Only SCN gave clear markers for photochemistry. Therefore, *LG* (4.r) was considered. A $^{13}C$ atom in the SCN would shift the absorption band of the free SCN, but should not impact the photochemistry.

Figure 5.31 on the following page shows the experimental steady-state FTIR spectra of the isotopomers synthesized by Matiss Reinfelds [150] (see chapter B on page 189 for details on the synthesis).

The top panel shows the unlabelled *p*HP SCN. The spectral features have been discussed in figure 5.18 on page 78. For the *p*HP with the $^{13}C$ label in the LG (green, 4.r) the spectral features are the mainly same. Only the absorption band of the SCN has been down shifted from 2162 $cm^{-1}$ to 2112 $cm^{-1}$. While the unlabelled species and the LG labelled species cannot be excited individually in the ring mode region when both are present in a mixture, they can be distinguished in the SCN region. For the ring labelled (blue) the SCN absorption is at the same wavenumber as for the unlabelled species. The ring modes are however significantly down shifted. The lowest ring mode has been shifted out of the shown wavenumber region. The carbonyl is also affected a little bit, but is not significantly shifted. The highest intensity band is shifted to 1547 $cm^{-1}$ (from 1600 $cm^{-1}$) and has no significant overlap with other species. The down shifted lower ring mode band (now at 1523 $cm^{-1}$, for other species it is found at 1576 $cm^{-1}$) is quite close to the 1517 $cm^{-1}$ band in the other species. Therefore, pre-excitation on this band might lead to a bad contrast. The same is true for the carbonyl band for unlabelled, LG and ring labelled species.

For the species with the label in the carbonyl (red) the ring mode bands and the SCN band are more or less unaffected. The carbonyl has been shifted from 1667 $cm^{-1}$ to 1630 $cm^{-1}$. Also the shape of the carbonyl absorption has changed a little bit. The band seems to be slightly more asymmetric.
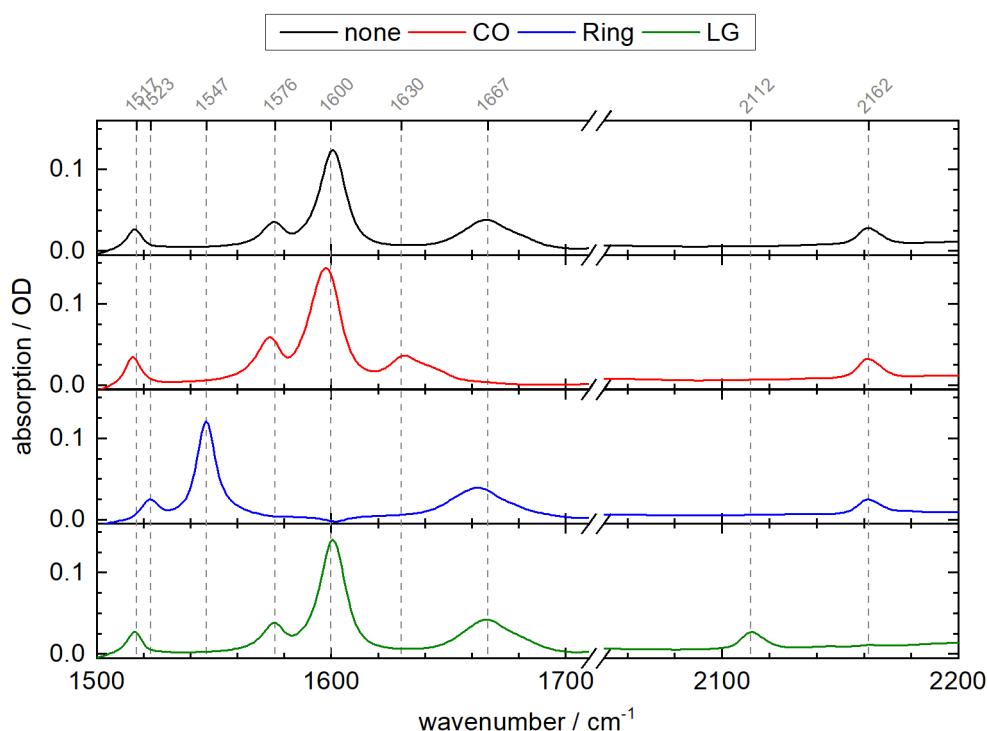
Figure 5.31: Steady-state FTIR spectra of *p*HP SCN isotopologues in 1:1
D$_2$O:actonitrile. *unlabelled*(4.l black), *carbonyl* (4.q red), *ring* (4.m
blue) and *LG* (4.r green). 50 $\mu$m spacer and 30 mM concentration.

In terms of selectivity the species with the label in the LG and with all C atoms
in the ring labelled seem to be most promising.

Infrared difference spectra under irradiation are shown in figure 5.32 on the next
page. The SCN region is of special interest. The free SCN$^-$ of the ring and the
LG labelled species need to be at different positions, in order to spectroscpicylly
observe the highest possible VIPER uncaging contrast in a mixture of these com-
pounds. Due to the down shift introduced by the $^{13}$C this is the case for the SCN
signals of these isotopologues. For the ring labelled species the positive feature
is at 2064 $cm^{-1}$, while for the LG labelled species it is at 2116 $cm^{-1}$. Luck-
ily the anharmonicity on both compounds is such that, also the bleaches of the
bound SCN do not overlap with the positive bands. The increase of the baseline
above 2160 $cm^{-1}$ is due to background absorption. The reason why this baseline
behaviour is not seen in the other species is probably a fluctuation in the water
content due to water vapour contaminating the sample, because the sample is con-
tinuously circulated (i.e. it is not perfectly sealed). The background absorption
is quite sensitive to this fluctuations, One would expect the carbonyl to form H-
bonds with the environment depending on the water content. Indeed the carbonyl
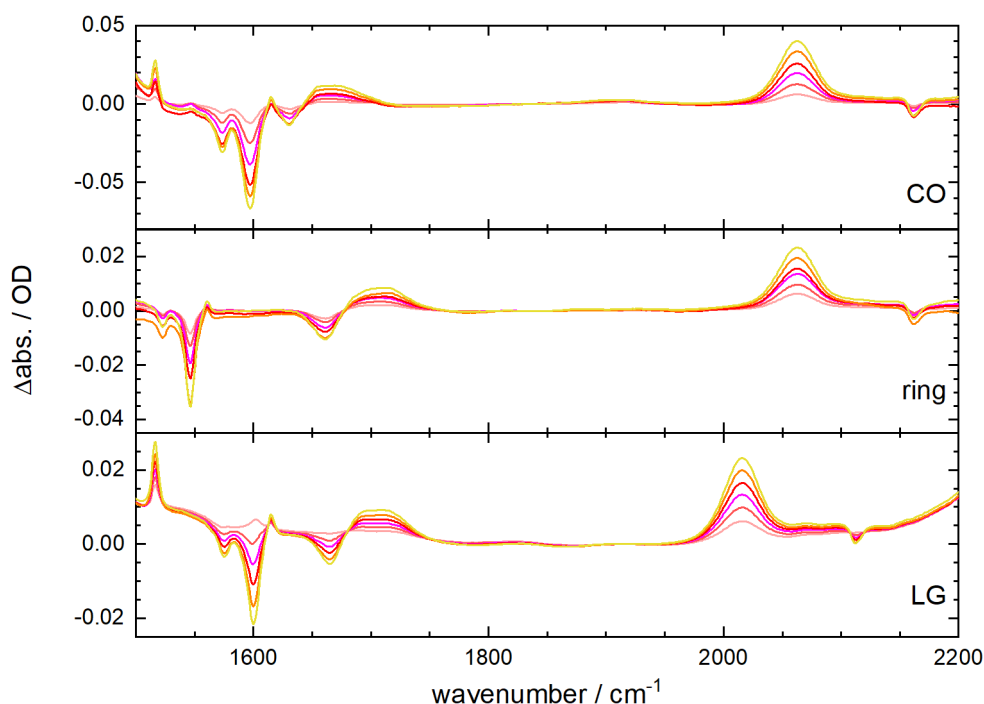
Figure 5.32: Difference infrared absoption spectra for various *p*HP SCN isotopo-
logues in 1:1 D₂O:ACN under irradiation with Britta water steriliza-
tion lamp. Irradiation time increases from pink to yellow.

bond is quite broad which is an indication for a heterogeneous environment as it
can be caused by H-bonds of various strengths. It is, however, not easily seen that
this H-bonding of the carbonyl is affected by changes in the water content in the
sample.

Comparing the ring labelled and the carbonyl labelled species, which could serve
as a second potential species mixture in case the selective uncaging of the unla-
belled and the LG species is not successful, the positions of the carbonyl bands look
less promising. The reason is that there is an overlap between the (down shifted
with respect to the unlabelled species) positive feature of the carbonyl labelled
species at approximately $1665 \ cm^{-1}$ and the bleach of the ring labelled species at
$1659 \ cm^{-1}$. A selective detection in this region would therefore probably not work
out as nicely as it did for DEACM, where the ring mode region provided the high
species-selectivity required for excitation and the carbonyl mode region allowed a
clear observation of each selected species.

However, there is not only the selective monitoring to consider, but also the
selective pre-excitation. A few thoughts on the band positions have already been
given in the discussion of figure 5.31 on the facing page. To elaborate, the VIPER

efficiency of the different infrared modes needs to be considered. For this purpose computations of the UV-Vis spectrum after pre-excitation were carried out.

## 5.2.4 Computation of IR-excited UV-Vis spectra

As for DEACM (see figure 5.13 on page 73) computations of the UV-Vis spectrum with various IR pre-excitations were done by Jan von Cosel from the Burghardt group [117] (see chapter B on page 189 for details on the computational methods).

In figure 5.33 on the next page the top panel shows the computed infrared spectrum of unlabelled *p*HP SCN convoluted with Lorentzians to fit to the experimental spectrum. This is meant to help identify the IR modes which influence the UV-Vis spectrum. A scaled experimental steady-state IR spectrum is shown by the dashed grey line. The positions of the computed IR modes do not match very well to the experimental positions (i.e. the computed wavenumbers are higher than the experimental bands), but the identification of the modes is possible. Since the parameters for the computations were chosen differently, the spectra are different from the spectra shown in figure 5.30 on page 90 which were used to identify the influences of the $^{13}$C label on the positions of the IR bands. The SCN band is not shown in figure 5.30 on page 90 because it is well-separated from the shown ring and carbonyl modes, and is not used for pre-excitation. Here only the identified IR modes 43-46 (the numbering corresponds to those produced by Gaussian [160]) are shown.

The UV-Vis spectra shown in the middle panel of figure 5.33 on the facing page are vibrationally resolved, shifted and broadened with Gaussians to match the experimental UV-Vis spectrum. In contrast to figure 2.11 on page 21 the computed UV-Vis spectrum is not shown as a *stick* spectrum and the vibrational resolution can no longer be seen because of this broadening. This alternative presentation was choosen to make the comparison to experimental data easier.

The overall agreement of the shape of computed spectrum to the experimental spectrum (figure 5.23 on page 84) is good. However, it becomes apparent that the positive feature at the low wavelength side in figure 5.33 on the next page is not a spectral feature in agreement with the experimental data but an computational artefact. As we are mostly concerned with the changes at the high wavelength side of the spectrum this does not hinder interpretation.

To see the differences between the spectrum without pre-excitation and with pre-excitation better, the difference spectra are shown in the bottom panel. The presentation of the changes in the computed spectra has been optimized to make assumptions about the experiments easier.

The different IR modes have significantly different influences on the UV-Vis spectrum. Mode nr. 43 (which corresponds to the smaller ring mode vibration at 1517 $cm^{-1}$ in figure 5.31 on page 92) modulates the UV-Vis spectrum only
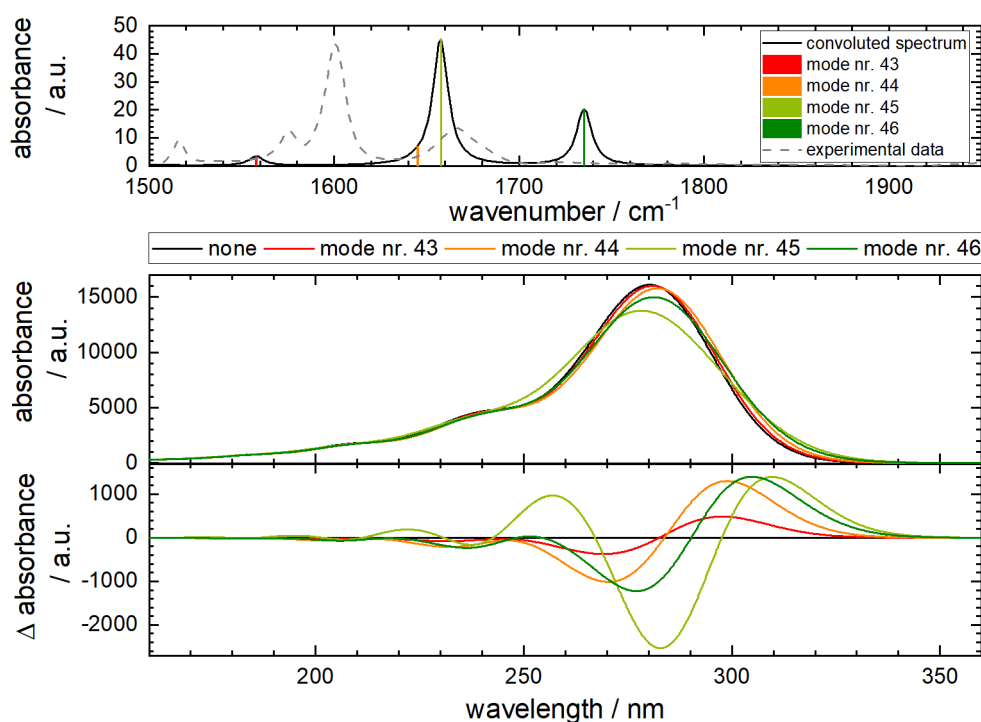
Figure 5.33: Computation of VIPER effect of *p*HP SCN in acetonitrile. Top: Computed IR spectrum with PBE0/Def2-TZVP. Convoluted with Lorentzians to fit experimental data (scaled data shown in dashed grey line). Modes are indicated by coloured bars. Middle: Computed UV-Vis spectra with PBE0/Def2-TZVP. Spectrum is vibrationally resolved and broadened with Gaussians and shifted to match the experimental spectrum. Black spectrum is without IR pre-excitation. Colours match the modes in top panel. Bottom: Difference between UV-Vis spectra with pre-excitation minus without pre-excitation. Computations by Jan von Cosel [117].

a little. The biggest effect can be seen for mode nr. 45 (which corresponds to the highest ring mode at 1600 $cm^{-1}$ in figure 5.31 on page 92). For this mode also a significant negative feature can be seen. With the UV-Vis pump pulse in this wavelength region, one would thus expect a sign-flipped VIPER signal, i.e. a VIPER signal which looks like the TRIR signal multiplied by -1. However, at this wavelength the UV-Vis pulse would be quite resonant with the UV-Vis absorption band and saturation effects due to the high optical density of the sample in this range might have limiting effects on the VIPER signal size. A more detailed study of these effects was carried out by Carsten Neumann [123].

As for DEACM (compare figure 2.11 on page 21), the vibrational modes of

various isotopologues were computed to see the influence of the label positions. The computed infrared spectra and the differences in the computed UV-Vis spectra after IR pre-excitation of four different ring and carbonyl modes are shown in figure 5.34.
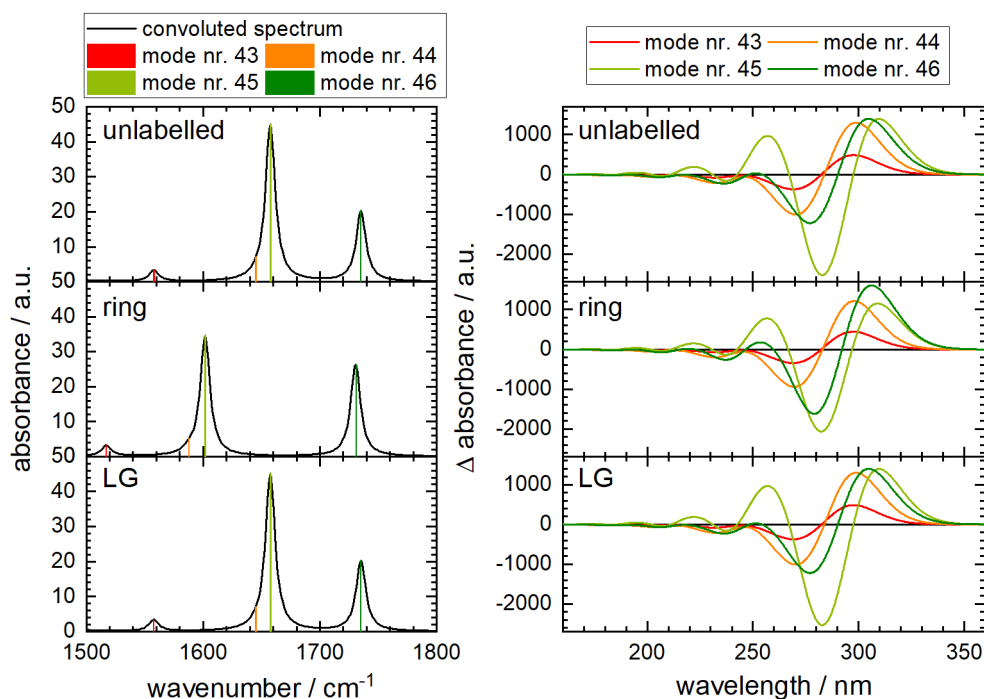


Figure 5.34: Computation of influence of isotopomers on VIPER effect of *p*HP SCN in acetonitrile. Left: Computed IR spectrum with PBE0/Def2-TZVP. Convoluted with Lorentzians to fit experimental data. Modes are indicated by coloured bars. Right: Difference between UV-Vis spectra (PBE0/Def2-TZVP, broadened with Gaussians and shifted to match the experimental spectrum) with pre-excitation minus without pre-excitation. Computations by Jan von Cosel [117].

The top row shows the IR modes (left column) and the influence of the position of the IR pre-excitation on the unlabelled *p*HP SCN (right column; same as in figure 5.33 on the preceding page). In the second row the computations for the species with the C-atoms in the *p*HP ring labelled by $^{13}C$ is shown. The position of mode nr. 46 (assigned to the carbonyl stretch mode) is mainly unaffected, while modes nr. 43 to 45 shift to lower wavenumbers. The changes in the computed UV-Vis spectra after pre-excitation are minor when compared to the unlabelled species. The different pre-excitations reveal only slight changes in relative intensity and the wavelength regions in which the effects can be seen stay more or less the

same. The $^{13}C$ atom in the LG does not effect the IR absorption band positions nor the IR excitation-induced UV-Vis difference spectra.
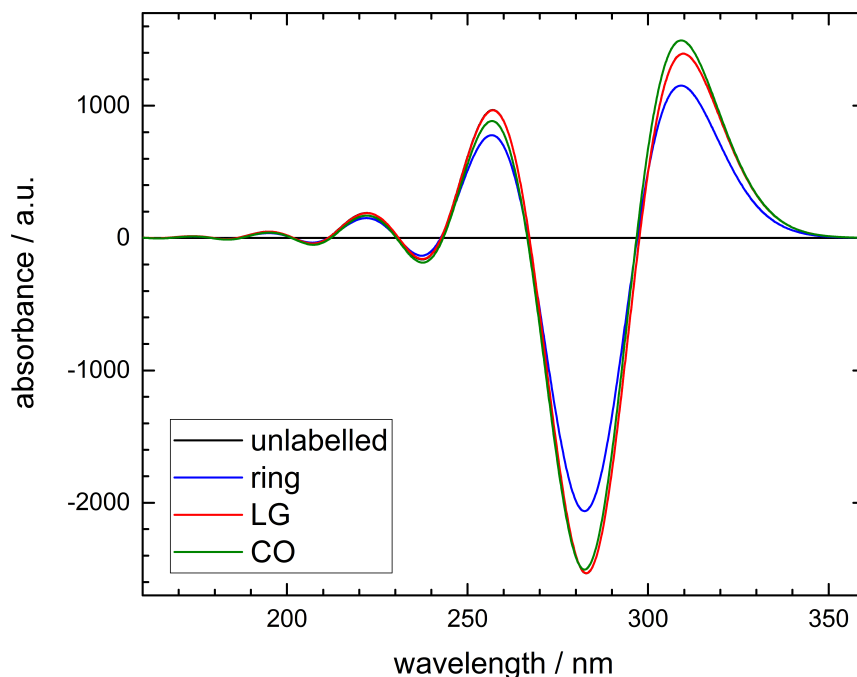


Figure 5.35: Computation of influence of isotopomers on VIPER effect of *p*HP SCN in acetonitrile (not normalized). Difference between UV-Vis spectra (PBE0/Def2-TZVP, broadened with Gaussians and shifted to match the experimental spectrum) with pre-excitation minus without pre-excitation on mode nr. 45 for the different isotopologues. Computations by Jan von Cosel [117].

To better compare the influences of the isotopomers, the computed UV-Vis difference spectra for mode nr. 45 (the highest wavenumber ring mode, which is also the mode showing the largest VIPER effect in terms of amplitude, see figure 5.34 on the preceding page) are plotted together in figure 5.35. Here the unlabelled species (4.l), the ring (4.m), the LG (4.r) and the carbonyl (4.q) labelled species are shown. Figure 5.35 shows that there is no difference between the unlabelled and the LG species (the black and the red spectrum overlap completely). For the ring species the relative intensity differences are a little smaller, but the wavelength regions in which effects can be expected are identical. The CO species

behaves very similar. This leads to the conclusion, that the different $^{13}C$ positions should not significantly influence the VIPER effect for $p$HP.

### 5.2.5 Testing for suitable VIPER parameters

After a measurement pause and experiments on Coumarin 6 (shown in Carsten Neumann's Thesis [123]) a second try was undertaken. The Coumarin 6 measurements and the computations had shown that the VIPER signal depended strongly on the UV-Vis wavelength, which had previously not been changed systematically for $p$HP.

In a first attempt the ring mode region of $p$-hydroxyacetophenone in a $D_2O$:ACN mixture was probed. This sample was chosen since it is commercially available and does not undergo photo reaction. A broadband VIPER signal was found for a UV-Vis-pump wavelength of 302 nm and a spacer thickness of 100 $\mu$m. The signal was quite small with 140 $\mu$OD for a broadband measurement and is not shown here.

The sample was then changed to $p$HP SCN and a broadband signal of the ringmode region is shown in figure 5.36 on the facing page.

The top panel shows the steady-state FTIR data of the ring mode region of $p$HP SCN for orientation. The second panel shows the VIPER data. A bleach can be seen at the position of the 1600 $cm^{-1}$ band. With approximately 50 $\mu$OD it is very small for a broadband signal. The signals for DEACM VIPER measured with the Fabry-Pérot (and using much lower IR-pump energy) were not much smaller than that. A small additional bleach might be next to the 1667 $cm^{-1}$ band, but this could also just be baseline fluctuation. A bleach would also be expected at 1576 $cm^{-1}$, but only a positive feature can be seen there. This is probably due to noise because of little probe light in that spectral region. The other two panels show the 2DIR and the TRIR difference spectra. In the 2DIR at 100.4 ps delay no significant signal is expected any more because of short lifetime of the vibrations.

To verify the vibrational liefetime a trace of the 2D-IR signal of the high intensity ring mode bleach is shown in figure 5.37 on page 100. An exponential fit to the data (shown in red) yields a decay time of 3.4(1) ps. As expected there is no remaining 2D-IR signal at times longer than 100 ps.

However, two bleaches at the positions of the ring mode absorptions can be seen in the third panel of figure 5.36 on the facing page. This might be due to starting material vanishing due to the photo reaction. As this is a broadband measurement with the probe and the pump light in the same spectral region straylight effects cannot be excluded.

The TRIR spectrum shows three negative features which correspond nicely to the steady-state absorption bands and are in agreement with the TRIR data in figure 5.27 on page 87 (the excited state lifetime was estimated to be 36.5 ps).
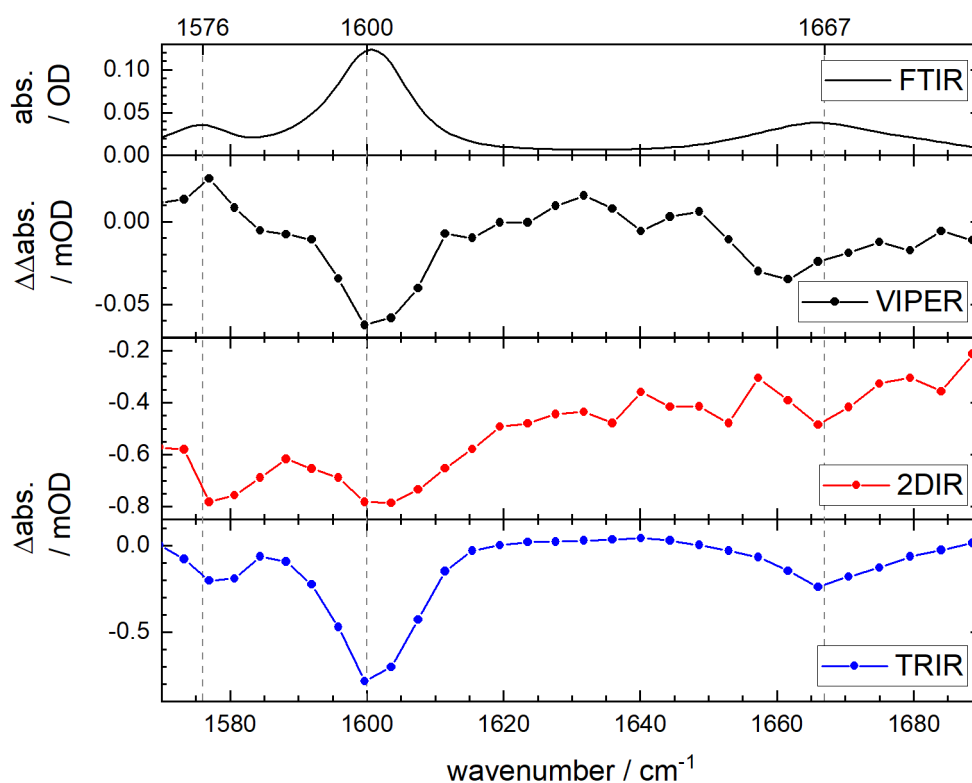
Figure 5.36: VIPER spectrum of *p*HP SCN in 1:1 $D_2O$:ACN with broadband IR-pump in the ring mode region. Delay between the pump pulses 0.4 ps. Delay between UV-pump and IR-probe 100 ps. UV-pump at 315 nm for VIPER and TRIR measurements. VIPER 525.

Since the broadband *p*HP SCN VIPER signal is smaller than expected, experimental parameters were varied systematically to optimize the signal. The polarizations between the pump and probe pulses was optimized. In theory the polarization between the pump pulses needs to match the angle between the IR and the UV-Vis transition dipole moment. The orientation of the probe pulse with regard to the pump pulses should not have an influence if the delay time between pump pulses and probe pulse is long (as it is here). Experimentally the biggest signal was achieved with an angle of 20 °C between the pump pulses and the probe pulse oriented parallel to the pump pulses.

Figure 5.38 on page 101 shows a variation of the UV-pump wavelength. The top panel shows the VIPER signal (determined at 1600 $cm^{-1}$ after subtraction of a -20 ps background). The second panel shows the corresponding 2DIR and TRIR signal sizes. The 2DIR signal size is determined at 2 ps and is the difference between the bleach and the ESA of the 1600 $cm^{-1}$ ring mode band. The TRIR
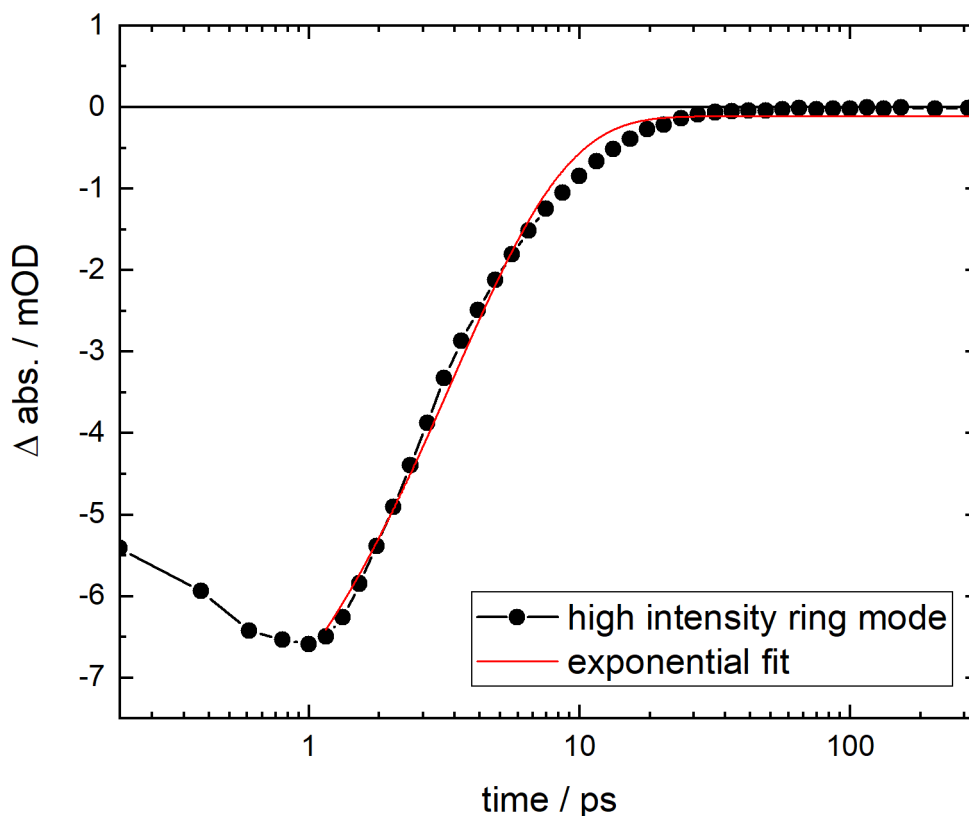
Figure 5.37: 2D-IR trace high intensity ring mode of $p$HP SCN in 125:1000 D$_2$O:ACN with narrow band IR-pump on the same ring mode. 30 mM concentration, 50 $\mu$m spacer. Sample is not circulated by a pump or moved up and down.

signal is determined at 100 ps from the 1600 $cm^{-1}$ bleach.

The 2DIR signal should not change as function of the UV wavelength. The changes which can be seen are fluctuations due to changes in alignment, OPA output and humidity. This has of course a significant influence on the VIPER signal, but could not be controlled better than seen here. The variations were carried out on the same day and the setup was flushed with dry air and the temperature in the laboratory was controlled, still the fluctuations are not negligible. For an in-depth analysis the ratio between VIPER and TRIR signals should be considered instead of the absolute signal sizes. At this point this was not in the focus as only the largest VIPER signal was of interest.

For the TRIR spectrum, one would expect the signal to be become bigger for smaller wavelengths since the UV-pump pulse becomes more resonant with the absorption band of $p$HP SCN. At some point the signal would no longer increase
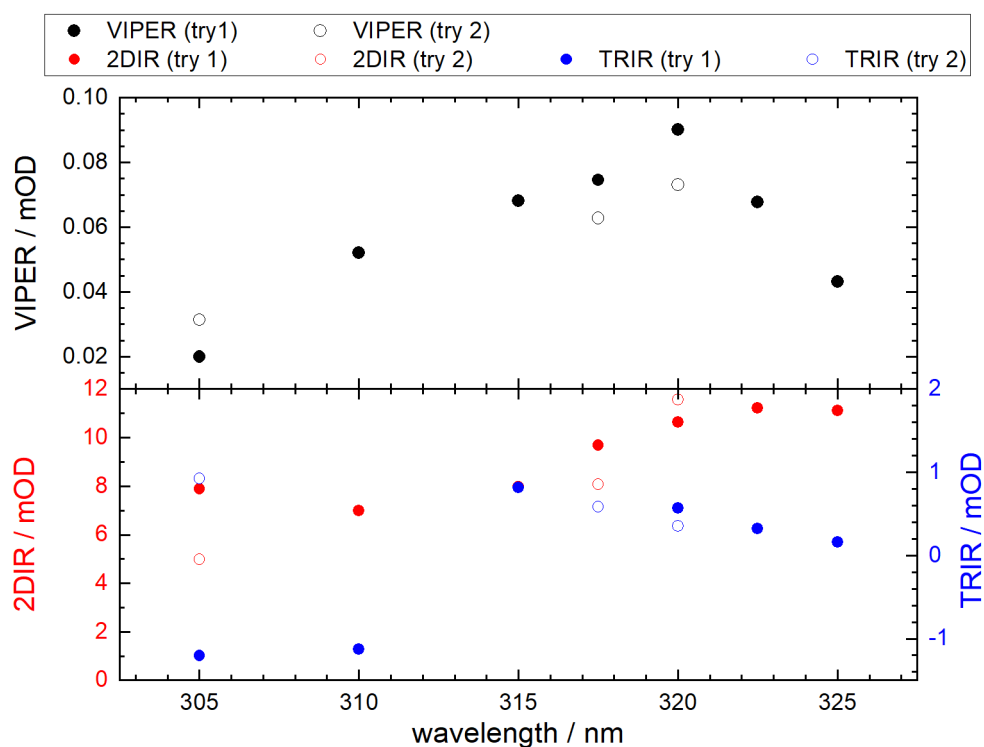
Figure 5.38: Top: Influence of wavelength variation on VIPER signal of *p*HP
SCN in 1:1 $D_2O$:ACN with broadband IR-pump in the ring mode
region. 30 mM concentration, 50 $\mu$m spacer, 20° angle between UV-
pump and IR-pump. UV-delay of 100 ps. Delay between pump pulses
varied between 0.2 ps and 0.6 ps, 0.4 ps for most points. Bottom:
Corresponding 2DIR (left y-axis) and TRIR (right y-axis) signals.
VIPER 548 to VIPER 554.

because of saturation effects , i.e. the UV absorption is so high that the first layers
of the sample absorb all the UV light, such that higher OD (or more resonant
excitation) do not lead to higher difference absorption signals. In this experiments
the TRIR signal becomes smaller for shorter wavelengths. This is probably because
the OPA's output becomes less in addition to it being less stable in this region.

In this thesis no systematically study of the influences on the VIPER signal was
undertaken, but the best conditions to measure VIPER on a *p*HP mixture were
searched. At this point only the size of the VIPER signal and not the contrast
to the unspecific background was taken into consideration. From this it becomes
clear that the UV-pump pulse has to be at 320 nm.

Some UV-wavelengths were measured twice. They are given in open circles. This
serves as an estimate how much the signal varies even if wavelength, concentration,

spacer and energy are chosen to be the same. As has been mentioned before the OPA outputs and alignments can change during measurement and strongly influence the signal sizes. Especially with signals so small, these fluctuations have major impacts. The 305 nm point shows how the changes in the UV-pump and the IR-pump can also compensate each other. The TRIR and the 2DIR signals for the solid and the open 305 nm data points are very different. But the VIPER signals are quite similar. All of this makes a systematic approach quite difficult. For this thesis only the changes which increased the VIPER signal were pursued.

The variations of concentration, optical path length and UV energy are shown in figure 5.39.
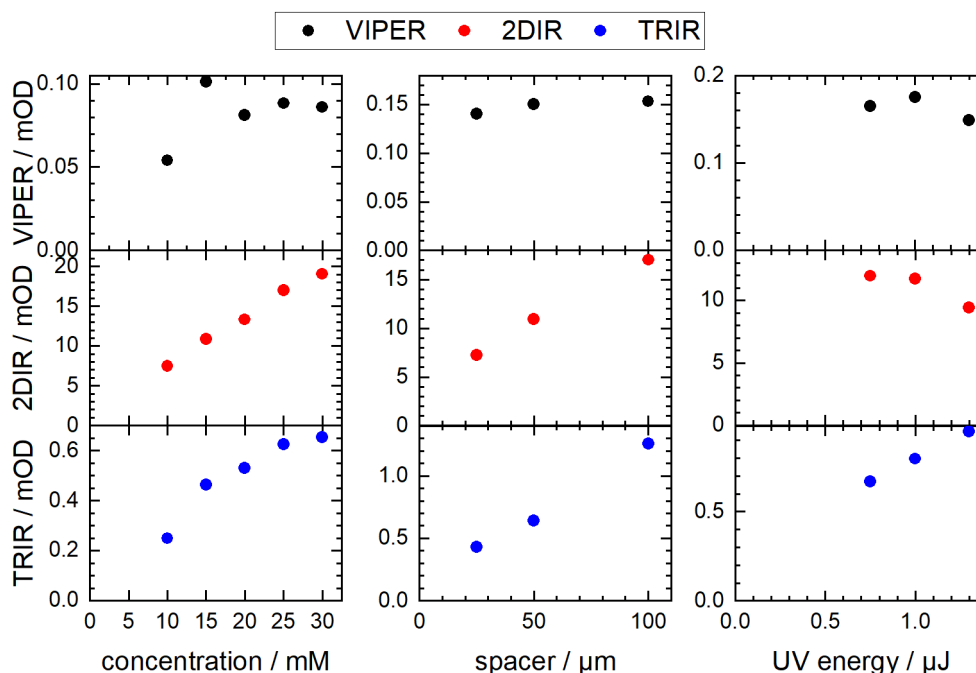


Figure 5.39: Parameter optimization for $p$HP SCN in 1:1 $D_2O$:ACN with broadband IR-pump in the ring mode region. UV-delay of 100 ps. Delay between pump pulses varied between 0.2 ps and 0.6 ps, 0.4 ps for most points. Left: VIPER, 2DIR and TRIR signals for a dilution series (VIPER 539 to VIPER 544) 100 $\mu$m spacer, 20° angle between UV-pump and IR-pump. Middle: VIPER, 2DIR and TRIR signals for different spacers (VIPER 566 to VIPER 568) 30 mM concentration, 20° angle between UV-pump and IR-pump. Right: VIPER, 2DIR and TRIR signals for various UV energies (VIPER 559 to VIPER 562) 30 mM concentration, 50 $\mu$m spacer, 20° angle between UV-pump and IR-pump.

It can nicely be seen that both 2DIR and TRIR signals depend on the concentration. For 2DIR the dependence seems to be linear and for the TRIR signal there seems to be a saturation for high concentrations. In the VIPER signal there is an outlier at 15 mM and the saturation begins at lower concentrations. Also the signals seems to become slightly smaller for high concentrations. 30 mM is close to saturation in a 1:1 $D_2O$:acetonitrile mixture and was deemed to be the optimum. Concerning the optical path lengths the dependence for 2DIR and TRIR are again linear, but for VIPER a large spacer does not lead to further increase in the signal size. Both 100 $\mu$m and 50 $\mu$m spacers were used.

The UV-pump energy directly influences the TRIR signal as can be seen in the lowest panel on the right. The 2DIR signal should be constant. However, it decreases dramatically. This is probably due to problems with the OPA output or the alignment. The VIPER signal also decreases. This is probably just due to the decrease in the IR-pump and has nothing to do with the increased UV-pump. Again for analysis this issue could be mostly solved when VIPER to TRIR or VIPER to 2DIR ratios are plotted instead of absolute values. The VIPER signal strongly depends on the IR-pump and is often limited by it. Therefore, we decided to use the maximal output of the UV OPA, which was around 1.5 $\mu$J for most of the time and at some point increased to 2.5 $\mu$J. We did not re-align the OPA or consciously change anything to create this improvement. Maybe the laser output changed favourably (but the energy stayed the same). Since the objective was to measure the largest VIPER signal possible, we did not spend time to investigate the origin of this improvement, but went on to measure the VIPER signal in the $p$HP SCN region.

Figure 5.40 on the following page shows the broadband VIPER signal probed in the SCN region. In the top panel the steady-state FTIR spectrum is given for orientation. The lowest panel shows the TRIR spectrum at 270 ps. A small bleach can be seen at the SCN absorption band position and a positive feature can be seen at approximately 2066 $cm^{-1}$. This is in agreement with the TRIR data in figure 5.27 on page 87. The 2DIR signal at 270 ps shows no spectral features as is expected for such long delay times. The VIPER signal shows the same positive feature as the TRIR spectrum. The bleach cannot be seen clearly. It probably vanishes in the noise of the baseline, because of the small signal size of the VIPER signal.

Again an optimization was carried out in order to obtain bigger VIPER signals to make the measurement with Fabry-Pérot in a mixture possible. The most promising candidate for improvement was to vary the $D_2O$ content. $D_2O$ is needed for the photo reaction, but it absorbs IR light in the ring mode region and therefore limits the spacer thickness. Also, the sample does dilute better in solvent mixtures with less $D_2O$. This means that the concentration could be increased above the

previous concentration limit.

VIPER signal sizes for 100 mM *p*HP SCN with a 50 $\mu$m spacer and different $D_2O$ content are shown in figure 5.41 on the facing page.

It can nicely be seen how the TRIR signal increases with the $D_2O$ content and saturates at approximately 12 %. The explanation is that the reaction rate for the photo cleavage depends on water. The 2DIR signal decreases with increasing water content, since the $D_2O$ absorbs the IR-pump light. The VIPER signal has a maximum at a mixture of 125 ml $D_2O$ with 1000 ml acetonitrile. This point also looks a bit like an outlier, but the increase of the $D_2O$ content above this percentage does not significantly increase the VIPER signal. Therefore, a 125:1000 mixture of $D_2O$:acetonitrile was chosen. Again the concentration, path length and UV wavelength dependencies were tested.

Furthermore, the characterization of the photo reaction at this solvent conditions was carried out, since the $D_2O$ content has an influence on the photo reaction. The infrared difference spectra under irradiation are shown in figure 5.42 on page 106.

The top panel shows again the 1:1 mixture and the bottom panel shows the
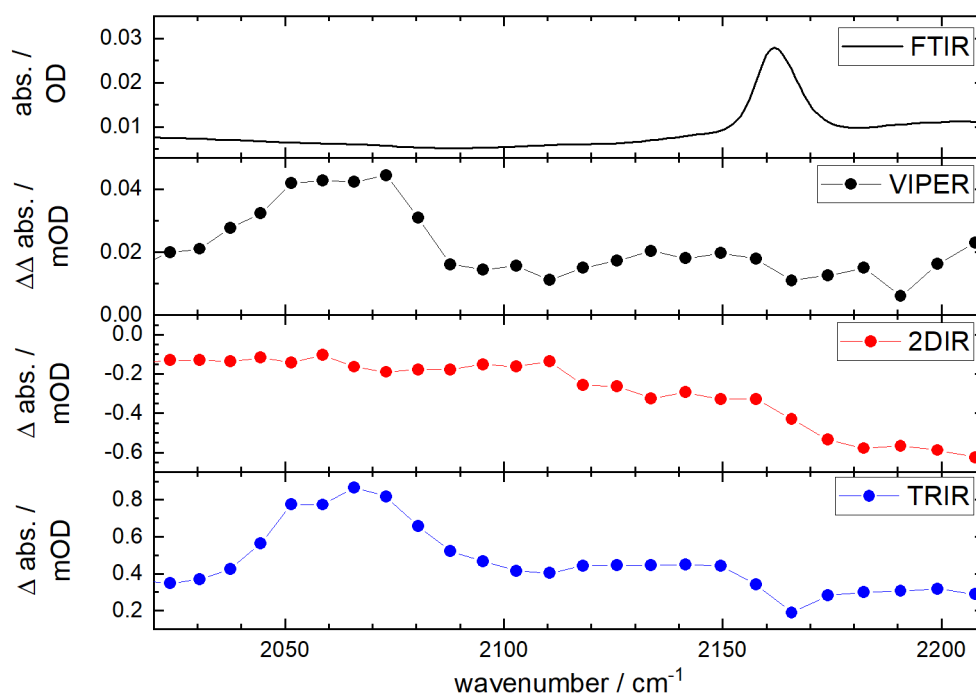


Figure 5.40: VIPER spectrum of *p*HP SCN in 1:1 $D_2O$:ACN with broadband IR-pump in the ring mode region. Delay between the pump pulses 0.4 ps. Delay between pump and probe 270 ps. UV-pump 2 $\mu$J at 315 nm. VIPER 573.
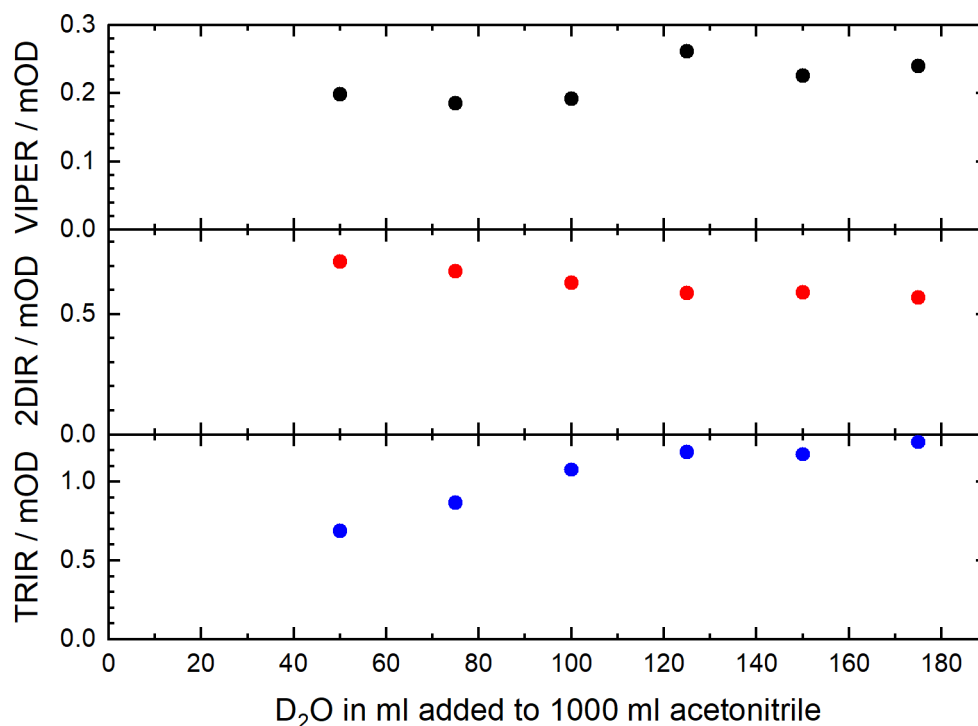
Figure 5.41: Influence of $D_2O$ content on VIPER spectrum of *p*HP SCN in a $D_2O$-acetonitrile mixture with broadband IR-pump in the ring mode region and IR-probe in the SCN region. 100 mM, 320 nm, 50 $\mu$m spacer, 20° angle between UV-pump and IR-pump. Pump pulses simultaneous. Delay between pump and probe 270 ps. VIPER 591 to VIPER 596.

125:1000 mixture. Comparing the spectral features no significant differences can be seen. The positions of the difference signals are more or less the same. The SCN bands are a little bit down shifted, but this could just be because of changes in the background and the shape of the positive carbonyl band is slightly different. This might be caused by a different ratio of H-bonded and free carbonyl due to the lower water content, but again it could just be changes in the background spectrum. In conclusion, the change of the water content has not changed the positions of the markers for the photo reaction.

A bigger impact would be expected for the kinetics of the reaction. Therefore, TRIR measurements in the 125:1000 mixture were carried out. The global analysis for the SCN region in a 1:1 mixture and in a 125:1000 mixture are shown in figure 5.43 on page 107.

Only the cleavage of the SCN is considered here. Comparing the results of the fit of the SCN region here to the global fit of whole data set in figure 5.27 on page 87, the first point to notice is the difference in the time constant for the appearance
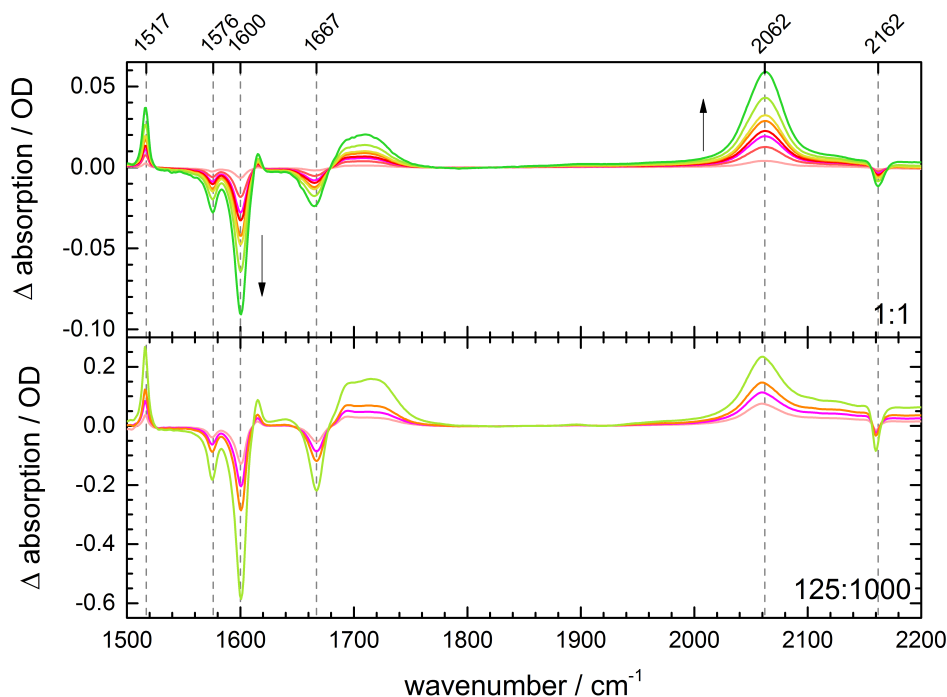
Figure 5.42: Difference infrared absorption under irradiation of *p*HP SCN in 1:1 D$_2$O:ACN (top) and in 125:1000 D$_2$O:ACN (bottom).

of the free SCN. For the fit of the whole data set this value was 11.5 ps. Here we get a value of 15 ps. Looking at the traces of both fits in the SCN region (not shown), both fits appear to be reasonable. The main difference between the fits is the number of time constants needed to fit the data. In the SCN region only 4 constants (without the artefact) are needed, while the whole data set is fitted with 5 constants. This is most likely the reason for the apparent change in the time constant.

In figure 5.43 on the facing page both the 1:1 and the 125:1000 data were fitted with the same number of time constants. Therefore the direct comparison between the resulting time constants is possible. The residues for the fits are given in figure C.2 on page 192 and figure C.3 on page 193.

As with the steady-state difference spectra under irradiation the position and shape of the spectral features are the same in both solvents. The time constants are a little different. The first time constant, which belongs to the S$_1$ lifetime and the ISC process to the triplet is a little bit shorter for the lower water content. The second time constant belonging to the SCN$^-$ appearance is slightly longer for less water. This would mean, that the cleavage is a little bit slower if less water is
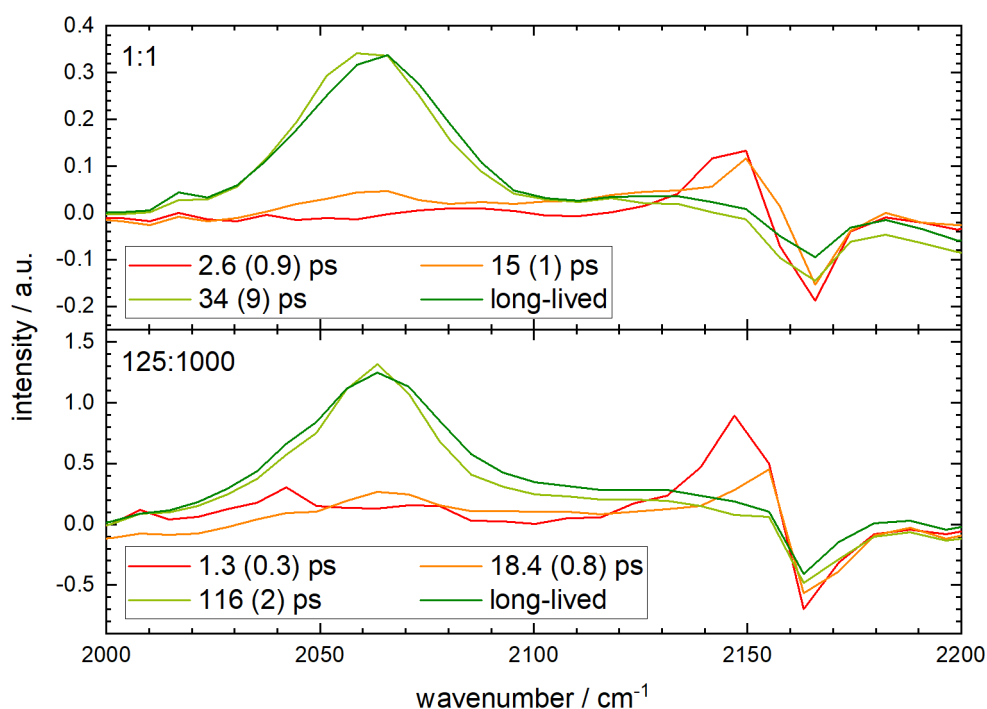
Figure 5.43: Species associated difference spectra (resulting from a global analysis with a sequential model applied to TRIR data). Top: *p*HP SCN in 1:1 D$_2$O:ACN (VIS 64). Bottom: *p*HP SCN in 125:1000 D$_2$O:ACN (VIS 87).

present, which is reasonable with the proposed photo reaction that relies on water. The third time constant which might be a solvation process of the free SCN ion is also slower if less water is present.

Since it has been confirmed that the photo reaction still works nicely with the lower water content, it was proceeded with the VIPER measurements on the chosen *p*HP isotopologues.

## 5.2.6 VIPER Uncaging on *p*HP isotopologue mixture

The data of the two chosen isotopologues (4.m and 4.r) in a 125:1000 D$_2$O:acetonitrile mixture are shown individually in figure 5.44 on page 109. The ring labelled species is on the left, the LG labelled species on the right. The top panel shows the steady-state FTIR spectrum. The two dots indicate the IR-pump positions for the VIPER experiment. In the left column, the light blue dot is on the most intense ring mode of the ring labelled species. According to the computations of the vibrationally excited UV-Vis spectra (figure 5.35 on page 97) this mode will give the biggest

VIPER effect. The light green dot is not on any band for this isotopologue. The IR-pump pulse has a spectral width of approximately 20 $cm^{-1}$. In the VIPER spectra of the ring labelled species a positive feature belonging to free SCN can be seen in the light blue curve at approximately 2060 $cm^{-1}$. The bleach would be expected at around 2160 $cm^{-1}$ for the bound SCN and there is a small negative feature at 2159 $cm^{-1}$ which fits. However, another negative feature of approximately the same magnitude at 2119 $cm^{-1}$, where none is expected, can be seen. The VIPER signals are very small and therefore in danger of being confused with baseline fluctuations. The green spectrum for the ring labelled species does not show any spectral features. The 2DIR spectra below are also without spectral features, because of the long delay time. The vibrational lifetime of $p$HP is expected to be much shorter. The TRIR spectra for both IR-pump positions are of course identical and exhibit a positive feature at 2060 $cm^{-1}$ and a negative feature at 2160 $cm^{-1}$. This is in agreement with the behaviour of this isotopologue in figure 5.32 on page 93.

On the right side of the figure the same data is shown for the LG labelled species. The IR-pump positions are again indicated by dots in the FTIR spectra. Now the light blue dot is not on any absorption band, while the light green dot is on top of the most intense ring mode absorption band. In the VIPER spectrum, we see a positive feature at 2012 $cm^{-1}$ and there might be a very small negative feature 2111 $cm^{-1}$. The blue curve is without any significant spectral features. The positive band seems to be broader and the bleach less sharp as for the isotopologue.

However, the VIPER signals are very small and thus a discussion of the shape of the signals is not valid. The 2DIR spectra for both IR-pump positions are completely without spectral features. The TRIR spectra show the positive signal for free SCN at 2012 $cm^{-1}$ and the negative signal for the bound SCN at 2111 $cm^{-1}$. The TRIR signal is smaller than for the other species. This is probably due to fluctuations of the UV-pump OPA output or the alignment.

In the next step a 50:50 mixture of both isotopologues is measured. Figure 5.45 on page 110 shows the normalized UV-Vis absorption spectra of the mixture and of the individual isotopologues. There can be seen no significant difference between the species. As in figure 5.23 on page 84 a small band at around 350 nm from the deprotonated phenol can be seen. This will quickly disappear under irradiation because of the change in pH by the photo reaction.

The UV-pump for the VIPER experiment is at 320 nm.

The VIPER uncaging experiment in a mixture of $p$HP isotopologues is shown in figure 5.46 on page 111. The top panel shows the steady-state spectrum of the isotopologue mixture. The spectra of the individual species are given in dashed lines for orientation. The dots indicate the IR-pump positions. The spectrum of the mixture is a clear superposition of the individual spectra. The high intensity
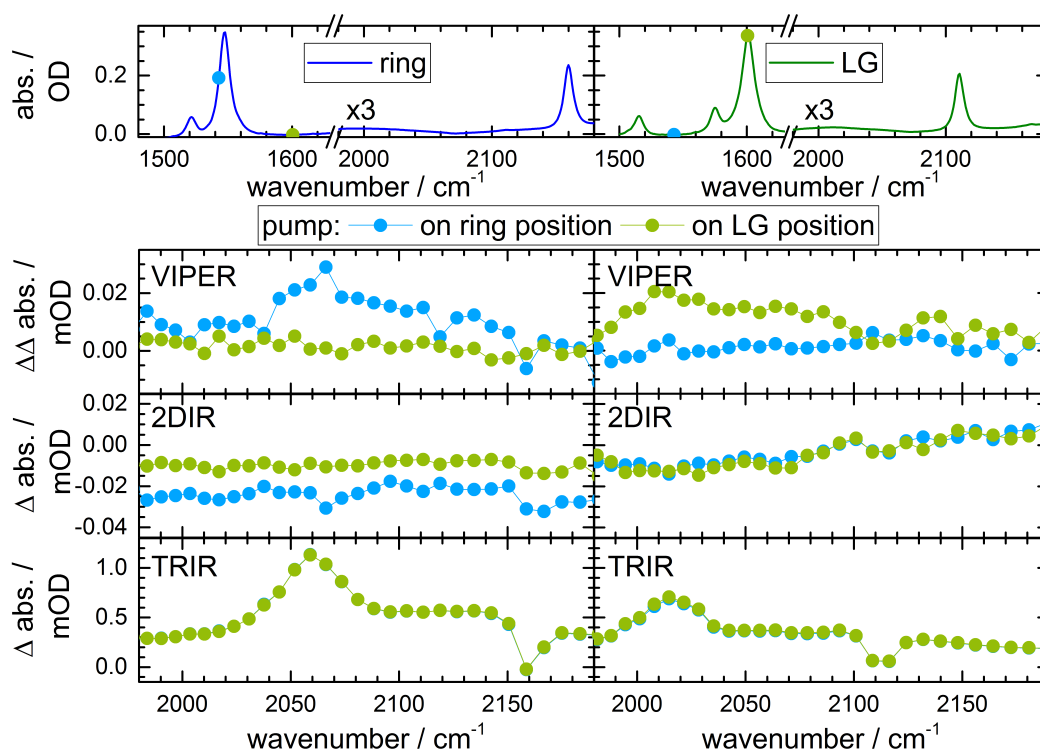
Figure 5.44: Top: FTIR spectra of LG labelled and ring labelled *p*HP SCN in 125:1000 D$_2$O:ACN. Bottom: VIPER, 2DIR and TRIR spectra of isotopologues. UV-delay 100 ps. Delay between pump pulses 1 ps. Coloured dots in top indicate IR-pump pulse positions. UV-pump at 320 nm. LG labelled: VIPER 660, Ring labelled: VIPER 655.

ring mode absorptions of both species are nicely separated.

The middle panel shows the TRIR spectrum of the mixture. It shows four spectral features. Two bleaches at 2111 $cm^{-1}$ and 2160 $cm^{-1}$ for the bound SCN with and without $^{13}C$ atom and two positive features at 2012 $cm^{-1}$ and 2060 $cm^{-1}$ for the free SCN$^-$ with and without $^{13}C$ atom. This is again a superposition of the individual TRIR spectra (compare to figure 5.44).

The bottom panel shows the VIPER spectra for the two IR-pump positions. The green curve belongs to the IR-pump on the LG labelled species. It shows a bleach at 2111 $cm^{-1}$ and a positive feature at 2012 $cm^{-1}$. These spectral features are in agreement with the VIPER and TRIR data for the LG labelled species when measured on its own. The blue spectrum shows the positive feature at 2060 $cm^{-1}$ and a bleach at 2160 $cm^{-1}$. This agrees with the spectra for the individually measured ring labelled species. The contrast between the isotopomers is quite nice, if only the VIPER spectra are compared. Even though the signals are very small
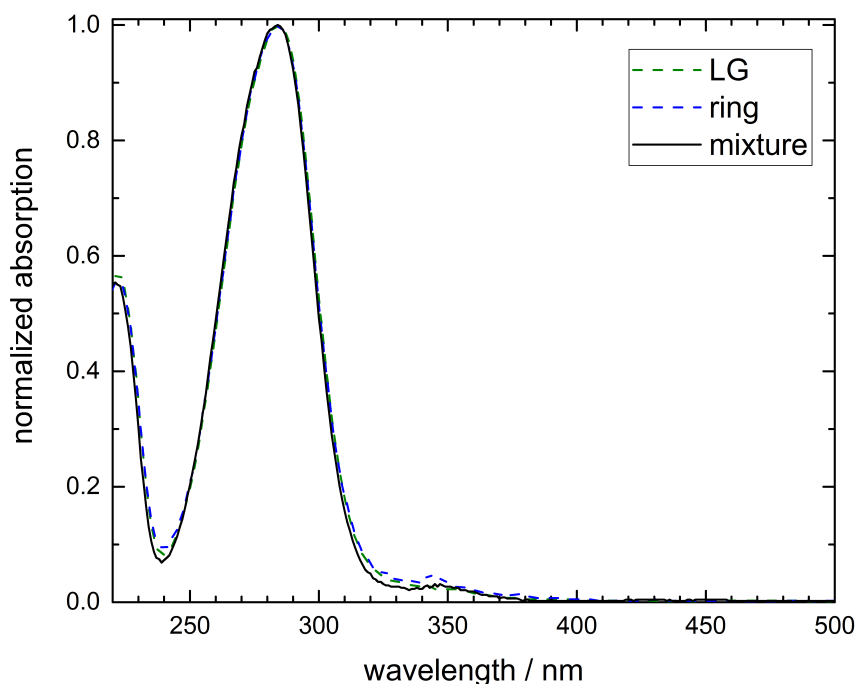
Figure 5.45:  Normalized UV-Vis absorption spectra of LG labelled and ring labelled *p*HP SCN and a 50:50 mixture of both in 125:1000 D$_2$O:ACN.

the spectral features can be seen very clearly. There is no significant contribution of the ring labelled species to the LG spectrum or the other way around. The photo cleavage of the two different LGs (SCN and S$^{13}C$N) can be monitored selectively. This is a important success on the way to species selective VIPER uncaging.

The contrast of the selective uncaging versus the unspecific background is unfortunately quite poor. The TRIR signal which is the unspecific background is upto a factor 30 bigger than the VIPER signal (compare the signal sizes in the TRIR and VIPER data). In this measurement round this was, however, not the main focus. Compared to the data shown on DEACM-N$_3$ we could now directly observe the LG instead of monitoring a vibration related to the electronic excitation of the cage. Also, the delay between the pump and the probe was much longer and therefore the VIPER signal was not measured during the lifetime of the vibrational excitation.
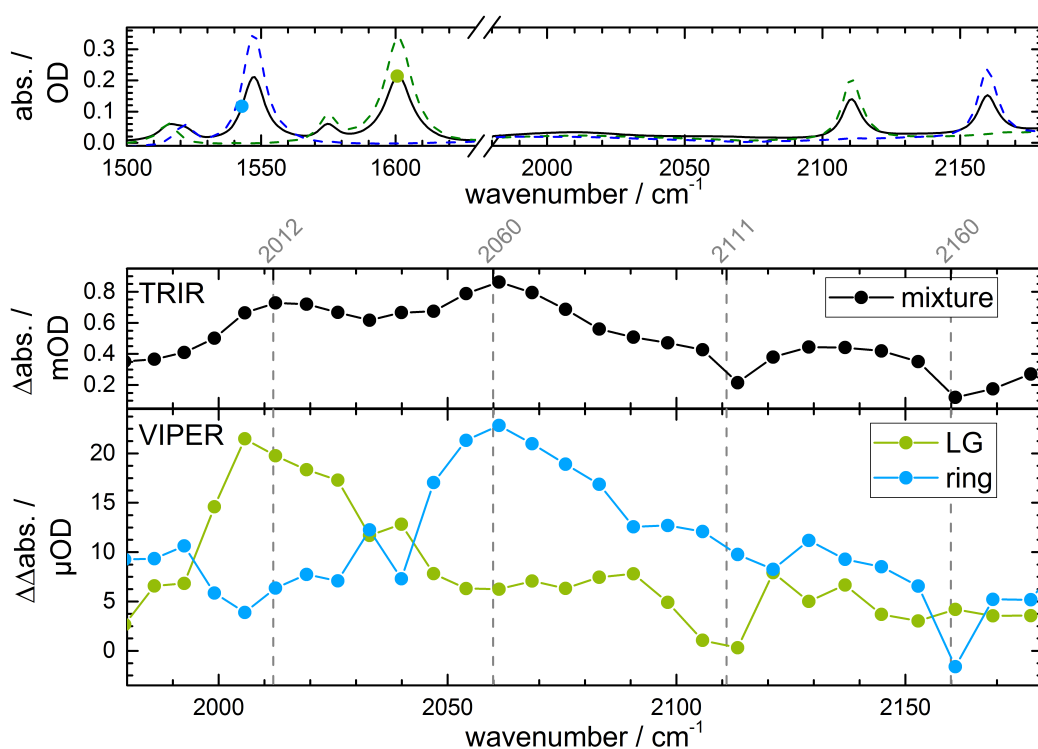
Figure 5.46: Top: FTIR spectra of LG labelled and ring labelled *p*HP SCN and a 50:50 mixture of both in 125:1000 D$_2$O:ACN. Middle: TRIR spectrum of the mixture at delay of 100 ps. Bottom: VIPER spectra of the mixture at a delay of 100 ps. Delay between pump pulses was 1 ps. The UV-pump wavelength was 320 nm and the UV energy was approximately 2 $\mu$J. VIPER 674.

## 5.3 NOPA Output and DFG

During the experiments on DEACM and *p*HP and the study of Coumarin 6 (part of Carsten Neumann's PhD thesis [123]) it became apparent, that the IR-pump energy is the major limiting factor. Therefore, alternative IR-pump sources were discussed. The IR-pump needs to be spectrally narrow and intense. At the moment 1.6 mJ of 800 nm fundamental are sent into an OPA, where a DFG between signal and idler results in 12 $\mu$J (depending on the wavenumber region) of mid-IR. The mid-IR is led to the sample and passes a FP to generate a narrowband pulse. After the FP the IR-pump energy is below 200 nJ and can no longer be measured with our powermeter.

There are different approaches too narrowband, high energy IR light. One would be to start with a ps-fundamental and generate a ps IR-pump from it [99]. The

pulses should, however, not become to long, since they need to match the vibrational lifetime. Such a ps-laser system has a number of disadvantages. One is that the OPA design has to be adjusted, since the current design needs short pulses for the white light generation. Furthermore, such a setup could no longer be used for broadband fs-laser detection, since the probe pulses would also be spectrally narrow and in the ps-range.

A different approach for generating the mid-IR with the current fs-laser system would not have this drawbacks. As has been mentioned in section 2.5 on page 27 a chirped fundamental could be mixed with a chirped NOPA output to result in narrowband mid-IR pulses.

For this project a collaboration with Prof. Riedles group in Munich was started. A sketch of the proposed setup is shown in figure 5.47.
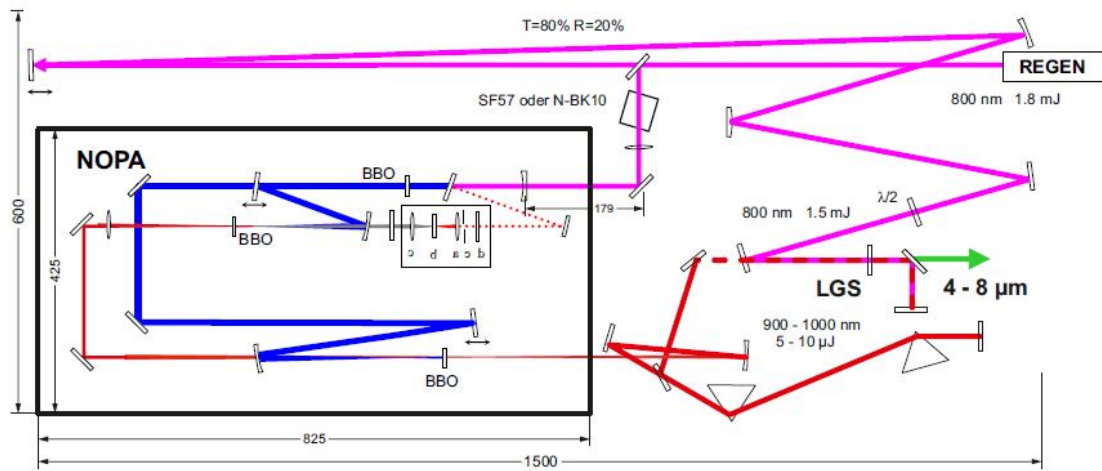


Figure 5.47: Sketch of the proposed setup for an alternative narrowband IR-pump source (as provided by Prof. Riedle and co-workers). The fundamental is given in magenta, the doubled fundamental in blue, the NOPA output in red and the mid-IR in green.

Starting with 1.8 mJ of chirped 800 nm light from the amplifier, the chirp being generated by translating the compressor stage, the beam is split by an 20:80 beam splitter. Approximately 300 $\mu$J are used as NOPA input. In front of the NOPA a glass block is passed by the beam multiple times to compensate the chirp as the beam cannot successfully be used as NOPA input otherwise. The now un-chirped pulse is sent into the NOPA and 5-10 $\mu$J of 900-1000 nm idler is generated. A NOPA was chosen because of its output wavelength range and since the design has already been established by the Riedle group. In theory, an OPA pumped at 400 nm could also be used to generate an idler in the appropriate wavelength range [161].

The NOPA output is sent through a prism compressor and thereby chirped again to match the chirped fundamental in the way shown in figure 2.15 on page 29. The fundamental needs to travel the same path length and to be turned by a $\lambda/2$ wave plate to make the DFG possible. The DFG is planned in a LiGaSe$_2$ (LGS) crystal. A dichroic mirror is needed to separate the fundamental and the NOPA output from the mid-IR. The expected range for the IR is between 4 and 8 $\mu$m.

The mid-IR energy is predicted to be up to 40 $\mu$J with a spectral width of 40 $cm^{-1}$. The energy per wavenumber would than be 1 $\mu$J/ $cm^{-1}$ while before it was closer to 0.025 $\mu$J/ $cm^{-1}$ with very similar input energies.

So far the NOPA has been installed in a test setup to demonstrate the principle, albeit not yet with the LGS crystal required for the target wavelength. The prism compressor and the path for the fundamental have been aligned and the temporal and spatial overlap between the NOPA output and the fundamental have been found. The LGS crystal was at this point not yet available and a LiInS$_2$ (LIS) crystal was used instead. Mixing between the 800 nm and the 940 nm NOPA output resulted in a small amount of IR-light at 1900 $cm^{-1}$. The installation and optimization was carried out together with Emanuel Wittmann, a PhD student in Prof. Riedle's group and one of his masterstudents. On a second visit the prism compressor was optimized with an autocorrelator to match the chirp of the fundamental. Also another crystal, LiNbO$_3$, was tried. A spectrum of the IR pulses genereated in this fashion is shown in figure 5.48 on the next page.

Since the dichroic mirror is not yet available a calcium fluoride prism was used to separate the mid IR beam from the generating beams. While the prism allows to block the fundamental and NOPA output and to characterize the mid-IR independently, it also distorts the beam and absorbs part of the energy. The maximum energy that could be measured so far was 2 $\mu$J.

The next steps towards a functional new IR-pump source are to establish the mixing with the right crystal and to include a suitable dichroic mirror to isolate the mid-IR without the problems of a prism. The wavenumber region that we reached with the LiNbO$_3$ might already be interesting for spectroscopic applications with azide or thiocyanate as a protein vibrational label [162]. For IR-excitation in the ring mode region the wavenumbers need to become lower. Also, the mid-IR energy needs to be higher. This is probably also limited by the chosen crystal and by the not yet fully optimized chirp.

Also the chirps should be further optimized to make the IR-pulse more narrow. If the IR-pump generation works as planed, the NOPA and subsequent DFG need to be moved to the setup were VIPER measurements are carried out. The amplifier there needs to produce chirped pulses, which will be compensated by glass blocks in front of the VIS-pump OPA and the IR-probe OPA. How well the OPAs perform with the glass blocks in front of them remains to be tested.
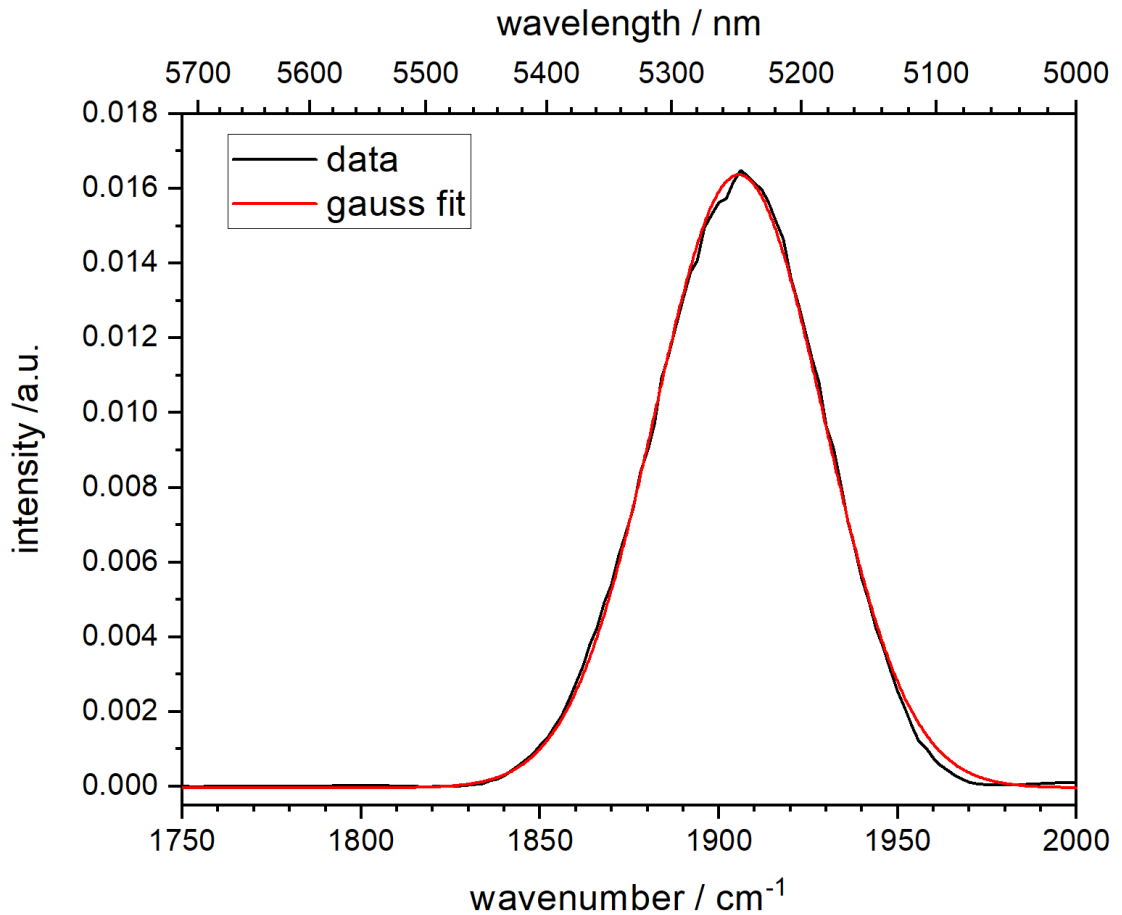
Figure 5.48: Spectrum of the mid-IR generated in LiNbO$_3$ in black with a Gaussian fitted to the data in red (central wavenumber: 1905.6 $cm^{-1}$ $\pm$ 0.1 $cm^{-1}$, width: 55.8 $cm^{-1}$ $\pm$ 0.2 $cm^{-1}$, R$^2$: 0.99908). The position of the prism in the prims compressor after the NOPA has been optimized with an autocorrelator by Emanuel Wittmann and the fundamental chirprhas been optimized by adjusting the amplifier compression on the IR output.

# 6 Conclusion and Outlook

An investigation and discussion of the concept and requirements to apply the VIPER pulse sequence to an selective uncaging scheme has been carried out. A number of possible PPGs has been compared and DEACM and *p*HP were chosen. The applicability of the two different photocages to the experimental scheme of VIPER uncaging could be shown. With *p*HP a VIPER signal from a different class of molecules was measured. So far VIPER experiments had only been carried out with coumarin and rhodamine molecules. After the successful selective monitoring of the electronic excitation with VIPER on DEACM isotopomers, we could directly monitor the released LG at long delay times with *p*HP. A mixture of *p*HP isotopologues was irradiated with the VIPER pulse sequence and isotope selective photochemistry in solution was observed.

This is an important step towards VIPER uncaging as a selective uncaging strategy. For applications in biologically or synthetically relevant context, the contrast to the unspecific background needs to be improved.

For both cages the VIPER signals were quite small and variation of experimental parameters was difficult. It seems that there are influences on the VIPER signal size, which are not yet controlled experimentally. Improvements in the measurement routine for VIPER spectra were implemented between the measurements of the cages, but the uncontrolled and unexplained fluctuation in the *p*HP VIPER signal size is still significant.

In particular for *p*HP the VIPER signal would be expected to be larger. The computations by Jan von Cosel [116, 117] show the VIPER effect to be similar for both *p*HP and DEACM. But the variation of the experimental parameters for *p*HP did not increase the signal to the hoped for signal size. Such a parameter variation was not carried out for DEACM. Maybe the signal size and the contrast can be improved for this cage, if for example the Vis-wavelength is varied.

However, the major limiting factor at the moment for VIPER uncaging of both cages is the IR-pump energy. As we found in our study on Coumarin 6 (part of Carsten Neumann's PhD thesis [123]) the VIPER signal increases linearly with the IR-pump power. This would improve the contrast to the unspecific background excitation. Also, a bigger signal makes optimization more feasible, which would then probably lead to additional improvements.

The first steps towards an alternative IR-pump sources have been undertaken. A NOPA and subsequent DFG between its idler and the fundamental have been

installed. The general principle has been demonstrated, however, since the used crystal is not yet the optimal choice, the energy and the wavenumber range of the mid-IR output are still below the expectations that the energy per wavenumber should be increased by a factor 40.

Another idea is to implement higher order VIPER experiments. The UV-Vis-pump pulse could be changed for two photon excitation, which would change the selection rules because of the different Franck-Condon factors for different transitions. Also, ladder climbing or overtone excitation with Near-IR could be used before the UV-Vis-pump. This should lead to a larger shift of the visible spectrum. Thereby, the selectivity might be increased.

In this thesis the aim was to monitor the selective photochemistry with fs-laser spectroscopy. As has been pointed out this imposes some limitations. Alternative detections methods for the LG are possible and might allow for irradiation conditions with better selectivity. If no VIPER signal needs to be detected by the relative insensitive approach of fs IR-probing, the UV-Vis energy can be decreased dramatically which leads to less unspecific excitation. In such an experimental scheme the irradiation of the mixture would be carried out in the laser setup without measuring the probe spectra and the irradiated sample would be analysed afterwards. Possibilities for this analysis are NMR-spectroscopy, chromatography, mass spectroscopy, even activity essays or fluorescence, which is most sensitive. A setup constructed specific for VIPER uncaging or VIPER photochemistry in general would not need the fs-time resolution and broad probe pulses. It could, therefore, be constructed with a ps-laser system with more narrowband high-energy IR-pump and the ratio between IR-pump and UV-Vis-pump could be optimized for the best contrast. High contrast is only needed if the selectivity of the photoreaction is in the focus, for spectroscopic applications the unspecific background is no problem at all, since it can be subtracted.

The expansion to more complicated and biologically interesting LGs is also a further step for the uncaging scheme, together with selecting between an increasing the number of species in a mixture. In this thesis only two species were mixed and excited selectively, but a larger number of isotopologues or isotopomers with various LG is possible.

Both DEACM and *p*HP are probably valid VIPER cages, if more IR-pump energy is available. For DEACM also the optimization of the experimental parameters is promising.

As an alternative PPG the second generation BODIPYs [140] are very promising. The spectra look very agreeable with a $S_{10}$ of 25 nm (870 $cm^{-1}$) and the higher quantum yields, improve significantly on the first generation BODIPY.

A tedious trial-and-error process was necessary to look for suitable experimental excitation conditions. This process was, as has been mentioned above, also plagued

by unexplained fluctuations in the signal sizes. Here a IR-pump Vis-probe setup will be helpful. It allows to study the UV-Vis spectrum of the vibrationally excited PPG and thereby to chose the experimental parameters leading to the largest modulation. This will also help with the selection of new VIPER cages.

# Deutsche Zusammenfassung

Um ein besseres Verständnis für die komplexen Vorgänge in biologischen Systemen erlangen zu können, ist die gleichzeitige Kontrolle über mehrere parallel ablaufende Prozesse entscheidend. Zu diesem Zweck wurde selektives Uncaging entwickelt. Bei einem Uncaging Experiment wird ein Molekül synthetisch inaktiviert und durch die Bestrahlung mit Licht wieder aktiviert. Üblicherweise wird eine chemische Bindung gebrochen und eine Abgangsgruppe frei gesetzt. Das Molekül, welches auf Licht reagiert und die Abgangsgruppe freisetzt, wird Cage genannt. Bei selektivem Uncaging werden mehrere Moleküle durch verschiedene Cages inaktiviert und können unabhängig voneinander, normalerweise durch Licht verschiedener Wellenlänge, freigesetzt werden. Es gibt jedoch ernstzunehmende Einschränkungen in der Umsetzung dieser Idee. Eine große Herausforderung ist die spektrale Breite der UV-Vis Absorptionen der Cages. Üblicherweise sind die Absorptionsbanden breit im Vergleich zum Wellenlängenbereich des genutzten Lichtes. Dies macht eine selektive Aktivierung durch Beleuchtung schwierig. Die Banden sind so breit, dass sie außer in wenigen Ausnahmen, überlappen und durch die Beleuchtung fast immer mehrere simultan angeregt werden. Dies limitieren auch die Anzahl der unabhängigen Cages stark.

Deshalb ist es das Ziel dieser Dokotorarbeit die **Vi**brationally **P**romoted **E**lectronic **R**esonance (VIPER) 2D-IR Pulssequenz als eine Alternative für selektives Uncaging einzuführen.
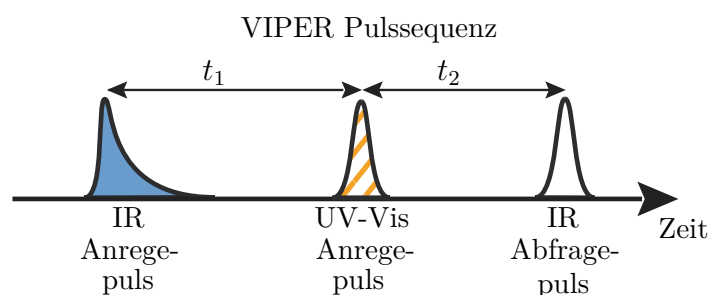


Zeitlicher Ablauf der VIPER Pulssequenz: Schmalbandinger infraroter Anregepuls in blau, nicht resonanter UV-Vis Anregepuls (orange gestreift), breitbandiger infraroter Abfragepuls in weiß. $t_1$ ist die Zeit zwischen IR Anregepuls und UV-Vis Anregepuls. $t_2$ ist die Zeit zwischen den Anregepulsen und dem Abfragepuls.

Die VIPER 2D-IR Pulsequenz ist ein spektroskopisches Werkzeug, welches erlaubt 2D-IR Signale zu erzeugen, deren Lebensdauer unabhängig von der Schwingungslebensdauer ist. Sie wurde als erstes eingesetzt, um chemischen Austausch zu untersuchen. Die Pulsesequenz besteht aus einem schmalbandigen infraroten Anregepuls, einem darauffolgenden UV-Vis Anregepuls und einem breitbandigen infraroten Abfragepuls. Der UV-Vis Anregepuls ist nicht resonant mit der UV-Vis Absorptionsbande. Die elektronische Anregung wird nur möglich, wenn der infrarote Anregepuls den UV-Vis Übergang der schwingungsangeregten Moleküle moduliert. Diese Modulation bringt den UV-Vis Übergang in Resonanz mit dem UV-Vis Anregepuls. Auf diese Weise können nur die Moleküle, die mit dem infraroten Anregepulse vorangeregt wurden, elektronisch angeregt werden. Eine Vorhersage der Modulation wurde von Jan von Cosel aus der Computerchemie Arbeitsgruppe von Irene Burghardt in Frankfurt durchgeführt.

Der schmalbandige infrarote Anregepuls kann verwendet werden, um selektiv ein Subensemble von Molekülen (z.B. eine Sorte Cages aus einer Mischung von verschiedenen Cages) in einen elektronisch angeregten Zustand zu bringen. Dies gelingt sogar wenn die UV-Vis Spektren aller Moleküle identisch sind. Allerdings muss das Subensemble dafür aus Molekülen mit jeweils eindeutig zu unterscheidenden Infrarotspektren bestehen. In Kombination mit der gezielten Einführung von Isotopmarkierungen, die zu Veränderungen im Infrarotspektrum führen, kann die größere Selektivität des Infrarotbereichs für die Entwicklung eines alternativen selektiven Uncagingansatzes verwendet werden. In diesem sogenannten VIPER Uncaging selektiert der infrarote Anregepuls die Spezies und der darauffolgende UV-Vis Anregepuls liefert die Energie für die elektronische Anregung, die die Grundlage für eine Photoreaktion ist.

Das Ziel dieser Doktorarbeit ist es das Konzept von VIPER Uncaging, wie es eben eingeführt wurde, zu etablieren und erste Proof-of-Concept Experimente durchzuführen. Die Beschränkungen und Anforderungen sowie einige Beispiele für mögliche VIPER Cages werden diskutiert.

Ein Coumarinmolekül (7-Diethylaminocoumarin), welches eine Azidgruppe freisetzen kann, wurde als erstes Testmolekül für VIPER Uncaging ausgewählt. Ausgewählte Isotopomere wurden charakterisiert, um geeignete spektroskopische Marker für die erfolgreiche Freisetzung der Abgangsgruppen zu bestimmen. Außerdem wurden geeignete experimentelle Bedingungen, wie etwa eine geeignete UV-Vis Wellenlänge oder ein passendes Abfragefenster, gesucht. Der ausgewählte Coumarin Cage hat seine UV-Vis Absorptionsbande bei ungefähr 380 nm und das Spektrum hat eine steile Flanke. Die Quantenausbeute für die Azidabgangsgruppe ist zwischen 10 und 20 % und abhängig vom Wasseranteil im Lösungsmittel. Die Freisetzung findet auf der Picosekundenzeitskala statt und gehört damit zu den schnellsten bekannten Uncagingreaktionen. Allerdings zeigte sich, dass der Mechanismus
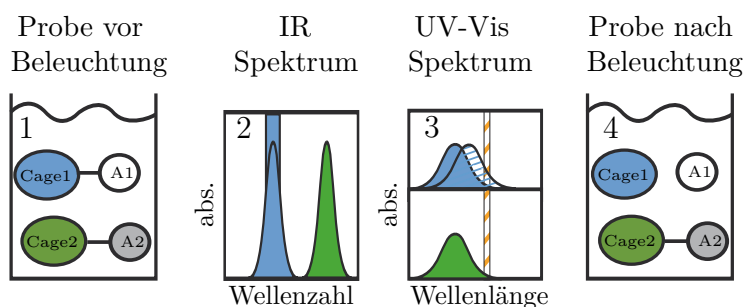
Skizze zum VIPER Uncaging Konzept. 1: Probe vor Beleuchtung mit zwei verschiedenen Cages (blau und grün) mit unterschiedlichen Abgangsgruppen A1 und A2. 2: Skizze des IR Spektrums, die blaue Bande gehört zum blauen Cage, die grüne zum grünen. Der blaue Balken zeigt die spektrale Position des IR Anregepulses an. 3: Modulation des UV-Vis Spektrums. Für den blauen Cage verändert sich das Spektrum (blau gestreift). Die gestreifte orangene Bande zeigt die spektrale Position des UV-Vis Anregepulses an. 4: Probe nach der Beleuchtung. Die Bindung zwischen Cage 1 und A1 ist gebrochen. Die Bindung zwischen Cage 2 und A2 ist unberührt.
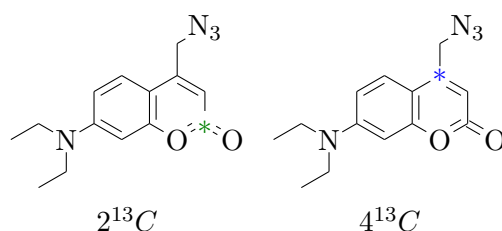


Molekülstrukturen der beiden Coumarincage Isotopomere.

der Photoreaktion nicht einfach zu Durchschauen ist. Für das VIPER Uncaging Experiment in einer Mischung wurden zwei Isotopomere mit jeweils einem $^{13}C$ Atom an verschiedenen Positionen ausgewählt. In einer der beiden Spezies ist die Infrarotabsorption der Ringmode des Coumarins durch das $^{13}C$ Atom verändert ($4^{13}C$ genannt). Im anderen Isotopomer wird die Carbonylstreckschwindung beeinflusst ($2^{13}C$ genannt). Die Veränderung im Ringmodenbereich erlaubt die Selektion einer Spezies mit der infraroten Voranregung. Aufgrund von experimentellen Schwierigkeiten konnten nur Isotopomere mit der gleichen Abgangsgruppe verwendet werden. Die erfolgreiche selektive elektronische Anregung der einzelnen Isotopomere in der Mischung konnte durch die Abfrage in der Carbonylregion verfolgt werden.

Als zweiter VIPER Cage wurde *para*-hydroxyphenacyl (*p*HP) ausgewählt. Die Abgangsgruppe ist eine Thiocyanatgruppe. *p*HP Cages haben ihre Absorption im
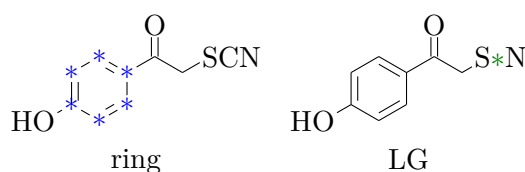
Molekülstrukturen der beiden *p*HP Thiocyanatisotopologe.
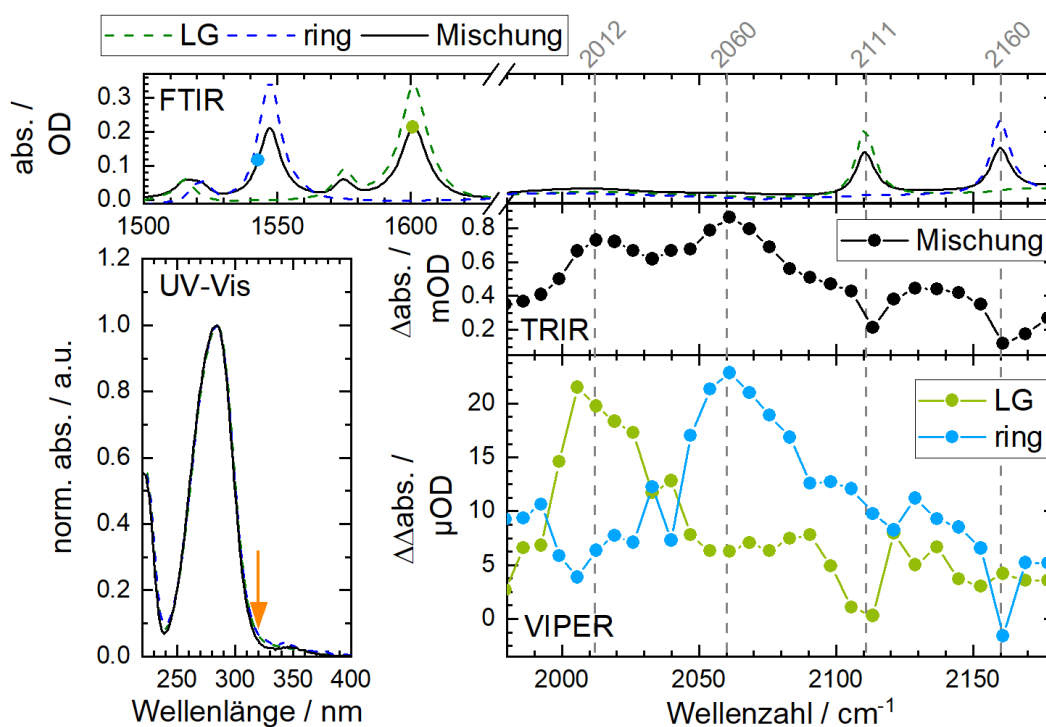


Spektren der *p*HP Mischung im VIPER Experiment. UV-Vis zeigt die UV-Vis Absorptionsspektren der Isotopologe und der 50:50 Mischung. In FTIR sind die entsprechenden infrarot Absorptionsspektren zu sehen. TRIR zeigt die transienten UV-Anrege IR-Abfragespektren der Mischung. Man sieht eine Überlagerung der spektralen Marker der Photoreaktionen für beide Isotopologe. Die Wellenlänge des UV-Anregelichtes ist als orangener Pfeil im UV-Vis Spektrum eingezeichnet. Die beiden VIPER Spektren zeigen die individuellen Marker der Photoreaktionen der einzelnen Isotopologe, obwohl wieder in der Mischung gemessen wurde. Die Wellenzahlen der IR-Anregepulse sind als Punkte im FTIR Spektrum eingezeichnet.

UV-Bereich mit einer maximalen Absorption bei 290 nm. Die Form des Spektrums ist geeignet und die Quantenausbeute ist sehr hoch. In der Literatur sind Werte

bis zu 90 % zu finden. Zusätzlich ist die Photoreaktion gut untersucht und die zu erwartenden Nebenprodukte sind bekannt. Die ausgewählten $p$HP Isotopologe wurden charakterisiert. Die dabei entstanden Daten über die Photoreaktion stimmen gut mit dem in der Literatur angenommenen Mechanismus überein. Die Mischung für das VIPER Experiment besteht aus zwei Isotopologen. Für eine Spezies sind alle Kohlenstoffatome im Ring durch $^{13}C$ Atome ersetzt (Die Spezies wird im folgenden ring genannt). Für die andere ist die Thiocyanatabgangsgruppe (hier als LG bezeichnet) isotopenmarkiert. In diesem Fall konnte die Freisetzung der unterschiedlichen Abgangsgruppen, markiert und nicht markiert, selektiv beobachtet werden. Das zeigt, dass es möglich ist, selektiv ein Molekül in einer Mischung aus gecagedten Molekülen freizusetzen indem die VIPER Pulssequenz eingesetzt wird.

Die Proben wurden von Matiss Reinfelds aus der organischen Chemie Arbeitsgruppe von Alexander Heckel synthetisiert und die VIPER Experimente wurden gemeinsam mit Carsten Neumann und Unterstützung durch die Bredenbeck Arbeitsgruppe durchgeführt.

Die in der Arbeit gezeigten Experimente sind ein wichtiger Schritt zum Erlangen der Kontrolle über Photoreaktionen in Mischungen. Der Fokus dieser Arbeit war auf Uncaging Photoreaktionen von Isotopomeren und Isotopologen gelegt, aber prinzipiell können auch andere Photoreaktionen auf diese Weise gesteuert werden. Damit sollte es möglich sein zu entscheiden welches Isomer in einer Mischung reagieren soll oder selektiv verschiedene Grundzustände in einem Protein anzuregen.

Die Abgangsgruppen wurden aufgrund ihrer Infrarotabsorption ausgewählt. Damit konnte der Uncagingerfolg direkt spektroskopisch verfolgt werden. Dies war wichtig, um das Funktionsprinzip von VIPER Uncaging zeigen zu können und um direkt die experimentellen Parameter am Femtosekundenaufbau optimieren zu können.

Betrachtet man die Selektivität des VIPER Uncaging Ansatzes, so ist diese im Moment hauptsächlich durch die Intensität des infraroten Anregepulses beschränkt. Die selektive VIPER Anregung konkurriert mit der unspezifischen elektronischen Anregung direkt durch den UV-Vis Anregepuls. Ein intensiverer infraroter Anregepuls würde nur die selektive VIPER Anregung verstärken und damit den Kontrast zum Hintergrund durch unspezifische Anregung verbessern.

Zur Umsetzung dieses Ansatzes, wurden die ersten Schritte zu einer alternativen Infrarotlichterzeugung unternommen. In diesem alternativen Ansatz wird das Infrarotlicht direkt durch eine Differenzfrequenzgeneration zwischen dem Laseroutput, d.h. der intensiven 800 nm Fundamentalen, und dem Output eines nichtlinearen optischen parametrischen Verstärkers (NOPA) erzeugt. Damit das Infrarotlicht schmalbandig ist, werden die Pulse vor dem Mischen gechirped. Der NOPA ist aufgebaut und das Mischen wurde in einem vorläufigen Kristallmedium getestet.

Andere Möglichkeiten, um den Kontrast zum unspezifischen Hintergrund durch die direkte Anregung durch das UV-Vis Licht zu verbessern, werden diskutiert. Für die Anwendung von VIPER Uncaging könnte zum Beispiel auf die Detektion mittels fs-Laserspektroskopie verzichtet werden. Stattdessen könnten andere Detektionsmethoden, wie zum Beispiel Chromatographie eingesetzt werden. Dadurch ließen sich die experimentellen Parameter so verändern, dass eine deutlich niedrigerer unspezifische Anregung erreicht werden kann.

# A Cage Overview

## A.1 Nitroaryl Cages

**1.1 *o*-nitrobenzyl (*o*NB) alcohol [163]**
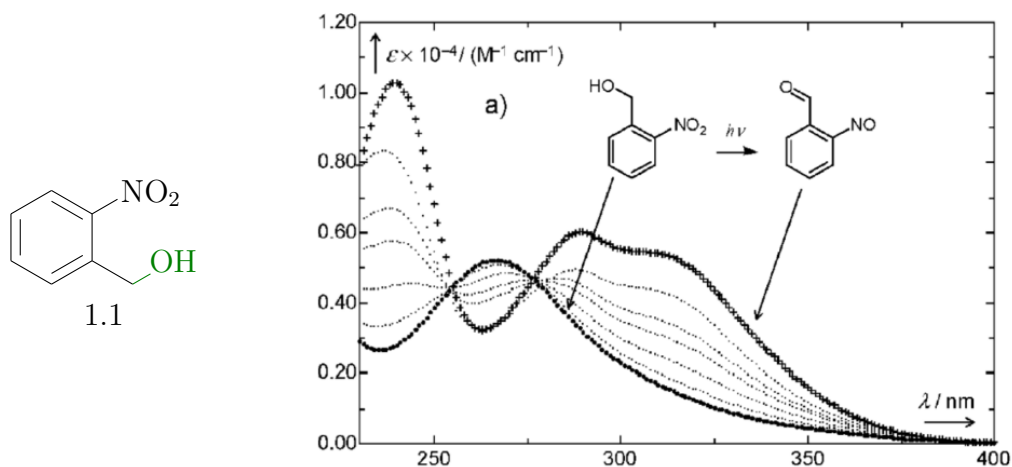


**Φ:** $0.52 \pm 0.05$

**Comments:** $7.0 \times 10^{-5}$ M in 1 mM aqueous HCl, irradiated at 365 nm. Adapted from [163] with permission from the European Society for Photobiology, the European Photochemistry Association, and The Royal Society of Chemistry. Additional spectroscopic data can be found in [164], [165] and on nitrobenzyl chelators in [166].

### 1.2 *o*-Nitrobenzyl methyl ether [167]
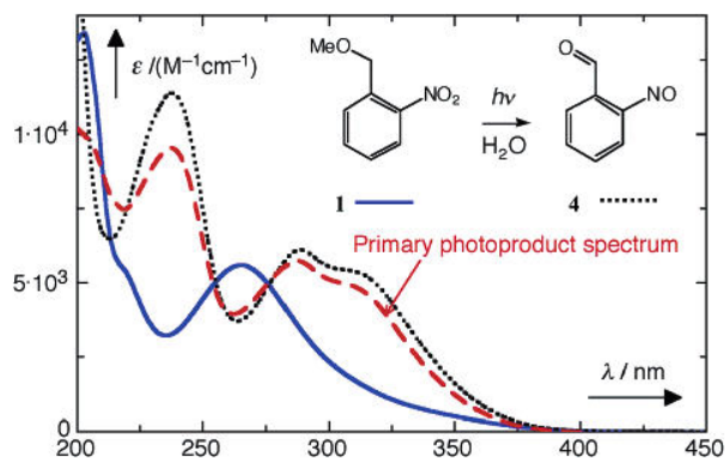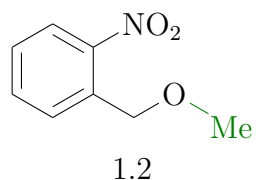


**Φ:** $0.49 \pm 0.05$

**Comments:** Measured in 1 x $10^{-3}$ M aqueous $HClO_4$, irradiation at 365 nm. Reprinted with permission from [167]. Copyright 2004 American Chemical Society. Additional spectroscopic data on oNB ethers can be found in [168].

## Substituents at Benzylic Position

### 1.3 1-(2-nitrophenyl)ethyl alcohol [163]
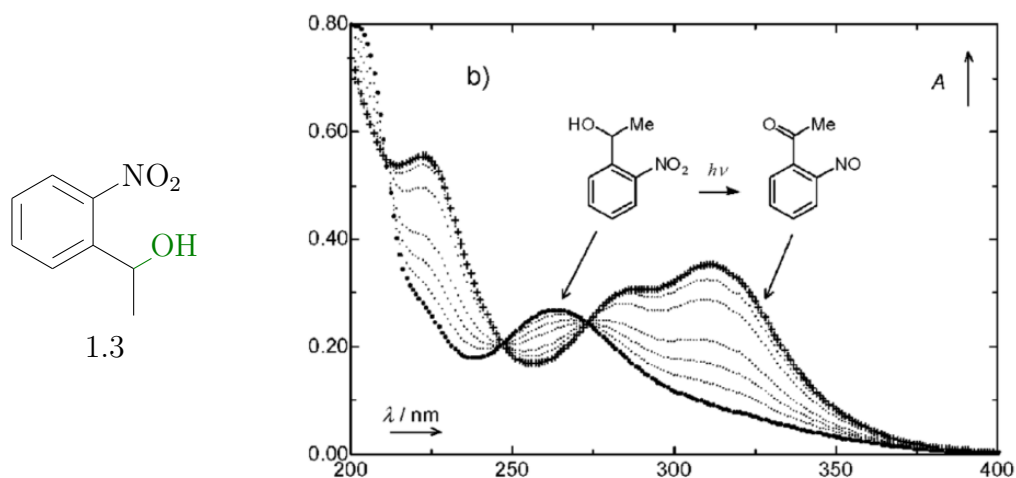


**Φ:** $0.67 \pm 0.10$

**Comments:** $6.4 \times 10^{-5}$ M in 1 mM aqueous HCl, irradiated at 365 nm. Adapted from [163] with permission from the European Society for Photobiology, the European Photochemistry Association, and The Royal Society of Chemistry. Additional spectroscopic data can be found in [169]. Other names: MeNB, 1-NPE, NPPOC alcohol. Spectroscopic data on caged DNA can be found in [17] and on caged acetate in [170].

### 1.4 *O*-[*o*-nitromandelyloxycarbonyl]-2,5-di(*tert*-butyl)hydroquinone (Nmoc-DBHQ) [171]
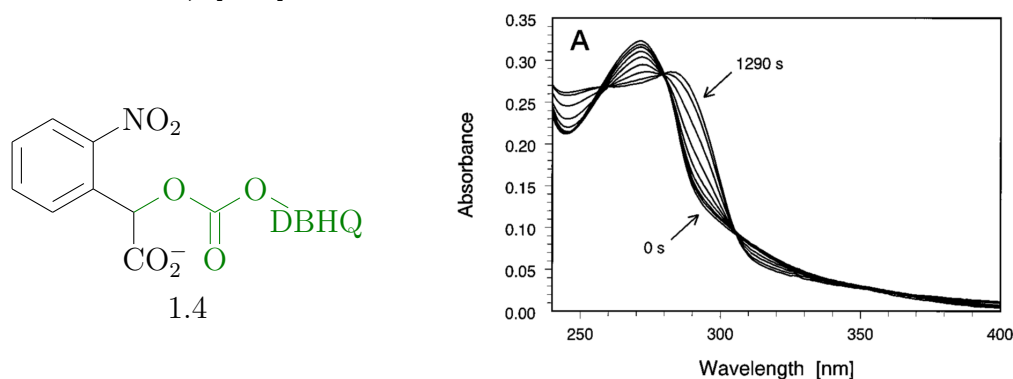


**Φ:** none given

**Comments:** 60 $\mu$M in 150 mM NaCl, 10 mM phosphate buffer, pH 7.2. Reprinted with permission from [171].

## 1.5 Thioxanthone/NPPOC conjugate T7T4-OR [172, 173]



1.5
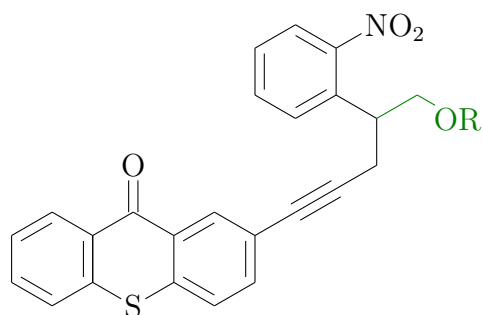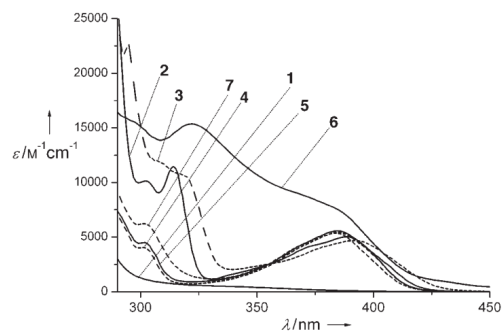
**Φ:** 0.42

**Comments:** Curve labeled **2**. In methanol. Reprinted with permission from [172].

## 1.6 Thioxanthone/NPPOC conjugate T7D4-OR [172, 173]



1.6
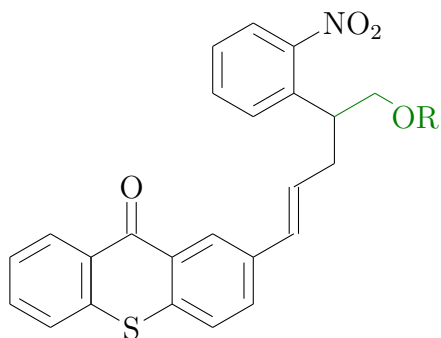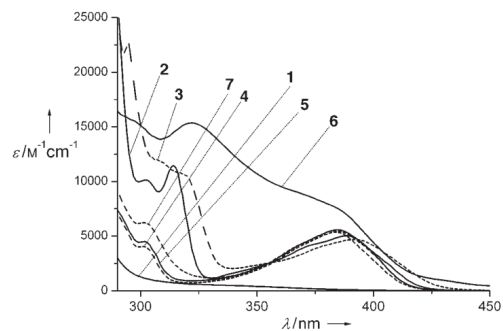
**Φ:** 0.08

**Comments:** Curve labeled **3**. In methanol. Reprinted with permission from [172].

**1.7 Thioxanthone/NPPOC conjugate T7S3-OR [172, 173]**



1.7
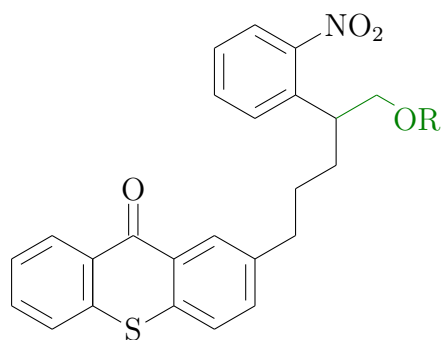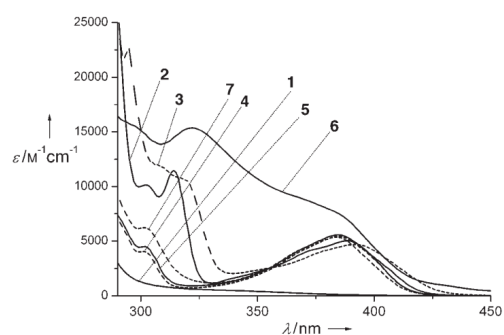
**Φ:** 0.21
**Comments:** Curve labeled **4**. In methanol. Reprinted with permission from [172].

**1.8 Thioxanthone/NPPOC conjugate T7S2-OR [172, 173]**



1.8
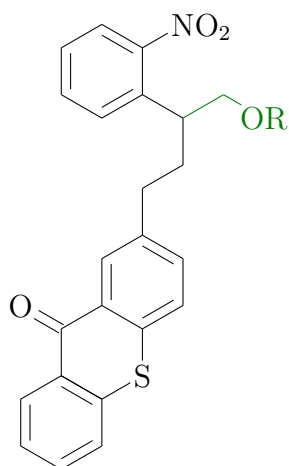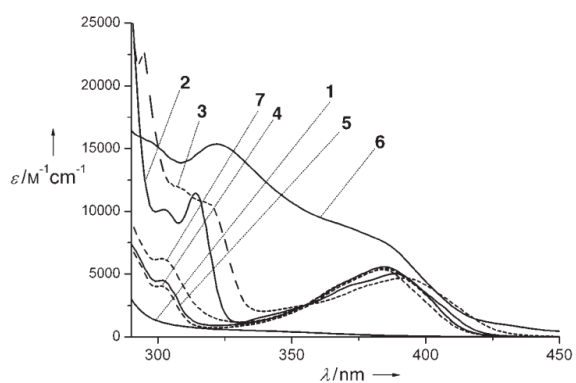
**Φ:** 0.21
**Comments:** Curve labeled **5**. In methanol. Reprinted with permission from [172].

### 1.9 N-(R-Carboxy-2-nitrobenzyl)(CNB) urea [174]
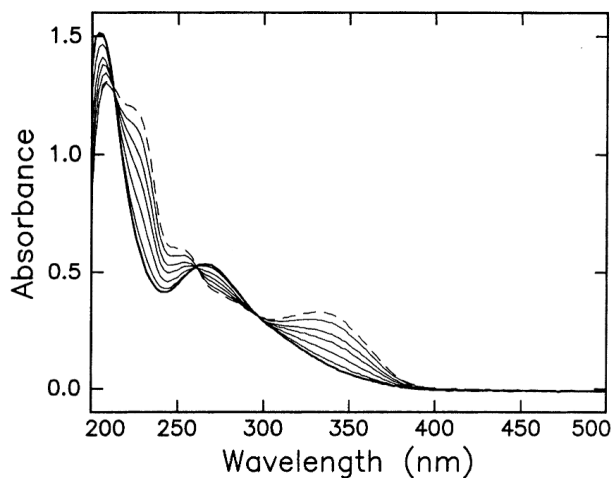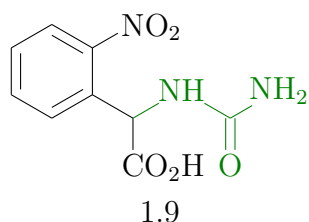


**Φ:** 0.56

**Comments:** 1.0 mM in 100 mM phosphate buffer adjusted to pH 7.5, irradiated with 337 nm in a 2 mm cuvette. Dark line is spectrum without irradiation. Reprinted with permission from [174]. Copyright 2002 American Chemical Society. Other names: Nmoc. Spectroscopic data on caged Glutamate can be found in [175], on caged DBHQ in [171], on caged Fmoc cysteine in [176, 177] and on caged serotonin in [178].

## Substituents on the Aromatic Ring

### 1.10 2-(2-chloro-6-nitrophenyl)ethyl acetate [170]
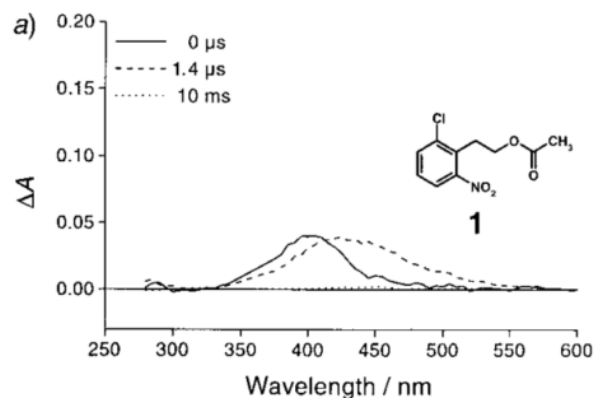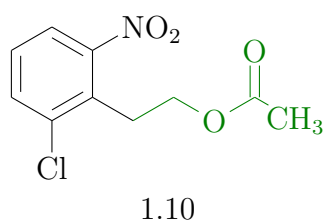


**Φ:** none given

**Comments:** 0.5 mM in MeCH/H$_2$O 1:1 mixture, after laser flash photolysis 355 nm. Reprinted with permission from [170].

**1.11 4,5 dimethoxy-nitrobenzyl (DMNB) alcohol [165]**
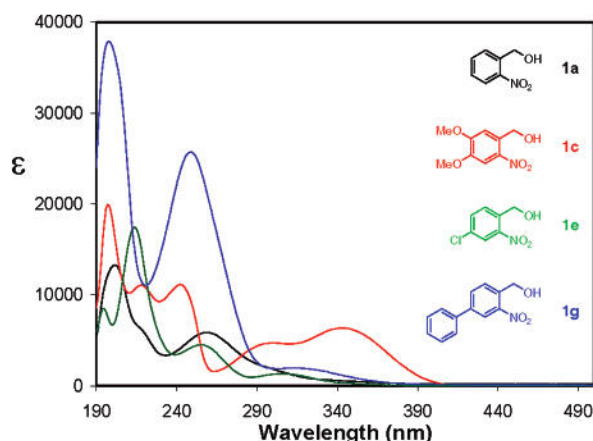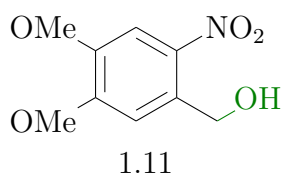


**Φ:** none given

**Comments:** Red curve. Measured in acetonitrile. Reprinted with permission from [165]. Copyright 2007 American Chemical Society. Additional spectroscopic data in [164, 179, 180]. Other names: NV, NVOC. Spectroscopic data for caged silane in [12, 181], for caged carboxylic esters in [182], caged thymin in [183] and DMNB crosslinkers in [184].

**1.12 4,5 dimethoxy-2-nitrobenzyl peptide model [136]**
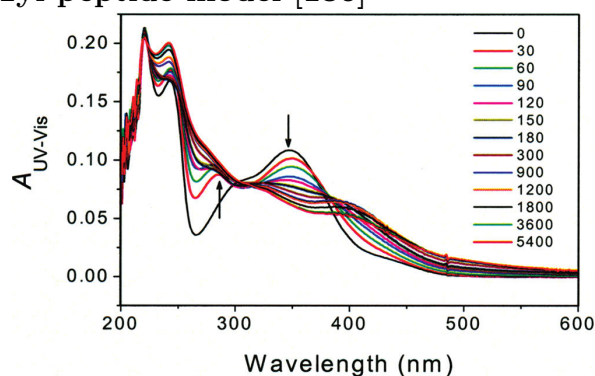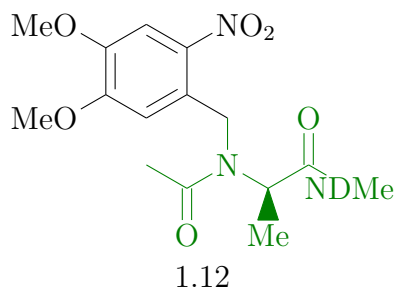


**Φ:** none given

**Comments:** 3 mM, 100 $\mu$m path length in $D_2O$ with 5 % DMSO-$d_6$, 355 nm, in the thesis as 1.a. Adapted with permission from [136]. Copyright 2008. American Chemical Society.

### 1.13 *para* chloride nitrobenzyl alcohol [165]
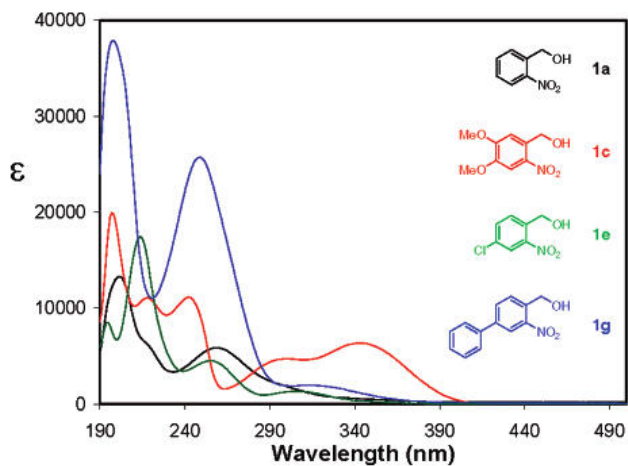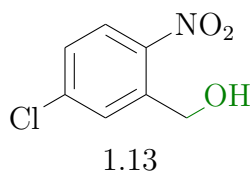


**Φ:** none given
**Comments:** Green curve. Measured in acetonitrile. Reprinted with permission from [165]. Copyright 2007 American Chemical Society.

### 1.14 *o*-nitrophenylpropyl alcohol [165]
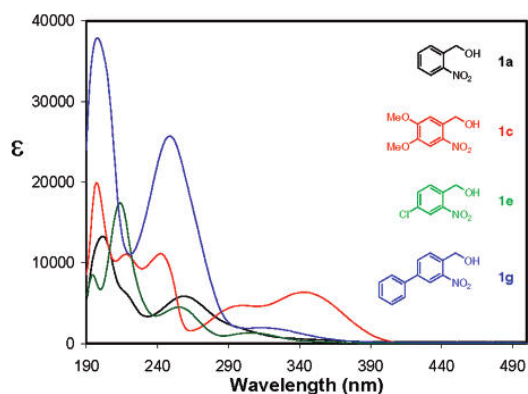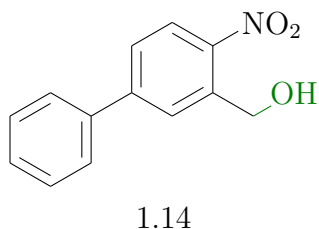


**Φ:** none given
**Comments:** Blue curve. Measured in acetonitrile. Reprinted with permission from [165]. Copyright 2007 American Chemical Society. Additional spectroscopic data in [177].

**1.15 *para*-extended nitrobenzyl [180]**
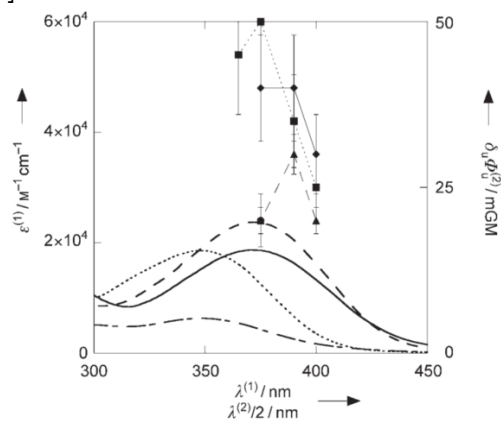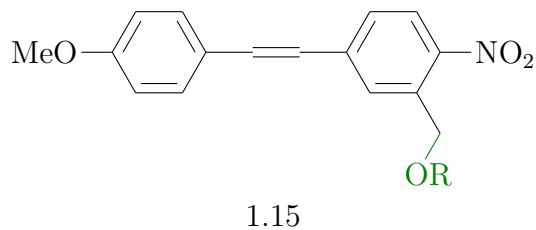


**Φ:** 0.1

**Comments:** Dotted curve measured in acetonitrile. Reprinted with permission [180].

**1.16 *para*-extended nitrobenzyl [180]**
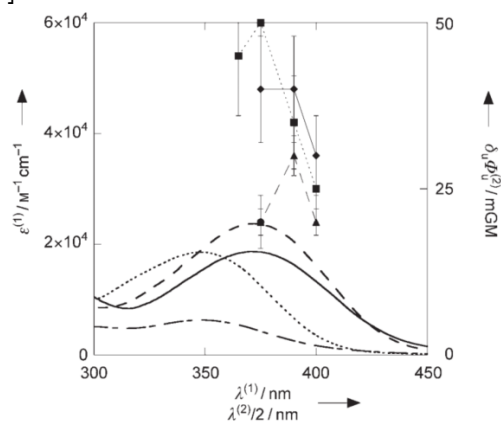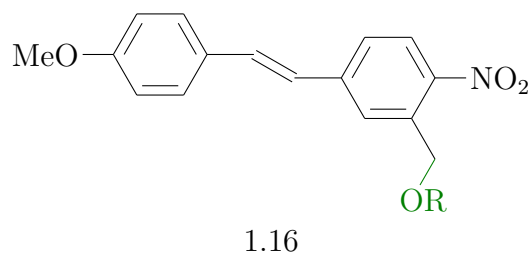


**Φ:** 0.1

**Comments:** Dashed curve measured in acetonitrile. Reprinted with permission [180].

### 1.17 *para*-extended nitrobenzyl [180]
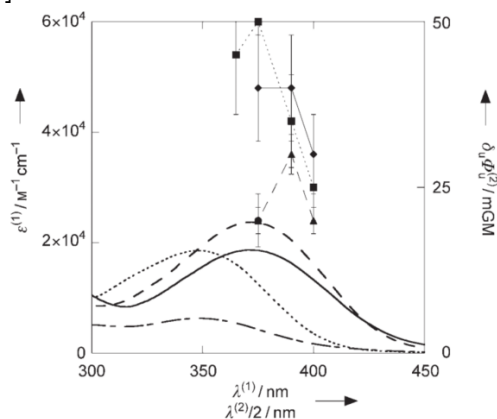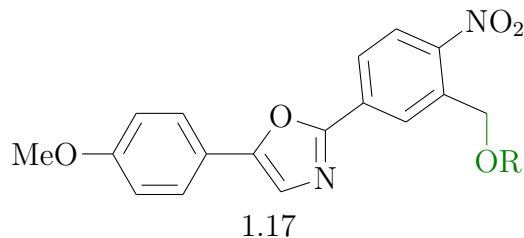


**Φ:** 0.1

**Comments:** Solid curve measured in acetonitrile. Reprinted with permission [180].

## Combination of Substituents

### 1.18 α-carboxy-4-methoxy-2-nitrobenzyl (C4MNB) Fmoc cysteine [176]
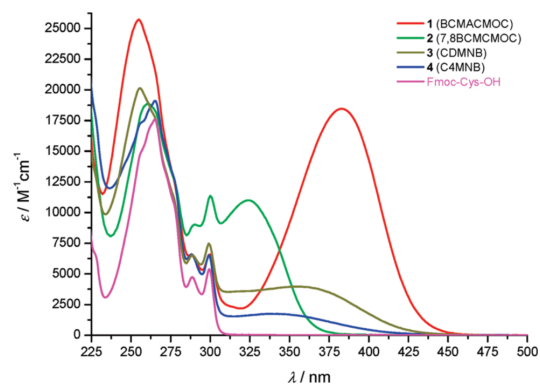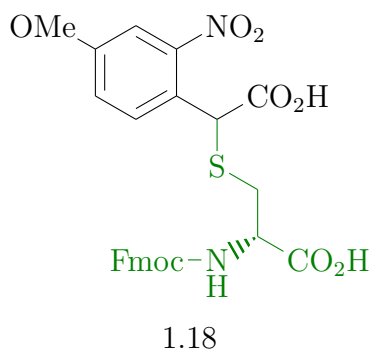


**Φ:** none given

**Comments:** Olive green curve. Measured in MeCN/HEPES buffer (5:95), pH 7.2. Reprinted with permission from [176]. Copyright 2009 American Chemical Society. Additional spectroscopic data in [177].

**1.19 α-carboxy-4,5-dimethoxy-2-nitrobenzyl (CDMNB) Fmoc cysteine [176]**
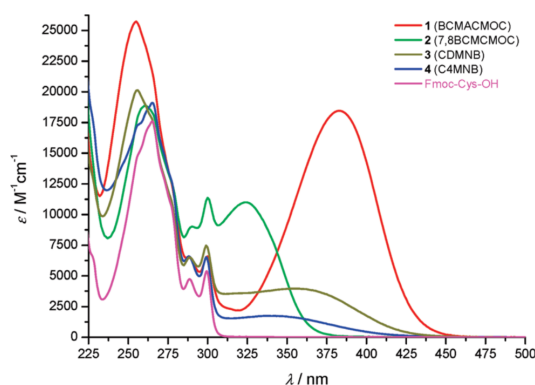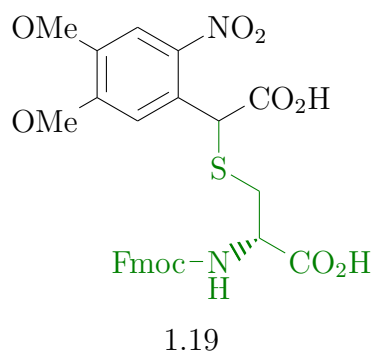


1.19

**Φ:** none given

**Comments:** Blue curve. Measured in MeCN/HEPES buffer (5:95), pH 7.2. Reprinted with permission from [176]. Copyright 2009 American Chemical Society. Spectroscopic data on caged carboxylic acid in [185],

**1.20 nitrobenzyl ether [28]**



1.20
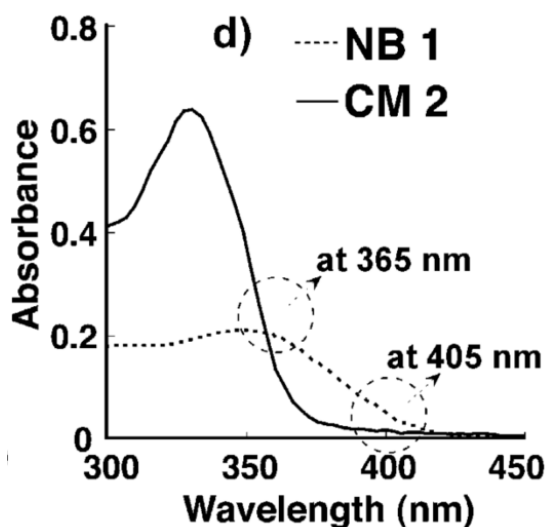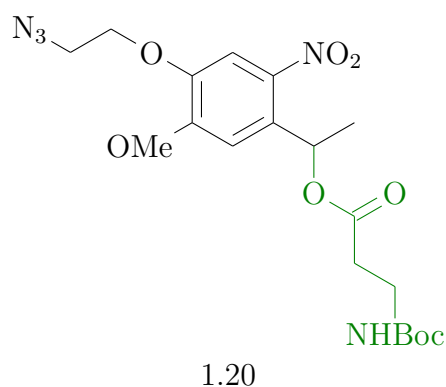
**Φ:** 0.16

**Comments:** Dashed curve. 0.4 mM in MeCN/PBS mixture (8:2). Reprinted with permission from [28].

**1.21 *p*-extended [2-(2-nitrophenyl)propoxy]carbonyl (NPPOC) glutamate [186]**



1.21
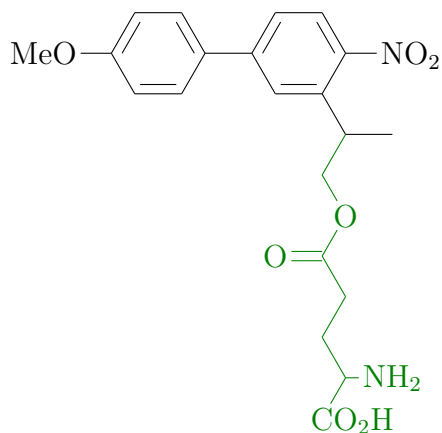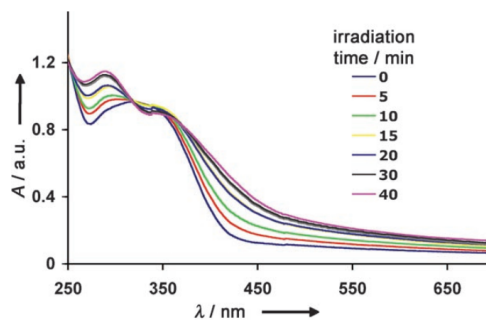
**Φ:** 0.9

**Comments:** In phosphate buffer (pH 7, 100 mM), irradiated at 364 nm. Reprinted with permission from [186].

**1.22 methoxynitrobiphenyl(PMNB) [7]**



1.22
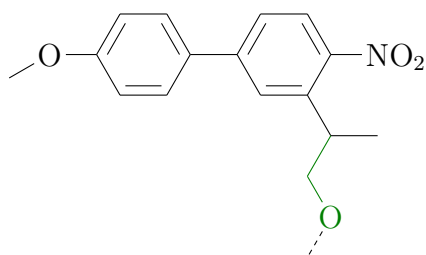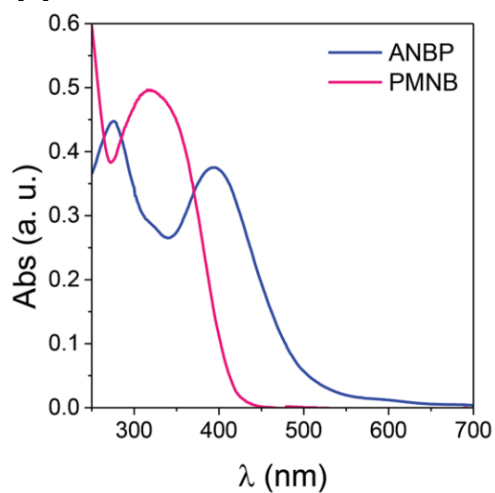
**Φ:** 0.09

**Comments:** Magenta curve. 50 $\mu$M in PBS pH=7.4, 50 mM. Reprinted with permission from [7].

### 1.23 *p*-dialkylaminonitrobiphenyl(ANBP) [7]
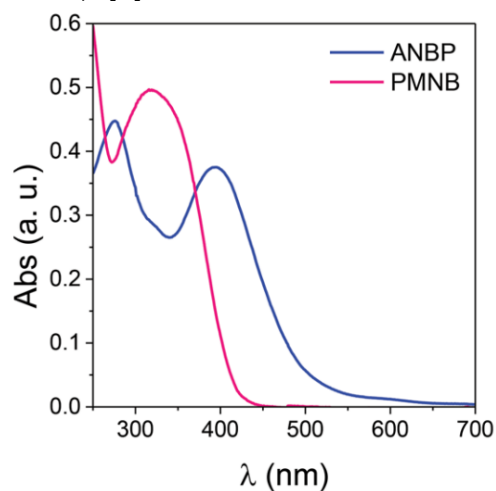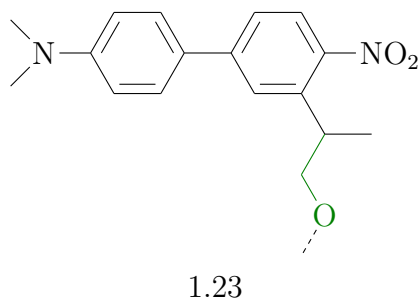


**Φ:** 0.15

**Comments:** Blue curve. 50 $\mu$M in PBS pH=7.4, 50 mM. Reprinted with permission from [7]. Additional spectroscopic data in [147] and on caged GABA in [23].

### 1.24 Thioxanthone/NPPOC conjugate T5S0-OR [172, 173]
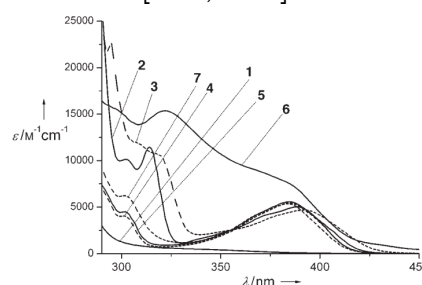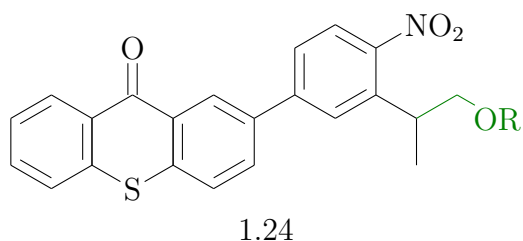


**Φ:** 0.26

**Comments:** Curve labelled **6**. In methanol. Reprinted with permission from [172].

### 1.25 Thioxanthone/NPPOC conjugate T4E2-OR [172, 173]



1.25
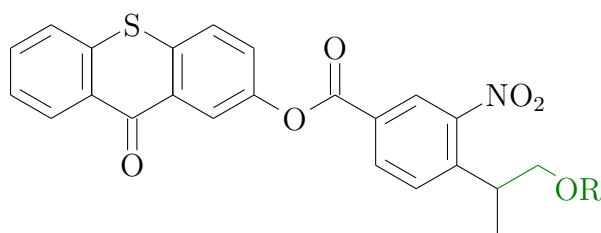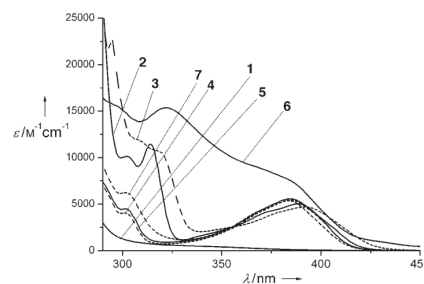
**Φ:** 0.09

**Comments:** Curve labelled **7**. In methanol. Reprinted with permission from [172].

## Extended Ring Nitrobenzyl Cages

### 1.26 3-nitro-2-naphthalenemethanol [179, 182]



1.26
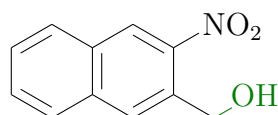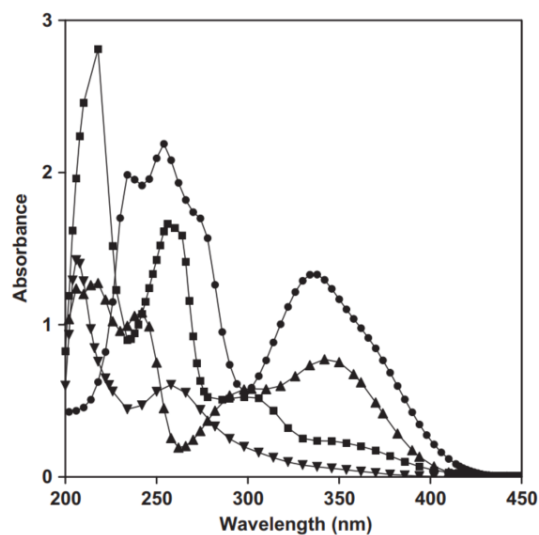
**Φ:** none given

**Comments:** Curve with rectangles. $1.0 \times 10^{-4}$ M measured in ethanol. Reprinted with permission from [179]. Additional spectroscopic data in [182].

**1.27 7-methoxy-3-nitro-2-naphtalene methanol (MNNM) [179]**
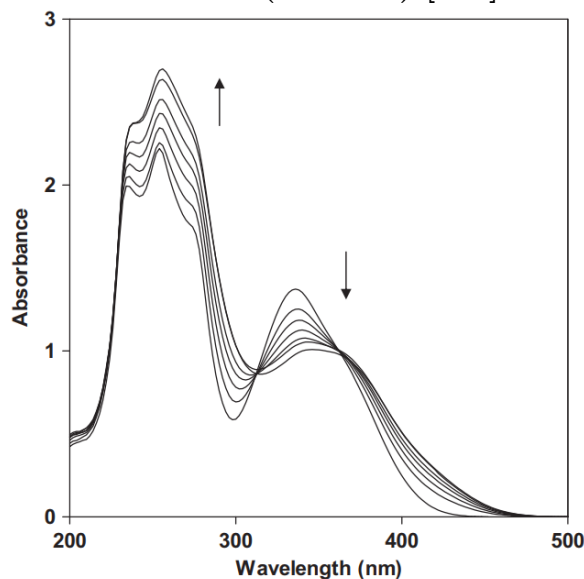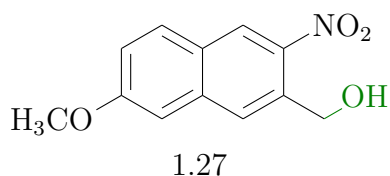


**Φ:** none given
**Comments:** $1.0 \times 10^{-4}$ M measured in ethanol. Arrows indicate the changes of absorbance during the irradiation time. Reprinted with permission from [179]

**1.28 4,5-methylenedioxy-2-nitrobenzyl alcohol [164]**
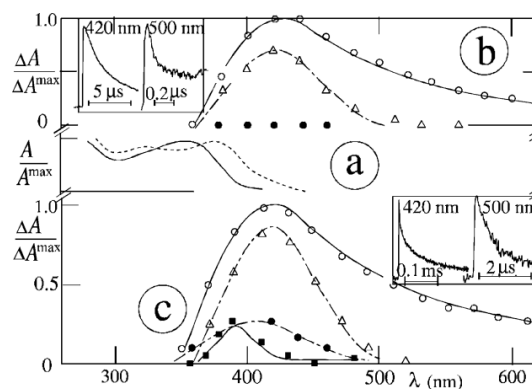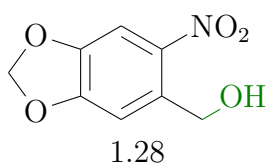


**Φ:** 0.8
**Comments:** Full Line (a) measured in acetonitrile. Reproduced from [164] with permission from the European Society for Photobiology, the European Photochemistry Association, and The Royal Society of Chemistry. Other spectroscopic data on 4,5-methylenedioxy-2-nitrobenzaldehyde in [164] and on $\alpha$-methyl-2-nitropiperonyloxycarbonyl (MeNPOC) and 2-(3,4-methylenedioxy-6-nitrophenyl)propoxycarbonyl (MNPPOC) thymin in [183].

### 1.29 nitrobenzofuran (NDBF) [187]
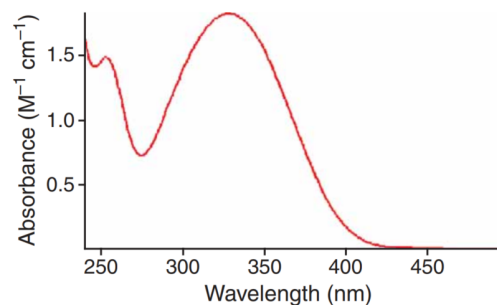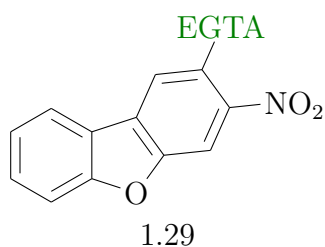


**Φ:** 0.7

**Comments:** 0.1 mM in aqueous buffer at PH 7.5 (40 mM Hepes, 100 mM KCl. Reprinted with permission from [187]. Other spectroscopic data on a NDBF Ferri cage in [188], on NDBF-BA in [189] and on NDBF caged DNA in [17].

## Nitroindoline Cages

### 1.30 1-Acyl-7-nitroindoline [190]
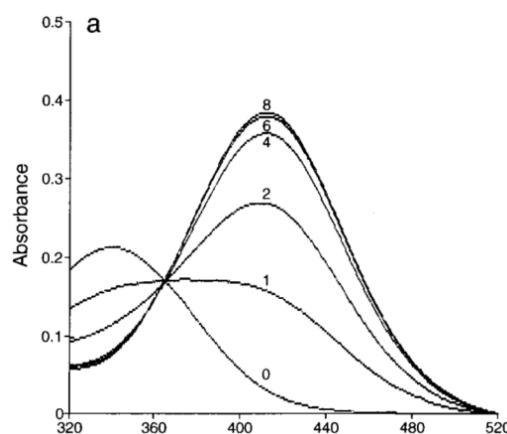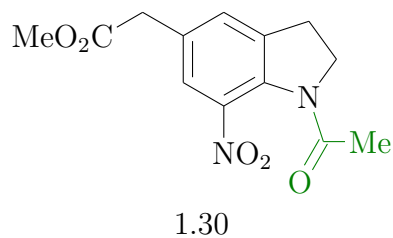


**Φ:** none given

**Comments:** Curve labelled 0 measured in neutral aqueous solution. Reprinted with permission from [190]. Other spectroscopic data in [191].

**1.31 1-Acetyl-4-methoxy-5,7-dinitroindoline (MDNI) [192]**
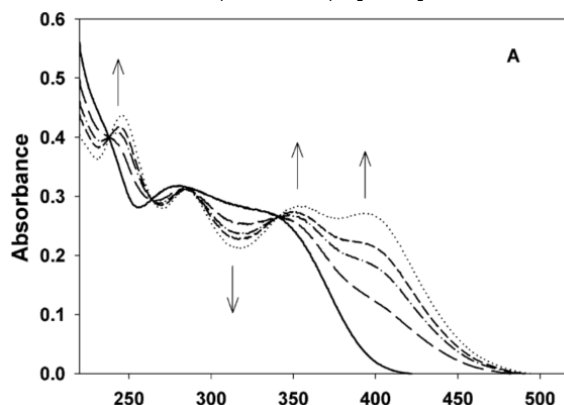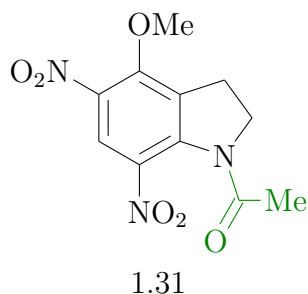


**Φ:** none given

**Comments:** Solid line measured in pH 7 aqueous solution. Reproduced from [192] with permission from the European Society for Photobiology, the European Photochemistry Association, and The Royal Society of Chemistry. Other spectroscopic data on caged glutamate in [193].

**1.32 1-Acetyl-4-methoxy-5,7-dinitroindoline (CDNI) [147]**
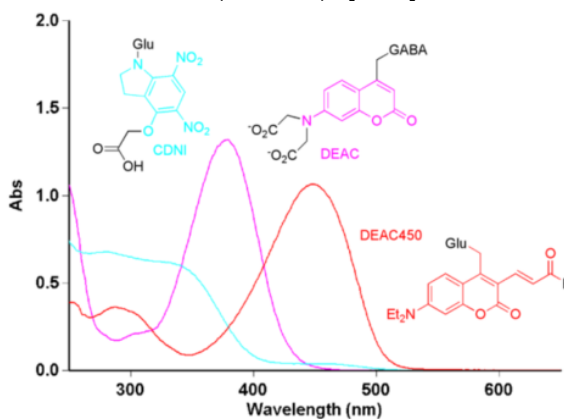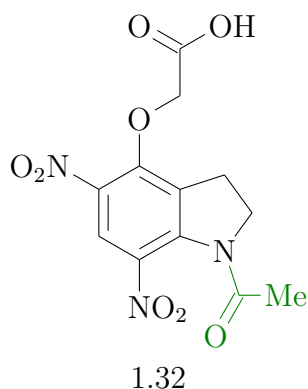


**Φ:** 0.5

**Comments:** Cyan curve. Reprinted with permission from [147]. Copyright (2013) American Chemical Society. Other spectroscopic data in [23] and on caged GABA in [22].

## A.2 Benzoin Cages

**2.1 benzoin [194]**



2.1

**Φ:** 0.1
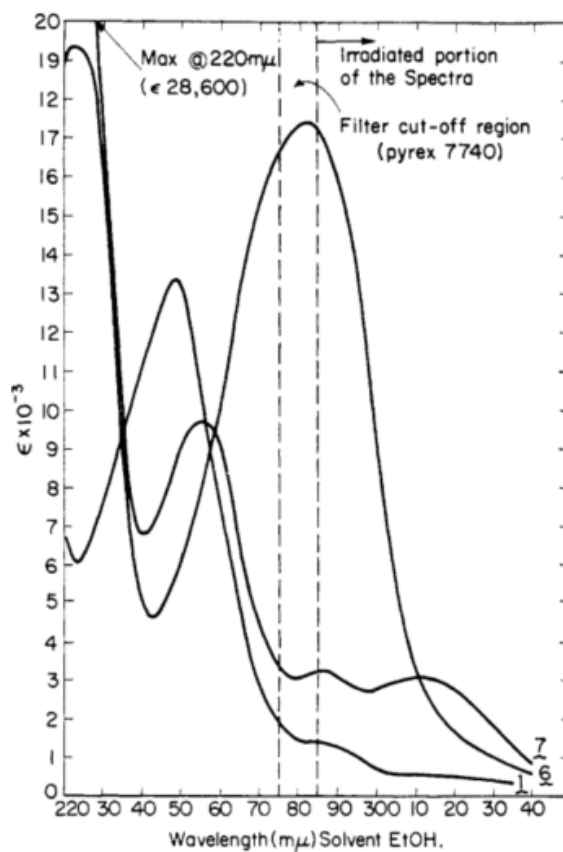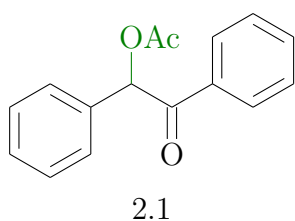
**Comments:** Curve labelled with 1 measured in ethanol. Reprinted with permission from [194]. Copyright 1964 American Chemical Society. Other spectroscopic data on caged phosphate in [195, 196].

**2.2 3' methoxy benzoin [197]**
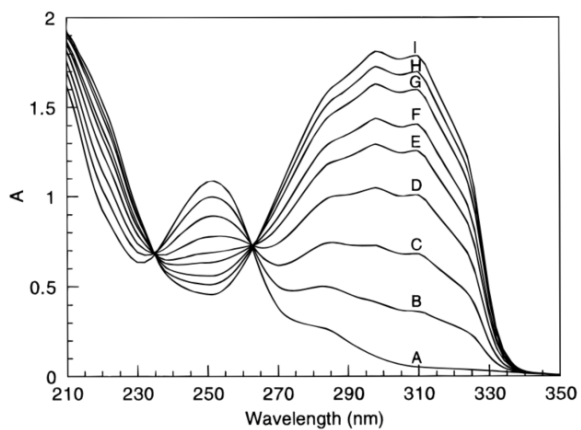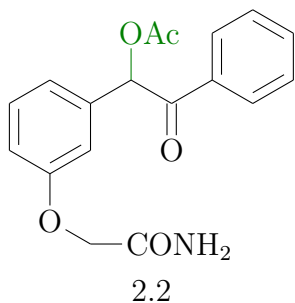


**Φ:** none given

**Comments:** Curve labelled A. 47.7 $\mu$M solution in 1:1 methanol/Tris-HCL (0.05 M, pH 7.40). Reprinted with permission from [197]. Copyright 1996 American Chemical Society.

**2.3 3,3' dimethoxy benzoin [194]**
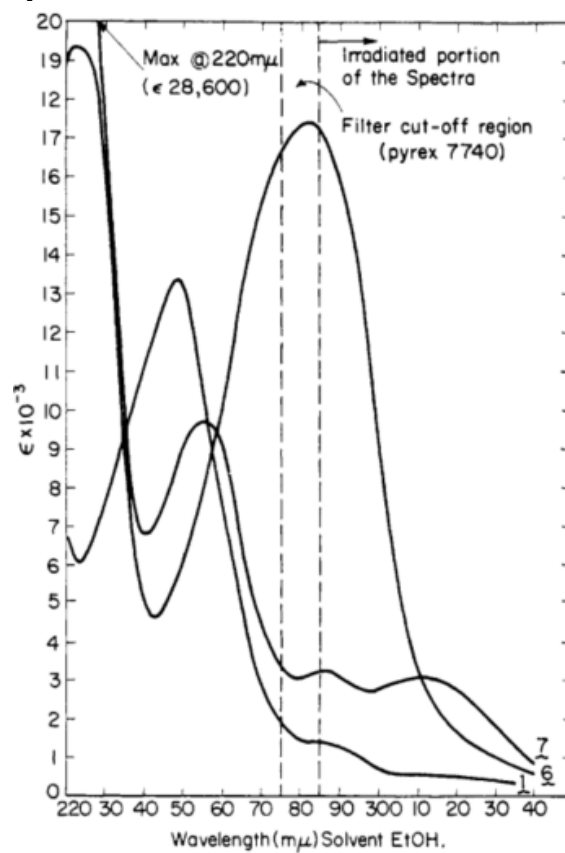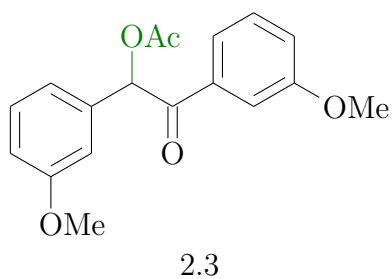


**Φ:** 0.02
**Comments:** Curve labelled with 7 measured in ethanol. Reprinted with permission from [194]. Copyright 1964 American Chemical Society.

**2.4 4,4' dimethoxy benzoin [194]**
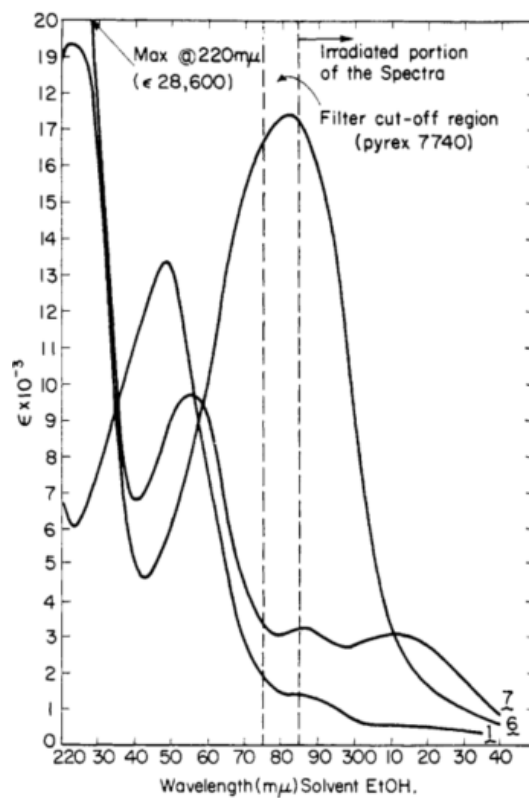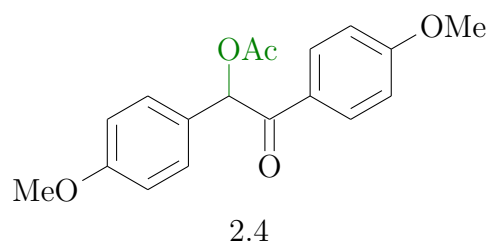


**Φ:** 0.01
**Comments:** Curve labelled with 6 measured in ethanol. Reprinted with permission from [194]. Copyright 1964 American Chemical Society.

**2.5 3',5' dimethoxy benzoin (DMB) [198]**
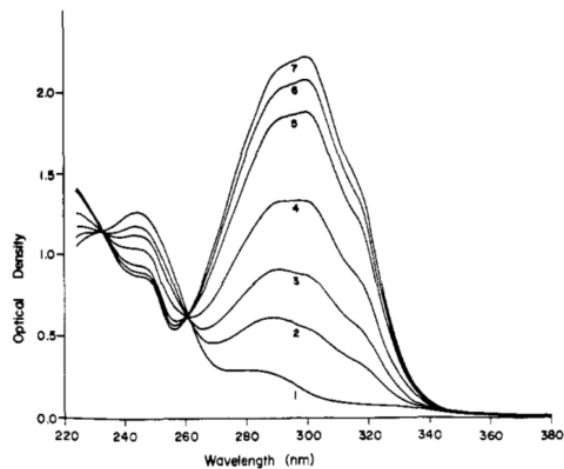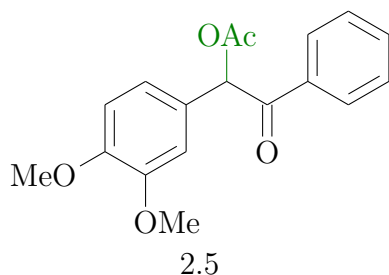


**Φ:** none given

**Comments:** Curve labelled with 1. 8.22 x $10^{-5}$ M in acetonitrile. Reprinted with permission from [198]. Copyright 1971 American Chemical Society. Other spectroscopic data on modified quartz substrates in [12], on caged ubiquinol-2 in [199], on caged acetyl salicyl in [200] and on caged diethyl phosphate in [142, 201]

**2.6 *O*-acetyl 3',5'-bis(carboxymethoxy)benzoin (BCMB) [202]**
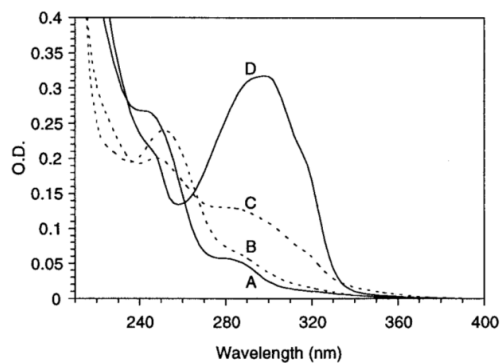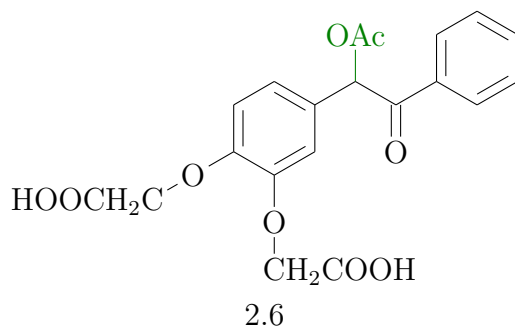


**Φ:** none given

**Comments:** 59.6 $\mu$M in methanol labelled A, in buffer (100 mM sodium phosphate, pH 7.40) labelled B. Reprinted with permission from [202]. Copyright 1998 American Chemical Society.

**2.7 3,3',5,5' Tetramethoxybenzoin carbamate [135]**
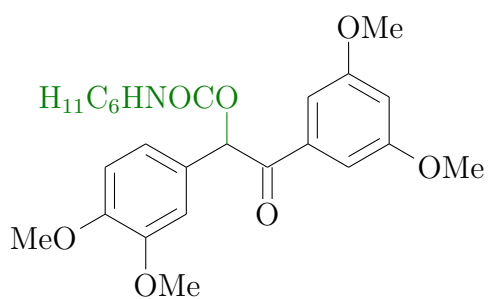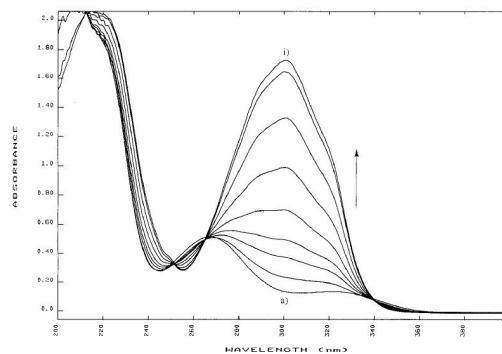


**Φ:** 0.067 (254 nm), 0.080 (313 nm), 0.054 (336 nm), 0.028 (365 nm)

**Comments:** $6.164 \times 10^{-5} M$ solution in MeCN, 350 nm, *a* is before irradiation, *i* is after an irradiation series, in the thesis as 2.a. Adapted with permission from [135]. Copyright 1996. American Chemical Society.

# A.3 Coumarin and Quinolin Cages

**3.1 coumarin (CM) various LG [146]**
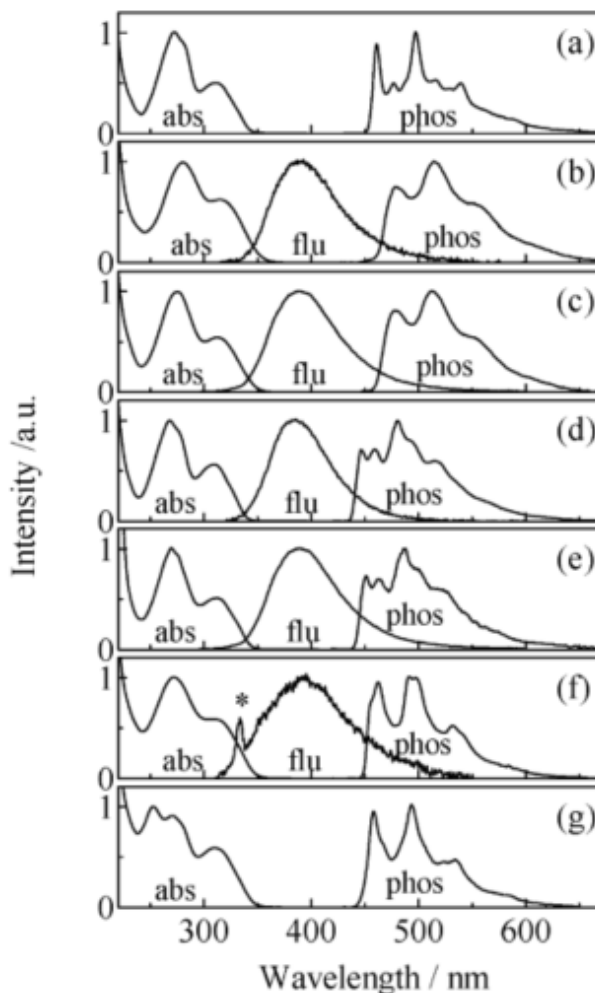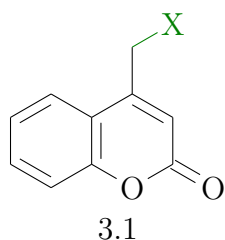


**Φ:** OH: 0, Cl: 0, SH: 0, Br: 0.24 ± 0.04, OPh: 0, Sph: 0.25 ± 0.04
**Comments:** CM labelled (a), CM-Br labelled (b), CM-Cl labelled (c), CM-OH labelled (d), CM-OPh labelled (e), CM-SM labelled (f) and CM-SPh labelled (g) in acetonitrile. Reprinted with permission from [146]. Copyright 2009 American Chemical Society. Other spectroscopic data on caged methanol in [131], on caged OH in [203].

# 7-subsituted coumarins

## 3.2 (7-methoxy coumarin-4-yl) methyl (7-MCM) cAMP [203]



**Φ:** 0.03
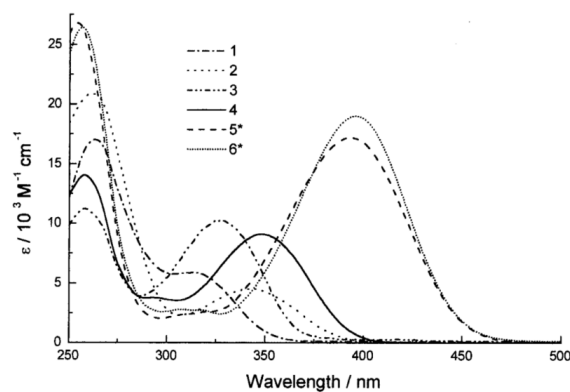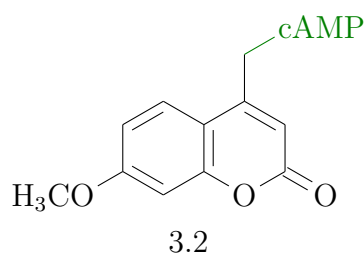
**Comments:** Dotted curve labelled 2. Measured in MeOH/HEPES, 1:4. Reprinted with permission from [203]. Copyright 2002 American Chemical Society. Other spectroscopic data in [204], on caged Br-cGMP in [205].

## 3.3 coumarin azide methylester [28]
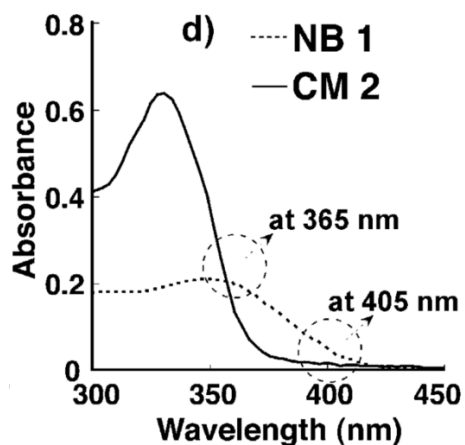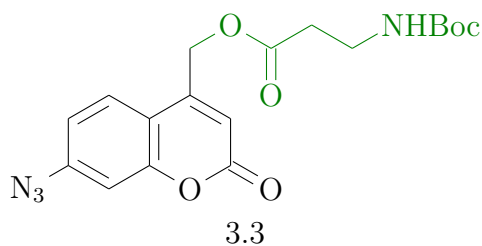


**Φ:** 0.57

**Comments:** Solid line. 0.4 mM dissolved in acetonitrile/PBS mixture (8:2). Preprinted with permission from [28].

### 3.4 [7-(dimethylamino)coumarin-4-yl]methyl (DMACM) ATP [206]



3.4
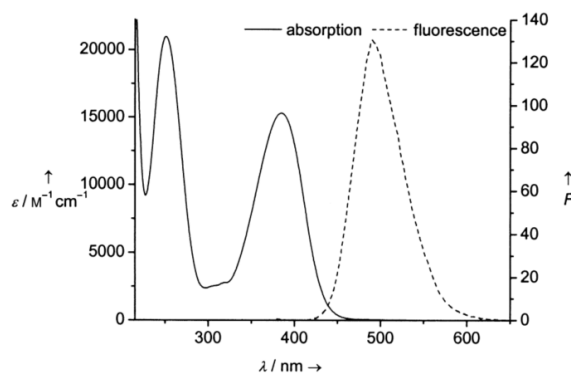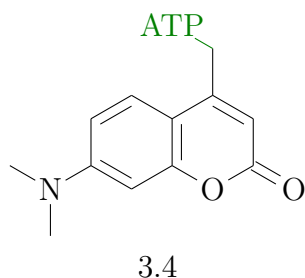


**Φ:** 0.086

**Comments:** 35 $\mu$M solutions of HEPES buffer, pH 7.2. Reprinted with permission from [206]. Other spectroscopic data on caged Br-cGMP in [205].

### 3.5 [7-[bis(carboxymethyl)amino]coumarin-4-yl] methyloxycarbonyl [207]



3.5
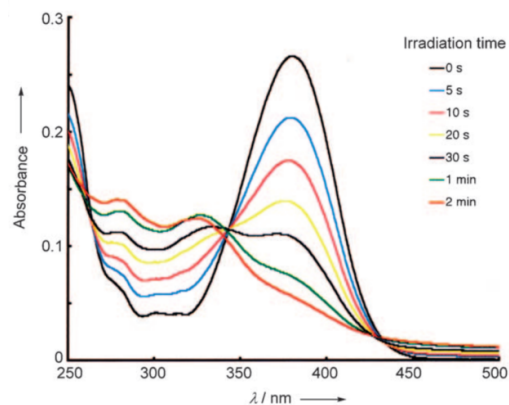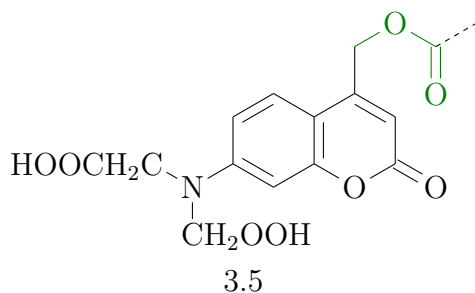


**Φ:** none given

**Comments:** Measured in phosphate buffered saline (PBS; pH 7.4, 1 % DMSO). Reprinted with permission from [207]. Other spectroscopic data on various LG in [208], on *S*-Protected Fmoc-Cys-OH in [176].

### 3.6 [7-(diethylamino)coumarin-4-yl]methyl (DEACM) ATP [138]



3.6
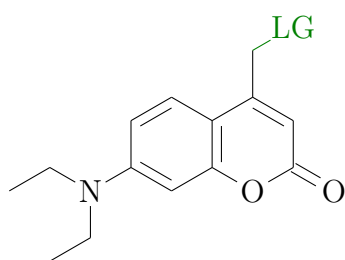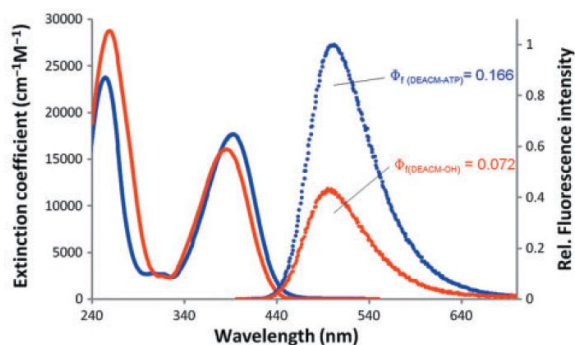


**Φ:** 0.076 (50 $\mu$M), 0.057 (91 $\mu$M), 0.045 (230 $\mu$M), 0.038 (450 $\mu$M)

**Comments:** 18.5 $\mu$M ATP and 20.8 $\mu$M OH in water pH 7.0, excited at 385 nm, in the thesis as 3.a. Reprinted from [138] by permission of Oxford University Press. Other spectroscopic data in [209], on caged phosphate in [209] and in [22], on caged cytidine 5'-diphosphate (CDP) in [210], on caged azide in [134], on application in drug delivery in [211], on silane in [181], on caged benzoic acid in [212], on caged cAMP in [203]., on caged glycine [213], on caged Br-cGMP in [205], on caged glutamate in [214].

## 6-subsituted coumarins

### 3.7 (6-methoxy coumarin-4-yl) methyl (6-MCM) cAMP [203]



3.7
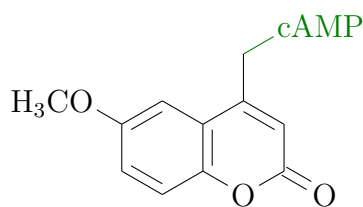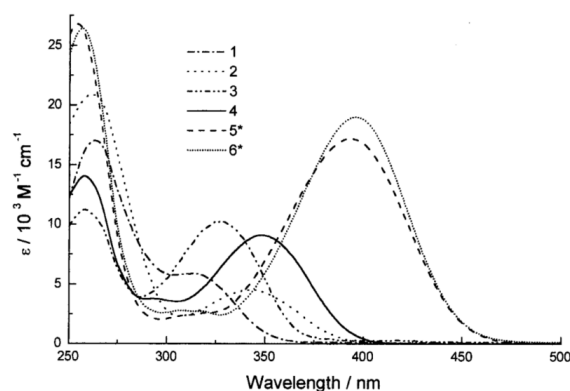


**Φ:** 0.13

**Comments:** Curve labelled 3. Measured in MeOH/HEPES, 1:4. Reprinted with permission from [203]. Copyright 2002 American Chemical Society.

## multiple substituted coumarins

### 3.8 (dimethoxy coumarin-4-yl) methyl (DMCM) cAMP [203]
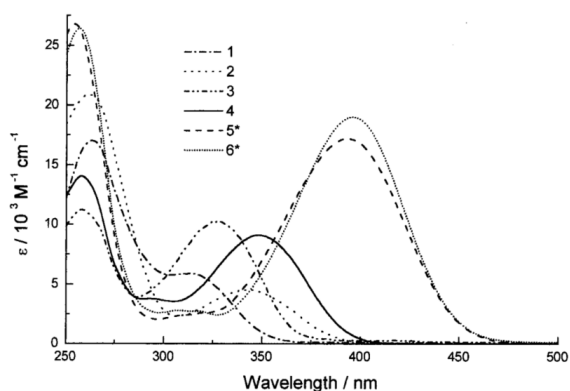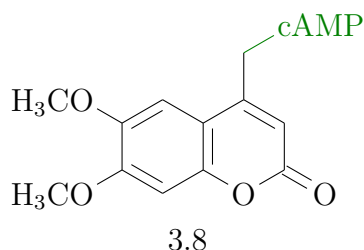


**Φ:** 0.04

**Comments:** Solid curve labelled 4. Measured in MeOH/HEPES, 1:4. Reprinted with permission from [203]. Copyright 2002 American Chemical Society. Other spectroscopic data on caged Br-cGMP in [205].

### 1.9 [7,8-Bis(carboxymethoxy)coumarin-4-yl]methoxycarbonyl [176]
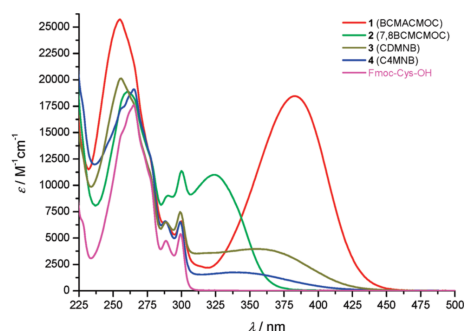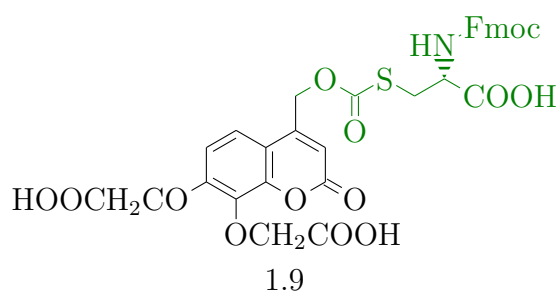


**Φ:** none given

**Comments:** Green curve. Measured in MeCN/HEPES buffer (5:95), pH 7.2. Reprinted with permission from [176]. Copyright 2009 American Chemical Society.

**3.10 Diethylaminocoumarin 450 (DEAC540) cAMP) [22]**



3.10
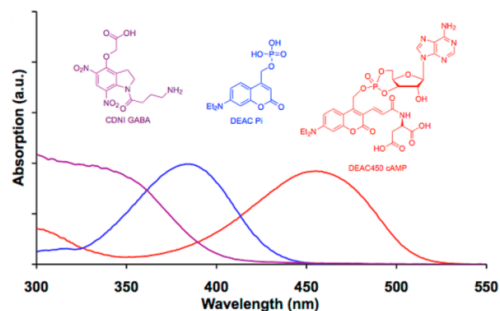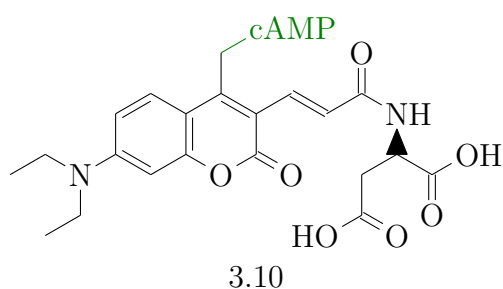
**Φ:** 0.78

**Comments:** Red curve. Reprinted with permission from [22]. Copyright 2013 American Chemical Society. Other spectroscopic data on caged GABA in [23].

**3.11 3-(*p*-cyano-phenyl-)diethyl amino coumarin Glu [22]**



3.11
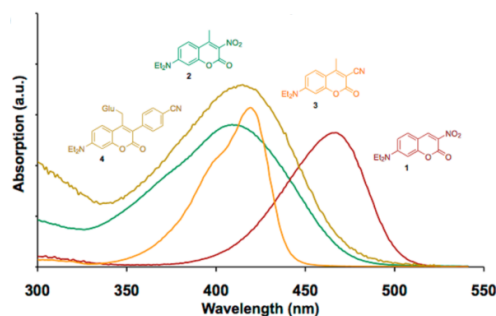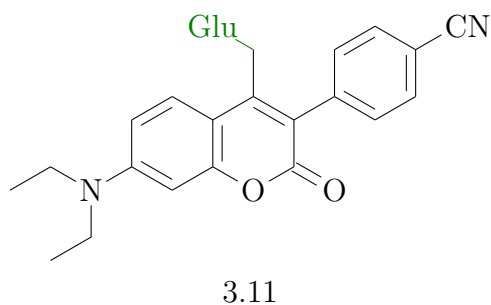
**Φ:** 0.05

**Comments:** Khaki curve. Reprinted with permission from [22]. Copyright 2013 American Chemical Society. Other spectroscopic data on cAMP in [203].

### 3.12 3-cyano-7-(diethylamino)coumarin benzoic acid [212]



3.12
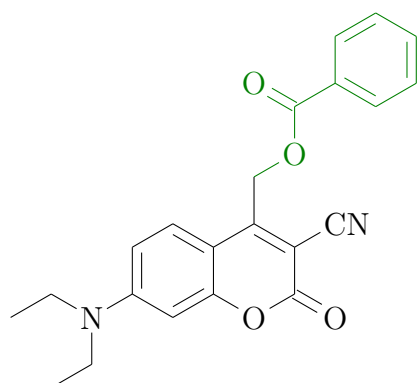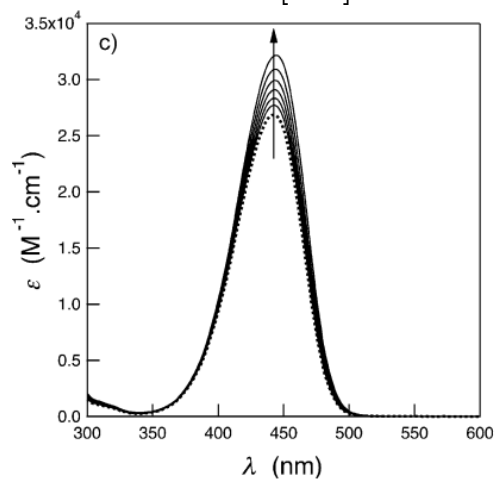
**Φ:** 0.09 ± 0.03
**Comments:** Dotted curve. 25 $\mu$M in 20 mM pH 7.5 Tris buffer/acetonitrile (v/v). Reprinted with permission from [212].

### 3.13 Dicyanocoumarin [215]



3.13
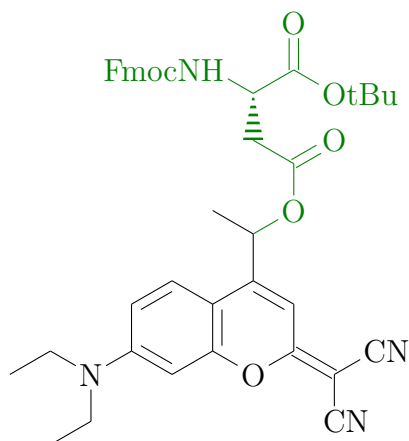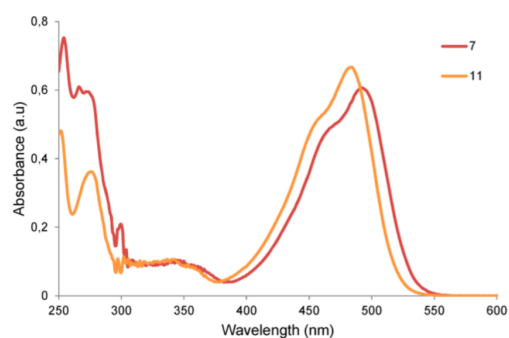
**Φ:** 0.24
**Comments:** Red curve labelled 7. 20 $\mu$M in Tris buffer pH 7.5/ACN 1:1. Reprinted with permission from [215]. Copyright 2016 American Chemical Society. Additional spectroscopic data in [212].

## 3.14 N-DCAC-GABA [147]



3.14
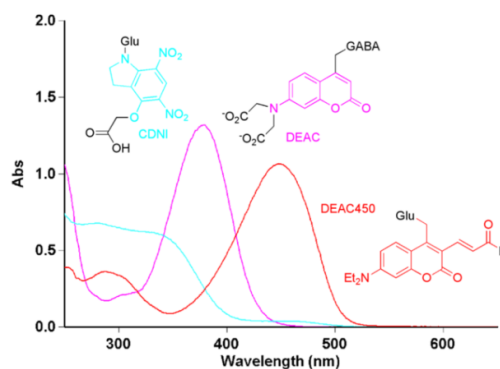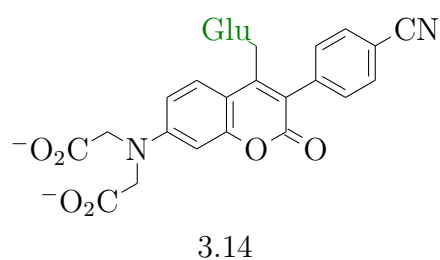
**Φ:** none given

**Comments:** Magenta curve. Reprinted with permission from [147]. Copyright 2013 American Chemical Society.

## 3.15 6-bromo-7-hydroxycoumarin-4-ylmethyl [216]



3.15
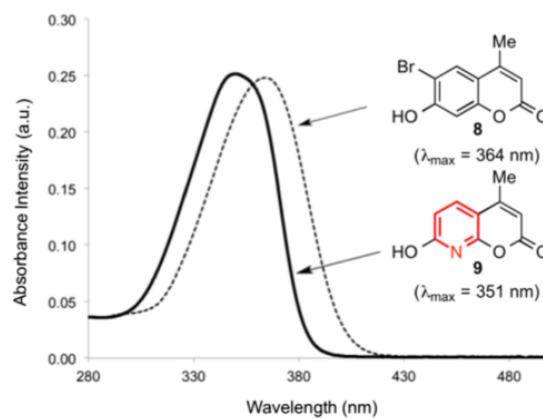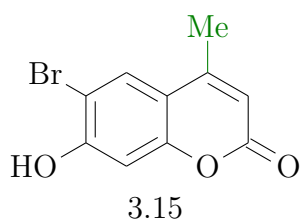
**Φ:** Glu ester: 0.11 Glu carbamate: 0.30

**Comments:** Dashed curve. Reprinted with permission from [216].

## benzocoumarins

### 3.16 5,6-benzocoumarinyl conjugate [217]



3.16
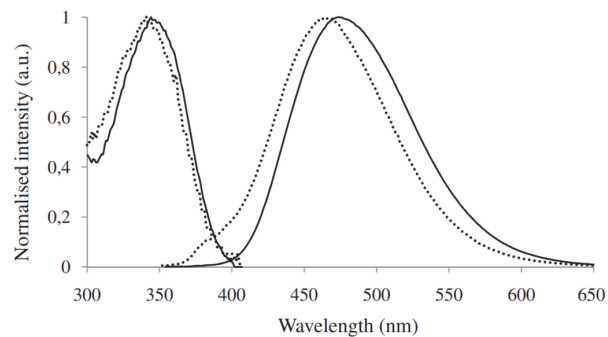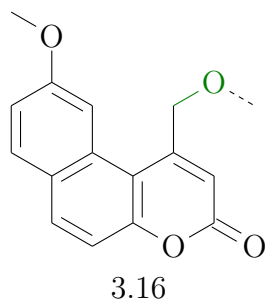
**Φ:** none given

**Comments:** Full curve data measured in MeOH/buffer (80:20)and spaced curve data measured in ACN/HEPES buffer (80:20). Reprinted with permission from [217].

### 3.17 6-Aminobenzocoumarin butric acid [218]



3.17
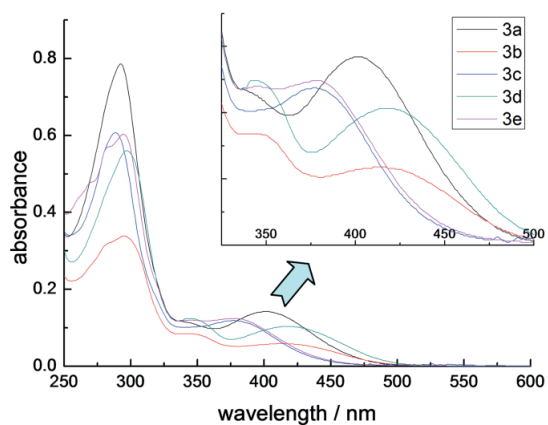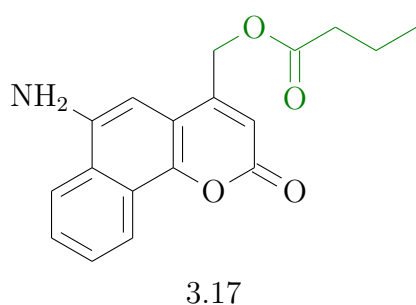
**Φ:** 245 nm: 0.047 300 nm: 0.011 350 nm: 0.0085 419 nm: 0.011

**Comments:** Black curve (labelled 3a) measured in methanol/HEPES buffer (80:20). Reprinted with permission from [218].

**3.18 mono methylated 6-Aminobenzocoumarin butric acid [218]**
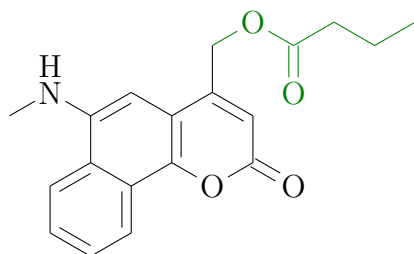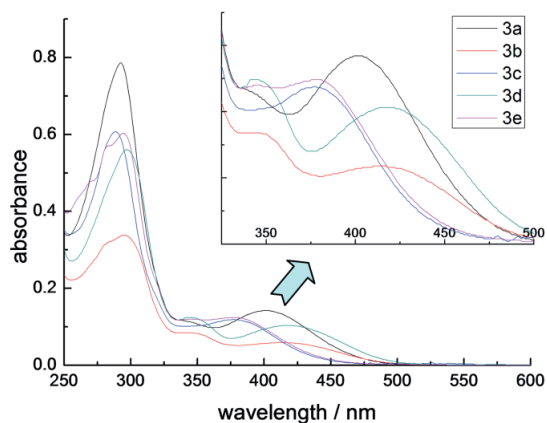


**Φ:** 245 nm: 0.025 300 nm: 0.0081 350 nm: 0.0067 419 nm: 0.0052
**Comments:** Red curve (labelled 3b) measured in methanol/HEPES buffer (80:20). Reprinted with permission from [218].

**3.19 di-methylated 6-Aminobenzocoumarin butric acid [218]**
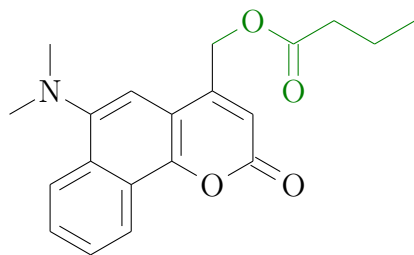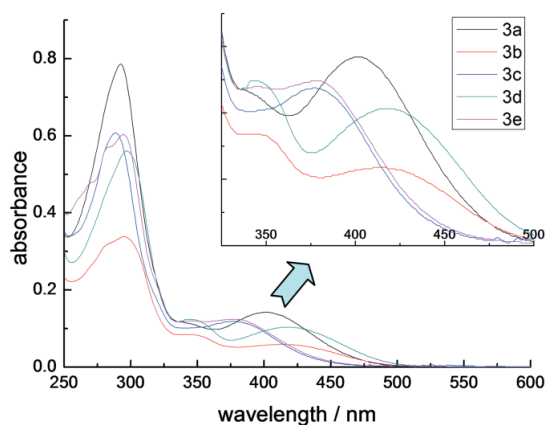


**Φ:** 245 nm: 0.060 300 nm: 0.024 350 nm: 0.0072 419 nm: 0.013
**Comments:** Blue curve (labelled 3c) measured in methanol/HEPES buffer (80:20). Reprinted with permission from [218].

### 3.20 mono ethylated 6-Aminobenzocoumarin butric acid [218]



3.20
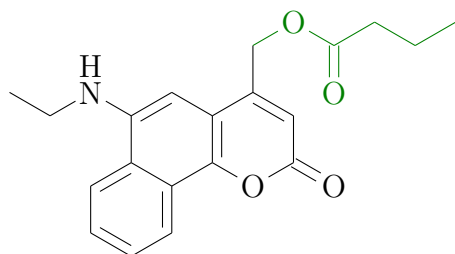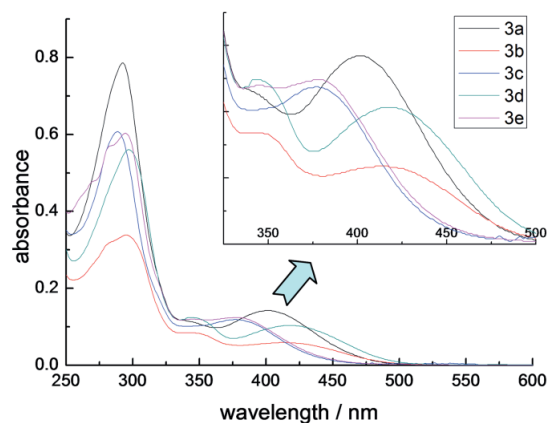
**Φ:** 245 nm: 0.88 300 nm: 0.38 350 nm: 0.25 419 nm: 0.31
**Comments:** Cyan curve (labelled 3d) measured in methanol/HEPES buffer (80:20). Reprinted with permission from [218].

### 3.21 di-ethylated 6-Aminobenzocoumarin butric acid [218]



3.21
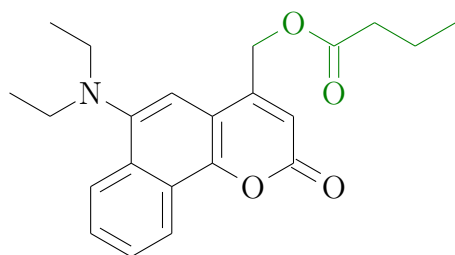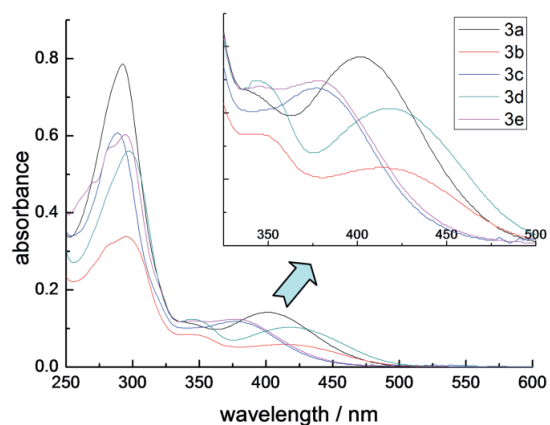
**Φ:** 245 nm: 0.45 300 nm: 0.20 350 nm: 0.15 419 nm: 0.10
**Comments:** Violet curve (labelled 3e) measured in methanol/HEPES buffer (80:20). Reprinted with permission from [218].

# Other coumarins

### 3.22 8-aza-7-hydroxycoumarin-4-ylmethyl [216]
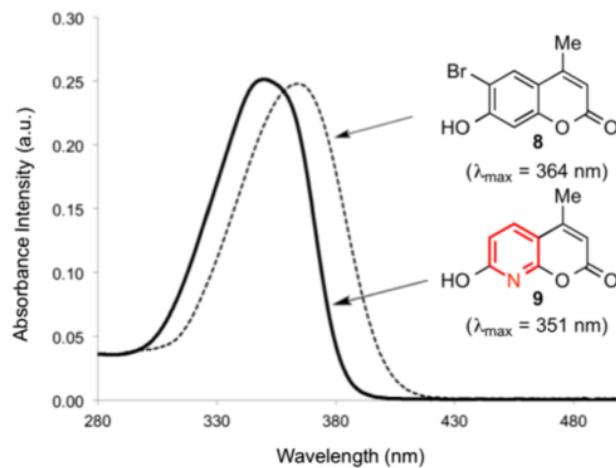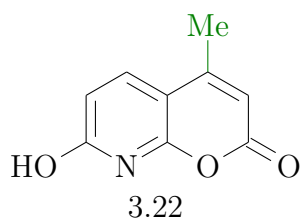


**Φ:** Glu ester: 0.17 Glu carbamate: 0.43
**Comments:** Solid curve. Reprinted with permission from [216].

### 3.23 Thiocoumarin [24]
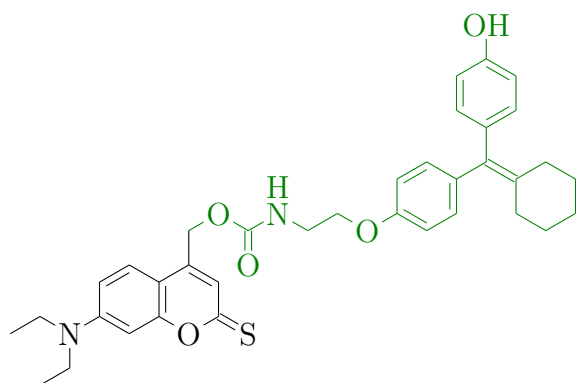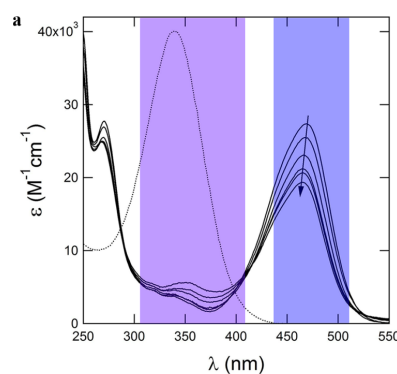


**Φ:** none given
**Comments:** Measured in 20 mM PH 7.5 Tris buffer/acetonitrile (v/v).Reprinted with permission from [24]. Copyright 2013 American Chemical Society.Additional spectroscopic data in [212].

# 7 substituted quinolins

### 3.24 7-hydroxyquinoline [219]
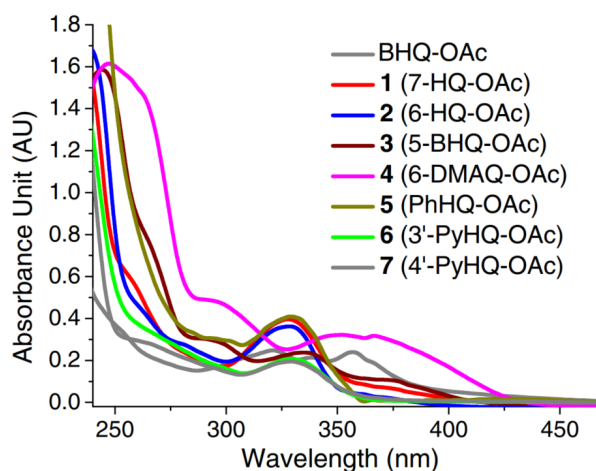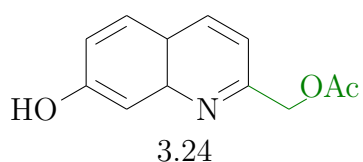


**Φ:** none given
**Comments:** Red curve labelled 1 (7-HQ-Oac). 100 $\mu$M in KMOPS. Reprinted with permission from [219].

### 3.25 7-dimethyl quinoline [220]
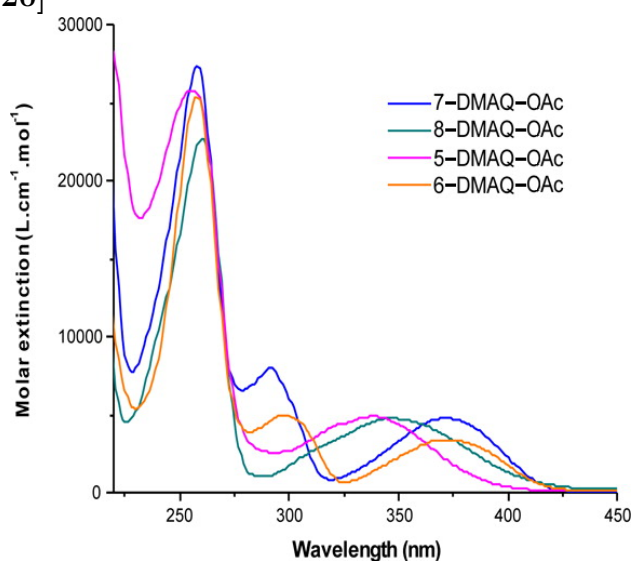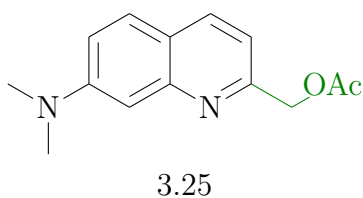


**Φ:** 0.03
**Comments:** Blue curve labelled 7-DMAQ. Measured in acetonitrile/TRIS buffer (20 mM) 1/1. Reprinted with permission from [220]. Copyright 2012 American Chemical Society. Other spectroscopic data in [221].

**3.26 7-thio-quinolin [221]**
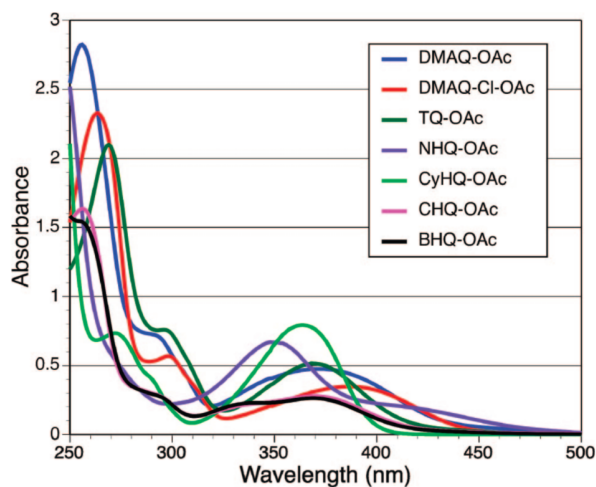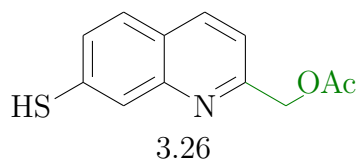


**Φ:** 0.063

**Comments:** Green curve labelled TQ-Cl-OAc. 100 $\mu$M in KMOPS. Reprinted with permission from [221]. Copyright 2009 American Chemical Society.

# 6 substituted quinolins

**3.27 6-hydroxyquinoline [219]**
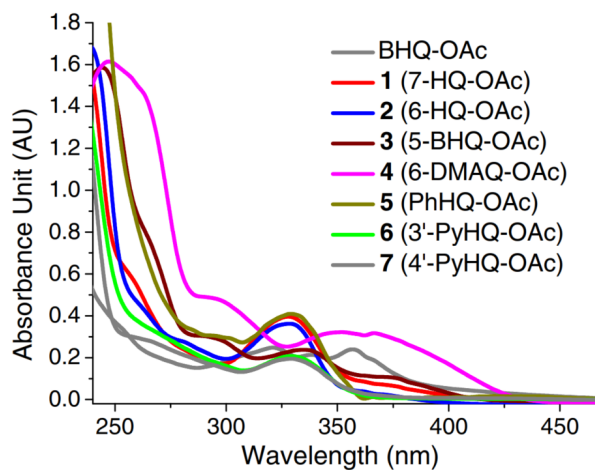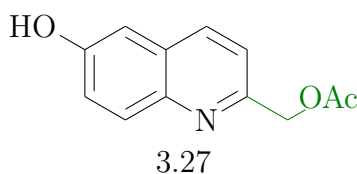


**Φ:** none given

**Comments:** Blue curve labelled 2 (6-HQ-Oac). 100 $\mu$M in KMOPS. Reprinted with permission from [219].

### 3.28 6-dimethyl quinoline [219]
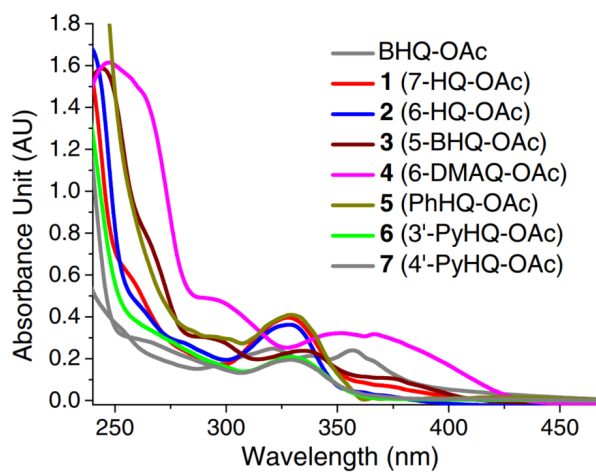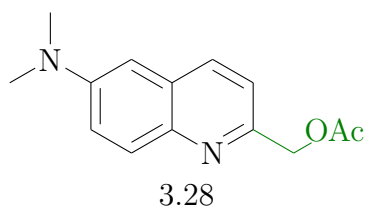


**Φ:** none given
**Comments:** Magenta curve labelled 4 (6-DMAQ-OAc). 100 $\mu$M in KMOPS.
Reprinted with permission from [219].Other spectroscopic data in [220].

## 8 substituted quinolins

### 3.29 1-acyl-8-nitro-1,2-dihydroquinoline carboxylic acid [222]
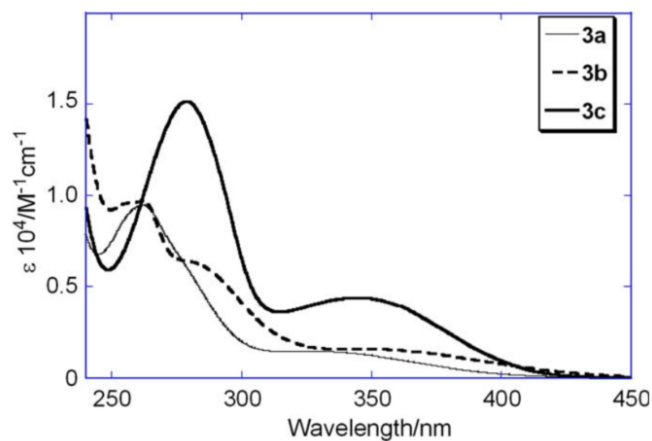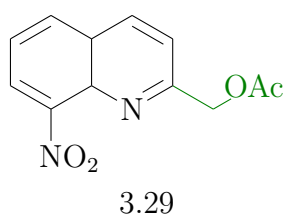


**Φ:**
**Comments:** Grey curve (labelled 3a) measured in MeOH/H$_2$O (1:1).
Reprinted with permission from [222].

### 3.30 8-dimethyl quinoline [220]
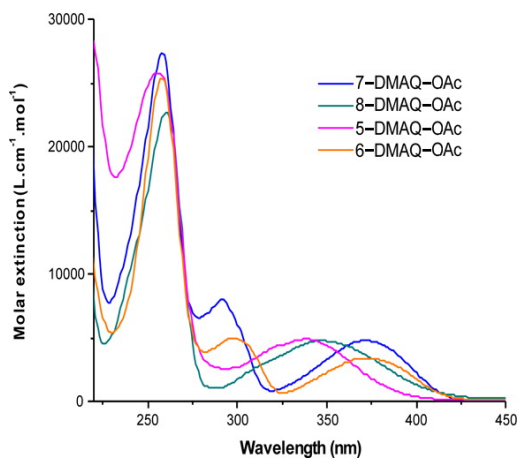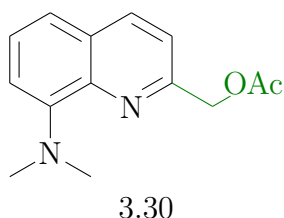


**Φ:** 0.173

**Comments:** Green curve labelled 8-DMAQ. Measured in acetonitrile/TRIS buffer (20 mM) 1/1. Reprinted with permission from [220]. Copyright 2012 American Chemical Society.

## 5 substituted quinolins

### 3.31 5-dimethyl quinoline [220]
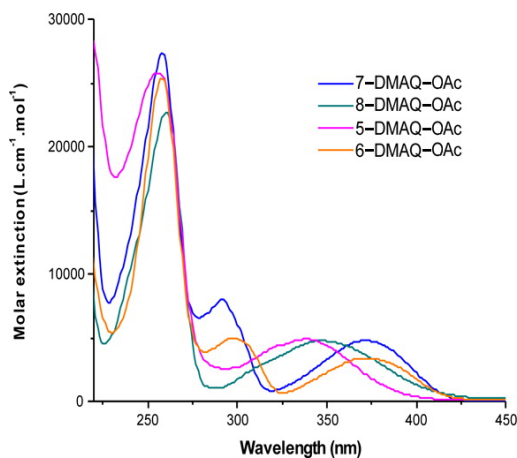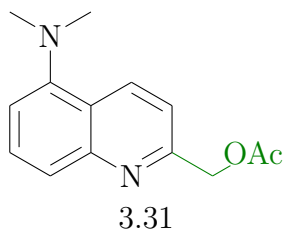


**Φ:** 0.00

**Comments:** Magenta curve labelled 5-DMAQ. Measured in acetonitrile/TRIS buffer (20 mM) 1/1. Reprinted with permission from [220]. Copyright 2012 American Chemical Society.

## multiple substituted quinolins

### 3.32    1-acyl-6-methoxy-8-nitro-1,2-dihydroquinoline    carboxylic acid [222]



**Φ:**
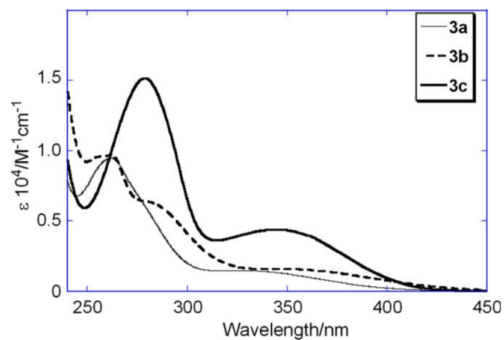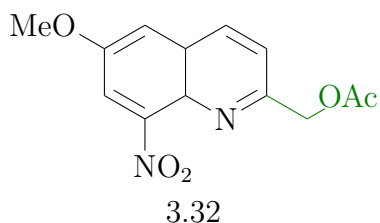
**Comments:** Dashed curve (labelled 3b) measured in MeOH/H$_2$O (1:1). Reprinted with permission from [222].

### 3.33    1-acyl-5-methoxy-8-nitro-1,2-dihydroquinoline    carboxylic acid [222]



**Φ:**
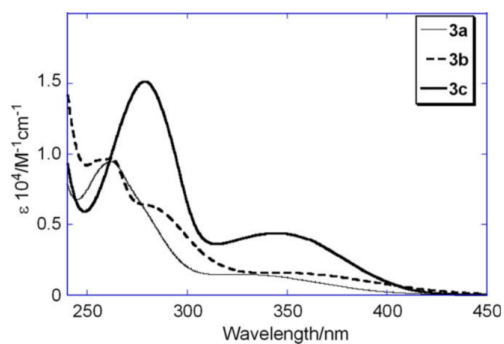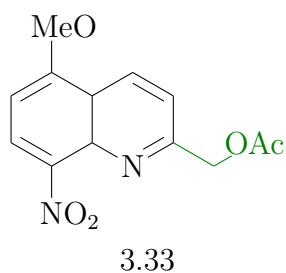
**Comments:** Solid curve (labelled 3c) measured in MeOH/H$_2$O (1:1). Reprinted with permission from [222].

**3.34 8-bromo-7-hydroxyquinolinyl [223]**
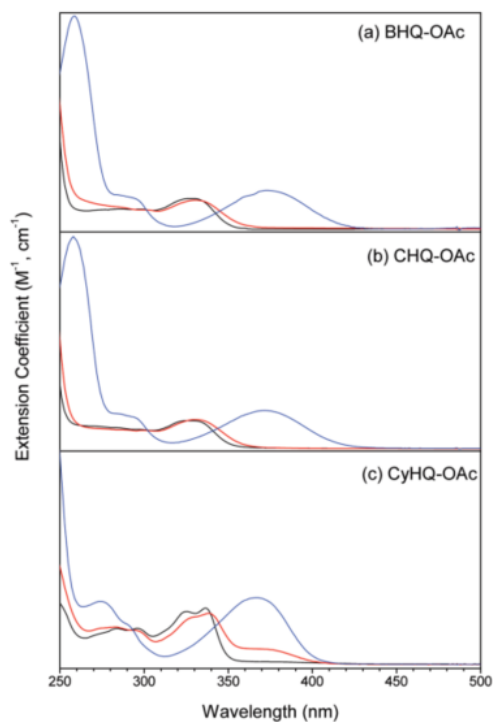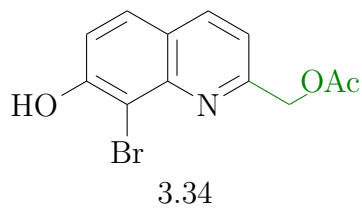


**Φ:** 0.29

**Comments:** Top panel. Measured in MeCN (black), neutral (red) and in alkaline (blue) mixed solvents. Reprinted with permission from [223]. Copyright 2002 American Chemical Society. Other spectroscopic data in [219, 224].

**3.35 8-chloro-7-hydroxyquinolinyl [223]**
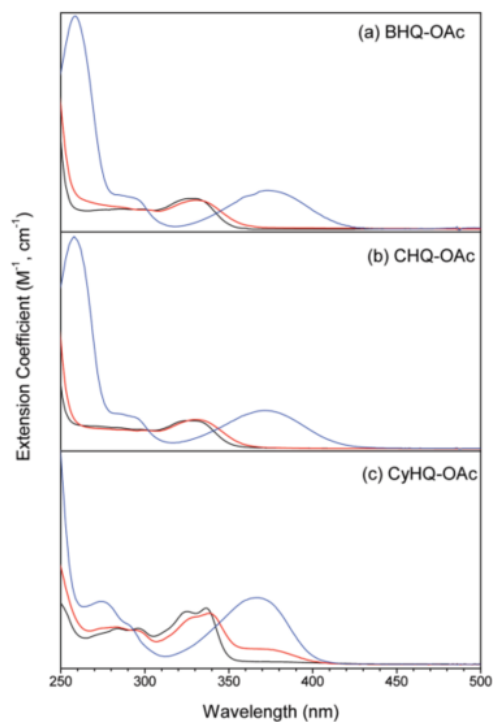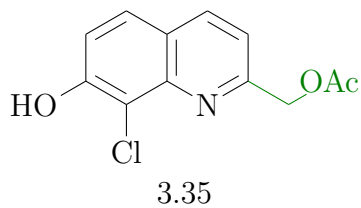


**Φ:** 0.1

**Comments:** Middle panel. Measured in MeCN (black), neutral (red) and in alkaline (blue) mixed solvents. Reprinted with permission from [223]. Copyright 2002 American Chemical Society. Other spectroscopic data in [221].

**3.36 8-cyano-7-hydroxyquinolinyl [223]**
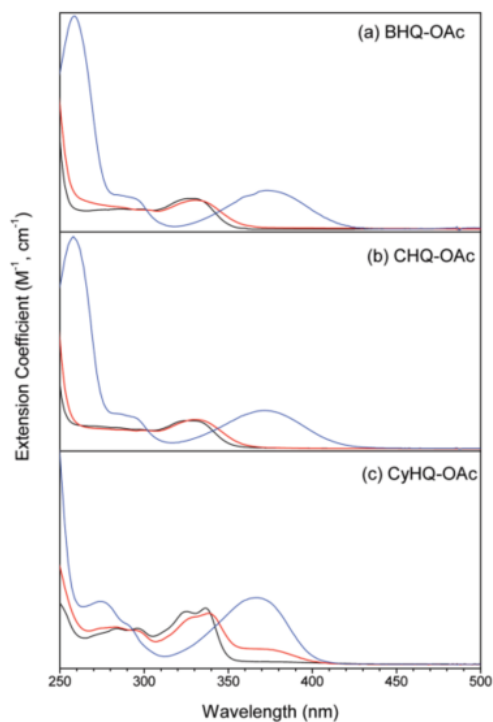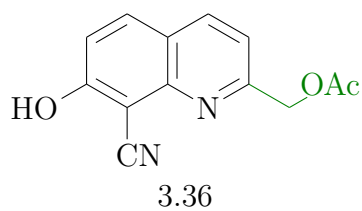


**Φ:** 0.31

**Comments:** Lower panel. Measured in MeCN (black), neutral (red) and in alkaline (blue) mixed solvents. Reprinted with permission from [223]. Copyright 2002 American Chemical Society. Other spectroscopic data in [221].

### 3.37 5-bromo-6-hydroxy quinolinyl [219]
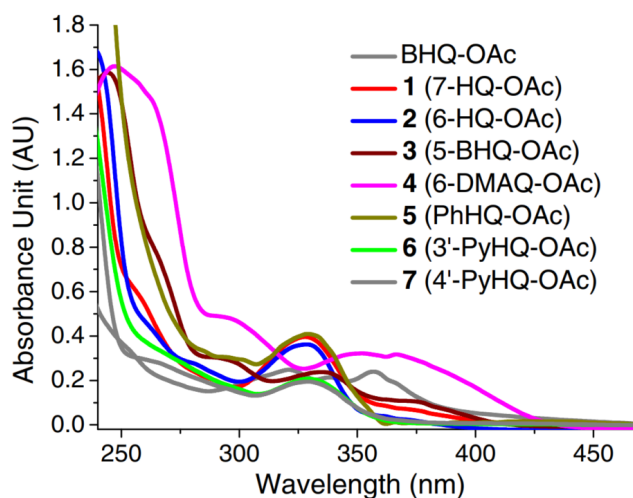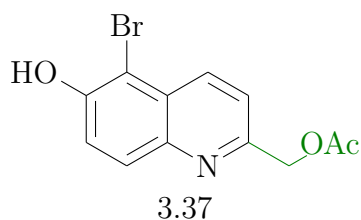


**Φ:** none given

**Comments:** Brown curve labelled 3(5-BHQ-OAc).  100 *μ*M in KMOPS. Reprinted with permission from [219].

### 3.38 8-nitro-7-hydroxyquinolinyl [221]
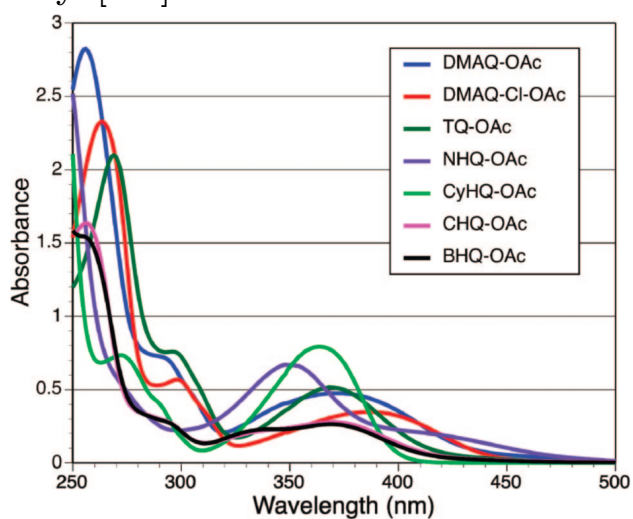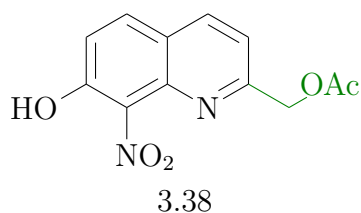


**Φ:** 0.00

**Comments:** Violet curve labelled NHQ-OAc. 100 *μ*M in KMOPS. Reprinted with permission from [221]. Copyright 2009 American Chemical Society.

## 3.39 7-dimethylamino-4-chloro-quinolin [221]
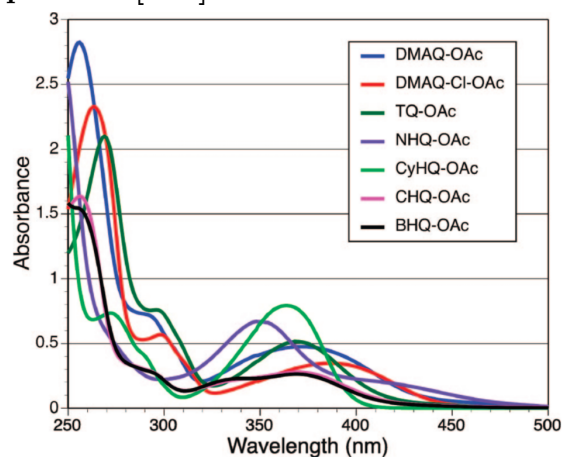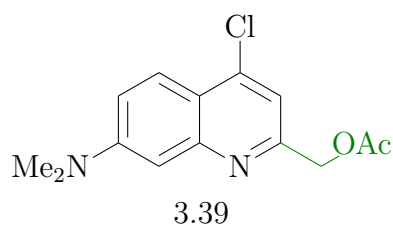


**Φ:** 0.09

**Comments:** Red curve labelled DMAQ-Cl-OAc. 100 $\mu$M in KMOPS. Reprinted with permission from [221]. Copyright 2009 American Chemical Society.

## 3.40 7-hydroxy-8-phenyl quinoline [219]
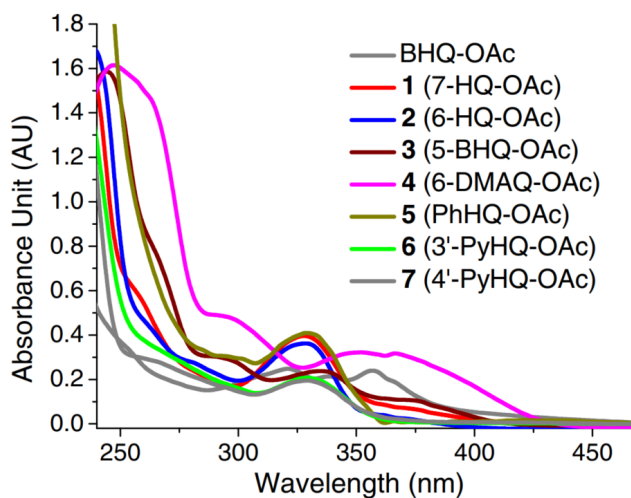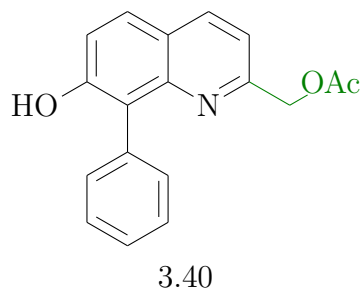


**Φ:** none given

**Comments:** Olive curve labelled 5 (PhHQ-OAc). 100 $\mu$M in KMOPS. Reprinted with permission from [219].

### 3.41 7-hydroxy-8-3'-pyridin quinoline [**219**]
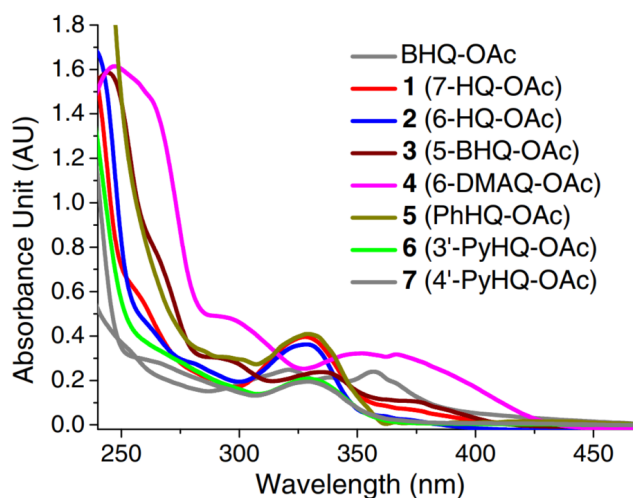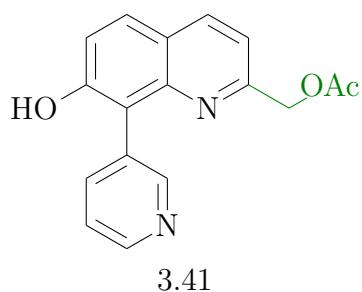


**Φ:** none given

**Comments:** Green curve labelled 6 (3'-PyHQ-OAc). 100 $\mu$M in KMOPS. Reprinted with permission from [219].

### 3.42 4'-PyHQ-OAc [**219**]
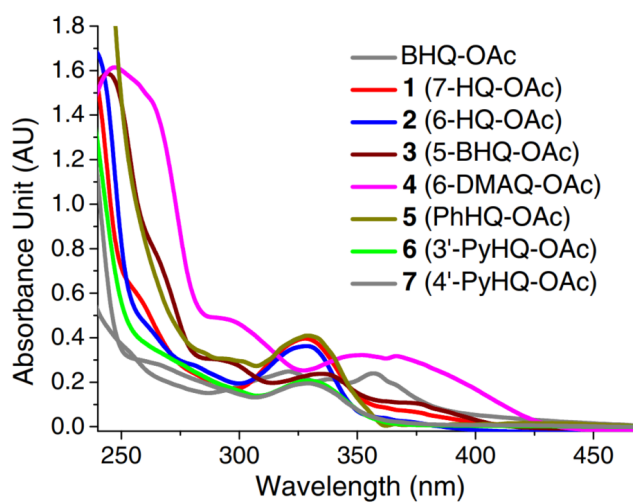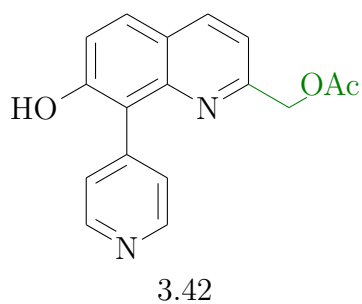


**Φ:** none given

**Comments:** Grey curve labelled 7 (4'-PyHQ-OAc). 100 $\mu$M in KMOPS. Reprinted with permission from [219].

**3.43 2-methyl-8-nitro-quinoline [225]**
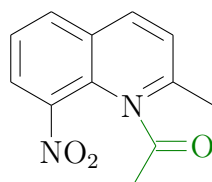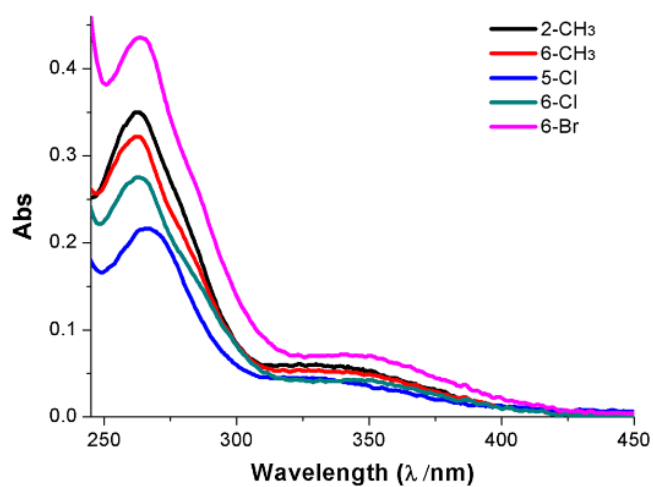


**Φ:** none given
**Comments:** Black curve labelled 2-CH$_3$. Measured in MeOH/H$_2$O (1:1). Reprinted with permission from [225].

**3.44 6-methyl-8-nitro-quinoline [225]**
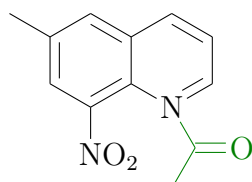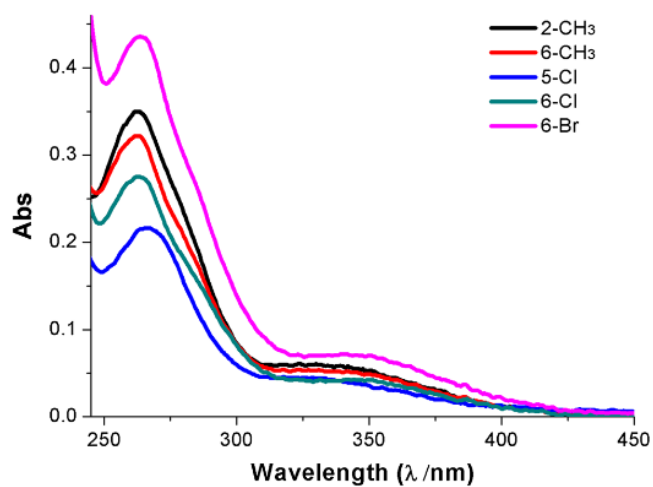


**Φ:** none given
**Comments:** Red curve labelled 6-CH$_3$. Measured in MeOH/H$_2$O (1:1). Reprinted with permission from [225].

171

### 3.45 5-chloro-8-nitro-quinoline [225]
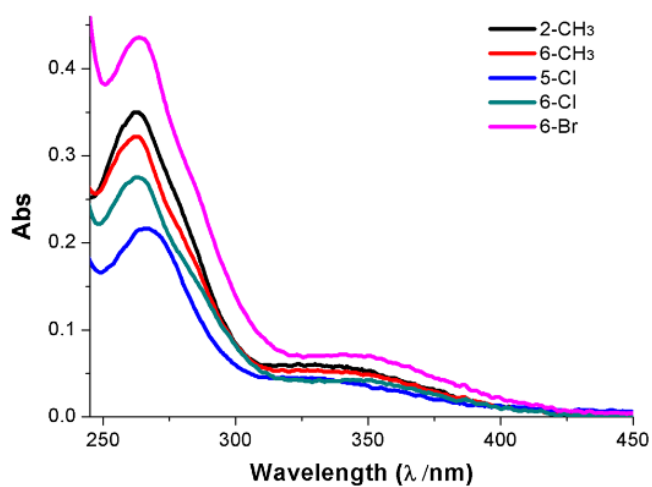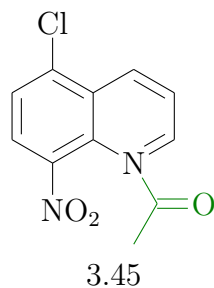


**Φ:** none given
**Comments:** Blue curve labelled 6-Cl. Measured in MeOH/H$_2$O (1:1). Reprinted with permission from [225].

### 3.46 6-chloro-8-nitro-quinoline [225]
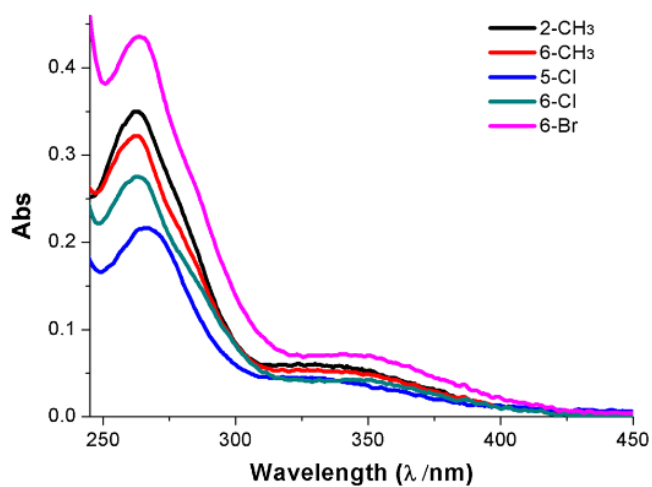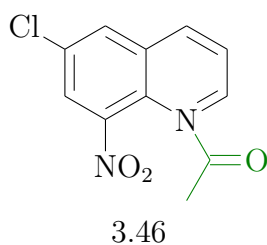


**Φ:** none given
**Comments:** Dark cyan curve labelled 6-Cl. Measured in MeOH/H$_2$O (1:1). Reprinted with permission from [225].

### 3.47 6-bromo-8-nitro-quinoline [225]
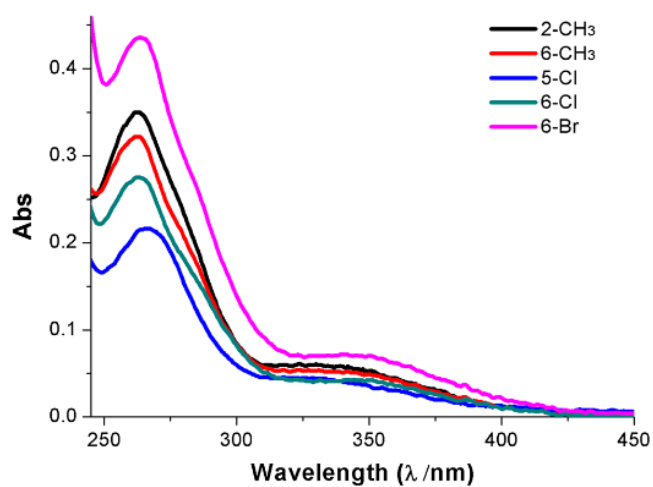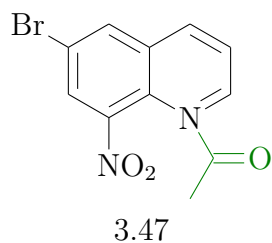


**Φ:** none given

**Comments:** Magenta curve labelled 6-Br. Measured in MeOH/H$_2$O (1:1). Reprinted with permission from [225].

# A.4 Phenacyl Cages

### 4.1 Phenacyl benzoate [226]
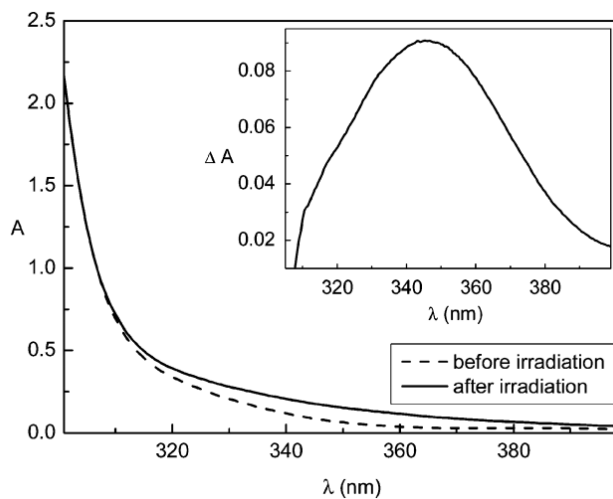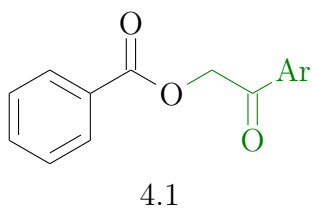


**Φ:** none given

**Comments:** Solid line measured in propan-2-ol (IPA). Ar = phenyl. The inset displays a differential spectrum of an light absorbing transient (LAT). Reprinted with permission from [226]. Copyright 2006 American Chemical Society.

## 4.2 Diethylphosphate Acetophenone (DPAP) [142]
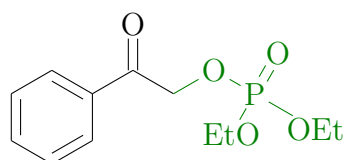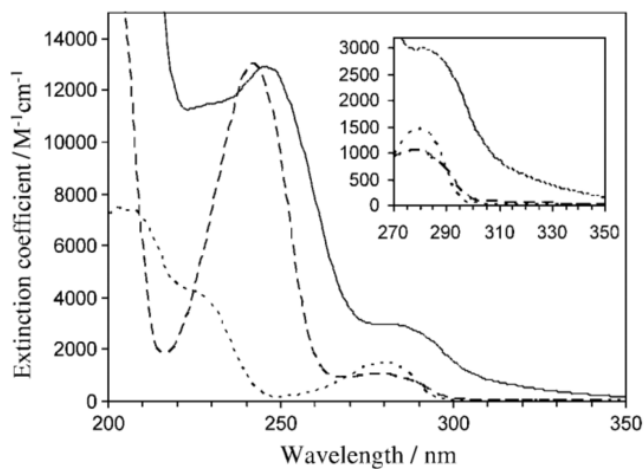


**Φ:** none given
**Comments:** Dashed line measured in CH$_3$CN. The inset shows enlarged spectra for the weak absorption in the 270 nm to 350 nm wavelength range. Reprinted with permission from [142].

## 4.3 2-(2-Hydroxyphenyl)-2-oxoethyl Benzoate [227]
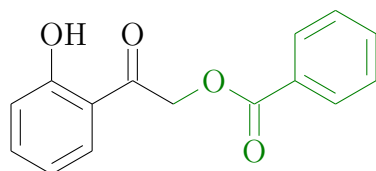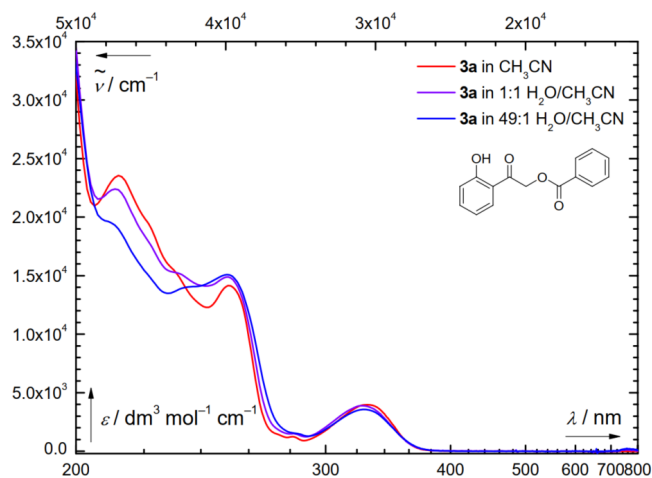


**Φ:** none given
**Comments:** Measured in dry and aqueous MeCN. Reprinted with permission from SI of [227].

### 4.4 2-(2-Methoxyphenyl)-2-oxoethyl Acetate [227]
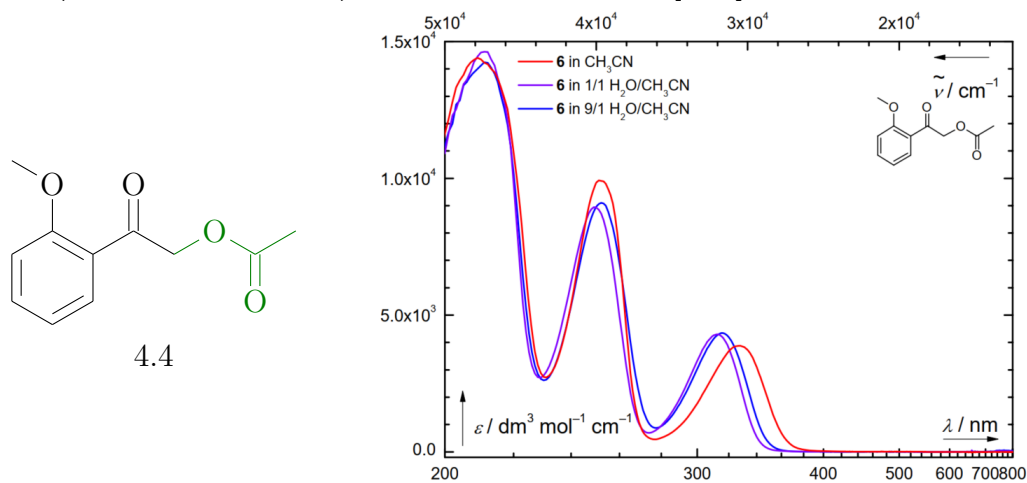


**Φ:** none given
**Comments:** Measured in dry and aqueous MeCN. Reprinted with permission from SI of [227].

### 4.5 Irgacure-2959 [228]
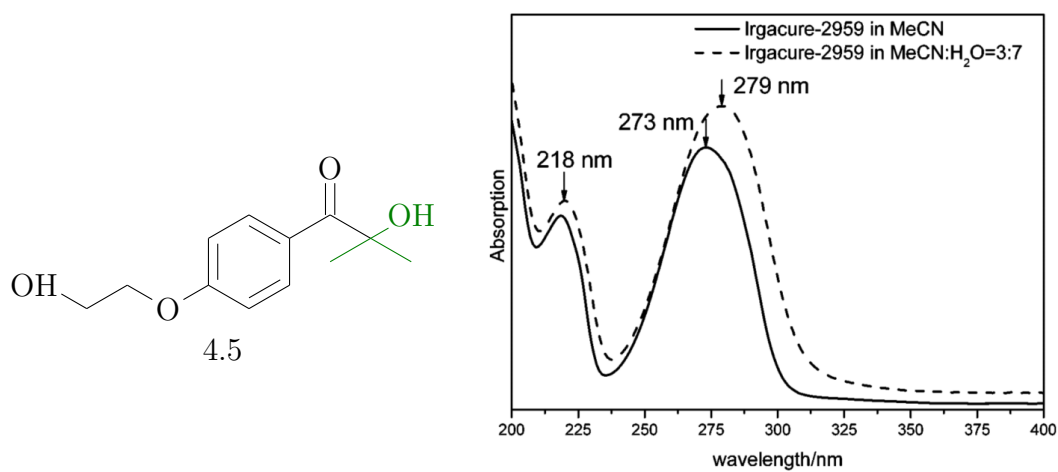


**Φ:** 0.29
**Comments:** Measured in MeCN and MeCN/$H_2O$ 3:7. Reprinted with permission from [228]. Copyright 2014 American Chemical Society.

## 4.6 3',5'-dimethoxybenzylic diethyl phosphate (DMBnDP) [142]
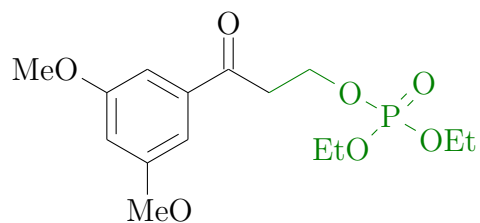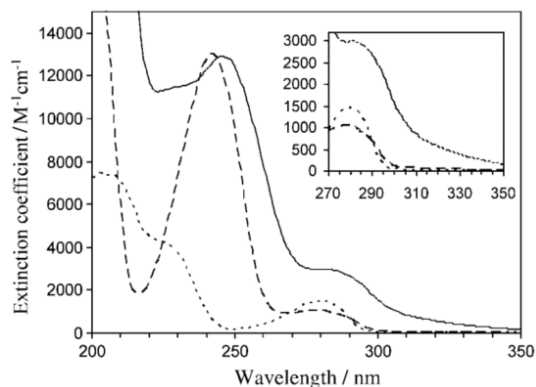


**Φ:** none given
**Comments:** Dotted line measured in CH$_3$CN. The inset shows enlarged spectra for the weak absorption in the 270 nm to 350 nm wavelength range. Reprinted with permission from [142].

## *p*-Hydroxyphenacyl

### 4.7 *p*-Hydroxyphenacyl phosphate [139]
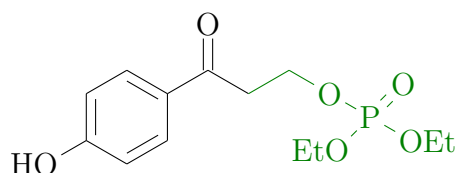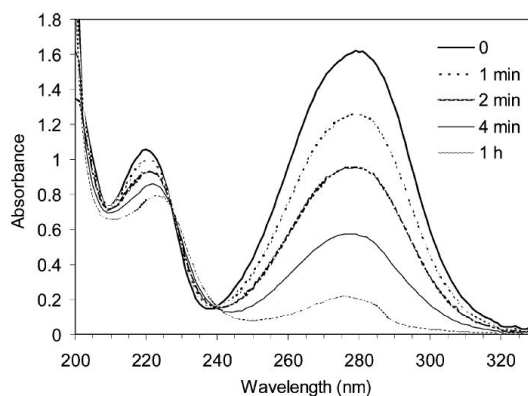


**Φ:** 0.4
**Comments:** 0.1 mM in H$_2$O:MeCN (1:1), irradiation with 267 nm, in the thesis as 4.a. Reprinted with permission from [139]. Copyright (2006) American Chemical Society. Other spectroscopic data on esters in [152], on Glu and GABA in [153], Diazo *p*HP in [229], various LG in [230].

### 4.8 extended *p*-Hydroxyphenacyl phosphate [231]



4.8
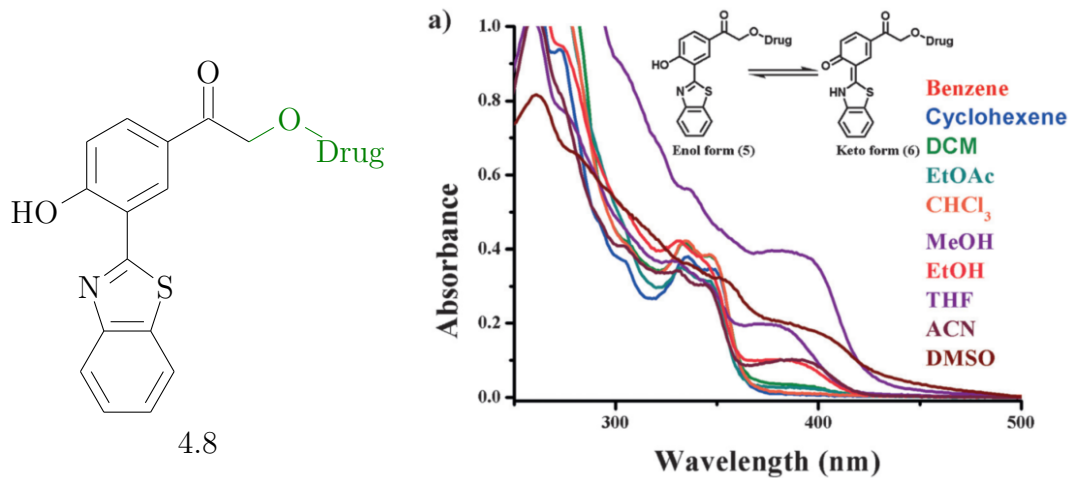
**Φ:** 0.46

**Comments:** Various solvents: ACN=acetonitrile, DCM=dichloromethane. Reprinted with permission from [231].

## pHP derivatives published in PhD theses

### 4.9 Meta Methoxy *p*-Hydroxyphenacyl phosphate [229]



4.9
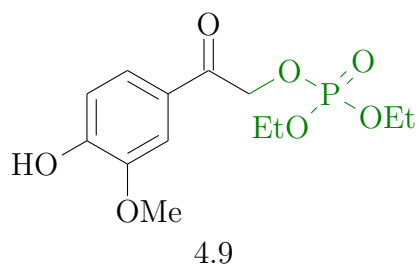
### 4.10 Meta Dimethoxy *p*-Hydroxyphenacyl phosphate [229]



4.10
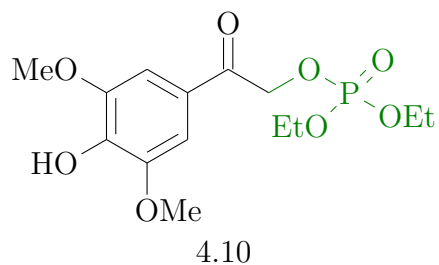
**4.11 Ortho Methoxy *p*-Hydroxyphenacyl phosphate [229]**
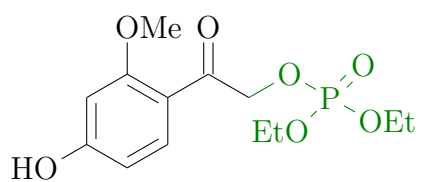


4.11

**4.12 Ortho Dimethoxy *p*-Hydroxyphenacyl phosphate [229]**
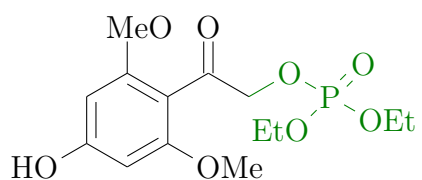


4.12

**4.13 Cyano *p*-Hydroxyphenacyl phosphate [232]**
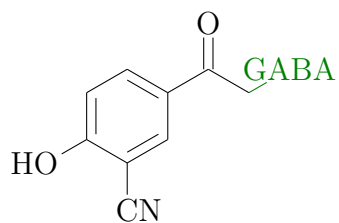


4.13

**4.14 *o*-Fluorinated *p*-Hydroxyphenacyl phosphate [233]**
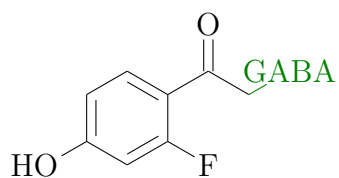


4.14

**4.15 Fluorinated *p*-Hydroxyphenacyl phosphate [233]**

4.15
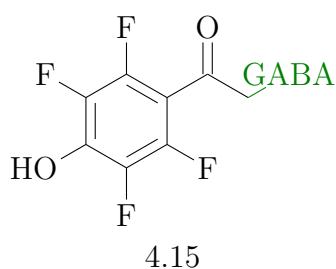
# A.5 Other Cages

**5.1 *meso*-methylhydroxy BODIPY [137]**

5.1
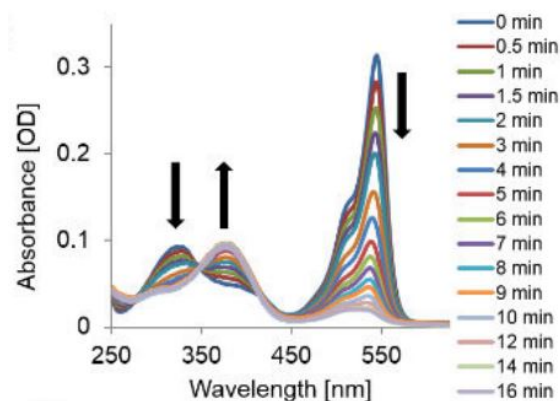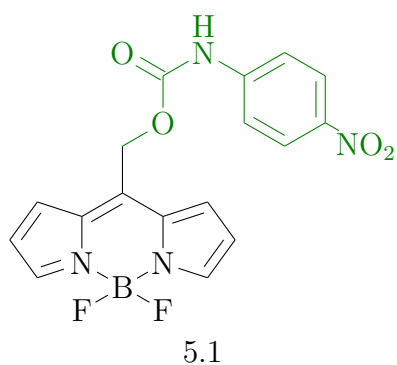
**Φ:** $6\times10^{-4}$

**Comments:** 100 $\mu$M in PBS pH 7.4 supplemented with 5 % ACN, 540/30 nm (49 mWcm$^2$, irradiated samples were diluted 20-folg for measurement. Adapted from [138] with permission from The Royal Society of Chemistry.

## 5.2 *m*-dimethylamino trityl (DMATr [234]



5.2
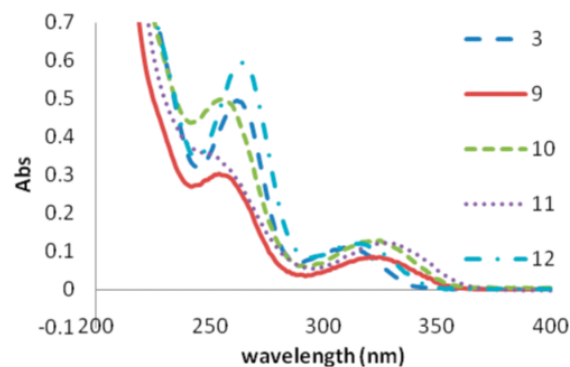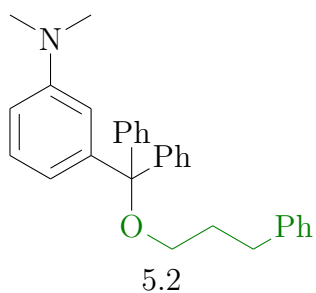
**Φ:** 0.2
**Comments:** Blue dashed curve labelled 3. Reprinted with permission from [234]. Copyright 2011 American Chemical Society.

## 5.3 methoxy *m*-dimethylamino trityl [234]



5.3
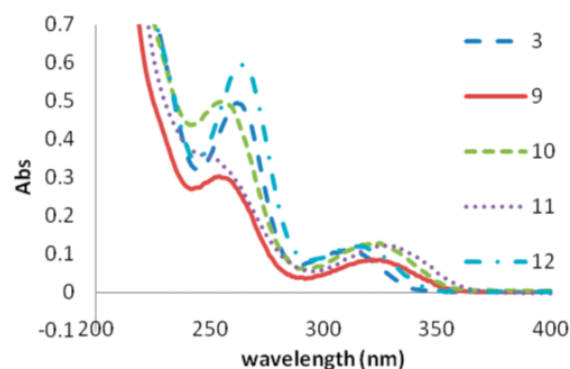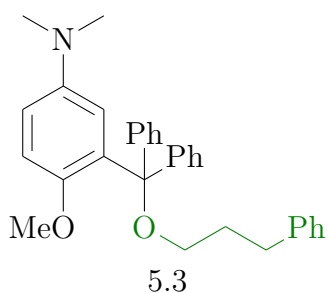
**Φ:** 0.19
**Comments:** Red solid curve labelled 9. Reprinted with permission from [234]. Copyright 2011 American Chemical Society.

## 5.4 TBDMSO *m*-dimethylamino trityl [**234**]
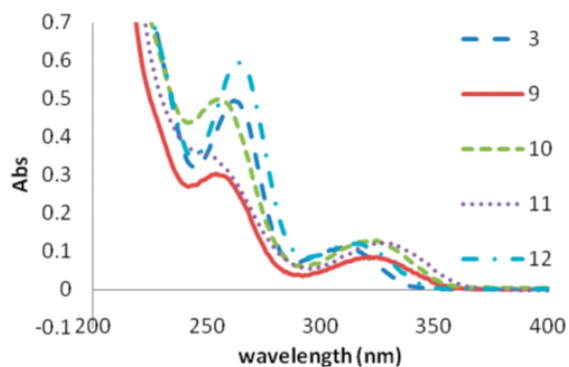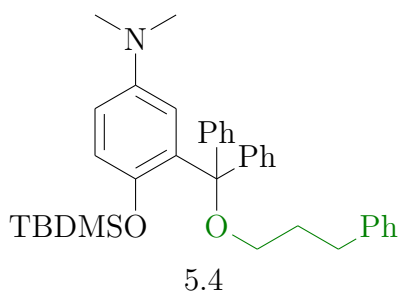


**Φ:** 0.2

**Comments:** Green dashed curve labelled 10. Reprinted with permission from [234]. Copyright 2011 American Chemical Society.

## 5.5 Hydroxy *m*-dimethylamino trityl [**234**]
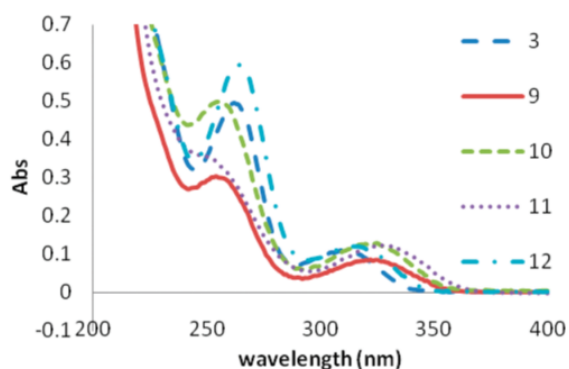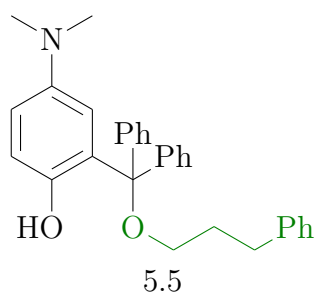


**Φ:** 0.2

**Comments:** Violet dotted curve labelled 11. Reprinted with permission from [234]. Copyright 2011 American Chemical Society.

## 5.6 Acetylether *m*-dimethylamino trityl [234]
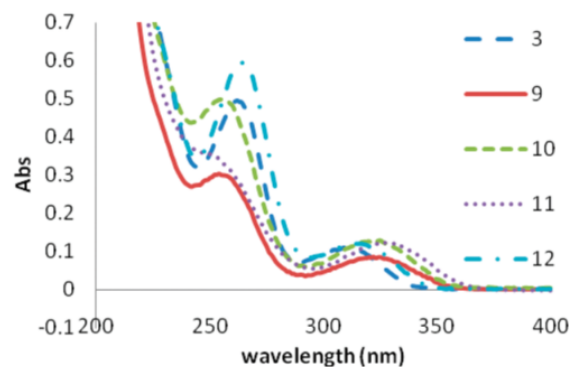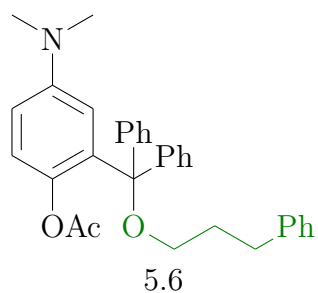


**Φ:** 0.07
**Comments:** Blue dashed curve labelled 12. Reprinted with permission from [234]. Copyright 2011 American Chemical Society.

## 5.7 *o*-hydroxyphenyl cinnamate [235]
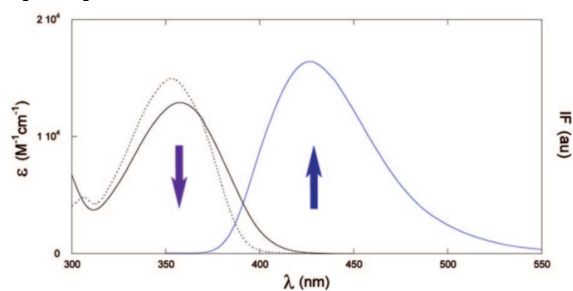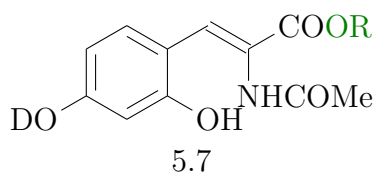


**Φ:** none given
**Comments:** Black solid line. Measured at 293 K in Tris PH 7, 20 mM NaCl, 100 mM buffer/acetonitrile 1/1 (v/v). Additional spectral data in [236].

### 5.8 Dibromohydroxyphenyl cinnamate [237]
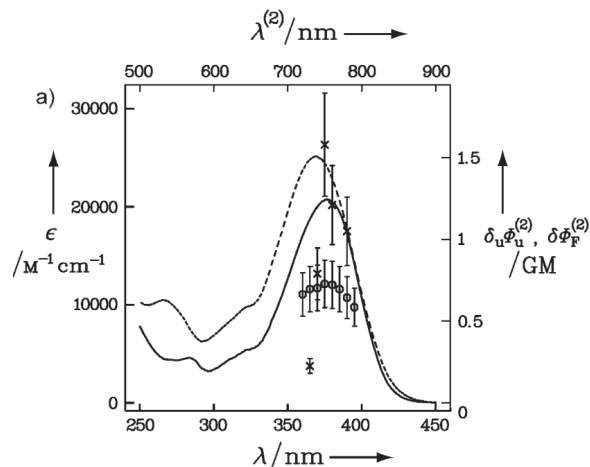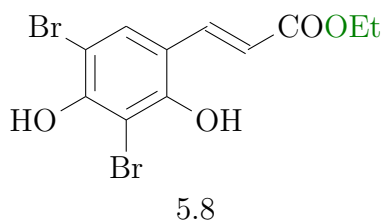


**Φ:** none given
**Comments:** Dashed line. Reprinted with permission from [237]. Copyright 2007 American Chemical Society.

### 5.9 Anthraquinon-2-ylmethoxycarbonyl (Aqmoc) [238]
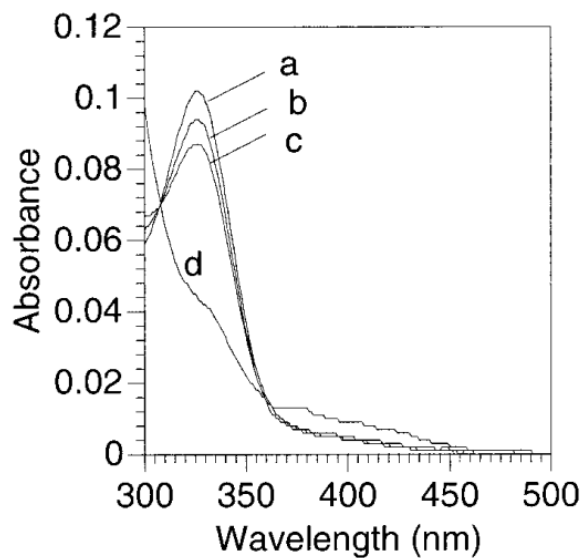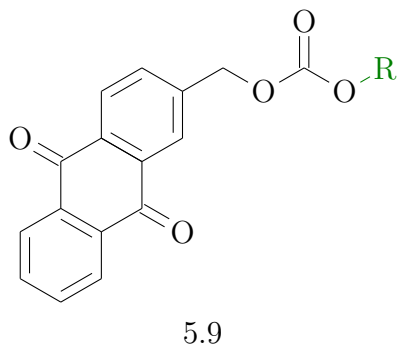


**Φ:** 0.1
**Comments:** Curve labelled a. 2.5 $\mu$M Aqmoc-Gal in THF-$H_2$O. Reprinted with permission from [238]. Copyright 2001 American Chemical Society.

**5.10 2-acetonaphthyl cage [169]**
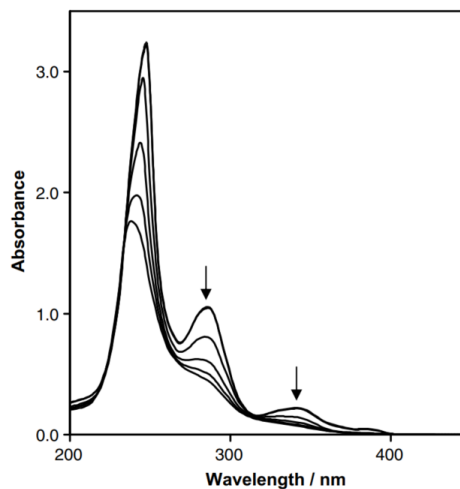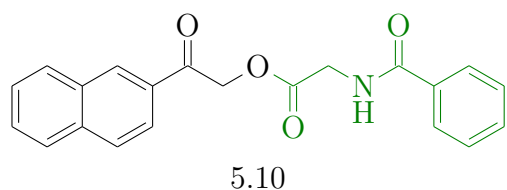


**Φ:** 0.117

**Comments:** Measured in THF-H$_2$O (1:1, v/v, 1x10$^{-4}$ M. Reprinted with permission from [169].

**5.11 5-(Ethylen-2-yl)-1,4-naphthoquinone [239]**
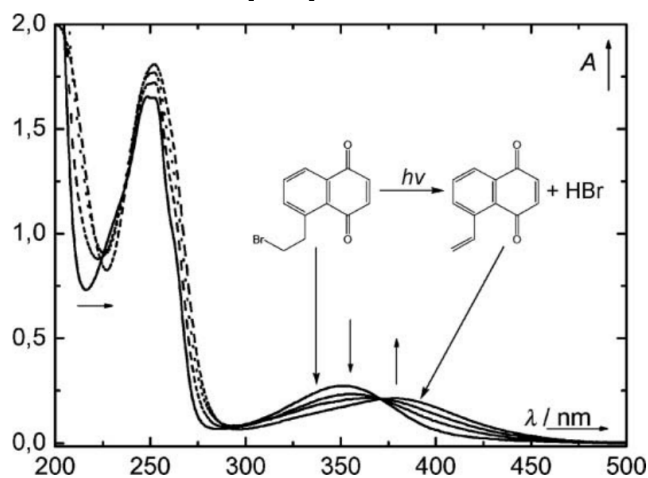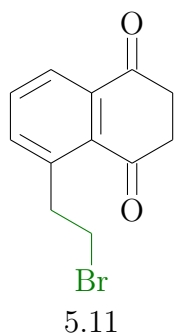


**Φ:** none given

**Comments:** 2.0 x 10$^{-4}$ M, cm path length in aqueous solution. Reproduced from [239] with permission from the European Society for Photobiology, the European Photochemistry Association, and The Royal Society of Chemistry.

### 5.12 Acetylpyrene [240]



5.12
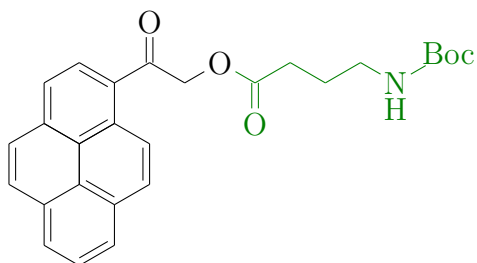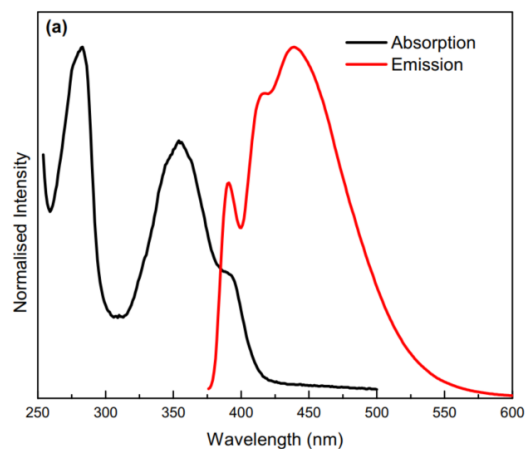
**Φ:**  0.28

**Comments:** Black line measured from 2.0 x $10^{-6}$ M in EtOH. Preprinter with permission from [240].

### 5.13 Ketoprofen [241]



5.13

$CO_2^-$
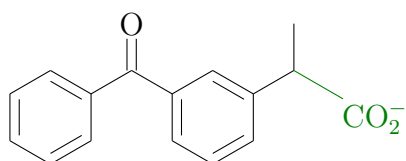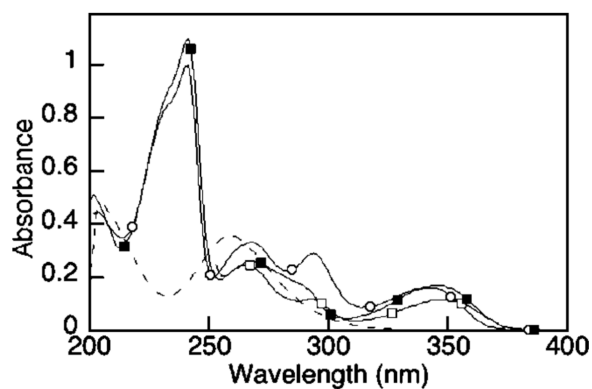
**Φ:**  none given

**Comments:** Dashed line measured from 2 x $10^{-5}$ M in pH 7.4 phosphate buffer.  Reprinted with permission from [241].  Copyright 2009 American Chemical Society.

**5.14 2-Xanthone [241]**
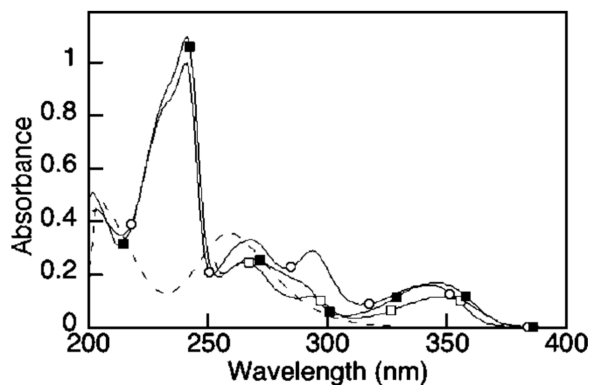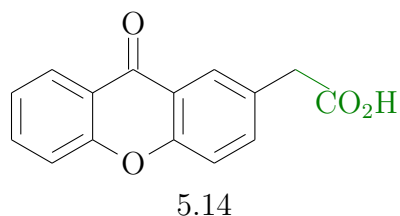


**Φ:** 0.67

**Comments:** Curve labelled with open squares measured from 2 x $10^{-5}$ M in pH 7.4 phosphate buffer. Reprinted with permission from [241]. Copyright 2009 American Chemical Society.

**5.15 3-Xanthone [241]**



**Φ:** < 0.01
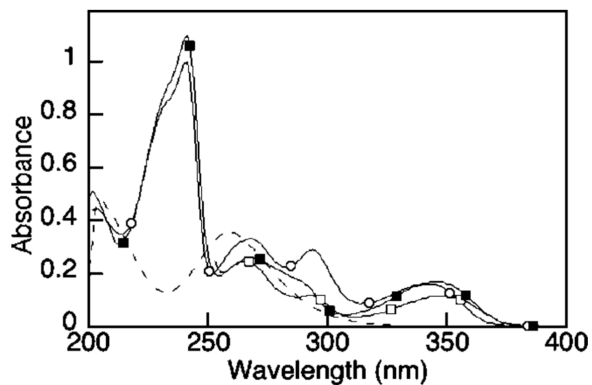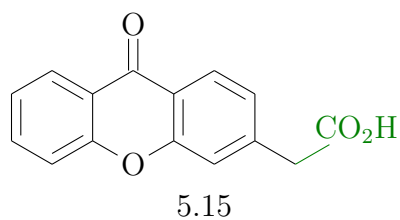
**Comments:** Curve labelled with open circles measured from 2 x $10^{-5}$ M in pH 7.4 phosphate buffer. Reprinted with permission from [241]. Copyright 2009 American Chemical Society.

**5.16 4-Xanthone [241]**
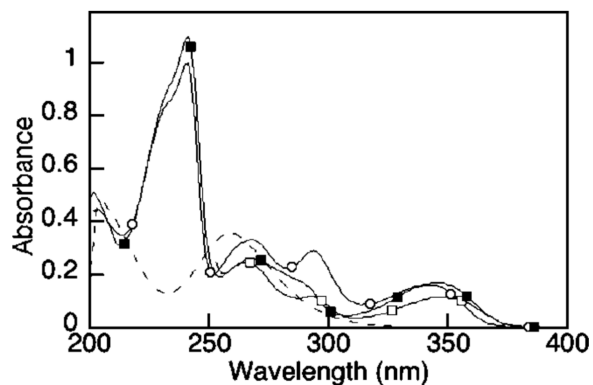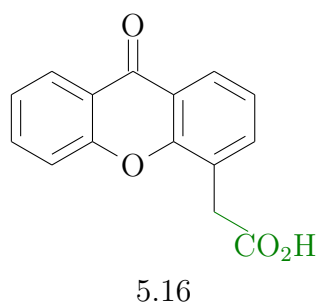


**Φ:** 0.64
**Comments:** Curve labelled with full squares measured from 2 x $10^{-5}$ M in pH 7.4 phosphate buffer. Reprinted with permission from [241]. Copyright 2009 American Chemical Society.

**5.17 Xanthonate acetate [241]**
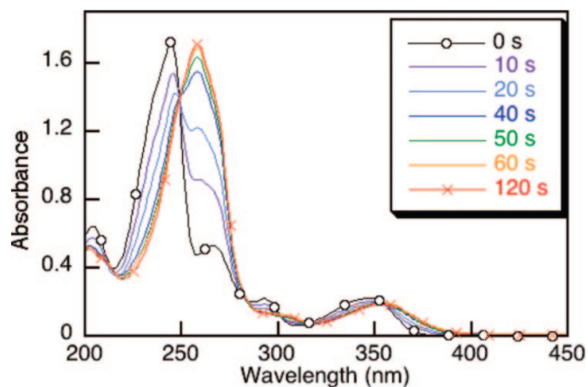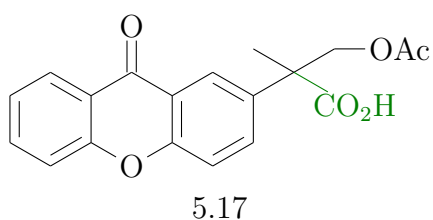


**Φ:** none given
**Comments:** Black curve labelled with open circles measured from 4.0 x $10^{-5}$ M. Reprinted with permission from [241]. Copyright 2009 American Chemical Society.

# B Synthetic & Computational Cooperation

As this thesis was part of a research training group the work was part of a tight cooperation of multiple PhD theses.

**Synthesis** The synthesis of the coumarin azide was started by Alexandre Correia of Prof. Heckels group. To synthesis isotopologues and isotomopers Matiss Reinfelds developed a synthesis strategy from $^{13}$C labelled starting material. A shortened synthesis way is shown in figure B.1 for the $2^{13}$C and $4^{13}$C isotopomers. The coumarin ring system is synthesized by Pechmann condensation and the azide leaving group is added via an enamine which is cleaved to an aldehyde and reduced to an alcohol. This was subsequently mesylated and reacted with sodium azide to yeld the DEACM azide.
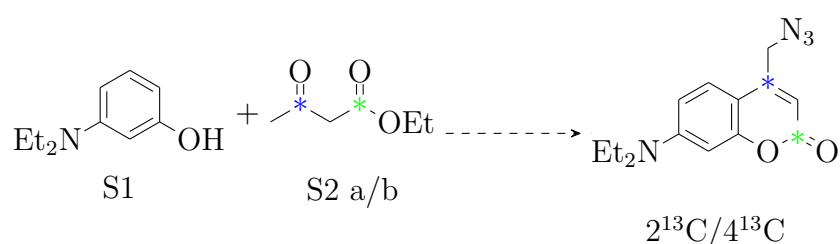


Figure B.1: Synthesis of $2^{13}$C and $4^{13}$C isotopomers from 3-Diethylaminophenol (S1) and ethyl acetoacetate-1-$^{13}$C (S2a) or ethyl acetoacetate-3-$^{13}$C (S2b).

The strategy is detailed in our publication [61] and in Matiss PhD thesis [150] which also includes an analysis of the photoproducts with chromatography and NMR spectroscopy methods.

Matiss also synthesised the *p*HP samples used in this work. For the species with $^{13}$C labelled LG commercially available *p*HP bromide was reacted with ammonium thiocyanate ( figure B.2 on the next page).

For the species in which all the ring atoms are labelled with $^{13}$C the *p*HP bromied was synthesised by a Friedel-Crafts acylation as shown in figure B.3.
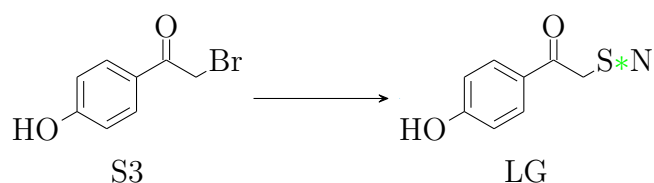
Figure B.2: Synthesis of *p*HP SCN with $^{13}$C label in LG from *p*HP bromide (S3).
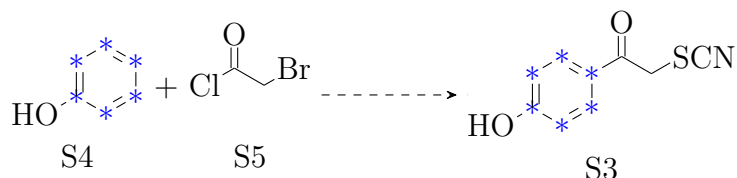


Figure B.3: Synthesis of *p*HP SCN with $^{13}$C labels in the ring from 13 C-labeled phenol (S4) and 2-bromoacetyl chloride (S5).

The synthesis details as well as analysis of the photo products are part of Matiss PhD thesis ([150]).

**Computations of IR excitatied UV-Vis spectra**   The computational prediction of the effect of the IR pre-excitation in the UV-Vis spectrum was carried out by Jan von Cosel in his PhD thesis [117] in the Burghardt group.

Multiple approaches were applied and are discussed in [116]. The data shown in this thesis was computed with the analytic time approach [242] based on an harmonic approximation of the potential energy surface (PES). The electronic structure calculations for DEACM and *p*HP were carried out with Gaussian09 (revision D.01) [160]. Density functional theory (DFT) was used for the ground state and the time-dependent extension (TD-DFT) was used for the excited state. Equilibrium geometries and normal modes were obtained. A harmonic PES was constructed within the Adiabatic Hessian (AH) [243] approach.

The vibronic absorption spectra were subsequently computed with a development version of the FCclasses code [244–246]. The spectrum without IR pre-excitation was computed from an initial state corresponding to the global vobrational ground state at zero Kelvin. For the spectra with IR pre-excitation one quantum was placed into a specific normal mode while all other modes were in the ground state.

Detail on the computations are given in our publications [61, 116] and Jan's PhD thesis [117].

# C Fit Residues

Fit residues belonging to global analysis data shown in figure 5.27 on page 87. For details the used data analysis see section 4.1 on page 54.
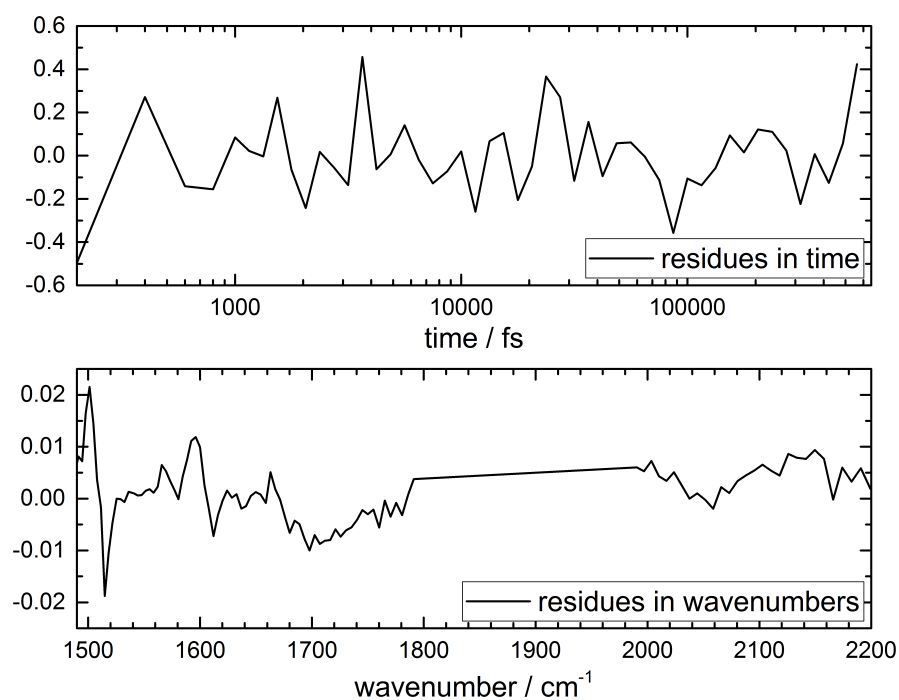


Figure C.1: Residues for global fit in figure 5.27 on page 87. Top: Averaged sum of the residuals in wavenumbers. Bottom: Averaged sum of the residuals in time. 7 components, SSE: 0.359. VIS 62, VIS 64-66
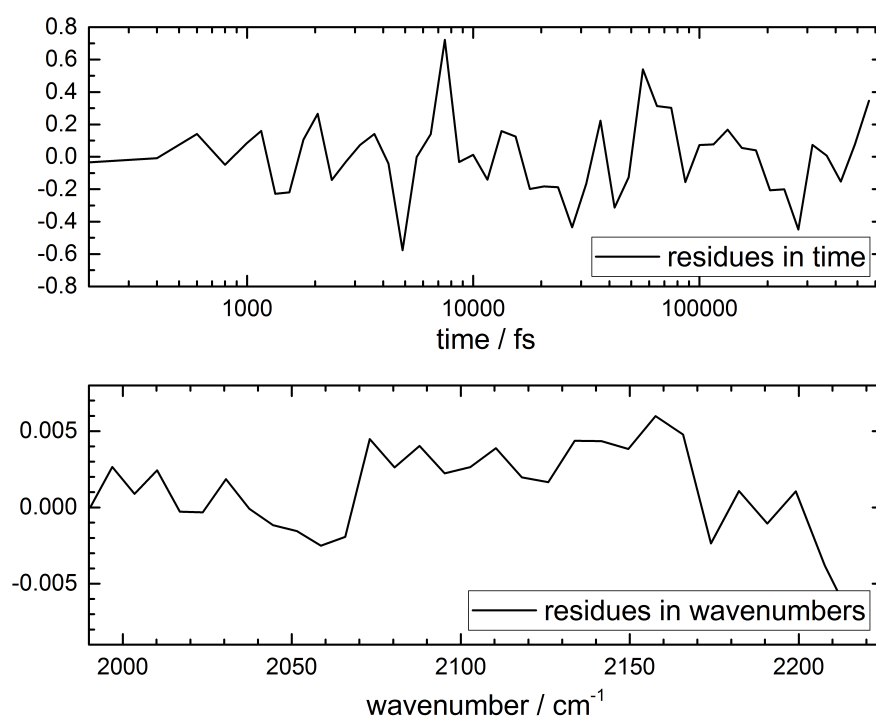
Figure C.2: Residues for global fit in upper panel of figure 5.43 on page 107. Top: Averaged sum of the residuals in wavenumbers. Bottom: Averaged sum of the residuals in time. N components, SSE: 0.17691. VIS 64
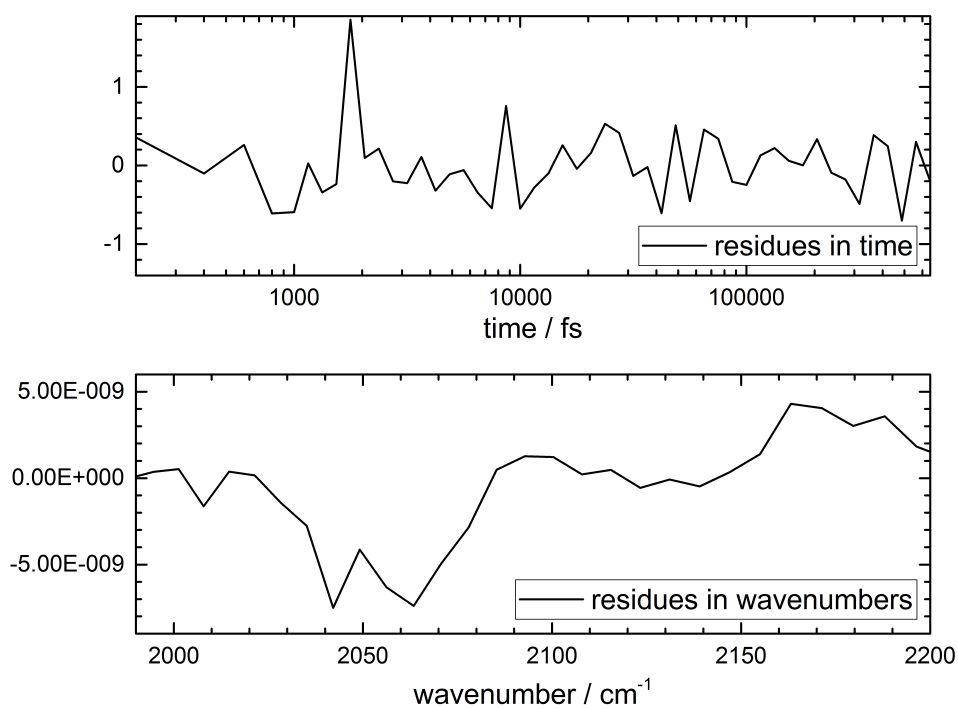
Figure C.3: Residues for global fit in lower panel of figure 5.43 on page 107. Top: Averaged sum of the residuals in wavenumbers. Bottom: Averaged sum of the residuals in time. N components, SSE: 0.7014. VIS 87

# Bibliography

(1)  Barltrop, J. A.; Schofield, P. *Tetrahedron Lett.* **1962**, *3*, 697–699.

(2)  Klán, P.; Šolomek, T.; Bochet, C. G.; Blanc, A.; Givens, R. S.; Rubina, M.; Popik, V. V.; Kostikov, A.; Wirz, J., *113*, 119–191.

(3)  Lee, H.-M.; Larson, D. R.; Lawrence, D. S. *ACS Chem. Biol.* **2009**, *4*, 409–427.

(4)  Mayer, G.; Heckel, A. *Angew. Chem.* **2006**, *45*, 4900–4921.

(5)  Specht, A.; Bolze, F.; Omran, Z.; Nicoud, J.; Goeldner, M. *HFSP journal* **2009**, *3*, 255–264.

(6)  Hansen, M. J.; Velema, W. A.; Lerch, M. M.; Szymański, W.; Feringa, B. L. *Chem. Soc. Rev.* **2015**, *44*, 3358–3377.

(7)  García-Fernández, L.; Herbivo, C.; Arranz, V. S. M.; Warther, D.; Donato, L.; Specht, A.; del Campo, A. *Adv. Mater.* **2014**, *26*, 5012–5017.

(8)  Rodrigues-Correia, A.; Knapp-Bühle, D.; Engels, J. W.; Heckel, A. *Org. Lett.* **2014**, *16*, 5128–5131.

(9)  Hayama, T.; Noguchi, J.; Watanabe, S.; Takahashi, N.; Hayashi-Takagi, A.; Ellis-Davies, G. C. R.; Matsuzaki, M.; Kasai, H. *Nat. Neurosci.* **2013**, *16*, 1409–1416.

(10)  Débieux, J.-L.; Bochet, C. G. *Chem. Sci.* **2012**, *3*, 405–406.

(11)  Bochet, C. G. *Tetrahedron Lett.* **2000**, *41*, 6341–6346.

(12)  del Campo, A.; Boos, D.; Spiess, H. W.; Jonas, U. *Angew. Chem.* **2005**, *44*, 4707–4712.

(13)  Scott, T. F.; Kowalski, B. A.; Sullivan, A. C.; Bowman, C. N.; McLeod, R. R. *Science* **2009**, *324*, 913–917.

(14)  San Miguel, V.; Bochet, C. G.; del Campo, A. *J. Am. Chem. Soc.* **2011**, *133*, 5380–5388.

(15)  Cui, J.; Miguel, V. S.; del Campo, A. *Macromol. Rapid Commun.* **2013**, *34*, 310–329.

(16)  Kessler, M.; Glatthar, R.; Giese, B.; Bochet, C. G. *Org. Lett.* **2003**, *5*, 1179–1181.

(17) Schäfer, F.; Joshi, K. B.; Fichte, M. A. H.; Mack, T.; Wachtveitl, J.; Heckel, A. *Org. Lett.* **2011**, *13*, 1450–1453.

(18) Menge, C.; Heckel, A. *Org. Lett.* **2011**, *13*, 4620–4623.

(19) Rodrigues-Correia, A.; Weyel, X. M. M.; Heckel, A. *Org. Lett.* **2013**, *15*, 5500–5503.

(20) Kantevari, S.; Matsuzaki, M.; Kanemoto, Y.; Kasai, H.; Ellis-Davies, G. C. R. *Nat. Methods* **2010**, *7*, 123–125.

(21) Stanton-Humphreys, M. N.; Taylor, R. D. T.; McDougall, C.; Hart, M. L.; Brown, C. T. A.; Emptage, N. J.; Conway, S. J. *ChemComm* **2012**, *48*, 657–659.

(22) Olson, J. P.; Banghart, M. R.; Sabatini, B. L.; Ellis-Davies, G. C. R. *J. Am. Chem. Soc.* **2013**, *135*, 15948–15954.

(23) Amatrudo, J. M.; Olson, J. P.; Agarwal, H. K.; Ellis-Davies, G. C. R. *Eur. J. Neurosci.* **2015**, *41*, 5–16.

(24) Fournier, L.; Gauron, C.; Xu, L.; Aujard, I.; Le Saux, T.; Gagey-Eilstein, N.; Maurin, S.; Dubruille, S.; Baudin, J.-B.; Bensimon, D.; Volovitch, M.; Vriz, S.; Jullien, L. *ACS Chem. Biol.* **2013**, *8*, 1528–1536.

(25) Yamazoe, S.; Liu, Q.; McQuade, L. E.; Deiters, A.; Chen, J. K. *Angew. Chem.* **2014**, *53*, 10114–10118.

(26) Priestman, M. A.; Sun, L.; Lawrence, D. S. *ACS Chem. Biol.* **2011**, *6*, 377–384.

(27) Goguen, B. N.; Aemissegger, A.; Imperiali, B. *J. Am. Chem. Soc.* **2011**, *133*, 11038–11041.

(28) Azagarsamy, M. A.; Anseth, K. S. *Angew. Chem.* **2013**, *52*, 13803–13807.

(29) Velema, W. A.; van der Berg, Jan Pieter; Szymański, W.; Driessen, A. J. M.; Feringa, B. L. *ACS Chem. Biol.* **2014**, *9*, 1969–1974.

(30) van Wilderen, L. J. G. W.; Messmer, A. T.; Bredenbeck, J. *Angew. Chem.* **2014**, *53*, 2667–2672.

(31) van Wilderen, L. J. G. W.; Bredenbeck, J. *Angew. Chem.* **2015**, *54*, 11624–11640.

(32) Bredenbeck, J.; Helbing, J.; Behrendt, R.; Renner, C.; Moroder, L.; Wachtveitl, J.; Hamm, P. *J. Phys. Chem. B* **2003**, *107*, 8654–8660.

(33) Andresen, E. R.; Hamm, P. *J. Phys. Chem. B* **2009**, *113*, 6520–6527.

(34) Cervetto, V.; Hamm, P.; Helbing, J. *J. Phys. Chem. B* **2008**, *112*, 8398–8405.

(35) Bredenbeck, J.; Helbing, J.; Sieg, A.; Schrader, T.; Zinth, W.; Renner, C.; Behrendt, R.; Moroder, L.; Wachtveitl, J.; Hamm, P. *Proc. Natl. Acad. Sci.* **2003**, *100*, 6452–6457.

(36) Kolano, C.; Helbing, J.; Kozinski, M.; Sander, W.; Hamm, P. *Nature* **2006**, *444*, 469–472.

(37) Tucker, M. J.; Abdo, M.; Courter, J. R.; Chen, J.; Brown, S. P.; Smith, A. B.; Hochstrasser, R. M. *Proc. Natl. Acad. Sci.* **2013**, *110*, 17314–17319.

(38) Delor, M.; Sazanovich, I. V.; Towrie, M.; Spall, S. J.; Keane, T.; Blake, A. J.; Wilson, C.; Meijer, Anthony J. H. M.; Weinstein, J. A. *J. Phys. Chem. B* **2014**, *118*, 11781–11791.

(39) Kiefer, L. M.; King, J. T.; Kubarych, K. J. *J. Phys. Chem. A* **2014**, *118*, 9853–9860.

(40) Kania, R.; Stewart, A. I.; Clark, I. P.; Greetham, G. M.; Parker, A. W.; Towrie, M.; Hunt, N. T. *Phys. Chem. Chem. Phys.* **2010**, *12*, 1051–1063.

(41) Lynch, M. S.; Slenkamp, K. M.; Khalil, M. *J. Chem. Phys.* **2012**, *136*, 241101.

(42) Lynch, M. S.; Slenkamp, K. M.; Cheng, M.; Khalil, M. *J. Phys. Chem. A* **2012**, *116*, 7023–7032.

(43) Bredenbeck, J.; Helbing, J.; Hamm, P. *J. Am. Chem. Soc.* **2004**, *126*, 990–991.

(44) Xiong, W.; Laaser, J. E.; Paoprasert, P.; Franking, R. A.; Hamers, R. J.; Gopalan, P.; Zanni, M. T. *J. Am. Chem. Soc.* **2009**, *131*, 18040–18041.

(45) Bredenbeck, J.; Helbing, J.; Nienhaus, K.; Nienhaus, G. U.; Hamm, P. *Proc. Natl. Acad. Sci.* **2007**, *104*, 14243–14248.

(46) Stewart, A. I.; Wright, J. A.; Greetham, G. M.; Kaziannis, S.; Santabarbara, S.; Towrie, M.; Parker, A. W.; Pickett, C. J.; Hunt, N. T. *Inorg. Chem.* **2010**, *49*, 9563–9573.

(47) Baiz, C. R.; McCanne, R.; Kubarych, K. J. *J. Am. Chem. Soc.* **2009**, *131*, 13590–13591.

(48) Delor, M.; Scattergood, P. A.; Sazanovich, I. V.; Parker, A. W.; Greetham, G. M.; Meijer, Anthony J. H. M.; Towrie, M.; Weinstein, J. A. *Science* **2014**, *346*, 1492–1495.

(49) Yue, Y.; Grusenmeyer, T.; Ma, Z.; Zhang, P.; Schmehl, R. H.; Beratan, D. N.; Rubtsov, I. V. *Dalton Trans.* **2015**, *44*, 8609–8616.

(50) Iwaki, L. K.; Dlott, D. D. *J. Phys. Chem. A* **2000**, *104*, 9101–9112.

(51) Dlott, D. D. *Chem. Phys.* **2001**, *266*, 149–166.

(52) Laubereau, A.; Kaiser, W. *Rev. Mod. Phys.* **1978**, *50*, 607–665.

(53) Wright, J. C. *Annu. Rev. Phys. Chem.* **2011**, *62*, 209–230.

(54) Fournier, F.; Guo, R.; Gardner, E. M.; Donaldson, P. M.; Loeffeld, C.; Gould, I. R.; Willison, K. R.; Klug, D. R. *Acc. Chem. Res.* **2009**, *42*, 1322–1331.

(55) Zhao, W.; Wright, J. C. *Phys. Rev. Lett.* **2000**, *84*, 1411–1414.

(56) Zhao, W.; Wright, J. C. *Phys. Rev. Lett.* **1999**, *83*, 1950–1953.

(57) Hübner, H.-J.; Wörner, M.; Kaiser, W.; Seilmeier, A. *Chem. Phys. Lett.* **1991**, *182*, 315–320.

(58) Dahinten, T.; Baier, J.; Seilmeier, A. *Chem. Phys.* **1998**, *232*, 239–245.

(59) Mastron, J. N.; Tokmakoff, A. *J. Phys. Chem. A* **2018**, *122*, 554–562.

(60) Mastron, J. N.; Tokmakoff, A. *J. Phys. Chem. A* **2016**, *120*, 9178–9187.

(61) Kern-Michler, D.; Neumann, C.; Mielke, N.; van Wilderen, L. J. G. W.; Reinfelds, M.; von Cosel, J.; Santoro, F.; Heckel, A.; Burghardt, I.; Bredenbeck, J. *J. Am. Chem. Soc.* **2018**, *140*, 926–931.

(62) Mortimer, C. E.; Müller, U.; Beck, J., *Chemie: Das Basiswissen der Chemie*, 11., vollst. überarb. Aufl.; Thieme: Stuttgart, 2014.

(63) Walla, P. J., *Modern Biophysical Chemistry: Detection and Analysis of Biomolecules*, 2nd ed.; Wiley: Hoboken, 2014.

(64) Mäntele, W., *Biophysik*, 1. Aufl.; utb-studi-e-book, Vol. 3270; UTB GmbH: Stuttgart, 2012.

(65) Schmidt, W., *Optische Spektroskopie*, 2nd ed.; Wiley: Hoboken, 2014.

(66) Günzler, H.; Gremlich, H.-U., *IR-Spektroskopie*; Wiley-VCH Verlag GmbH & Co. KGaA: Weinheim, Germany, 2003.

(67) Winter, R., *Methoden der biophysikalischen Chemie*; Teubner: Stuttgart, 1998.

(68) Hamm, P.; Zanni, M. T., *Concepts and methods of 2d infrared spectroscopy*; Cambridge University Press: Cambridge, 2011.

(69) Lakowicz, J. R., *Principles of fluorescence spectroscopy*, Third edition, corrected at 4. printing; Springer: New York, NY, 2010.

(70) Young, D. D.; Deiters, A. *Org. Biomol. Chem.* **2007**, *5*, 999–1005.

(71) Curley, K.; Lawrence, D. S. *Pharmacol. Ther.* **1999**, *82*, 347–354.

(72) Dormán, G.; Prestwich, G. D. *Trends Biotechnol.* **2000**, *18*, 64–77.

(73) Tang, X.; Dmochowski, I. J. *Mol. Omics* **2007**, *3*, 100–110.

(74) Pelliccioli, A. P.; Wirz, J. *Photochem. Photobiol. Sci.* **2002**, *1*, 441–458.

(75) Bochet, C. G. *Angew. Chem.* **2001**, *40*, 2071–2073.

(76) Blanc, A.; Bochet, C. G. *J. Org. Chem.* **2002**, *67*, 5567–5577.

(77) Demtröder, W., *Laserspektroskopie 2: Experimentelle Techniken*, 6. neu bearb. und aktualisierte Aufl.; Springer: Berlin and Heidelberg, 2013.

(78) Abraham, H.; Lemoine, T. *Compt. Rend.* **1899**, *129, 206.*

(79) Zewail, A. H. *Angew. Chem.* **2000**, *39*, 2586–2631.

(80) Bloembergen, N. In *More Things in Heaven and Earth*, Bederson, B., Ed.; Springer New York: New York, NY, 1999, pp 474–481.

(81) Shapiro, S. L., *Ultrashort Light Pulses: Picosecond Techniques and Applications*; Topics in Applied Physics, Vol. 18; Springer: Berlin and Heidelberg, 1977.

(82) Fleming, G. R. *Annu. Rev. Phys. Chem.* **1986**, *37*, 81–104.

(83) Ataka, K.; Kottke, T.; Heberle, J. *Angew. Chem.* **2010**, *49*, 5416–5424.

(84) Anfinrud, P. A.; Han, C.; Hochstrasser, R. M. *Proc. Natl. Acad. Sci.* **1989**, *86*, 8387–8391.

(85) George, M. W. *Coord. Chem. Rev.* **1998**, *177*, 201–217.

(86) Groot, M. L.; van Wilderen, L. J. G. W.; Di Donato, M. *Photochem. Photobiol. Sci.* **2007**, *6*, 501.

(87) Dyer, R. B.; Woodruff, W. H. In *Encyclopedia of Inorganic and Bioinorganic Chemistry*, Scott, R. A., Ed.; John Wiley & Sons, Ltd: Chichester, UK, 2011; Vol. 25, p 131.

(88) Wynne, K.; Hochstrasser, R. M. *Chem. Phys.* **1995**, *193*, 211–236.

(89) Hamm, P.; Lim, M.; Hochstrasser, R. M. *J. Phys. Chem. B* **1998**, *102*, 6123–6138.

(90) Khalil, M.; Demirdöven, N.; Tokmakoff, A. *J. Phys. Chem. A* **2003**, *107*, 5258–5279.

(91) Hunt, N. T. *Chem. Soc. Rev.* **2009**, *38*, 1837–1848.

(92) Asplund, M. C.; Zanni, M. T.; Hochstrasser, R. M. *Proc. Natl. Acad. Sci.* **2000**, *97*, 8219–8224.

(93) Cervetto, V.; Helbing, J.; Bredenbeck, J.; Hamm, P. *J. Chem. Phys.* **2004**, *121*, 5935–5942.

(94)   Zanni, M. T.; Asplund, M. C.; Hochstrasser, R. M. *J. Am. Chem. Soc.* **2001**, *114*, 4579.

(95)   Demirdöven, N.; Khalil, M.; Tokmakoff, A. *J. Chem. Phys.* **2002**, *89*, 1612.

(96)   Roberts, S. T.; Loparo, J. J.; Tokmakoff, A. *J. Chem. Phys.* **2006**, *125*, 084502.

(97)   Kwak, K.; Park, S.; Finkelstein, I. J.; Fayer, M. D. *J. Chem. Phys.* **2007**, *127*, 124503.

(98)   Woutersen, S.; Hamm, P. *J. Phys. Chem. B* **2000**, *104*, 11316–11320.

(99)   Bian, H.; Li, J.; Wen, X.; Sun, Z.; Song, J.; Zhuang, W.; Zheng, J. *J. Phys. Chem. A* **2011**, *115*, 3357–3365.

(100)  Messmer, A. T.; Lippert, K. M.; Steinwand, S.; Lerch, E.-B. W.; Hof, K.; Ley, D.; Gerbig, D.; Hausmann, H.; Schreiner, P. R.; Bredenbeck, J. *Chem.: Eur. J.* **2012**, *18*, 14989–14995.

(101)  Messmer, A. T.; Lippert, K. M.; Schreiner, P. R.; Bredenbeck, J. *Phys. Chem. Chem. Phys.* **2013**, *15*, 1509–1517.

(102)  Kurochkin, D. V.; Naraharisetty, S. R. G.; Rubtsov, I. V. *Proc. Natl. Acad. Sci.* **2007**, *104*, 14209–14214.

(103)  Rubtsov, I. V. *Acc. Chem. Res.* **2009**, *42*, 1385–1394.

(104)  Müller-Werkmeister, H. M.; Li, Y.-L.; Lerch, E.-B. W.; Bigourd, D.; Bredenbeck, J. *Angew. Chem.* **2013**, *52*, 6214–6217.

(105)  Chen, H.; Bian, H.; Li, J.; Wen, X.; Zheng, J. *J. Phys. Chem. A* **2013**, *117*, 6052–6065.

(106)  Chen, H.; Bian, H.; Li, J.; Wen, X.; Zhang, Q.; Zhuang, W.; Zheng, J. *J. Phys. Chem. B* **2015**, *119*, 4333–4349.

(107)  Woutersen, S.; Mu, Y.; Stock, G.; Hamm, P. *Chem. Phys.* **2001**, *266*, 137–147.

(108)  Zheng, J.; Kwak, K.; Asbury, J.; Chen, X.; Piletic, I. R.; Fayer, M. D. *Science* **2005**, *309*, 1338–1343.

(109)  Zheng, J.-S. *Science* **2006**, *313*, 1951–1955.

(110)  Cahoon, J. F.; Sawyer, K. R.; Schlegel, J. P.; Harris, C. B. *Science* **2008**, *319*, 1820–1823.

(111)  Fayer, M. D. *Annu. Rev. Phys. Chem.* **2009**, *60*, 21–38.

(112)  Kim, Y. S.; Hochstrasser, R. M. *Proc. Natl. Acad. Sci.* **2005**, *102*, 11185–11190.

(113)   Ishikawa, H.; Kwak, K.; Chung, J. K.; Kim, S.; Fayer, M. D. *Proc. Natl. Acad. Sci.* **2008**, *105*, 8619–8624.

(114)   Ji, M.; Odelius, M.; Gaffney, K. J. *Science* **2010**, *328*, 1003–1005.

(115)   Olschewski, M.; Lindner, J.; Vöhringer, P. *Angew. Chem.* **2013**, *52*, 2375.

(116)   Von Cosel, J.; Cerezo, J.; Kern-Michler, D.; Neumann, C.; van Wilderen, L. J. G. W.; Bredenbeck, J.; Santoro, F.; Burghardt, I. *J. Chem. Phys.* **2017**, *147*, 164116.

(117)   Von Cosel, J. Simulation and Optimization of Viper Uncaging., Dissertation, Frankfurt am Main: Johann Wolfgang Goethe-Universität, 2018.

(118)   Courtney, T. L.; Fox, Z. W.; Slenkamp, K. M.; Khalil, M. *J. Chem. Phys.* **2015**, *143*, 154201.

(119)   Cheatum, C. M.; Heckscher, M. M.; Bingemann, D.; Crim, F. F. *J. Chem. Phys.* **2001**, *115*, 7086–7093.

(120)   Bredenbeck, J.; Helbing, J.; Hamm, P. *J. Chem. Phys.* **2004**, *121*, 5943–5957.

(121)   Messmer, A. T. Shedding Light on Reaction Mechanisms: Structure Determination of Reactive Intermediates and Investigation of Protein Structural Dynamics Using 2D-IR Spectroscopy., Dissertation, Frankfurt am Main: Johann Wolfgang Goethe-Universität.

(122)   Bakker, H. J.; Skinner, J. L. *Chem. Rev.* **2010**, *110*, 1498–1517.

(123)   Neumann, C. Analyzing and Optimizing the VIPER Effect., Dissertation, Frankfurt am Main: Johann Wolfgang Goethe-Universität, 2019.

(124)   Baiz, C. R.; Nee, M. J.; McCanne, R.; Kubarych, K. J. *Opt. Lett.* **2008**, *33*, 2533–2535.

(125)   Dieter Meschede, *Optik, Licht und Laser*; Vieweg+Teubner: Wiesbaden, 2008.

(126)   Boyd, R. W., *Nonlinear optics*, 3. ed.; Elsevier/Academic Press: Amsterdam, 2008.

(127)   Piel, J.; Beutter, M.; Riedle, E. *Opt. Lett.* **2000**, *25*, 180.

(128)   Riedle, E.; Beutter, M.; Lochbrunner, S.; Piel, J.; Schenkl, S.; Spörlein, S.; Zinth, W. *Appl. Phys. B* **2000**, *71*, 457–465.

(129)   Wang, P. *AsianJOC* **2013**, *2*, 452–464.

(130)   Brieke, C.; Rohrbach, F.; Gottschalk, A.; Mayer, G.; Heckel, A. *Angew. Chem.* **2012**, *51*, 8446–8476.

(131) Corrie, J. E. T.; Furuta, T.; Givens, R. S.; Yousef, A. L.; Goeldner, M. In *Dynamic Studies in Biology*, Goeldner, M., Givens, R. S., Eds.; Wiley-VCH Verlag GmbH & Co. KGaA: Weinheim, FRG, 2005, pp 1–94.

(132) Dormán, G.; Prestwich, G. D. *Trends Biotechnol.* **2000**, *18*, 64–77.

(133) Yu, H.; Li, J.; Wu, D.; Qiu, Z.; Zhang, Y. *Chem. Soc. Rev.* **2010**, *39*, 464–473.

(134) van Wilderen, L. J. G. W.; Neumann, C.; Rodrigues-Correia, A.; Kern-Michler, D.; Mielke, N.; Reinfelds, M.; Heckel, A.; Bredenbeck, J. *Phys. Chem. Chem. Phys.* **2017**, DOI: `10.1039/C6CP07022A`.

(135) Cameron, J. F.; Willson, C. G.; Fréchet, J. M. J. *J. Am. Chem. Soc.* **1996**, *118*, 12925–12937.

(136) Rhee, H.; Lee, J.-S.; Lee, J.; Joo, C.; Han, H.; Cho, M. *J. Phys. Chem. B* **2008**, *112*, 2128–2135.

(137) Rubinstein, N.; Liu, P.; Miller, E. W.; Weinstain, R. *ChemComm* **2015**, *51*, 6369–6372.

(138) Pinheiro, A. V.; Baptista, P. V.; Lima, J. C. *Nucleic Acids Res.* **2008**, *36*, e90.

(139) Ma, C.; Kwok, W. M.; Chan, W. S.; Du, Y.; Kan, J. T. W.; Toy, P. H.; Phillips, D. L. *J. Am. Chem. Soc.* **2006**, *128*, 2558–2570.

(140) Slanina, T.; Shrestha, P.; Palao, E.; Kand, D.; Peterson, J. A.; Dutton, A. S.; Rubinstein, N.; Weinstain, R.; Winter, A. H.; Klán, P. *J. Am. Chem. Soc.* **2017**, *139*, 15168–15175.

(141) Givens, R. S.; Heger, D.; Hellrung, B.; Kamdzhilov, Y.; Mac, M.; Conrad, P. G.; Cope, E. D.; Lee, J. I.; Mata-Segreda, J. F.; Schowen, R. L.; Wirz, J. *J. Am. Chem. Soc.* **2008**, *130*, 3307–3309.

(142) Ma, C.; Kwok, W. M.; An, H.-Y.; Guan, X.; Fu, M. Y.; Toy, P. H.; Phillips, D. L. *Chem.: Eur. J.* **2010**, *16*, 5102–5118.

(143) Schade, B.; Hagen, V.; Schmidt, R.; Herbrich, R.; Krause, E.; Eckardt, T.; Bendig, J. *J. Org. Chem.* **1999**, *64*, 9109–9117.

(144) Seibert, N. Charakterisierung von orthogonalen Coumarincages für VIPER Uncaging., Masterthesis, Frankfurt am Main: Johann Wolfgang Goethe-Universität, 2015.

(145) Givens, R. S.; Matuszewski, B. *J. Am. Chem. Soc.* **1984**, *106*, 6860–6861.

(146) Yamaji, M.; Nozaki, K.; Allonas, X.; Nakajima, S.; Tero-Kubota, S.; Marciniak, B. *J. Phys. Chem. A* **2009**, *113*, 5815–5822.

(147) Olson, J. P.; Kwon, H.-B.; Takasaki, K. T.; Chiu, C. Q.; Higley, M. J.; Sabatini, B. L.; Ellis-Davies, G. C. R. *J. Am. Chem. Soc.* **2013**, *135*, 5954–5957.

(148) Schmidt, R.; Geissler, D.; Hagen, V.; Bendig, J. *J. Phys. Chem. A* **2007**, *111*, 5768–5774.

(149) Schmidt, R.; Geissler, D.; Hagen, V.; Bendig, J. *J. Phys. Chem. A* **2005**, *109*, 5000–5004.

(150) Reinfelds, M. Design and Synthesis of New Photolabile Protecting Groups., Dissertation, Frankfurt am Main: Johann Wolfgang Goethe-Universität, 2018.

(151) Givens, R. S.; Park, C.-H. *Tetrahedron Lett.* **1996**, *37*, 6259–6262.

(152) Zhang, K.; Corrie, J. E. T.; Munasinghe, V. R. N.; Wan, P. *J. Am. Chem. Soc.* **1999**, *121*, 5625–5632.

(153) Conrad, P. G.; Givens, R. S.; Weber, J. F. W.; Kandler, K. *Org. Lett.* **2000**, *2*, 1545–1547.

(154) Givens, R. S.; Rubina, M.; Stensrud, K. F. *J. Org. Chem.* **2013**, *78*, 1709–1717.

(155) Ma, C.; Kwok, W. M.; Chan, W. S.; Zuo, P.; Wai Kan, J. T.; Toy, P. H.; Phillips, D. L. *J. Am. Chem. Soc.* **2005**, *127*, 1463–1472.

(156) Klicova, L.; Šebej, P.; Šolomek, T.; Hellrung, B.; Slavicek, P.; Klán, P.; Heger, D.; Wirz, J. *J. Phys. Chem. A* **2012**, *116*, 2935–2944.

(157) Bredenbeck, J.; Hamm, P. *Rev. Sci. Instrum.* **2003**, *74*, 3188.

(158) van Wilderen, L. J. G. W.; Lincoln, C. N.; van Thor, J. J. *PLOS ONE* **2011**, *6*, e17373.

(159) Neumann, C. Investigating Photocleavage Kinetics and Mechanism of Coumarin-Caged Compounds., Master thesis, Frankfurt am Main: Johann Wolfgang Goethe-Universität, 2014.

(160) M. J. Frisch, G. W. Trucks, H. B. Schlegel, G. E. Scuseria, M. A. Robb, J. R. Cheeseman, G. Scalmani, V. Barone, B. Mennucci, G. A. Petersson, H. Nakatsuji, M. Caricato, X. Li, H. P. Hratchian, A. F. Izmaylov, J. Bloino, G. Zheng, J. L. Sonnenberg, M. Hada, M. Ehara, K. Toyota, R. Fukuda, J. Hasegawa, M. Ishida, T. Nakajima, Y. Honda, O. Kitao, H. Nakai, T. Vreven, J. A. Montgomery, Jr., J. E. Peralta, F. Ogliaro, M. Bearpark, J. J. Heyd, E. Brothers, K. N. Kudin, V. N. Staroverov, R. Kobayashi, J. Normand, K. Raghavachari, A. Rendell, J. C. Burant, S. S. Iyengar, J. Tomasi, M. Cossi, N. Rega, J. M. Millam, M. Klene, J. E. Knox, J. B.

Cross, V. Bakken, C. Adamo, J. Jaramillo, R. Gomperts, R. E. Stratmann, O. Yazyev, A. J. Austin, R. Cammi, C. Pomelli, J. W. Ochterski, R. L. Martin, K. Morokuma, V. G. Zakrzewski, G. A. Voth, P. Salvador, J. J. Dannenberg, S. Dapprich, A. D. Daniels, O. Farkas, J. B. Foresman, J. V. Ortiz, J. Cioslowski; Fox, D. J. GAUSSIAN 09 Tevision D.01., Wallingford, CT, 2009.

(161) Cerullo, G.; de Silvestri, S. *Phys. Rev. Lett.* **2003**, *74*, 1–18.

(162) van Wilderen, L. J. G. W.; Kern-Michler, D.; Müller-Werkmeister, H. M.; Bredenbeck, J. *Phys. Chem. Chem. Phys.* **2014**, *16*, 19643–19653.

(163) Gaplovsky, M.; Il'ichev, Y. V.; Kamdzhilov, Y.; Kombarova, S. V.; Mac, M.; Schworer, M. A.; Wirz, J. *Photochem. Photobiol. Sci.* **2005**, *4*, 33–42.

(164) Görner, H. *Photochem. Photobiol. Sci.* **2005**, *4*, 822–828.

(165) Blanc, A.; Bochet, C. G. *Org. Lett.* **2007**, *9*, 2649–2651.

(166) Ellis-Davies, G. C. R.; Barsotti, R. J. *Cell calcium* **2006**, *39*, 75–83.

(167) Il'ichev, Y. V.; Schworer, M. A.; Wirz, J. *J. Am. Chem. Soc.* **2004**, *126*, 4581–4595.

(168) Blanc, A.; Bochet, C. G. *J. Am. Chem. Soc.* **2004**, *126*, 7174–7175.

(169) Khade, P. K.; Singh, A. K. *Tetrahedron Lett.* **2007**, *48*, 6920–6923.

(170) Walbert, S.; Pfleiderer, W.; Steiner, U. E. *Helv. Chim. Acta* **2001**, *84*, 1601–1611.

(171) Rossi, F. M.; Kao, J. P. Y. *J. Biol. Chem.* **1997**, *272*, 3266–3271.

(172) Wöll, D.; Smirnova, J.; Pfleiderer, W.; Steiner, U. E. *Angew. Chem.* **2006**, *45*, 2975–2978.

(173) Wöll, D.; Smirnova, J.; Galetskaya, M.; Prykota, T.; Buhler, J.; Stengele, K.-P.; Pfleiderer, W.; Steiner, U. E. *Chem.: Eur. J.* **2008**, *14*, 6490–6497.

(174) Wieboldt, R.; Ramesh, D.; Jabri, E.; Karplus, P. A.; Carpenter, B. K.; Hess, G. P. *J. Org. Chem.* **2002**, *67*, 8827–8831.

(175) Rossi, F. M.; Margulis, M.; Tang, C.-M.; Kao, J. P. Y. *J. Biol. Chem.* **1997**, *272*, 32933–32939.

(176) Kotzur, N.; Briand, B.; Beyermann, M.; Hagen, V. *J. Am. Chem. Soc.* **2009**, *131*, 16927–16931.

(177) Kotzur, N.; Briand, B.; Beyermann, M.; Hagen, V., 3255–3257.

(178) Breitinger, H.-G. A.; Wieboldt, R.; Ramesh, D.; Carpenter, B. K.; Hess, G. P. *Biochemistry* **2000**, *39*, 5500–5508.

(179)  Singh, A. K.; Khade, P. K. *Tetrahedron Lett.* **2011**, *38*, 4899–4902.

(180)  Aujard, I.; Benbrahim, C.; Gouget, M.; Ruel, O.; Baudin, J.-B.; Neveu, P.; Jullien, L. *Chem.: Eur. J.* **2006**, *12*, 6865–6879.

(181)  Stegmaier, P.; Alonso, J. M.; del Campo, A. *Langmuir* **2008**, *24*, 11872–11879.

(182)  Singh, A. K.; Khade, P. K. *Tetrahedron* **2005**, *61*, 10007–10012.

(183)  Berroy, P.; Viriot, M. L.; Carré, M. C. *Sens Actuator B Chem* **2001**, *74*, 186–189.

(184)  Omran, Z.; Specht, A. *J. Photochem. Photobiol. 208*, 125–130.

(185)  Russell, A. G.; Ragoussi, M.-E.; Ramalho, R.; Wharton, C. W.; Carteau, D.; Bassani, D. M.; Snaith, J. S. *J. Org. Chem. 75*, 4648–4651.

(186)  Gug, S.; Charon, S.; Specht, A.; Alarcon, K.; Ogden, D. C.; Zietz, B.; Leonard, J.; Haacke, S.; Bolze, F.; Nicoud, J.; Goeldner, M. *ChemBioChem* **2008**, *9*, 1303–1307.

(187)  Momotake, A.; Lindegger, N.; Niggli, E.; Barsotti, R. J.; Ellis-Davies, G. C. R. *Nat. Methods* **2006**, *3*, 35–40.

(188)  Kennedy, D. P.; Brown, D. C.; Burdette, S. C. *Org. Lett.* **2010**, *12*, 4486–4489.

(189)  Komori, N.; Jakkampudi, S.; Motoishi, R.; Abe, M.; Kamada, K.; Furukawa, K.; Katan, C.; Sawada, W.; Takahashi, N.; Kasai, H.; Xue, B.; Kobayashi, T. *ChemComm* **2016**, *52*, 331–334.

(190)  Papageorgiou, G.; Corrie, J. E. T. *Tetrahedron* **2000**, *56*, 8197–8205.

(191)  Morrison, J.; Wan, P.; Corrie, J. E. T.; Papageorgiou, G. *Photochem. Photobiol. Sci.* **2002**, *1*, 960.

(192)  Papageorgiou, G.; Ogden, D. C.; Kelly, G.; Corrie, J. E. T. *Photochem. Photobiol. Sci.* **2005**, *4*, 887–896.

(193)  Fedoryak, O. D.; Sul, J.-Y.; Haydon, P. G.; Ellis-Davies, G. C. R. *ChemComm* **2005**, 3664–3666.

(194)  Sheehan, J. C.; Wilson, R. M. *J. Am. Chem. Soc.* **1964**, *86*, 5277–5281.

(195)  Chan, W. S.; Ma, C.; Kwok, W. M.; Zuo, P.; Phillips, D. L. *J. Phys. Chem. A* **2004**, *108*, 4047–4058.

(196)  Ma, C.; Du, Y.; Kwok, W. M.; Phillips, D. L. *Chem.: Eur. J.* **2007**, *13*, 2290–2305.

(197)  Rock, R. S.; Chan, S. I. *J. Org. Chem.* **1996**, *61*, 1526–1529.

(198) Sheehan, J. C.; Wilson, R. M.; Oxford, A. W. *J. Am. Chem. Soc.* **1971**, *93*, 7222–7228.

(199) Stowell, M. H. B.; Wang, G.; Day, M. W.; Chan, S. I. *J. Am. Chem. Soc.* **1998**, *120*, 1657–1664.

(200) McCoy, C. P.; Rooney, C.; Edwards, C. R.; Jones, D. S.; Gorman, S. P. *J. Am. Chem. Soc.* **2007**, *129*, 9572–9573.

(201) Pirrung, M. C.; Shuey, S. W. *J. Org. Chem.* **1994**, *59*, 3890–3897.

(202) Rock, R. S.; Chan, S. I. *J. Am. Chem. Soc.* **1998**, *120*, 10766–10767.

(203) Eckardt, T.; Hagen, V.; Schade, B.; Schmidt, R.; Schweitzer, C.; Bendig, J. *J. Org. Chem.* **2002**, *67*, 703–710.

(204) Kamatham, N.; Mendes, D. C.; Da Silva, J. P.; Givens, R. S.; Ramamurthy, V. *Org. Lett.* **2016**, *18*, 5480–5483.

(205) Hagen, V.; Frings, S.; Wiesner, B.; Helm, S.; Kaupp, U. B.; Bendig, J. *ChemBioChem* **2003**, *4*, 434–442.

(206) Geissler, D.; Kresse, W.; Wiesner, B.; Bendig, J.; Kettenmann, H.; Hagen, V. *ChemBioChem* **2003**, *4*, 162–170.

(207) Taniguchi, A.; Skwarczynski, M.; Sohma, Y.; Okada, T.; Ikeda, K.; Prakash, H.; Mukai, H.; Hayashi, Y.; Kimura, T.; Hirota, S.; Matsuzaki, K.; Kiso, Y. *ChemBioChem* **2008**, *9*, 3055–3065.

(208) Hagen, V.; Dekowski, B.; Kotzur, N.; Lechler, R.; Wiesner, B.; Briand, B.; Beyermann, M. *Chem.: Eur. J.* **2008**, *14*, 1621–1627.

(209) Pinheiro, A. V.; Parola, A. J.; Baptista, P. V.; Lima, J. C. *J. Phys. Chem. A* **2010**, *114*, 12795–12803.

(210) Schönleber, R. O.; Bendig, J.; Hagen, V.; Giese, B. *Bioorg. Med. Chem.* **2002**, *10*, 97–101.

(211) Skwarczynski, M.; Noguchi, M.; Hirota, S.; Sohma, Y.; Kimura, T.; Hayashi, Y.; Kiso, Y. *Bioorg. Med. Chem. Lett.* **2006**, *16*, 4492–4496.

(212) Fournier, L.; Aujard, I.; Le Saux, T.; Maurin, S.; Beaupierre, S.; Baudin, J.-B.; Jullien, L. *Chem.: Eur. J.* **2013**, *19*, 17494–17507.

(213) Shembekar, V. R.; Chen, Y.; Carpenter, B. K.; Hess, G. P. *Biochemistry* **2007**, *46*, 5479–5484.

(214) Shembekar, V. R.; Chen, Y.; Carpenter, B. K.; Hess, G. P. *Biochemistry* **2005**, *44*, 7107–7114.

(215) Gandioso, A.; Cano, M.; Massaguer, A.; Marchan, V. *J. Org. Chem.* **2016**, *81*, 11556–11564.

(216) Takano, H.; Narumi, T.; Ohashi, N.; Suzuki, A. Z.; Furuta, T.; Nomura, W.; Tamamura, H. *Tetrahedron* **2014**, *70*, 4400–4404.

(217) Fernandes, M. J. G.; Costa, S. P. G.; Gonçalves, M. S. T. *Tetrahedron* **2011**, *67*, 2422–2426.

(218) Soares, A. M. S.; Hungerford, G.; Costa, S. P. G.; Gonçalves, M. S. T. *Eur. J. Org. Chem* **2015**, *2015*, 5979–5986.

(219) Li, Y.-M.; Shi, J.; Cai, R.; Chen, X.-Y.; Guo, Q.-X.; Liu, L. *Tetrahedron Lett.* **2010**, *51*, 1609–1612.

(220) Petit, M.; Tran, C.; Roger, T.; Gallavardin, T.; Dhimane, H.; Palma-Cerda, F.; Blanchard-Desce, M.; Acher, F. C.; Ogden, D. C.; Dalko, P. I. *Org. Lett.* **2012**, *14*, 6366–6369.

(221) Davis, M. J.; Kragor, C. H.; Reddie, K. G.; Wilson, H. C.; Zhu, Y.; Dore, T. M. *J. Org. Chem.* **2009**, *74*, 1721–1729.

(222) Obi, N.; Momotake, A.; Kanemoto, Y.; Matsuzaki, M.; Kasai, H.; Arai, T. *Tetrahedron Lett.* **2010**, *51*, 1642–1647.

(223) An, H.-Y.; Ma, C.; Li, W.; Harris, K. T.; Dore, T. M.; Phillips, D. L. *J. Phys. Chem. A*, *114*, 2498–2505.

(224) Ma, J.; Cheng, S. C.; An, H.-Y.; Li, M.-D.; Ma, C.; Rea, A. C.; Zhu, Y.; Nganga, J. L.; Dore, T. M.; Phillips, D. L.

(225) Sun, F.; Zhang, L.; Yan, J.; Xu, L.; Fang, D.; Luo, S.-Z. *J. Phys. Org. Chem.* **2014**, *27*, 981–985.

(226) Literák, J.; Dostalova, A.; Klán, P. *J. Org. Chem.* **2006**, *71*, 713–723.

(227) Ngoy, B. P.; Šebej, P.; Šolomek, T.; Lim, B. H.; Pastierik, T.; Park, B. S.; Givens, R. S.; Heger, D.; Klán, P. *Photochem. Photobiol. Sci.* **2012**, *11*, 1465.

(228) Liu, M.; Li, M.-D.; Xue, J.; Phillips, D. L. *J. Phys. Chem. A* **2014**, *118*, 8701–8707.

(229) Senadheera, S. N. I. A Crossover Mechanistic Investigation of the Wolff vs. photoFavorskii Rearrangement of DiazopHydroxyacetophenone: Methoxy Substituent Effects on pHydroxyphenacyl Cage II. Exploratory Studies of HydroxyquinolineBased Phototriggers., Kansas, 2010.

(230) Cope, E. D. The Role of the Leaving Group in the Photo-Favorskii Rearrangement of p-Hydroxyphenacyl., Kansas, 2008.

(231) Barman, S.; Mukhopadhyay, S. K.; Biswas, S.; Nandi, S.; Gangopadhyay, M.; Dey, S.; Anoop, A.; Pradeep Singh, N. D. *Angew. Chem.* **2016**, *55*, 4194–4198.

(232) Perera, C. Exploratory Photochemistry: Pushing the Boundaries of the p-Hydroxyphenacyl Photoremovable Protecting Group., Kansas, 2009.

(233) Stensrud, K. F. Investigative Photochemistry: Elucidating the Mechanism of the Photo-Favorskii Rearrangement., Kansas, 2008.

(234) Zhou, L.; Yang, H.; Wang, P. *J. Org. Chem.* **2011**, *76*, 5873–5881.

(235) Gagey, N.; Emond, M.; Neveu, P.; Benbrahim, C.; Goetz, B.; Aujard, I.; Baudin, J.-B.; Jullien, L. *Org. Lett.* **2008**, *10*, 2341–2344.

(236) Gagey, N.; Neveu, P.; Benbrahim, C.; Goetz, B.; Aujard, I.; Baudin, J.-B.; Jullien, L. *J. Am. Chem. Soc.* **2007**, *129*, 9986–9998.

(237) Gagey, N.; Neveu, P.; Jullien, L. *Angew. Chem.* **2007**, *46*, 2467–2469.

(238) Furuta, T.; Hirayama, Y.; Iwamura, M. *Org. Lett.* **2001**, *3*, 1809–1812.

(239) Kamdzhilov, Y.; Wirz, J. *Photochem. Photobiol. Sci.* **2007**, *6*, 865–872.

(240) Jana, A.; Atta, S.; Sarkar, S. K.; Singh, P. N. D. *Tetrahedron* **2010**, *66*, 9798–9807.

(241) Blake, J. A.; Lukeman, M.; Scaiano, J. C. *J. Am. Chem. Soc.* **2009**, *131*, 4127–4135.

(242) Avila Ferrer, F. J.; Cerezo, J.; Soto, J.; Improta, R.; Santoro, F. *Comp. Theor. Chem.* **2014**, *1040-1041*, 328–337.

(243) Avila Ferrer F. J.; Santoro, F. *Phys. Chem. Chem. Phys.* **2012**, *14*, 13549–13563.

(244) Santoro, F., a Fortran 77 code, available at http://village.pi.iccom.cnr.it.

(245) Santoro, F.; Improta, R.; Lami, A.; Bloino, J.; Barone, V. *J. Chem. Phys.* **2007**, *126*, 84509.

(246) Santoro, F.; Lami, A.; Improta, R.; Barone, V. *J. Chem. Phys.* **2007**, *126*, 184102.

# Abbreviations

| | |
|---|---|
| 2D-IR . . . . . . . . . . . . . . . . . . . . | two-dimensional infrared |
| ACN . . . . . . . . . . . . . . . . . . . . | acetonitrile |
| ATP . . . . . . . . . . . . . . . . . . . . . | adenosintriphosphate |
| BBO . . . . . . . . . . . . . . . . . . . . | Barium boron oxide |
| BODIPY . . . . . . . . . . . . . . . . | boron dipyrromethene core |
| CLiC . . . . . . . . . . . . . . . . . . . . | Complex Scenarios of Light Control |
| $cm^{-1}$ . . . . . . . . . . . . . . . . . . . . | wavenumber |
| DEACM . . . . . . . . . . . . . . . . . | [7-(diethylamino)coumarin-4-yl]methyl |
| DFG . . . . . . . . . . . . . . . . . . . . | difference frequency generation |
| DMB . . . . . . . . . . . . . . . . . . . . | dimethoxybenzoin |
| DMNB . . . . . . . . . . . . . . . . . . | dimethoxybenzyl |
| ESA . . . . . . . . . . . . . . . . . . . . . | excited state absorption |
| EXSY . . . . . . . . . . . . . . . . . . . | exchange spectroscopy |
| FEIR . . . . . . . . . . . . . . . . . . . . | fluorescence-encoded infrared |
| FP . . . . . . . . . . . . . . . . . . . . . . | Fabry-Pérot |
| FTIR . . . . . . . . . . . . . . . . . . . . | Fourier transformation infrared |
| fs . . . . . . . . . . . . . . . . . . . . . . . | femtosecond |
| HPLC . . . . . . . . . . . . . . . . . . . | high-performance liquid chromatography |
| IR . . . . . . . . . . . . . . . . . . . . . . | infrared |
| IVR . . . . . . . . . . . . . . . . . . . . . | internal vibrational redistribution |
| LG . . . . . . . . . . . . . . . . . . . . . | leaving group |
| M . . . . . . . . . . . . . . . . . . . . . . | molar |
| nm . . . . . . . . . . . . . . . . . . . . . | nanometer |
| NMR . . . . . . . . . . . . . . . . . . . | nuclear magnetic resonance |
| NOPA . . . . . . . . . . . . . . . . . . | non-collinear optical parametric amplifier |
| OD . . . . . . . . . . . . . . . . . . . . . | optical density |
| OH . . . . . . . . . . . . . . . . . . . . . | hydroxyl group |
| OPA . . . . . . . . . . . . . . . . . . . . | optical parametric amplifier |
| $p$ . . . . . . . . . . . . . . . . . . . . . . | *para* |
| pH . . . . . . . . . . . . . . . . . . . . . | measure of acidity or alkalinity |
| $p$HP . . . . . . . . . . . . . . . . . . . . | *para*-hydroxyphenacyl |
| PPG . . . . . . . . . . . . . . . . . . . . | photolabile protection group |
| ps . . . . . . . . . . . . . . . . . . . . . . | picosecond |
| $S_1$ . . . . . . . . . . . . . . . . . . . . . | singulet state |
| $S_{10}$ . . . . . . . . . . . . . . . . . . . . | steepness factor |

SHG ...................... second harmonic generation
SFG ...................... sum frequency generation
$T_1$ ...................... triplet state
T2D-IR ................. transient two-dimensional infrared
TRIR ................... transient infrared
Vis ...................... visible
VIPER ................. Vibrationally promoted electronic resonance
UV-Vis ................. ultraviolet-visible

212

# List of Figures

224

# Danksagung

Herzlichen Dank an alle Menschen, die diese Arbeit möglich gemacht und unterstützt haben. Diese Doktorarbeit gehört zu einem tollen, anspruchvollen, spannenden Projekt und dieses Projekt wird von so vielen großartigen, fleißigen und starken Forscher*innen begleitet. Bevor ich mich bei einigen davon persönlich bedanke, möchte ich mich bei der Deutschen Forschungs Gesellschaft für die Finanzierung der ersten drei Jahre meiner Promotion über die Research Training Group *CLiC - Complex Scenarios of Light Control* bedanken und bei Professor Jens Bredenbeck für den Rest.

Zusätzlich danke ich Jens Bredenbeck für die Möglichkeit meine Promotion mit seiner Betreuung durchzuführen. Vielen Dank für alles was ich von Dir lernen durfte, für die Erklärungen, die Diskussionen, das Verständnis und die Überraschungsabschiedswaffeln. Vier Jahre sind eine lange Zeit um sich beim Danksagung schreiben an alle tollen und wichtigen Momente zu erinnern. Also bleibt vielleicht übrig: Danke, dass ich mich gerne daran erinnere.

Prof. Josef Wachtveitl danke ich für die Zweitkorrektur dieser Arbeit und seine Arbeit als Teil meines Mentoring-Meetings in *CLiC*.

Prof. Irene Burghardt danke ich für Ihre Mentor*innentätigkeit im Rahmen von *CLiC* und die Betreuung in den Mentoring-Meetings.

Luuk van Wilderen danke ich für die Hilfe im Labor, bei der Datenauswertung und ganz besonders für das Gegenlesen dieser Arbeit. Aber auch für die vielen schönen Diskussionen und das gemeinsame Paper schreiben und das Teilen und Übersetzten von niederländischen Sprichworten. *Zwei Seelen - ein Gedanke* wird mir noch lange als schönes Beispiel bleiben.

Carsten, mein Carsten!

Matiss Reinfelds danke ich für die wundervolle Versorgung mit Proben. Ich schätze mich sehr glücklich, dass ich mit Dir arbeiten durfte. Es war eine Freude. Vielen Dank auch, dass Du diesen Vortrag gehalten hast!

Jan von Cosel danke ich für die Theorie-Unterstützung. Danke für die Rechnungen und ihre Erklärungen und unsere gemeinsamen Versuche VIPER und Photochemie etwas besser zu verstehen.

Bei den Professor*innen Heckel und Burghhardt und ihren Arbeitsgruppen bedanke ich mich für die schöne und erfolgreiche Kooperation. Ohne diese wäre das Projekt nicht möglich.

Mein Dank an die Organisator\*innen, Professor\*innen und Promotionsstudierenden, die das Graduiertenkolleg *CLiC* bilden in dessen Rahmen meine Promotion stattgefunden hat und durch welches die wichtigen Kollaborationen ermöglicht wurden.

Der AG Riedle, Prof. Riedle und Emanuel Wittmann danke ich für die Kooperation zur Entwicklung einer neuen IR Quelle.

Herzlich danke ich den wundervollen Menschen in meinem Büro für die wundervolle gemeinsame Zeit. Das war schon eine lange und bewegte Zeit... und ich hatte viel Spaß mit Euch. Ich könnte mir jetzt Mühe geben hier ganz viele tolle Erinnerungen aufzuschreiben und die gibt es auch, aber stattdessen schreibe ich Euch lieber eine Mail, ob wir mal wieder was zusammen machen wollen!

Meinen Teetrink-Verbündeten danke ich für die gemeinsamen Teestunden, unsere Teeschublade mit ihrer riesigen Auswahl, die Gesellschaft beim Wasserkochen... Ach einfach alles... Wenn ich in meinem neuen Büro Teetrinke, denke ich an Euch.

Vielen Dank an den gesamten AKB! Danke für die Ausflüge, ob das nun coole Gruppentagesausflüge waren oder auch nur mal schnell in den Baumarkt um ein Ventil zum Chillerbasteln zu holen (Danke Julian). Danke für all den Kuchen und die tollen Gespräche beim Mittagessen. Wo sonst diskutiert man Fragen wie *Welches Tier in der Savanne wärst Du gerne? Welche Farben haben Drache? Was hättest Du lieber, Dich in ein Tier Deiner Wahl verwandeln zu können (immer das selbe Tier, keine Fabelwesen!) oder einen fliegenden Besen/Teppich?* Danke Jan, dass Du mein Essen aufgegessen hast, wenn ich es nicht geschafft habe. Danke auch, dass ihr meine Stand-Up Versuche so angefeuert habt. Ich besorge Karten, wenn es soweit ist.

Danke an die Menschen, die in ihren Projekten das Labor und das Setup zu dem aufgebaut haben was es heute ist und damit diese anspruchsvollen Experimente überhaupt erst möglich gemacht haben.

Vielen Dank an alle Menschen mit denen ich in dieser Zeit zusammen arbeiten und von denen ich lernen durfte.

Danke auch an Gwion D. Ragnell *for benevolence and kind assistance.*

Von Herzen danke ich meinen Liebsten, meiner Familie und meinen Freunden. Schön, dass ihr da seid und Danke, dass ich Euch kennen darf.

# Lebenslauf

Daniela Kern-Michler
In der Wink 3
60437 Frankfurt am Main


\* 31.12.1989 Seligenstadt


### Akademisch Laufbahn

| | |
|---|---|
| seit November 2014 | Promotion im Graduiertenkolleg Complex Scenarios of Light-Control (CLiC), Arbeitsgruppe von Prof. Bredenbeck, Institut für Biophysik, Fachbereich 13 Physik, Goethe-Universität, Frankfurt am Main. |
| 01/2013 - 10/2014 | Master of Science Biophysik, Goethe-Universität, Frankfurt am Main (1,0). *Masterthesis:* Using Frequency Fluctuations to Probe Molecular Dynamics (1,0). |
| 10/2009 - 01/2013 | Bachelor of Science Biophysik, Goethe-Universität, Frankfurt am Main (1,9). *Bachelorthesis:* Introduction of a Thiocyanate Label into PDZ (1,0). |
| 02.07.2009 | Allgemeine Hochschulreife (1,2), Frankfurt. |


### Lehrerfahrung

| | |
|---|---|
| 2016-2018 | Tutorin für Biophysik 1, Goethe-Universität, Frankfurt am Main. |
| 10/2013-02/2014 | Tutorin für Experimentalphysik 1, Goethe-Universität, Frankfurt am Main. |


### Preise

| | |
|---|---|
| 05/2016 | PCCP Posterpreis |
| 11/2012 | Posterpreis der Physikerinnentagung |

**Akademische Lehrer:**

B. Averhoff, W. Aßmus, N. Auner, P. Bernardi, M. Braun, J. Bredenbeck, I. Burghardt, C. Büchel, R. Dörner, V. Dötsch, I. Ebersberger, E. Engel, K.-D. Entian, E. Egert, K. Fendler, A. Heckel, R. Hegger, M. Heilemann, O. Klein, I. Koch, W. Mäntele, V. Müller, H. D. Osiewacz, M. Piepenbring, D.-H. Rischke, H. Roskos, L. Schäfer, E. Schleiff, M.U. Schmidt, H. Schwalbe, J. Soppa, A. Starzinski-Powitz, M. Thomson, J. Wachtveitl, G. Wille, , J. Wöhnert.

# Veröffentlichungen und Konferenzbeiträge

## Veröffentlichungen

**Controlling photochemistry via isotopomers and IR pre-excitation** Daniela Kern-Michler,* Carsten Neumann,* Nicole Mielke, Luuk J.G.W. van Wilderen, Matiss Reinfelds, Jan von Cosel, Fabrizio Santoro, Alexander Heckel, Irene Burghardt, Jens Bredenbeck
*J. Am. Chem. Soc. 2018, 140, 3, 926-931*, DOI: 10.1021/jacs.7b08723.

**Vibrationally resolved electronic spectra including vibrational pre-excitation: Theory and application to VIPER spectroscopy** Jan von Cosel, Javier Cerezo, Daniela Kern-Michler, Carsten Neumann, Luuk J. G. W. van Wilderen, Jens Bredenbeck, Fabrizio Santoro, and Irene Burghardt
*J. Chem. Phys. 147, 164116 (2017)*, DOI: 10.1063/1.4999455.

**Correction: Vibrational dynamics and solvatochromism of the label SCN in various solvents and hemoglobin by time dependent IR and 2D-IR spectroscopy** Luuk J. G. W. van Wilderen, Daniela Kern-Michler, Henrike M. Müller-Werkmeister, Jens Bredenbeck
*Phys. Chem. Chem. Phys. 19, 9676-9678 (2017)*, DOI: 10.1039/c7cp90063e

**Picosecond activation of the DEACM photocage unravelled by VIS-pump-IR-probe spectroscopy** Luuk J. G. W. van Wilderen*, Carsten Neumann*, Alexandre Rodrigues-Correia, Daniela Kern-Michler, Nicole Mielke, Mattis Reinfelds, Alexander Heckel, and Jens Bredenbeck
*Phys. Chem. Chem. Phys. 19, 6487-6496 (2017)*, DOI: 10.1039/C6CP07022A.

**Ultrafast species-selective photochemistry in mixtures** Daniela Kern-Michler, Carsten Neumann, Nicole Seibert, Luuk J. G. W. van Wilderen, Matiss Reinfelds,Jan von Cosel, Alexander Heckel, Irene Burghardt, Jens Bredenbeck.
*Bunsenmagazin 2016 (5), 189.*

**Vibrational dynamics and solvatochromism of the label SCN in various solvents and hemoglobin by time dependent IR and 2D-IR spectroscopy** Luuk J. G. W. van Wilderen\*, Daniela Kern-Michler\*, Henrike M. Müller-Werkmeister, Jens Bredenbeck
*Phys. Chem. Chem. Phys. 16, 19643-19653 (2014)*, DOI: 10.1039/C4CP01498G

## In Vorbereitung

**Working Title: Photochemical mechanism of DEACM uncaging: A combined computational and time-resolved spectroscopic study**
Preliminary List of Authors: Carsten Hamerla\*, Carsten Neumann\*, Jan von Cosel\*, Konstantin Falahati\*, Madhava Niraghatam, Daniela Kern-Michler, Luuk J. G. W. van Wilderen, Jens Bredenbeck, Irene Burghardt

**Working Title: Selecting between isotopologues of a photocage by IR preexcitation**
Preliminary List of Authors: Daniela Kern-Michler\*, Carsten Neumann\*, Matiss Reinfelds, Luuk J. G. W. van Wilderen, Alexander Heckel, Jens Bredenbeck

## Konferenzbeiträge

**Controlling Photochemistry by VIPER 2D-IR - Application and Requirements**, *Poster & Postertalk* Daniela Kern-Michler, Carsten Neumann, Luuk J. G. W. van Wilderen, Nicole Mielke, Matiss Reinfelds, Jan von Cosel, Alexander Heckel, Irene Burghardt, Jens Bredenbeck. Design and Light Control, 30.08.-01.09.2017, Niedernberg, Deutschland.

**Photochemistry by VIPER 2D-IR - Experiments & Computations**, *Poster* Daniela Kern-Michler, Carsten Neumann, Luuk J. G. W. van Wilderen, Nicole Mielke, Matiss Reinfelds, Jan von Cosel, Alexander Heckel, Irene Burghardt, Jens Bredenbeck. Quantum Dynamics and Spectroscopy in Condensed-Phase Materials and Bio-Systems, 21.-26.05.2017, Les Houches, Frankreich.

**Ultrafast species-selective photochemistry in mixtures by VIPER 2D-IR**, *Poster* Daniela Kern-Michler, Carsten Neumann, Nicole Seibert, Luuk J. G. W. van Wilderen, Matiss Reinfelds, Jan von Cosel, Alexander Heckel, Irene Burghardt, Jens Bredenbeck. Conference on Photochemistry, 26.-28.09.2016, Jena, Deutschland.

**Ultrafast species-selective photochemistry in mixtures**, *Poster* Daniela Kern-Michler, Carsten Neumann, Nicole Seibert, Luuk J. G. W. van Wilderen, Matiss Reinfelds, Jan von Cosel, Alexander Heckel, Irene Burghardt, Jens Bredenbeck. 115. Bunsentagung, 05.-07.05.2016, Rostock, Deutschland.

**Femtosecond 2D-IR spectroscopy of SCN**, *Vortrag* Daniela Kern-Michler, Luuk J. G. W. van Wilderen, Henrike M. Müller-Werkmeister, Jens Bredenbeck. DPG-Frühjahrstagung, AMOP Sektion, 17.-21.03.2014, Berlin, Deutschland.

**IR-Spectroscopy and Artificial Amino Acids: A Great Couple for Protein Biophysics**, *Poster* Larissa Blankenburg, Jens Bredenbeck, Katharina Eberl, Martin Essig, Daniela Kern-Michler, Henrike M. Müller-Werkmeister. Physikerinnentagung, 25.-28.11.2012, Freiburg, Deutschland.

## Anderen Veranstaltungen

**Woher wissen wir das? Ausgewählte Wahrheiten über die molekularen Grundlagen des Lebens**, *Vortrag* Night of Science, 09.06.2017, Frankfurt, Deutschland.

**VIPER 2D-IR Spectroscopy**, *Vortrag* Heinrich Heine Universität, Arbeitsgruppenseminar Gilch, 24.11.2016, Düsseldorf, Deutschland.

**Ultrafast species-selective photochemistry in mixtures**, *Poster* Daniela Kern-Michler, Carsten Neumann, Nicole Seibert, Luuk J. G. W. van Wilderen, Matiss Reinfelds, Jan von Cosel, Alexander Heckel, Irene Burghardt, Jens Bredenbeck. Treffen Graduiertenkollegs CLiC und GRK2039, 05.-06.04.2016, Freudenstadt-Lauterbad, Deutschland.